The Dissertation Committee for Xiaotang Lu Certifies that this is the approved version of the following dissertation:

Silicon and Germanium Nanostructures: Synthesis and In Situ TEM Study

Committee:

Brian A. Korgel, Supervisor

John G. Ekerdt

James R. Chelikowsky

Allan H. MacDonald

Guihua Yu

Silicon and Germanium Nanostructures: Synthesis and In Situ TEM Study

by

Xiaotang Lu, B.E.; M.S.

Dissertation

Presented to the Faculty of the Graduate School of

The University of Texas at Austin

in Partial Fulfillment

of the Requirements

for the Degree of

Doctor of Philosophy

The University of Texas at Austin

August 2015

Dedication

For my loving husband and family.

Acknowledgements

I would like to thank my graduate advisor, Dr. Brian Korgel, for all of the guidance, insight, and opportunities he has provided for me throughout my graduate career. It is remarkable to reflect on how much I have learned during the past four years. I would also like to thank Dr. Ekerdt, Dr. Chelikowsky, Dr. MacDonald and Dr. Yu for their support and for agreeing to serve on my committee.

There are dozens of Korgel group members who deserve recognition for their contributions they have made to my success. I am indebted to Timothy Bogart who did not only teach me the fundamentals of nanowire synthesis at the beginning of my Ph.D study and also worked as a great partner for the rest three years. Colin Hessel and Yixuan Yu got me involved with and taught me the basics of luminescent silicon, which became the focus of my research. I would also like to thank Vincent Holmberg, Aaron Chockla and Justin Harris for their support and guidance through my initial year. Heartfelt thanks are in order for the remaining members of the Korgel group that I have been fortunate enough to work with, including Taylor Harvey, Jackson Stolle, Christian Bosoy, Julian Villareal, Doug Pernik, Philip Liu, Emily Adkins, Dorothy Silbaugh, Vikas Reddy-Vogu, Cherrelle Thomas, Adrien Guillaussier, and Jon Peck.

I also owe thanks to the experts who have helped me with characterization techniques along the way: Dwight Romanovicz for SEM and low resolution TEM, Ji-Ping Zhou and Karalee Jarvis for help with high-resolution TEM, Vince Lynch for XRD training, Hugo Celio for his help with FTIR.

I owe a debt of gratitude to my collaborators: Dr. Chongmin Wang, Dr. Meng Gu and Yang He at the Pacific Northwest National Laboratory for their work with in situ

TEM study; Dr. Philip Boudjouk and Kenny Anderson at North Dakota State University for providing cyclohexasilanes and all the valuable discussions; Dr. Jordi Arbiol and his group at Institut Català de Nanociència i Nanotecnologia for all the advanced TEM charaterizations; Dr. Francisco Meseguer and his group at Universitat Politècnica de València for the collaboration in optical study of amorphous silicon particles.

There are none more deserving of thanks than those who work behind the scenes to make my research possible: Dr. Desiderio Kovar for his advising every semester in my initial years that kept me in the right track of degree pursuing, Rebecca Christian and Bonnie Stewart-Richlen for making sure my registration and paperwork was always in order, Eddie Ibarra for helping place orders and making sure they arrived on time, Kevin Haynes for assistance with shipping and receiving, Jim Smitherman and Butch Cunningham for various maintenance items.

I would also like to thank my master advisors, Dr. Yadong Li and Dr. Qing Peng, at Tsinghua University for introducing me to scientific research and encouraging me to pursue a Ph.D abroad. Yunping Fei is the best roommate that I have had the pleasure to live with. Lastly, but most importantly, I wish to thank my family and friends for their love, support, and encouragement over the years, making me the person I am today.

Silicon and Germanium Nanostructures: Synthesis and In Situ TEM Study

Xiaotang Lu, Ph. D

The University of Texas at Austin, 2015

Supervisor: Brian A. Korgel

A variety of chemical routes exist for a wide range of nanomaterials with tunable size, shape, composition and surface chemistry. Of these materials, silicon (Si) and germanium (Ge) nanomaterials have been some of the most challenging to synthesize. Solution-liquid-solid (SLS) growth of Si was studied using tin (Sn) as the seeding metal. Si nanorods with narrow diameters can be grown by the decomposition of trisilane in hot squalane in the presence of Sn nanocrystals. Photoluminescence could be obtained from the Si nanorods by thermal hydrosilylation passivation. This colloidal synthesis could be further simplified to a single-step reaction procedure by the *in situ* formation of Sn seed particles. In addition to trisilane as a Si source, isotetrasilane, neopentasilane and cyclohexasilane were studied for Si nanorod growth: all three reactants enabled nanorod formation at lower growth temperatures. A monophenylsilane (MPS) enhanced growth was discovered for supercritical fluid-liquid-solid (SFLS) growth of Ge nanowires that enables the Ge conversion of ~100%. A variety of metalorganic compounds were studied for replacing pre-synthesized metal nanoparticles to induce Ge nanowire growth.

Si and Ge nanowires are some of the most promising anode materials in lithium ion batteries (LIBs) because of their high lithium storage capacity. However, the significant chemical and physical changes that occur during cycling hamper their

practical uses. *In situ* transmission electron microscopy (TEM) techniques were conducted to observe and understand structural and interfacial changes of the Si and Ge nanowires during electrochemical cycling; and, therefore, resolving the problems with current anodes by materials modification. The *in situ* TEM experiments showed that the incorporation of Sn into Si nanowires can enhance their rate capability. But the enhanced Li diffusion leads to the premature pore formation in Si nanowires. Ge nanowires has been discovered the potential as sodium ion battery anodes after an initial activation with a lithiation step to amorphize the nanowires.

Table of Contents

List of Tables

List of Figures

SECTION I: *SYNTHESIS OF SILICON AND GERMANIUM NANOSTRUCTURES*

Chapter 1: Introduction to Silicon and Germanium Nanostructures

1.1 Introduction to Silicon and Germanium Nanowire Synthesis

Nanowires is a nanostructure with diameters in the order of a nanometer and lengths ranging from micrometers to millimeters. Nanowires are an interesting class of materials with a wide range of applications, including field effect transistors,[1,2] light emitting diodes,[3,4] photovoltaics[5,6] and high-performance lithium ion batteries.[7,8] Nanorods is a similar one-dimensional nanostructure with aspect ratio lower than nanowires. Figure 1.1 shows scanning electron microscope (SEM) image of gold (Au) seeded germanium (Ge) nanowires and transmission electron microscope image of Au seeded silicon (Si) nanorods. Since nanowires and nanorods are similar nanostructure with the only difference in aspect ratios and synthesized with basically the same growth mechanism, the following introduction of the synthetic methods will not differentiate nanorods from nanowires.

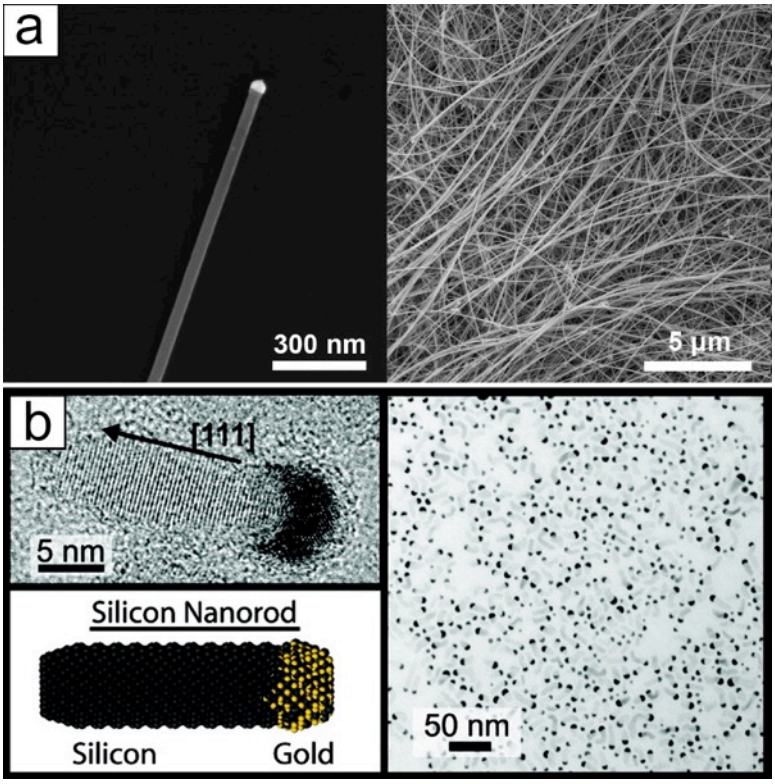

Figure 1.1 (a) SEM image of Au-seeded Ge nanowires and (b) TEM image of Au-seeded Si nanorods.

1.1.1 Seeded Growth of Nanowire

In 1964, Wagner and Ellis reported the growth of Si whiskers from Au droplets in a chemical vapor deposition (CVD) system.[9] This work introduced the term vapor-liquid-solid (VLS) to describe the growth mechanism: the ***vapor*** refers to the reaction medium; the ***liquid*** refers to the fact that the metal seed forms a liquid alloy with the semiconductor; the ***solid*** refers to the crystalline nanowire that extrudes as the resulting product.[10] The VLS growth process can be traced on the binary phase diagram. Figure 1.2 shows the Au-Si binary phase diagram to rationalize the growth mechanism of Au-seeded Si nanowires. From the left side of the phase diagram, at a temperature above the eutectic

temperature, the Au seed particles start in the solid phase. Si precursors decompose into Si atoms, which diffuse into the Au particles (region I). Si keeps accumulating in the solid particle. When the composition of the particle passes the left liquidus line, the particle liquefies into an Au-Si alloy droplet (region II). After the Au-Si alloy droplet supersaturated with Si, Si precipitates from the liquid surface and crystallizes. Continually feeding of Si in this supersaturated system results in the growth of a crystalline Si nanowire (region 3). In this seeded growth, the nanowire diameter could be controlled by the diameter of metal seeds, while the length could be adjusted by the semiconductor-metal atomic ratio.

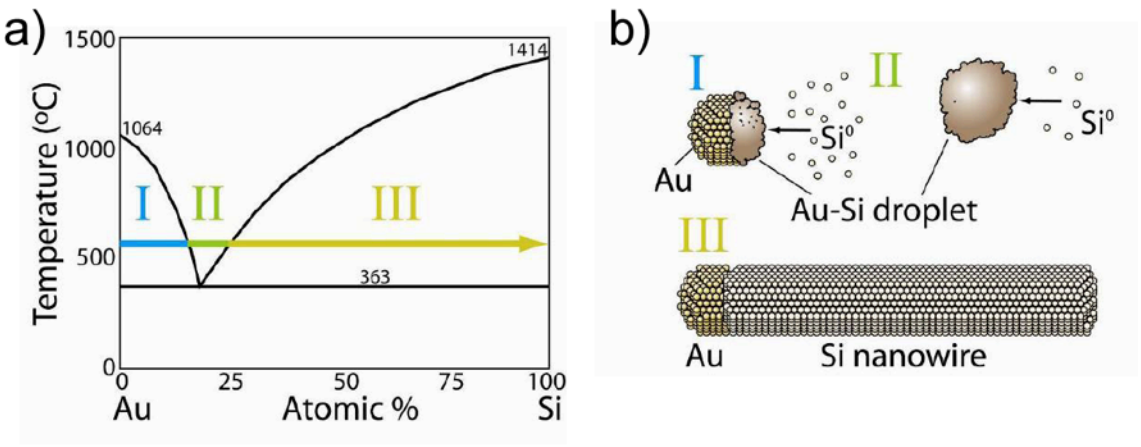

Figure 1.2 Illustration of a typical growth of Au seeded Si nanowires. (a) Au-Si phase diagram: the arrows track the composition change as Si adding to Au and divide the growth process into three steps. (b) Schematics of the nanowire at different growth step.

1.1.2 Solution-based Synthesis

In1995，Buhro group developed the seeded growth of III-V semiconductor nanowires in solution and named their growth mechanism as solution-liquid-solid (SLS)

following the naming convention from VLS growth.[11] The SLS has been shown effectiveness in growing both III-V semiconductor nanowires[12–14] and II-VI semiconductor nanowires.[14,15] The SLS growth of Si and Ge nanowires is more difficult, since they require much higher growth temperature. High boiling point solvents such as squalane, trioctylphosphine and octacosane must be used to reach the high reaction temperature (> 350ºC) at atmospheric pressure. It has been recently shown that Si and Ge nanowires can be grown in solution by using those high boiling point solvents.[16–18]

To overcome the limit of solvent, an alternative is to use the common solvents, such as hexane and toluene, and pressurize above their critical points to form the high-temperature, high-pressure, supercritical fluid phase. Supercritical fluid enables high reaction temperatures that require for growing Si and Ge nanowires. This method is pioneered by Korgel group and named as supercritical fluid-liquid-solid (SFLS) growth. The SFLS method has been demonstrated success in producing high quality Si and Ge nanowires and also the capability of scaled-up production.[19–22]

1.2 PHOTOLUMINESCENT SILICON NANOMATERIALS

1.2.1 Light Emission from Silicon

Si is an indirect band gap semiconductor, of which the top of the valance band and the bottom of the conduction band are not aligned in the momentum space. Due to the momentum conservation law, the recombination of the electron and the hole in the indirect band gap semiconductor must involve the absorption or emission of a phonon, where the difference between the electron and hole momentum is compensated by the phonon (Figure 1.3). The involvement of phonon makes the light absorption and emission highly inefficient in Si.

To improve the absorption/emission of Si, one of the approaches is to shrink the size of crystalline Si until it is smaller than its Bohr radius (~ 4.5 nm). When the electron and the hole are confined in such small nanocrystals, their wave functions would expand and overlap in momentum space, leading to the direct electron-hole recombination. This effect is known as quantum confinement.[23] Quantum confinement could be achieved in not only 0-dimensional nanostructures, i.e. Si nanoparticles,[24,25] but also in 1-dimensional nanostructures, i.e. Si nanowires and nanorods,[26] when their diameters are approaching the Bohr radius. The density of states in quantum-confined nanostructures is also different from that of the bulk counterpart. Shrinking the size leads the energy density more close to a molecule or atom. This makes the photoluminescence (PL) can be adjusted by changing the size of quantum-confined Si nanomaterials.

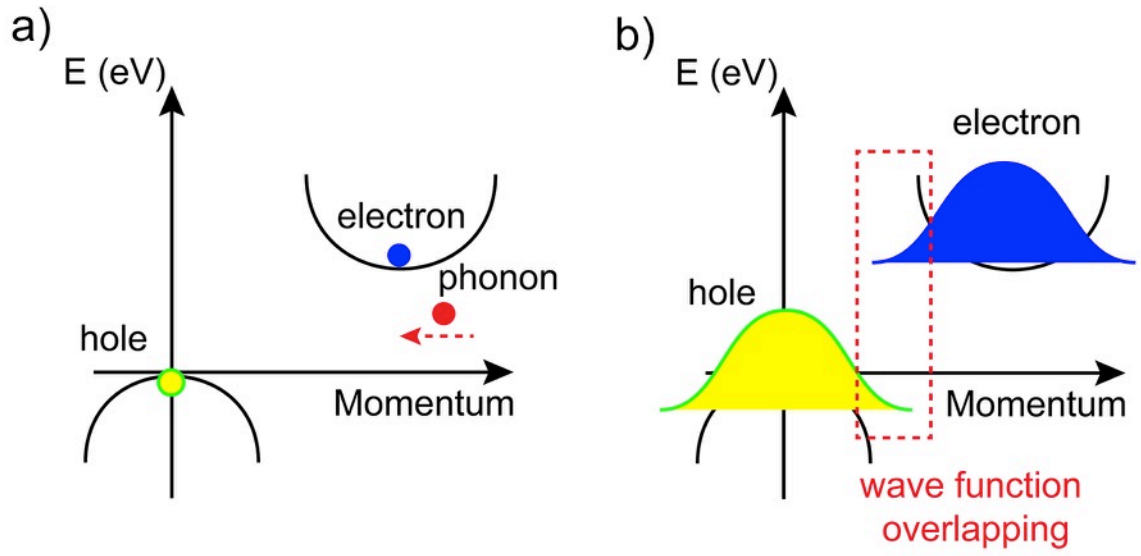

Figure 1.3 Schematics show (a) electron-hole recombination in an indirect band gap semiconductor and (b) overlapping of electron and hole wavefunctions in a quantum-confined nanostructure.

1.2.2 Synthesis of Quantum-confined Silicon Nanomaterials

Up to date, many methods have been developed for synthesizing Si nanocrystals. Si nanocrystals embedded in the SiO_2 thin film could be obtained by thermal annealing substoichiometric glass (SiO_x, $x<2$) under inert atmosphere at temperatures around 1100ºC.[27–29] Cannon et al. demonstrated that Si clusters could be obtained by the laser-induced pyrolysis of silanes.[30,31] Si nanocrystals could also be synthesized by the plasma-induced dissociation of silane molecules.[32,33] However, those methods either have poor control over the size distribution of Si nanocrystals or have low production yield.

In 2006, Hessel et al. demonstrated the synthesis of Si nanocrystals by thermal decomposition of hydrogen silsesquioxane (HSQ).[34] Figure 1. Illustrates the reaction pathway of this synthesis.[25,35] HSQ is first annealed under forming gas at temperature ranging from 1000ºC to 1400ºC for an hour to form silicon crystallites embedded in SiO_2 matrix. Annealing temperature could control the size of nanocrystals. The obtained powder is then etched in a mixture of hydrofluoric acid and hydrochloric acid to form hydride-determinated Si nanocrystals, which can be passivated by alkenes through the hydrosilylation reaction. This method has good control over the size of the Si nanocrystals and is adopted by our group for the Si quantum dots study.

However, synthesis of quantum-confined Si nanostructures in solution is still challenging. The difficulties come from the identification of suitable silicon precursor for colloidal synthesis, relative high crystallization temperature that beyond the processing range of most organic solvents, tendency to oxidize and different capping ligand chemistry.[36] The exploration of the colloidal synthesis of quantum-confined Si nanorods will be the focus in this section.

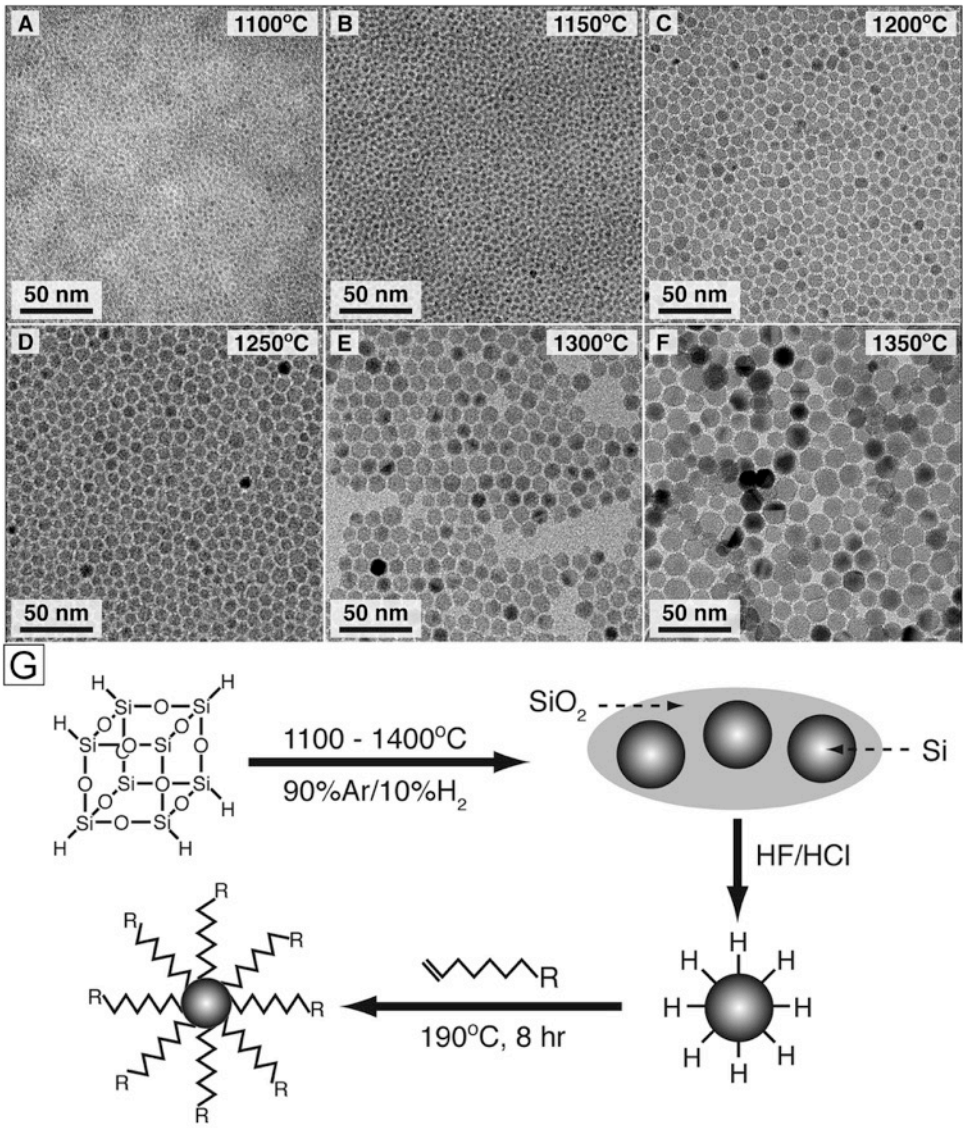

Figure 1.4 (a-f) TEM images of alkene-passivated Si nanocrystals obtained at different annealing temperatures, (g) scheme of the synthesis of alkene-passivated Si nanocrystals by HSQ decomposition.

1.3 SECTION OVERVIEW

This section focuses on developing solution-based syntheses for one-dimensional Si and Ge nanostructures. Chapter 2 demonstrates the synthesis of Si nanorods by

trisilane decomposition in hot squalane in the presence of Sn nanocrystals. Bright photoluminescence has been induced in those Si nanorods by hydrofluoric acid etching and then hydrosilylation with 1-octadecene. Chapter 3 discusses a simplified, single-step reaction for colloidal quantum-size Si and Ge nanorods, where Sn seed particles prepared by *in situ* reduction of a molecular tin(II) complex by trisilane. Chapter 4 investigates isotetrasilane, neopentasilane and cyclohexasilane as reactants for Si nanorod growth. These polysilane hydrides were found to enable lower growth temperatures in solution than any other silane reactants used to date. Chapter 5 explores the SFLS growth of Ge nanowires using either Au or Ni seeds. It is found that the addition of monophenylsilane (MPS) could dramatically improve the yield and quality of both Au- and Ni-seeded Ge nanowires, producing straight nanowires with nearly 100% conversion of diphenylgermane (DPG) to Ge. Chapter 6 demonstrates that Ge nanowires can be produced using a wide range of commercially available metalorganic compounds as catalysts instead of pre-synthesized metal nanoparticles including those with Mn, Fe, Ni, Cu, Ga, In, Pb and Bi. Chapter 7 summarizes the conclusions from this section and provides ideas for further studies.

1.4 REFERENCES

1. Cui, Y.; Zhong, Z.; Wang, D.; Wang, W. U.; Lieber, C. M. High Performance Silicon Nanowire Field Effect Transistors. *Nano Lett*. **2003**, *3* (2), 149–152.

2. Greytak, A. B.; Lauhon, L. J.; Gudiksen, M. S.; Lieber, C. M. Growth and Transport Properties of Complementary Germanium Nanowire Field-Effect Transistors. *Appl. Phys. Lett*. **2004**, *84* (21), 4176–4178.

3. Kõnenkamp, R.; Word, R. C.; Schlegel, C. Vertical Nanowire Light-Emitting Diode. *Appl. Phys. Lett*. **2004**, *85* (24), 6004.

4. Qian, F.; Gradecak, S.; Li, Y.; Wen, C.-Y.; Lieber, C. M. Core/multishell Nanowire Heterostructures as Multicolor, High-Efficiency Light-Emitting Diodes. *Nano Lett*. **2005**, *5* (11), 2287–2291.

5. Tian, B.; Zheng, X.; Kempa, T. J.; Fang, Y.; Yu, N.; Yu, G.; Huang, J.; Lieber, C. M. Coaxial Silicon Nanowires as Solar Cells and Nanoelectronic Power Sources. *Nature* **2007**, *449* (7164), 885–889.

6. Garnett, E.; Yang, P. Light Trapping in Silicon Nanowire Solar Cells. *Nano Lett.* **2010**, *10* (3), 1082–1087.

7. Chan, C. K.; Peng, H.; Liu, G.; McIlwrath, K.; Zhang, X. F.; Huggins, R. A.; Cui, Y. High-Performance Lithium Battery Anodes Using Silicon Nanowires. *Nat. Nanotechnol.* **2008**, *3* (1), 31–35.

8. Nitta, N.; Wu, F.; Lee, J. T.; Yushin, G. Li-Ion Battery Materials: Present and Future. *Mater. Today* **2015**, *18* (5), 252–264.

9. Wagner, R. S.; Ellis, W. C.; Jackson, K. A.; Arnold, S. M. Study of the Filamentary Growth of Silicon Crystals from the Vapor. *J. Appl. Phys.* **1964**, *35* (10), 2993.

10. Wagner, R. S.; Ellis, W. C. Vapor-Liquid-Solid Mechanism of Single Crystal Growth. *Appl. Phys. Lett.* **1964**, *4* (5), 89–90.

11. Trentler, T. J.; Hickman, K. M.; Goel, S. C.; Viano, a. M.; Gibbons, P. C.; Buhro, W. E. Solution-Liquid-Solid Growth of Crystalline III-V Semiconductors: An Analogy to Vapor-Liquid-Solid Growth. *Science*, 1995, *270*, 1791–1794.

12. Yu, H.; Buhro, W. E. Solution-Liquid-Solid Growth of Soluble GaAs Nanowires. *Adv. Mater.* **2003**, *15* (5), 416–419.

13. Fanfair, D. D.; Korgel, B. A. Bismuth Nanocrystal-Seeded III-V Semiconductor Nanowire Synthesis. *Cryst. Growth Des.* **2005**, *5* (5), 1971–1976.

14. Dong, A.; Wang, F.; Daulton, T. L.; Buhro, W. E. Solution-Liquid-Solid (SLS) Growth of ZnSe-ZnTe Quantum Wires Having Axial Heterojunctions. *Nano Lett.* **2007**, *7* (5), 1308–1313.

15. Wang, F.; Dong, A.; Sun, J.; Tang, R.; Yu, H.; Buhro, W. E. Solution-Liquid-Solid Growth of Semiconductor Nanowires. *Inorg. Chem.* **2006**, *45* (19), 7511–7521.

16. Lu, X.; Fanfair, D. D.; Johnston, K. P.; Korgel, B. A. High Yield Solution-Liquid-Solid Synthesis of Germanium Nanowires. *J. Am. Chem. Soc.* **2005**, *127* (45), 15718–15719.

17. Heitsch, A. T.; Fanfair, D. D.; Tuan, H.-Y.; Korgel, B. A. Solution-Liquid-Solid (SLS) Growth of Silicon Nanowires. *J. Am. Chem. Soc.* **2008**, *130* (16), 5436–5437.

18. Chockla, A. M.; Korgel, B. A. Seeded Germanium Nanowire Synthesis in Solution. *J. Mater. Chem.* **2009**, *19* (7), 996.

19. Holmes, J. D. Control of Thickness and Orientation of Solution-Grown Silicon Nanowires. *Science*, 2000, *287*, 1471–1473.

20. Hanrath, T.; Korgel, B. A. Nucleation and Growth of Germanium Nanowires Seeded by Organic Monolayer-Coated Gold Nanocrystals. *J. Am. Chem. Soc.* **2002**, *124* (7), 1424–1429.

21. Hanrath, T.; Korgel, B. A. Supercritical Fluid–Liquid–Solid (SFLS) Synthesis of Si and Ge Nanowires Seeded by Colloidal Metal Nanocrystals. *Adv. Mater.* **2003**, *15* (5), 437–440.

22. Korgel, B. A. Semiconductor Nanowires: A Chemical Engineering Perspective. *AIChE J.* **2009**, *55* (4), 842–848.

23. Alivisatos, A. P. Semiconductor Clusters, Nanocrystals, and Quantum Dots. *Science*, 1996, *271*, 933–937.

24. Mastronardi, M. L.; Maier-Flaig, F.; Faulkner, D.; Henderson, E. J.; Kübel, C.; Lemmer, U.; Ozin, G. a. Size-Dependent Absolute Quantum Yields for Size-Separated Colloidally-Stable Silicon Nanocrystals. *Nano Lett.* **2012**, *12* (1), 337–342.

25. Hessel, C. M.; Reid, D.; Panthani, M. G.; Rasch, M. R.; Goodfellow, B. W.; Wei, J.; Fujii, H.; Akhavan, V.; Korgel, B. a. Synthesis of Ligand-Stabilized Silicon Nanocrystals with Size-Dependent Photoluminescence Spanning Visible to near-Infrared Wavelengths. *Chem. Mater.* **2012**, *24* (2), 393–401.

26. Guichard, A. R.; Barsic, D. N.; Sharma, S.; Kamins, T. I.; Brongersma, M. L. Tunable Light Emission from Quantum-Confined Excitons in TiSi 2-Catalyzed Silicon Nanowires. *Nano Lett.* **2006**, *6* (9), 2140–2144.

27. Pavesi, L.; Dal Negro, L.; Mazzoleni, C.; Franzò, G.; Priolo, F. Optical Gain in Silicon Nanocrystals. *Nature* **2000**, *408* (6811), 440–444.

28. Hayashi, S.; Nagareda, T.; Kanzawa, Y.; Yamamoto, K. Photoluminescence of Si-Rich SiO2 Films: Si Clusters as Luminescent Centers. *Jpn. J. Appl. Phys.* **1993**, *32* (Part 1, No. 9A), 3840–3845.

29. Lu, Z. H.; Lockwood, D. J.; Baribeau, J.-M. Quantum Confinement and Light Emission in SiO2/Si Superlattices. *Nature* **1995**, *378* (6554), 258–260.

30. CANNON, W. R.; DANFORTH, S. C.; FLINT, J. H.; HAGGERTY, J. S.; MARRA, R. A. Sinterable Ceramic Powders from Laser-Driven Reactions: I, Process Description and Modeling. *J. Am. Ceram. Soc.* **1982**, *65* (7), 324–330.

31. CANNON, W. R.; DANFORTH, S. C.; HAGGERTY, J. S.; MARRA, R. A. Sinterable Ceramic Powders from Laser-Driven Reactions: II, Powder Characteristics and Process Variables. *J. Am. Ceram. Soc.* **1982**, *65* (7), 330–335.

32. Mangolini, L.; Thimsen, E.; Kortshagen, U. High-Yield Plasma Synthesis of Luminescent Silicon Nanocrystals. *Nano Lett.* **2005**, *5* (4), 655–659.

33. Mangolini, L.; Kortshagen, U. Plasma-Assisted Synthesis of Silicon Nanocrystal Inks. *Adv. Mater.* **2007**, *19* (18), 2513–2519.

34. Hessel, C. M.; Henderson, E. J.; Veinot, J. G. C.; Uni, V.; February, R. V; Re, V.; Recei, M.; August, V. Hydrogen Silsesquioxane : A Molecular Precursor for Nanocrystalline Si - SiO 2 Composites and Freestanding Hydride-Surface-Terminated Silicon Nanoparticles. **2006**, No. 1, 6139–6146.

35. Yu, Y.; Hessel, C. M.; Bogart, T. D.; Panthani, M. G.; Rasch, M. R.; Korgel, B. a. Room Temperature Hydrosilylation of Silicon Nanocrystals with Bifunctional Terminal Alkenes. *Langmuir* **2013**, *29* (5), 1533–1540.

36. Kovalenko, M. V; Manna, L.; Cabot, A.; Hens, Z.; Talapin, D. V; Kagan, C. R.; Klimov, X. V. I.; Rogach, A. L.; Reiss, P.; Milliron, D. J.; Guyot-sionnnest, P.; Konstantatos, G.; Parak, W. J.; Hyeon, T.; Korgel, B. A.; Murray, C. B.; Heiss, W. Prospects of Nanoscience with Nanocrystals. *ACS Nano* **2015**, *9* (2), 1012–1057.

Chapter 2: Luminescent Silicon Nanorods[§]

2.1 INTRODUCTION

Many different nanomaterials can be made with controlled size and shape using colloidal synthesis[1–4] and various strategies have been developed for semiconductor nanorods, including ligand-assisted growth,[5–11] oriented attachment,[12–14] and metal nanoparticle seed-induced solution–liquid–solid (SLS) growth controlled by the addition of capping ligands.[15–17] Quantum-size nanorods are interesting because their optical properties can differ significantly from spherical nanocrystals.[18] For example, radiative electron–hole recombination rates and other photophysical processes like Auger recombination can be significantly different in nanorods compared to nanocrystals[19,20] and can lower thresholds for multiexciton generation (MEG)[21] and optical gain,[22] which are important for higher-efficiency photovoltaic devices and nanocrystal-based lasers. To date, silicon (Si) nanorods have been grown colloidally only in one instance by ligand-assisted SLS growth using gold nanocrystal seeds.[16] Although these nanorods were less than 5 nm in diameter and small enough for quantum confinement, they were not found to be photoluminescent.[16,23] Bulk Si is a poor light emitter because of its indirect band gap, but nanoscale Si can exhibit bright luminescence because conservation of crystal momentum is relaxed[24,25] and a variety of synthetic routes have been developed for producing luminescent colloidal Si nanocrystals.[26–36] Kamins and co-workers[37] have shown that gold seeds can quench photoluminescence (PL) in Si nanowires, at least in the case of those grown by the vapor–liquid–solid (VLS) approach. Therefore, Si nanorods grown using Au seeds may not have been luminescent because of Au contamination.

[§] This chapter appears in *Nano letters* **2013**, 13, 3101-3105.

Other seed metals have been used to grow Si nanowires by VLS-like approaches, including Ni,[38] Co,[39] Cu,[40] and Sn.[41–47] The transition metals all create trap states deep within the Si band gap[48] that could quench Si PL. Sn on the other hand does not create deep trap levels in Si;[48] therefore, Sn was explored as a seed metal for Si nanorod synthesis in an attempt to generate luminescent colloidal Si nanorods. Here, we report that Si nanorods can indeed be synthesized using Sn seeds and show that these nanorods can exhibit bright photoluminescence.

2.2 Experimental Details

2.2.1 Materials

Diphenyl ether (Aldrich, >99%), bis[bis(trimethylsilyl)amino]tin(II) ($Sn[N(SiMe_3)_2]_2$, Aldrich), sodium bis(trimethylsilyl)amide solution ($Na[N(SiMe_3)_2]$, Aldrich, 1.0 M in THF), dodecylamine (98%, Aldrich), squalane (>95%, Aldrich) were purchased and used without further purification. Poly(vinylpyrrolidinone)-hexadecane (PVP/HDE) copolymer (Ganex V-216, MW= 7300 g/mol, product ID 72289D) was obtained from ISP Technologies, Inc. Trisilane (Si_3H_8, 100%) was purchased from Voltaix.

2.2.2 Sn Nanoparticle Synthesis

For the synthesis of 8 nm Sn nanoparticles, 2 g of PVP-HDE copolymer and 18 g diphenyl ether were degassed under vacuum at 80ºC for 30 min, then blanketed with N_2 and heated to 180ºC. A reactant solution of 348 μL of $Sn[N(SiMe_3)_2]_2$ and 1800 μL of $Na[N(SiMe_3)_2]$ in THF (1.0 M) was prepared in the glovebox and loaded into a syringe. Once the PVP-HDE solution reached 180ºC, the Sn reactant solution was quickly injected

through a septum into the hot solution. The reaction was maintained at 180ºC for 30 min under N_2 flow and then removed from the heating mantle to cool the reaction.

The Sn nanoparticles were purified by washing with toluene and ethanol followed by centrifugation for three times. For a typical purification step, about 20 mL of toluene was added, followed by the addition of ethanol until the mixture began to appear slightly turbid. The mixture was then centrifuged to precipitate and isolate the nanoparticles. Excessive ethanol addition led to phase separation, which can be relieved by adding more toluene. Purified Sn nanoparticles were then dispersed in dodecylamine to concentration of 0.1 M based on total Sn composition, degassed and stored in a nitrogen-filled glovebox prior to use.

2.2.3 Si Nanorod Synthesis

The Si nanorod synthesis was carried out on a Schlenk line installed in a nitrogen-filled glovebox. 10 mL of degassed squalane and a glass stir bar were added to a flat-bottom flask and attached to the Schlenk line and heated to 410ºC under N_2 flow. In a 1 mL vial, a reactant solution consisting of 125 μL of trisilane and 600 μL of the dodecylamine-dispersed Sn nanoparticles were mixed and drawn into a syringe equipped with a 6" needle. Immediately prior to injection, the stopcock valve was closed to isolate the flask. The reactant solution was then quickly injected into the hot solvent. After 1 min, the stopcock valve was reopened and the heating mantle was removed to cool the reaction. (Caution: trisilane is pyrophoric and must be handled with care.)

Si nanorods were purified by centrifugation for four times with toluene and ethanol mixture. The first precipitation with ethanol should be conducted carefully to prevent phase separation as described in washing Sn seeds. After washing, the nanorods were redispersed in chloroform.

2.2.4 Surface Passivation of Si Nanorods

The dispersion of Si nanorods was dried in a Teflon cup, followed by addition of 4 mL of 37.5% HCl and 10 mL of 40% HF. The Si nanorods were etched under vigorous stirring in the dark for 7 hours, and then isolated from the HF solution by centrifugation. After centrifugation, the supernatant was discarded. The precipitate was washed with ethanol, and then transferred to glass centrifuge tube and washed with chloroform. The precipitate was dispersed in 6 mL of 1-octadecene and loaded into a 10 mL syringe and injected into a sealed flask through a septum and degassed with several freeze-pump-thaw cycles on a Schlenk line. The dispersion was then heated at 190ºC for 15 hours under N_2. The 1-octadecene passivated Si NRs were washed four times with toluene and ethanol, and then dispersed in chloroform for further characterization.

2.2.5 Materials Characterization

Low-resolution transmission electron microscopy (TEM) images were acquired on a FEI Tecnai Spirit Bio Twin operated at 80 kV. High-resolution transmission microscopy (HRTEM) images were acquired on a field emission JEOL 2010F TEM operated at 200 kV. TEM samples were prepared by drop-casting 5 μL of dilute Si nanorods dispersion in chloroform onto a 200 mesh carbon-coated 200 mesh copper TEM grid (Electron Microscopy Science).

X-ray diffraction (XRD) was performed on a Rigaku R-Axis Spider diffractometer with an image plate detector using Cu Kα radiation (λ=1.54 Å) and a graphite monochromator. XRD samples were prepared by mixing a small amount of dried Si nanorods with a droplet of mineral oil and mounting on a cryoloop.

Attenuated total reflectance Fourier transform infrared (ATR-FTIR) spectra were obtained on a Thermo Mattson Infinity Gold FTIR spectrometer equipped with a Spectra-Tech Thermal ARK attenuated total reflectance module.

X-ray photoelectron spectroscopy (XPS) was performed on a Krato Axis Ultra X-ray photoelectron spectrometer, utilizing a monochromatic Al K X-ray source (h=1486.5 eV), hybrid optics (simultaneously employing magnetic and electrostatic lens) and a multi-channel plate detector coupled to a hemispherical analyzer. Si nanorods were drop-cast onto indium tin oxide (ITO) coated glass slides. Measurements were taken with the photoelectron take-off angle normal to the surface of the sample and 45° to the X-ray beam. All spectra were recorded using a single sweep with the aperture slot of 300 m by 700 m. High-resolution spectra were collected with 20 eV pass energy. Spectra were collected at 0.1 eV intervals and 1500 ms integration time through a tungsten coil set at 4.8 V bias with respect to the sample. The pressure in the analysis chamber was typically 3×10^{-9} Torr during data acquisition. Sample charging was corrected by shifting the Si^0 $2p_{3/2}$ to a binding energy of 99.3 eV. Background subtraction was done using a Shirley background model. The Si^0 $2p_{3/2}$ and Si^0 $2p_{1/2}$ peaks were fit with Voigt profiles (30% Gaussian character) centered at 99.3 eV and 99.8 eV, respectively, and the intensity ratio was held at 2:1, corresponding to the spin-orbit splitting ratio for p-orbitals. The Si^{1+}, Si^{2+}, Si^{3+}, Si^{4+}, and Si-C peak contributions were fit using Voigt profiles, which include contributions from both the $2p_{3/2}$ and $2p_{1/2}$ energy states.

Photoluminescence (PL) spectra were acquired on a Varian Cary Eclipse fluorescence spectrophotometer using a quartz cuvette with a 10 mm optical path length. Si nanorods quantum yield was determined by comparing the integrated photon count of nanorod samples to a Rhodamine 101 standard in anhydrous ethanol.

Photoluminescence lifetime was measured by applying the time-corrected single photon counting method, on a Fluorolog-3 spectrophotometer (Horiba Jobin Yvon) with InGaAs photomultiplier tube for visible detection and a Hamamatsu H10330-45 detector for NIR detection. 3.0 mL of 0.05 mg/mL Si nanorods solution was transferred into a

quartz cuvette and secured with the sample holder. A NanoLED with wavelength of 372 nm was used as excitation light source, PL decay was measured at a detection wavelength of 695 nm, and the time resolution of the measurement was 0.2 ns. The PL decay data was fit by a double exponential curve.

2.3 RESULTS AND DISCUSSIONS

The Si nanorods were made by decomposing trisilane (Si_3H_8) in squalane at 410ºC in the presence of Sn nanoparticles and dodecylamine. Trisilane has been shown to be a useful reactant for colloidal growth of Si nanowires[49] and nanorods,[16] as it rapidly decomposes to Si at temperatures below the boiling point of some high boiling solvents, like squalane. Sn has also been shown to be a good seed metal for supercritical fluid–liquid–solid (SFLS) growth of Si nanowires in solvents at slightly higher temperature,[47] and with a low melting point (232°C) and formation of a eutectic with Si it can also seed SLS growth.[50–53] Without addition of Sn or other metal seed particles, trisilane decomposes to amorphous Si particles.[54,55] Dodecylamine is added as a size-stabilizing ligand, as demonstrated first by Heitsch et al.[16] for gold-seeded SLS Si nanorod synthesis. The as-made nanorods were non-luminescent. Only after a subsequent etching procedure to remove surface oxide and an organic capping ligand passivation to prevent further oxidation was luminescence observed from the Sn-seeded Si nanorods. A similar etching and passivation procedure carried out on Au-seeded Si nanorods did not lead to luminescent material.

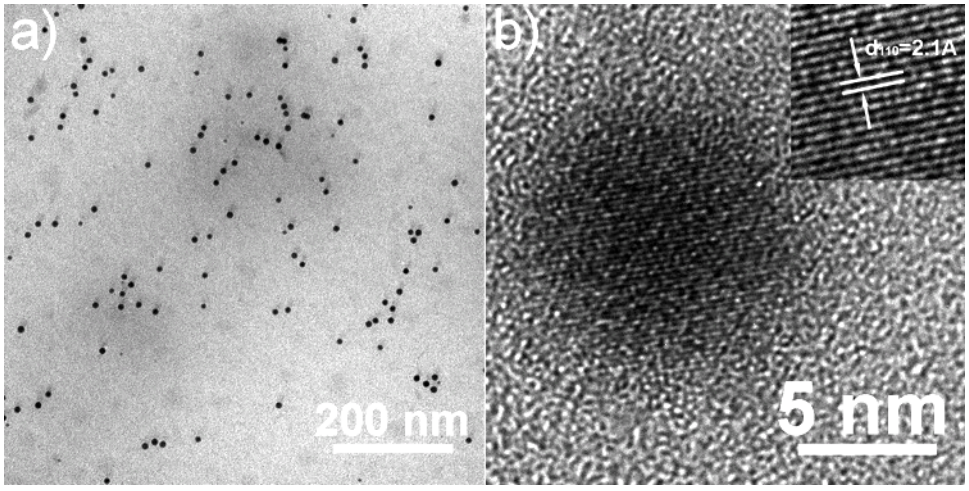

Figure 2.1 (a) Low and (b) high resolution TEM images of of Sn nanocrystals used to seed Si nanorod synthesis. The interplanar spacing of 2.1 Å measured in the TEM image in the inset of (b) corresponds to (110) lattice planes of tetragonal Sn.

Figure 2.2a shows a TEM image of Si nanorods produced by this method. The nanorods are relatively monodisperse with typical lengths of 10–20 nm and diameters ranging from 3 to 4 nm. X- ray diffraction (XRD) confirmed that the nanorods are crystalline, diamond cubic Si (Figure 2.3). Diffraction peaks are also observed from tetragonal Sn.

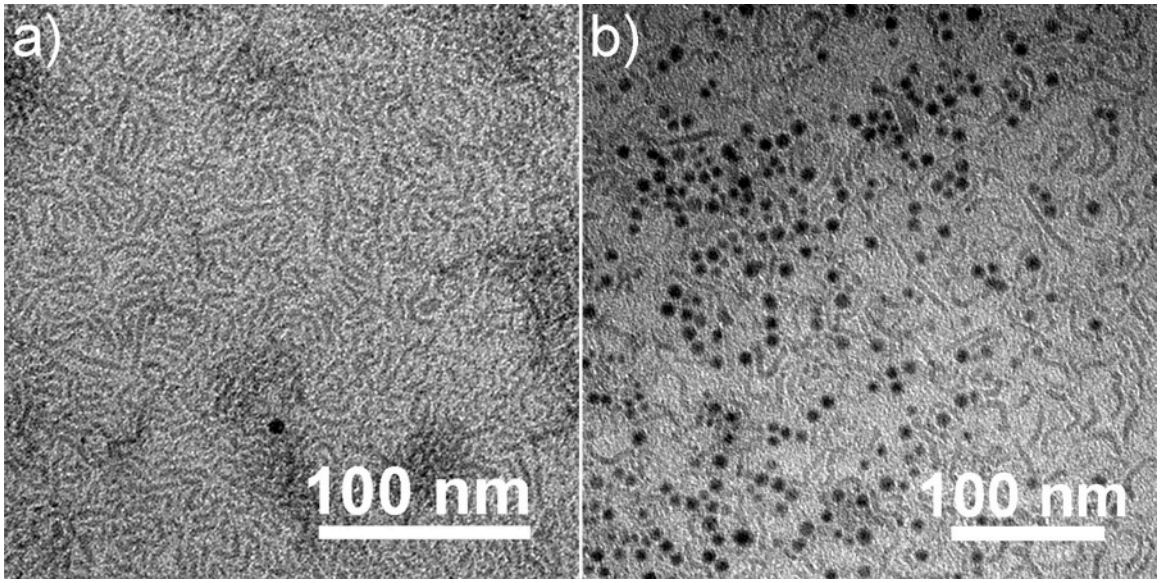

Figure 2.2 TEM images of as-made Sn-seeded Si nanorods prior to surface etching and passivation. The dark dots in (b) are Sn nanoparticles that peeled off from Si nanorods during cooling.

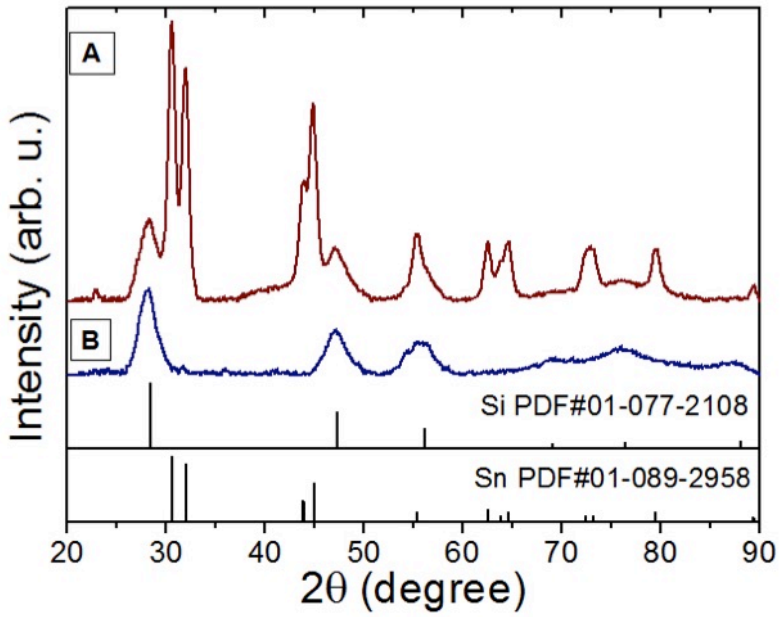

Figure 2.3 XRD of Sn-seeded Si nanorods (a) as-synthesized and (b) after HF etching and hydrosilylation with 1-octadecene. Reference patterns are shown for diamond cubic Si (PDF no.: 01-077-2108) and tetragonal Sn (PDF no.: 01-089-2958)

With an average diameter of less than 4 nm, the as-prepared nanorods are small enough for quantum confinement[26] but do not luminesce. X-ray photoelectron spectroscopy (XPS) (Figure 2.4) showed that the surfaces of the nanorods were oxidized, and the presence of excess amine could be a source of PL quenching, as alkylamines are known to quench the PL of porous Si.[56] Therefore, to induce PL from the nanorods, they were stripped of surface oxide by HF etching. Since alkenes are known to provide good surface passivation of luminescent Si nanocrystals,[26,29,30] the nanorods were also passivated with 1-octadecene by a thermal hydrosilylation to prevent subsequent oxidation. Figure 2.5 illustrates the synthesis procedure.

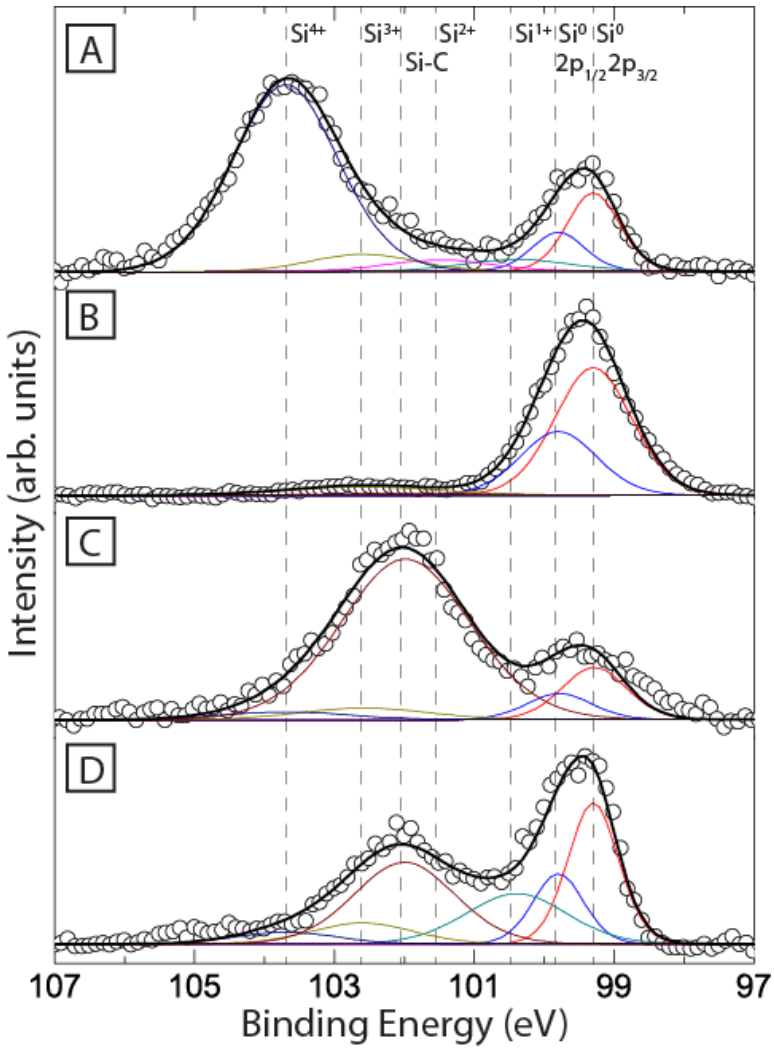

Figure 2.4 XPS of Sn-seeded Si nanorods (A) as-synthesized, (B) after HF etch, (C) after hydrosilylation with 1-octadecene, and (D) after 2 months of air exposure. Data points represented by black circles were fit (black line) by separate peak contributions of the Si^0 $2p_{3/2}$, Si^0 $2p_{1/2}$, Si^{1+}, Si^{2+}, Si^{3+}, Si^{4+}, and Si–C signals.

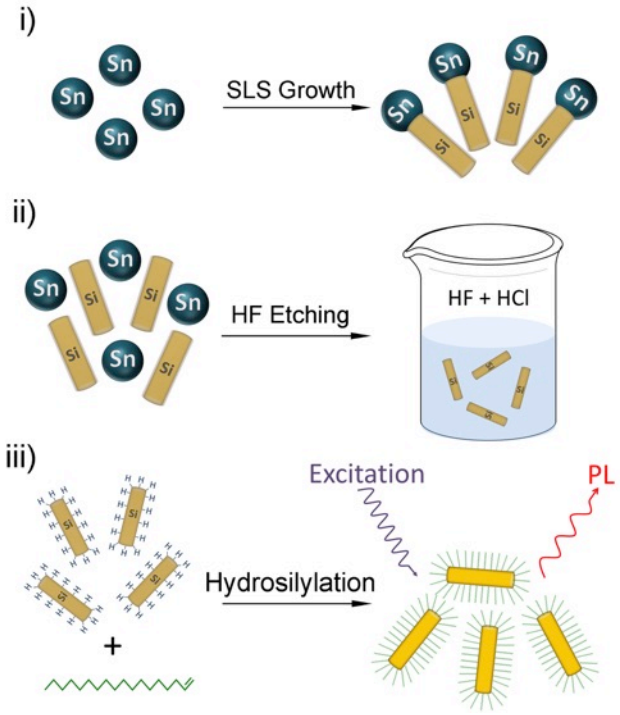

Figure 2.5 (i–iii) Illustration of photoluminescent Si nanorod preparation. (i) Si nanorods are made by Sn-seeded SLS growth. (ii) Hydride-terminated Si nanorods are obtained by HF etching in dark. (iii) Hydride-terminated Si nanorods then react with 1- octadecene to grow an alkyl monolayer via thermal hydrosilylation. The octadecene-passivated nanorods are luminescent under UV excitation.

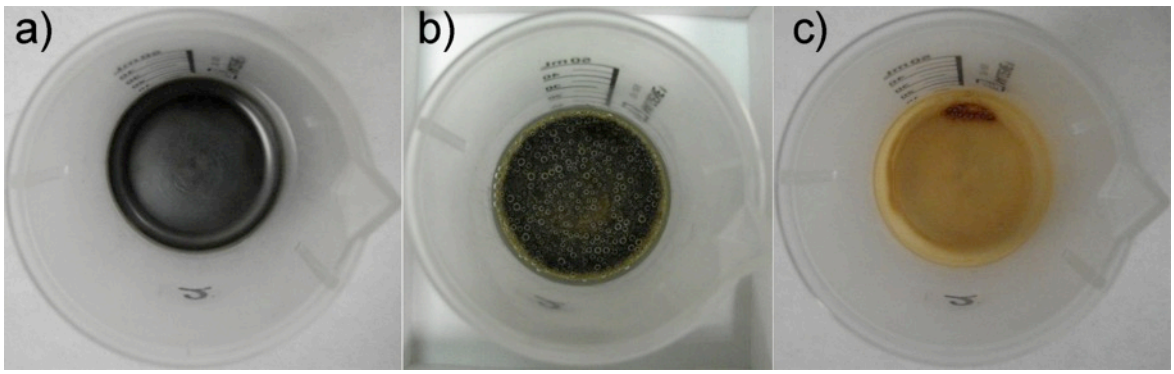

Figure 2.6 Photos show the changes occurring during etching: (a) as-made Sn seeded Si nanorods after washing and drying; (b) bubbling is observed immediately after adding HCl; (c) the nanorods become yellowish brown, which is the color of Si nanocrystals. After etching, the weight of Si nanorods decreases by ~40%, indicating most of the Sn has been etched away.

After 1-octadecene passivation, the Si nanorods exhibit bright orange photoluminescence (Figure 2.7). The absorbance and photoluminescence excitation (PLE) and emission spectra of the nanorods are qualitatively similar to those of luminescent alkene-passivated Si nanocrystals, with relatively broad PL emission peak, a large apparent Stokes shift between the PLE and PL, and featureless absorbance spectra.[26] The fluorescence is relatively bright for nanorods with a PL quantum yield (QY) of 4.3%.

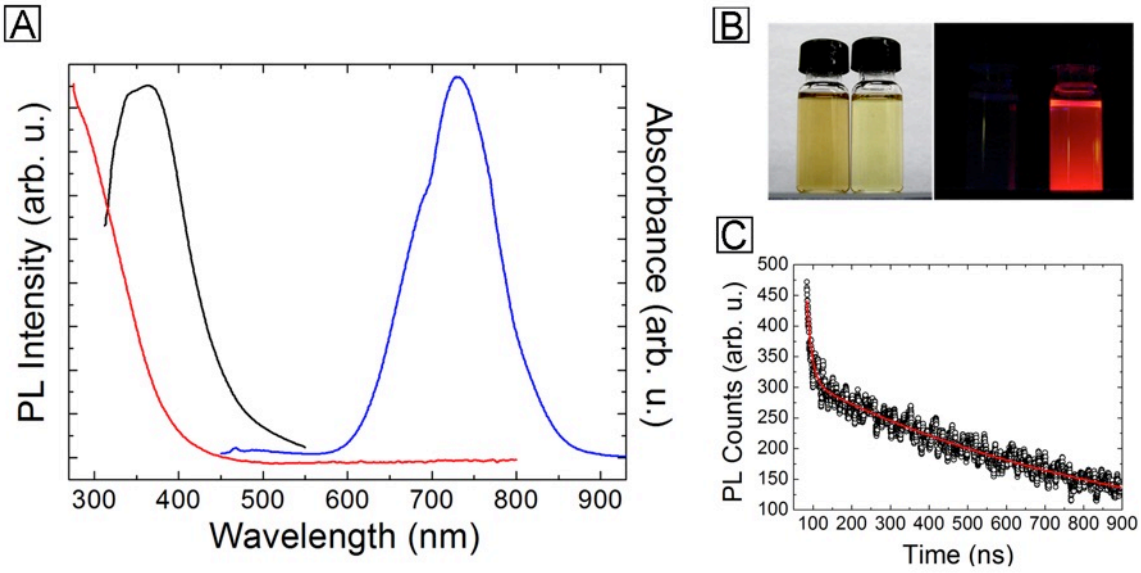

Figure 2.7 (A) Room-temperature optical absorbance (red line), PLE (λ_{em} = 720 nm; black line) and PL spectra (λ_{exc} = 370 nm; blue line) of octadecene-passivated Si nanorods dispersed in chloroform. (B) Photographs of (left vials) as-made and (right vials) 1-octadene-passivated Si nanorod dispersions under room and UV (365 nm) light. The as-made nanorods are not luminescent. The nanorods disperse in organic solvents and remain dispersed without settling for days. (C) The photoluminescence decay trace of passivated Si nanorods (λ_{exc} = 372 nm; λ_{em} = 695 nm). The PL decay lifetime was fitted by using a double exponential function (red curve).

Figure 2.8 shows TEM and high-angle annular dark field scanning transmission electron microscopy (HAADF STEM) images of the nanorods after the etching and

passivation procedure. The etching and passivation procedure has little effect on the nanorod dimensions. XRD (Figure 2.3b) showed that the nanorods also retain their diamond cubic crystal structure with no loss in crystallinity. XPS (Figure 2.4b,c) confirmed that the etching and passivation procedure removes the surface oxide layer and leaves a covalently Si–C bonded organic monolayer. There are no perceptible oxide signals in the XPS of nanorods after hydrosilylation with 1-octadecene (Si^{3+} (102.6 eV), Si^{2+} (101.5 eV) and Si^{1+} (100.4 eV)). The prominent XPS peak at 102.0 eV in the passivated sample results from Si–C bonding of the ligand after hydrosilylation, confirming covalent ligand attachment.[57]

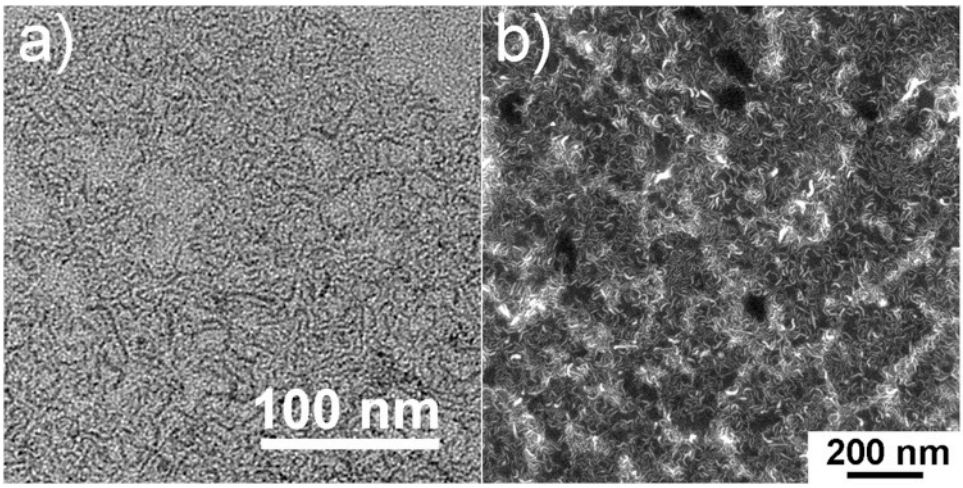

Figure 2.8 (a) TEM images and (b) HAADF STEM image of Sn-seeded Si nanorods after 1-octadecene passivation.

The octadecene nanorods imaged by high resolution TEM are crystalline with distinct interfaces. Figure 2.9 shows several high-resolution TEM images of the octadecene-passivated Si nanorods. Observed interplanar spacings are consistent with diamond cubic Si with mostly {111} lattice fringes appearing. Straight nanorods tend to have ⟨111⟩ growth direction, similar to Au-seeded Si nanorods.[16] Many kinked nanorods

also appear in the sample, which often contain crystallographic defects, including twins. (111) twins are also a common defect in SFLS-grown Si nanowires.[58]

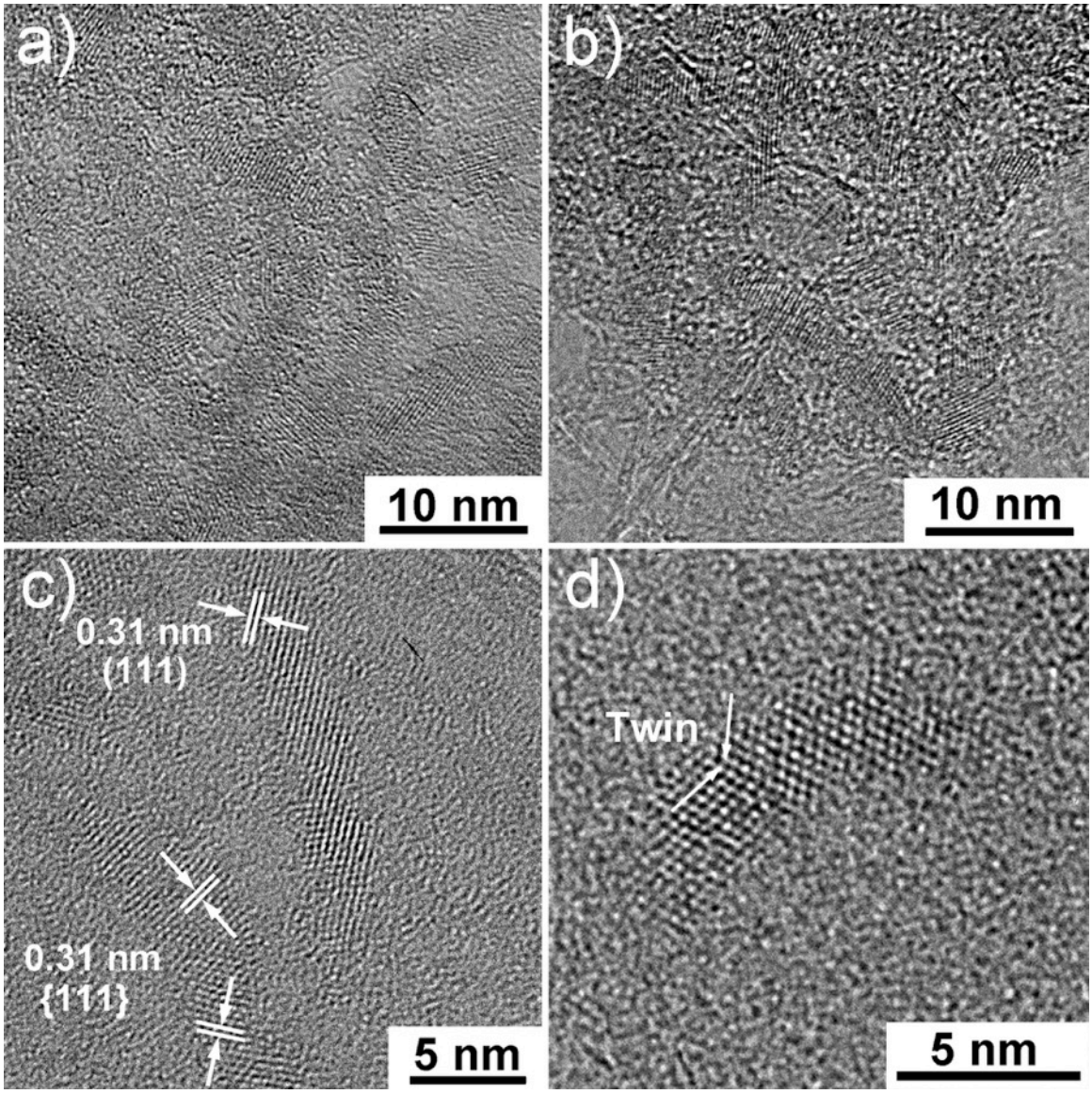

Figure 2.9 (a–d) HRTEM images of Si nanorods after 1-octadecene passivation. (c) The nanorod on the left is straight and exhibits fringes corresponding to (111) interplanar spacings of diamond cubic Si. The nanorod on the right also exhibits {111} fringes, but changes growth direction in the middle. The nanorod in (d) provides an example of a twin defect.

ATR-FTIR spectra (Figure 2.10) are also consistent with effective surface passivation of the nanorods by hydrosilylation. FTIR spectra of the as-prepared nanorods have a broad band at 1070 cm^{-1} related to Si–O–Si stretches, which is consistent with the oxidized Si surface observed by XPS. After HF etching, the Si–O–Si signal has nearly disappeared and intense bands at 2103 and 2083 cm^{-1} corresponding to $Si–H_2$ and Si–H stretching and at 903 cm^{-1} due to $Si–H_2$ scissoring appear, consistent with H-termination. (The remaining weak absorption of Si–O–Si species at 1070 cm^{-1} most likely forms during the washing procedure, which leads to about 2 hours of air exposure.) After reacting with 1-octadecene, the absorption related to Si–H stretching and scissoring disappear, and strong sp^3 $C–H_x$ stretching absorption at 2853, 2919, and 2954 cm^{-1} as well as a sharp peak at 1462 cm^{-1} corresponding to $C–CH_3$ deformations appear. Compared with Figure 2.10D, which shows an FTIR spectrum of 1-octadecene, C=C stretching at 1640 cm^{-1} and $C–H_2$ sp^2 carbon stretching above 3000 cm^{-1} are not evident in the passivated Si nanorod sample, further indicating that hydrosilylation has proceeded on the Si nanorods.

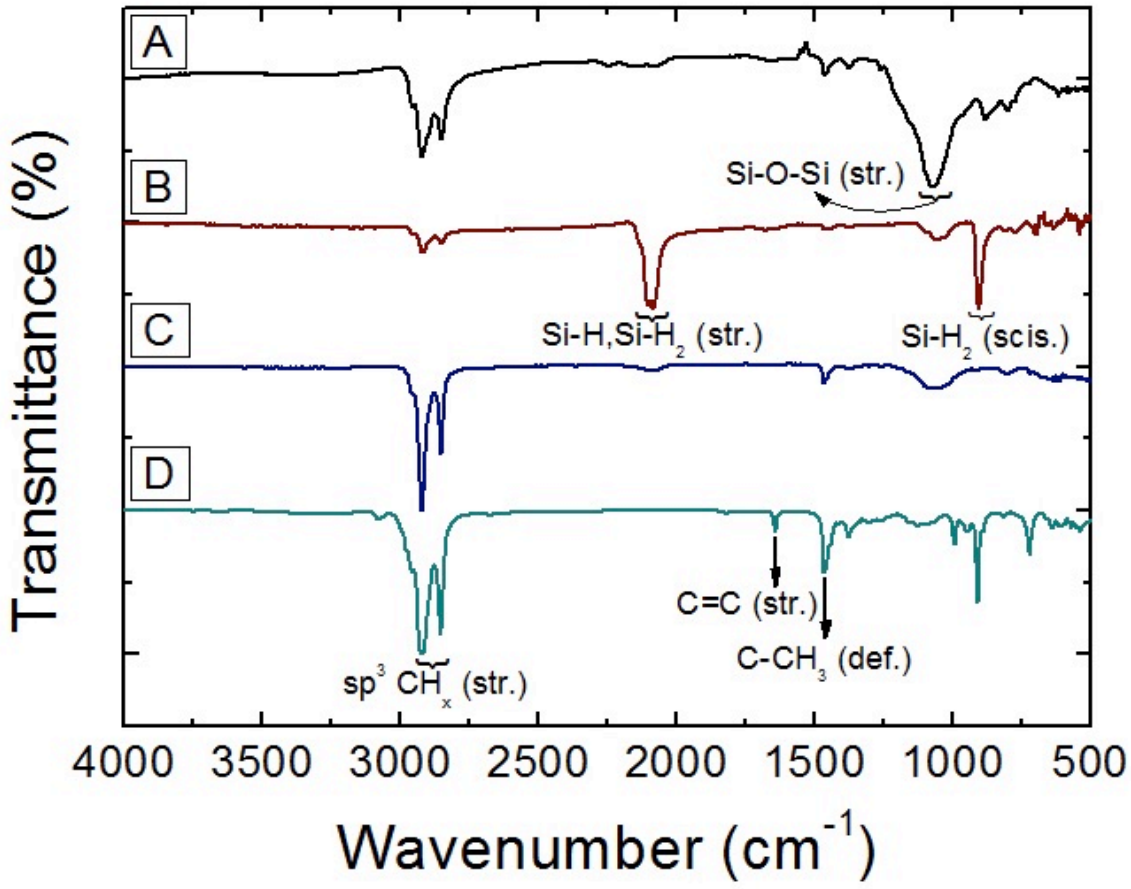

Figure 2.10 ATR-FTIR spectra of (a) as-prepared Sn-seeded Si nanorods, (b) HF-etched Si nanorods, (c) 1-octadecene passivated Si nanorods, and (d) pure 1-octadecene.

The etching procedure also removes Sn from the sample. After etching and passivation of the nanorods, Sn particles are no longer found in TEM images and Sn peaks are no longer observed by XRD. EDS (Figure 2.11) also shows no sign of residual Sn after etching and passivation. The removal of Sn during the etching procedure is also observed visually as the dispersion changes color nearly instantaneously after HF addition from dark brown to yellowish brown, the color of the pure Si nanorods (Figure 2.6). One additional point here is that the same etching procedure does not work with Au-

seeded Si nanorods. As shown in Figure 2.12, residual Au in the nanorods catalyzes HF etching of Si and damages the nanorods. It has not been possible to controllably etch Au-seeded Si nanorods with HF without destroying the sample. The Sn-seeded Si nanorods on the other hand are reliably and controllably etched and passivated to yield the luminescent nanorod sample.

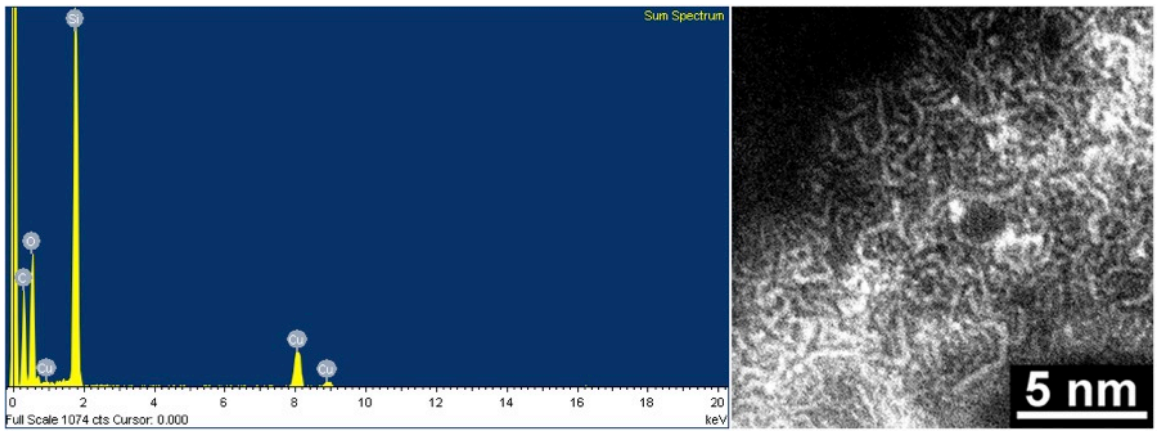

Figure 2.11 (Left) EDS spectrum obtained from the region of 1-octadecene passivated Si nanorods shown in the (Right) HAADF STEM image. There is no Sn signal. The predominant Si signal confirms that the nanorods are composed of Si. The Cu signal is from the Cu TEM grid and C and O are background signals.

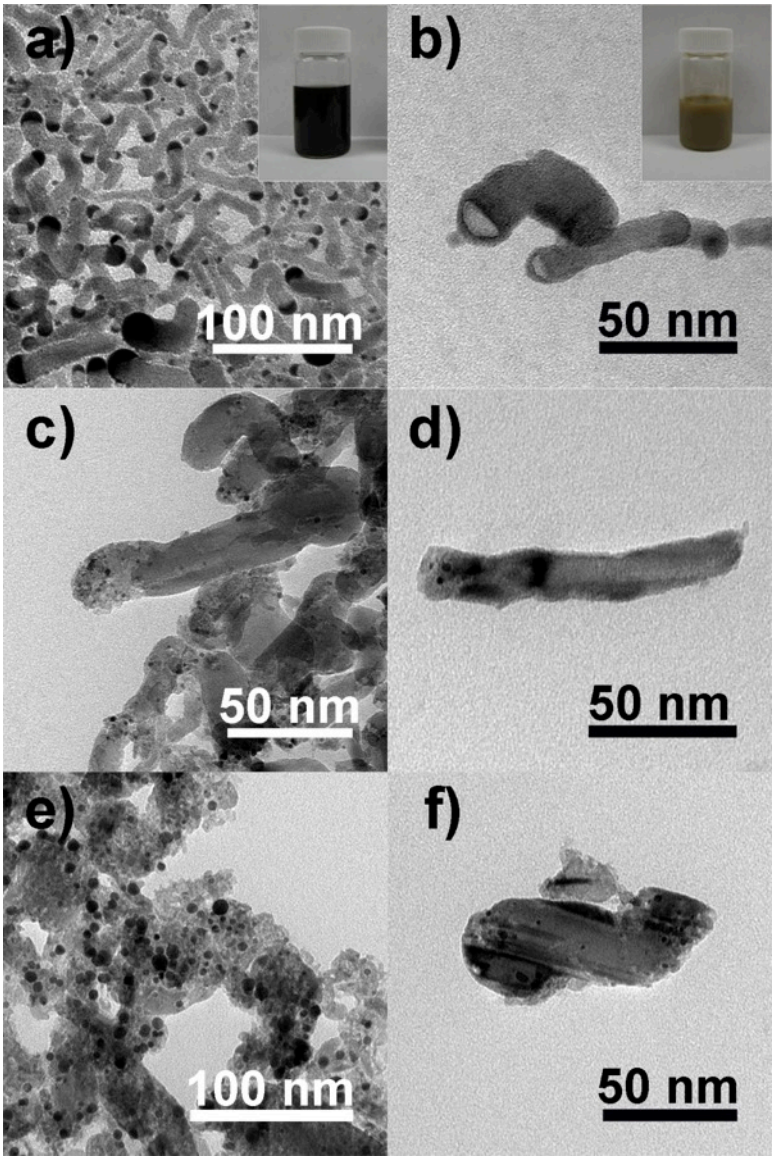

Figure 2.12 TEM images of (a) as-made Au-seeded Si nanorods, and (b) Si nanorods after removal of the Au seed particles at the nanorod tips by Aqua Regia. The inset photos show the color change before and after Au removal. (c) and (d) show the Si nanorods after exposure to HF for 5 min. The dark particles are newly formed Au particles. (e) and (f) show the nanorods after one hour of HF exposure; the dark particles are newly formed Au particles.

The PL lifetime of the Si nanorods was also measured for comparison to spherical Si nanocrystals. The decay trace in Figure 2.7c exhibits two distinct decay times that can be fit with a double exponential function of the form[59]

$$N(t) = A_1 \exp\left[-\frac{t}{\tau_s}\right] + A_2 \exp\left[-\frac{t}{\tau_d}\right]$$

indicating that there are competing fast and slow electron–hole recombination processes that occur in the nanorods. Fitting equation to the data in Figure 2.7c gives values of τ_s = 12.7 ns and τ_d = 838.8 ns. For comparison, the PL liftetimes were measured for spherical 2.3 nm diameter 10-undecenoic acid-capped Si nanocrystals and found to have similar τ_s (14.9 ns) but shorter τ_d (494.2 ns). The nanorods, however, have a slightly larger average diameter (between 3 and 4 nm) than these nanocrystals. Since lifetimes increase with increasing nanocrystal size,[60] further work is needed to verify whether the electron–hole recombination rates are indeed significantly slower in nanorods than in spherical nanocrystals of the same size.

The 1-octadecene passivated Si nanorods remained luminescent after two months of storage in air, but the PL quantum yield decreased from 4.3 to 2.0%. XPS (Figure 2.4d) showed that some oxidation occurred during this time with the appearance of a Si1+ suboxide peak. There is also a noticeable decrease in Si–C signal, which perhaps indicates that Si–O forms at the expense of Si–C bonds. The loss of Si–C passivation is probably related to the decreased quantum yield.

2.4 Conclusions

Luminescent Si nanorods can be synthesized by SLS growth using Sn seeds. The as-synthesized material does not emit light, but can be made luminescent after HF etching and 1-octadecene surface passivation. The etching and organic ligand passivation procedure removes tin, surface oxide, and excess amine. XPS showed that the ligand passivated nanorods are relatively stable with respect to oxidation and retain most of their luminescence when stored in air. The data presented here confirm that the seed metal can significantly impact the optical properties of quantum-sized Si nanorods and need to be considered. Sn appears to be a relatively benign seed metal for Si nanomaterials. These luminescent Si nanorods now offer samples useful for a variety of future studies, including those focused on multiple exciton generation and optical gain.

2.5 Acknowledgements

We thank J. P. Zhou for assistance with HRTEM. We acknowledge financial support of this work by the Robert A. Welch Foundation (Grant F-1464) and the Energy Frontier Research Center (EFRC) funded by the U.S. Department of Energy Office of Science and Office of Basic Energy Sciences, under Award No. DESC0001091.

2.6 References

1. Murray, C. B.; Kagan, C. R.; Bawendi, M. G. SYNTHESIS AND CHARACTERIZATION OF MONODISPERSE NANOCRYSTALS AND CLOSE-PACKED NANOCRYSTAL ASSEMBLIES. *Annu. Rev. Mater. Res.* **2000**, *30* (1), 545–610.

2. Burda, C.; Chen, X.; Narayanan, R.; El-Sayed, M. a. Chemistry and Properties of Nanocrystals of Different Shapes. *Chem. Rev.* **2005**, *105* (4), 1025–1102.

3. Lee, D. C.; Smith, D. K.; Heitsch, A. T.; Korgel, B. A. Colloidal Magnetic Nanocrystals: Synthesis, Properties and Applications. *Annual Reports Section "C" (Physical Chemistry)*, 2007, *103*, 351.

4. Talapin, D. V; Lee, J. S.; Kovalenko, M. V; Shevchenko, E. V. Prospects of Colloidal Nanocrystals for Electronic and Optoelectronic Applications. *Chem. Rev.* **2010**, *110* (1), 389–458.

5. Peng, X.; Manna, L.; Yang, W.; Wickham, J.; Scher, E.; Kadavanich, A.; Alivisatos, A. Shape Control of CdSe Nanocrystals. *Nature* **2000**, *404* (6773), 59–61.

6. Manna, L.; Scher, E. C.; Alivisatos, a. P. Synthesis of Soluble and Processable Rod-, Arrow-, Teardrop-, and Tetrapod-Shaped CdSe Nanocrystals. *J. Am. Chem. Soc.* **2000**, *122* (51), 12700–12706.

7. Peng, Z. A.; Peng, X. Formation of High-Quality CdTe, CdSe, and CdS Nanocrystals Using CdO as Precursor. *Journal of the American Chemical Society*, 2001, *123*, 183–184.

8. Jun, Y. W.; Lee, S. M.; Kang, N. J.; Cheon, J. Controlled Synthesis of Multi-Armed CdS Nanorod Architectures Using Monosurfactant System. *Journal of the American Chemical Society*, 2001, *123*, 5150–5151.

9. Park, J.; Koo, B.; Yoon, K. Y.; Hwang, Y.; Kang, M.; Park, J. G.; Hyeon, T. Generalized Synthesis of Metal Phosphide Nanorods via Thermal Decomposition of Continuously Delivered Metal-Phosphine Complexes Using a Syringe Pump. *J. Am. Chem. Soc.* **2005**, *127* (23), 8433–8440.

10. Shieh, F.; Saunders, A. E.; Korgel, B. a. General Shape Control of Colloidal CdS, CdSe, CdTe Quantum Rods and Quantum Rod Heterostructures. *J. Phys. Chem. B* **2005**, *109* (18), 8538–8542.

11. Saunders, A. E.; Ghezelbash, A.; Sood, P.; Korgel, B. a. Synthesis of High Aspect Ratio Quantum-Size CdS Nanorods and Their Surface-Dependent Photoluminescence. *Langmuir* **2008**, *24* (16), 9043–9049.

12. Tang, Z.; Kotov, N. a; Giersig, M. Spontaneous Organization of Single CdTe Nanoparticles into Luminescent Nanowires. *Science* **2002**, *297* (5579), 237–240.

13. Cho, K. S.; Talapin, D. V.; Gaschler, W.; Murray, C. B. Designing PbSe Nanowires and Nanorings through Oriented Attachment of Nanoparticles. *J. Am. Chem. Soc.* **2005**, *127* (19), 7140–7147.

14. Barnard, A. S.; Xu, H. First Principles and Thermodynamic Modeling of CdS Surfaces and Nanorods. *J. Phys. Chem. C* **2007**, *111* (49), 18112–18117.

15. Kan, S.; Mokari, T.; Rothenberg, E.; Banin, U. Synthesis and Size-Dependent Properties of Zinc-Blende Semiconductor Quantum Rods. *Nat. Mater.* **2003**, *2* (3), 155–158.

16. Heitsch, A. T.; Hessel, C. M.; Akhavan, V. A.; Korgel, B. A. Colloidal Silicon Nanorod Synthesis. *Nano Lett.* **2009**, *9* (8), 3042–3047.

17. Chockla, A. M.; Harris, J. T.; Korgel, B. a. Colloidal Synthesis of Germanium Nanorods. *Chem. Mater.* **2011**, *23* (7), 1964–1970.

18. Shabaev, a.; Efros, A. L. 1D Exciton Spectroscopy of Semiconductor Nanorods. *Nano Lett.* **2004**, *4* (10), 1821–1825.

19. Mohamed, M. B.; Burda, C.; El-Sayed, M. a. Shape Dependent Ultrafast Relaxation Dynamics of CdSe Nanocrystals: Nanorods vs Nanodots. *Nano Lett.* **2001**, *1* (11), 589–593.

20. Robel, I.; Bunker, B. a.; Kamat, P. V.; Kuno, M. Exciton Recombination Dynamics in CdSe Nanowires: Bimolecular to Three-Carrier Auger Kinetics. *Nano Lett.* **2006**, *6* (7), 1344–1349.

21. Cunningham, P. D.; Boercker, J. E.; Foos, E. E.; Lumb, M. P.; Smith, A. R.; Tischler, J. G.; Melinger, J. S. Enhanced Multiple Exciton Generation in Quasi-One-Dimensional Semiconductors. *Nano Lett.* **2011**, *11* (8), 3476–3481.

22. Htoon, H.; Hollingworth, J. a.; Malko, a. V.; Dickerson, R.; Klimov, V. I. Light Amplification in Semiconductor Nanocrystals: Quantum Rods versus Quantum Dots. *Appl. Phys. Lett.* **2003**, *82* (26), 4776–4778.

23. Hessel, C. M.; Heitsch, A. T.; Korgel, B. A. Gold Seed Removal from the Tips of Silicon Nanorods. *Nano Lett.* **2010**, *10* (1), 176–180.

24. Brus, L. Luminescence of Silicon Materials: Chains, Sheets, Nanocrystals, Nanowires, Microcrystals, and Porous Silicon. *J. Phys. Chem.* **1994**, *98* (14), 3575–3581.

25. Hessel, C. M.; Wei, J.; Reid, D.; Fujii, H.; Downer, M. C.; Korgel, B. a. Raman Spectroscopy of Oxide-Embedded and Ligand-Stabilized Silicon Nanocrystals. *J. Phys. Chem. Lett.* **2012**, *3* (9), 1089–1093.

26. Hessel, C. M.; Reid, D.; Panthani, M. G.; Rasch, M. R.; Goodfellow, B. W.; Wei, J.; Fujii, H.; Akhavan, V.; Korgel, B. a. Synthesis of Ligand-Stabilized Silicon Nanocrystals with Size-Dependent Photoluminescence Spanning Visible to Near-Infrared Wavelengths. *Chem. Mater.* **2012**, *24* (2), 393–401.

27. English, D. S.; Pell, L. E.; Yu, Z.; Barbara, P. F.; Korgel, B. a. Size Tunable Visible Luminescence from Individual Organic Monolayer Stabilized Silicon Nanocrystal Quantum Dots. *Nano Lett.* **2002**, *2* (7), 681–685.

28. Hessel, C. M.; Henderson, E. J.; Veinot, J. G. C.; Uni, V.; February, R. V; Re, V.; Recei, M.; August, V. Hydrogen Silsesquioxane : A Molecular Precursor for Nanocrystalline Si - SiO 2 Composites and Freestanding Hydride-Surface-Terminated Silicon Nanoparticles. **2006**, No. 1, 6139–6146.

29. Jurbergs, D.; Rogojina, E.; Mangolini, L.; Kortshagen, U. Silicon Nanocrystals with Ensemble Quantum Yields Exceeding 60%. *Appl. Phys. Lett.* **2006**, *88* (23), 60–63.

30. Li, X.; He, Y.; Talukdar, S. S.; Swihart, M. T. Process for Preparing Macroscopic Quantities of Brightly Photoluminescent Silicon Nanoparticles with Emission Spanning the Visible Spectrum. *Langmuir* **2003**, *19* (20), 8490–8496.

31. Yang, C. S.; Bley, R. A.; Kauzlarich, S. M.; Lee, H. W. H.; Delgado, G. R. Synthesis of Alkyl-Terminated Silicon Nanoclusters by a Solution Route. *J. Am. Chem. Soc.* **1999**, *121* (22), 5191–5195.

32. Wilson, W. L.; Szajowski, P. F.; Brus, L. E. Quantum Confinement in Size-Selected, Surface-Oxidized Silicon Nanocrystals. *Science* **1993**, *262* (5137), 1242–1244.

33. Wilcoxon, J. P.; Samara, G. a. Tailorable, Visible Light Emission from Silicon Nanocrystals. *Appl. Phys. Lett.* **1999**, *74* (21), 3164.

34. Tilley, R. D.; Warner, J. H.; Yamamoto, K.; Matsui, I.; Fujimori, H. Micro-Emulsion Synthesis of Monodisperse Surface Stabilized Silicon Nanocrystals. *Chem. Commun. (Camb).* **2005**, No. 14, 1833–1835.

35. Mastronardi, M. L.; Hennrich, F.; Henderson, E. J.; Maier-Flaig, F.; Blum, C.; Reichenbach, J.; Lemmer, U.; Kübel, C.; Wang, D.; Kappes, M. M.; Ozin, G. a. Preparation of Monodisperse Silicon Nanocrystals Using Density Gradient Ultracentrifugation. *J. Am. Chem. Soc.* **2011**, *133* (31), 11928–11931.

36. Sankaran, R. M.; Holunga, D.; Flagan, R. C.; Giapis, K. P. Synthesis of Blue Luminescent Si Nanoparticles Using Atmospheric-Pressure Microdischarges. *Nano Lett.* **2005**, *5* (3), 537–541.

37. Guichard, A. R.; Barsic, D. N.; Sharma, S.; Kamins, T. I.; Brongersma, M. L. Tunable Light Emission from Quantum-Confined Excitons in TiSi 2-Catalyzed Silicon Nanowires. *Nano Lett.* **2006**, *6* (9), 2140–2144.

38. Tuan, H.-Y.; Lee, D. C.; Hanrath, T.; Korgel, B. A. Catalytic Solid-Phase Seeding of Silicon Nanowires by Nickel Nanocrystals in Organic Solvents. *Nano Lett.* **2005**, *5* (4), 681–684.

39. Tuan, H.-Y.; Lee, D. C.; Korgel, B. A. Nanocrystal-Mediated Crystallization of Silicon and Germanium Nanowires in Organic Solvents: The Role of Catalysis and Solid-Phase Seeding. *Angew. Chem. Int. Ed. Engl.* **2006**, *45* (31), 5184–5187.

40. Korgel, B. a; Tuan, H. Y.; Ghezelbash, A. Silicon Nanowires and Silica Nanotubes Seeded by Copper Nanoparticles in an Organic Solvent. *Chem. Mater.* **2008**, *20* (6), 2306–2313.

41. Jeon, M.; Kamisako, K. Synthesis and Characterization of Silicon Nanowires Using Tin Catalyst for Solar Cells Application. *Mater. Lett.* **2009**, *63* (9-10), 777–779.

42. Rathi, S. J.; Jariwala, B. N.; Beach, J. D.; Stradins, P.; Taylor, P. C.; Weng, X.; Ke, Y.; Redwing, J. M.; Agarwal, S.; Collins, R. T. Tin-Catalyzed Plasma-Assisted Growth of Silicon Nanowires. *J. Phys. Chem. C* **2011**, *115* (10), 3833–3839.

43. Cheng, S.; Ren, T.; Ying, P.; Yu, R.; Zhang, W.; Zhang, J.; Li, C. Enhanced Growth of Crystalline-Amorphous Core-Shell Silicon Nanowires by Catalytic Thermal CVD Using in Situ Generated Tin Catalyst. *Sci. China Chem.* **2012**, *55* (12), 2573–2579.

44. Yu, L.; O'Donnell, B.; Alet, P.-J.; Conesa-Boj, S.; Peiró, F.; Arbiol, J.; Cabarrocas, P. R. I. Plasma-Enhanced Low Temperature Growth of Silicon Nanowires and Hierarchical Structures by Using Tin and Indium Catalysts. *Nanotechnology* **2009**, *20* (22), 225604.

45. Mullane, E.; Kennedy, T.; Geaney, H.; Dickinson, C.; Ryan, K. M. Synthesis of Tin Catalyzed Silicon and Germanium Nanowires in a Solvent–Vapor System and Optimization of the Seed/Nanowire Interface for Dual Lithium Cycling. *Chem. Mater.* **2013**, *25* (9), 1816–1822.

46. Geaney, H.; Mullane, E.; Ramasse, Q. M.; Ryan, K. M. Atomically Abrupt Silicon-Germanium Axial Heterostructure Nanowires Synthesized in a Solvent Vapor Growth System. *Nano Lett.* **2013**, *13* (4), 1675–1680.

47. Chockla, A. M.; Klavetter, K. C.; Mullins, C. B.; Korgel, B. A. Tin-Seeded Silicon Nanowires for High Capacity Li-Ion Batteries. *Chem. Mater.* **2012**, *24* (19), 3738–3745.

48. Sze, S. M.; Ng, K. K. *Physics of Semiconductor Devices*; John Wiley & Sons, 2006; Vol. 3.

49. Heitsch, A. T.; Fanfair, D. D.; Tuan, H.-Y.; Korgel, B. A. Solution-Liquid-Solid (SLS) Growth of Silicon Nanowires. *J. Am. Chem. Soc.* **2008**, *130* (16), 5436–5437.

50. Wang, F.; Tang, R.; Yu, H. Size-and Shape-Controlled Synthesis of Bismuth Nanoparticles. *Chem. …* **2008**, No. 28, 3656–3662.

51. Trentler, T. J.; Hickman, K. M.; Goel, S. C.; Viano, a. M.; Gibbons, P. C.; Buhro, W. E. Solution-Liquid-Solid Growth of Crystalline III-V Semiconductors: An Analogy to Vapor-Liquid-Solid Growth. *Science*, 1995, *270*, 1791–1794.

52. Wang, F.; Dong, A.; Sun, J.; Tang, R.; Yu, H.; Buhro, W. E. Solution-Liquid-Solid Growth of Semiconductor Nanowires. *Inorg. Chem.* **2006**, *45* (19), 7511–7521.

53. Lu, X.; Fanfair, D. D.; Johnston, K. P.; Korgel, B. A. High Yield Solution-Liquid-Solid Synthesis of Germanium Nanowires. *J. Am. Chem. Soc.* **2005**, *127* (45), 15718–15719.

54. Pell, L. E.; Schricker, A. D.; Mikulec, F. V; Korgel, B. a. Synthesis of Amorphous Silicon Colloids by Trisilane Thermolysis in High Temperature Supercritical Solvents. *Langmuir* **2004**, *20* (16), 6546–6548.

55. Harris, J. T.; Hueso, J. L.; Korgel, B. a. Hydrogenated Amorphous Silicon (a-Si:H) Colloids. *Chem. Mater.* **2010**, *22* (23), 6378–6383.

56. Chandler-Henderson, R. R.; Sweryda-Krawiec, B.; Coffer, J. L. Steric Considerations in the Amine-Induced Quenching of Luminescent Porous Silicon. *J. Phys. Chem.* **1995**, *99* (21), 8851–8855.

57. Yu, Y.; Hessel, C. M.; Bogart, T. D.; Panthani, M. G.; Rasch, M. R.; Korgel, B. a. Room Temperature Hydrosilylation of Silicon Nanocrystals with Bifunctional Terminal Alkenes. *Langmuir* **2013**, *29* (5), 1533–1540.

58. Davidson, F. M.; Lee, D. C.; Fanfair, D. D. D.; Korgel, B. A. Lamellar Twinning in Semiconductor Nanowires. *J. Phys. Chem. C* **2007**, *111* (7), 2929–2935.

59. Guichard, A. R.; Kekatpure, R. D.; Brongersma, M. L.; Kamins, T. I. Temperature-Dependent Auger Recombination Dynamics in Luminescent Silicon Nanowires. *Phys. Rev. B - Condens. Matter Mater. Phys.* **2008**, *78* (23), 235422.

60. Beard, M. C.; Knutsen, K. P.; Yu, P.; Luther, J. M.; Song, Q.; Metzger, W. K.; Ellingson, R. J.; Nozik, A. J. Multiple Exciton Generation in Colloidal Silicon Nanocrystals. *Nano Lett.* **2007**, *7* (8), 2506–2512.

Chapter 3: A Single-Step Reaction for Silicon and Germanium Nanorods**

3.1 INTRODUCTION

Silicon (Si) and germanium (Ge) are two of the most widely used semiconductors in commercial electronic and optoelectronic devices, but they are poor light emitters and weak light absorbers due to their indirect band gaps. Si and Ge quantum dots, however, can exhibit very bright visible-light emission with size-tunable color and a variety of synthetic methods have been developed for Si and Ge nanocrystals.[1–14] Quantum rods of Si also luminescence,[15] and—like other semiconductor nanorods—should exhibit an even wider range of unique optical properties,[16,17] such as enhanced birefringence,[18] faster carrier relaxation,[19] and higher photon absorption cross sections,[20] but their synthesis is much less developed.

Si and Ge nanorods have been synthesized by solution–liquid–solid (SLS) growth with capping ligand stabilization, using either gold (Au), bismuth (Bi) or tin (Sn) nanocrystals as seeds,[15,21–24] and relatively bright photoluminescence was obtained from Sn nanoparticle-seeded nanorods after appropriate surface passivation.[15] Alternative synthetic approaches developed for other types of semiconductor nanorods, such as oriented attachment[25–27] and ligand-directed growth,[28–32] probably cannot be applied to Si and Ge. Similar to vapor–liquid–solid (VLS) growth of nanowires,[33–35] SLS growth relies on the use of a metal that forms a eutectic with the semiconductor to induce crystallization at relatively low temperature.[36] To achieve nanorod growth—as opposed to much higher aspect ratio nanowires—the amount of semiconductor added to the reaction compared to seed metal is relatively low and capping ligands are introduced to prevent agglomeration.[37]

** This chapter appears in *Chemistry - A European Journal* **2014**, *20*, 5874-5879.

This chapter reports that SLS-induced Si and Ge nanorods growth can be carried out using only a single reaction step, by adding a tin(II) complex instead of pre-formed Sn particles. This approach eliminates a reaction step, simplifies the synthesis, and improves reproducibility by eliminating the need for relatively unstable seed particles as reagents. Nanocrystals of low-melting metals like Bi,[23,24,38–42] In,[43,44] and Sn,[15] that are needed for SLS growth can be difficult to prepare and introduce as stable reagents. In fact, the synthesis of these nanoparticles was the biggest challenge facing the early development of SLS nanowire growth and required new chemistry, like Kuno's[45] Au–Bi core–shell nanocrystals and Buhro's[38,39] poly(1-hexadecene-co-1-vinylpyrrolidinone) (PVP-HDE)-stabilized Bi nanocrystals. Small Au nanoparticles with depressed melting temperature[37,46,47] were also explored, but usually still had melting temperatures that were too high to achieve relatively long nanorods. To circumvent the need for stable nanocrystals as reagents, Mews[48] and Kuno[49] both showed that CdSe nanowires could be made by adding bismuth salts instead of Bi nanoparticles. In their reactions, the capping ligand (trioctylphosphine) reduced the Bi salt to Bi nanoparticles in situ. Our work builds off Lu's[15] approach of seeding Si nanorod growth with Sn nanocrystals and the work of Chockla[50] and Bogart,[51] who have shown that direct injection of a tin(II) complex into a supercritical-fluid–liquid–solid (SFLS) growth reaction could seed Si nanowires.

3.2 Experimental Details

3.2.1 Materials

Bis[bis(trimethylsilyl)amino]tin(II) ([$Sn(hmds)_2$] , Aldrich), trisilane (Si_3H_8, Voltaix), diphenylgermane (DPG, Gelest), dodecylamine (98%, Aldrich), octadecane (99%, Aldrich), squalane (>95%, Aldrich), trioctylphosphine oxide (TOPO, 99 %, Sigma

Aldrich), poly(vinylpyrrolidinone)hexadecane (PVP-HDE) copolymer (Ganex V-216, ISP Technologies, Inc.) were used without further purification. Solutions of PVP-HDE dissolved in dodecylamine (33% w/w), PVP-HDE in dissolved octadecane (33% w/w) and squalane were degassed under vacuum at 80ºC for 45 min, and then stored in a nitrogen- filled glovebox prior to use.

3.2.2 Nanorod Synthesis

The synthesis was carried out on a Schlenk line operated inside a glovebox. For a typical growth of the Si nanorods, squalane (10 mL) was heated to 410ºC under N_2 flow in a flat-bottomed flask attached to the Schlenk line. Separately, a precursor solution consisting of PVP-HDE dodecylamine solution (1.2 mL), [$Sn(hmds)_2$] (20 mL) and trisilane (75 mL) was prepared in a 3 mL vial, which immediately turned dark brown after mixing. The precursor solution was then drawn into a syringe equipped with a 6“ needle. Prior to injection, the stopcock valve was closed. The mixture was quickly injected through the septum into the hot solvent. After 1 min, the heating mantle was removed. The stopcock valve was closed throughout the whole reaction to reduce evaporation. (Caution: trisilane is relatively volatile, highly flammable and pyrophoric. It ignites spontaneously in air, creating a thermal burn risk. Must be handled with care!) Ge nanorods were synthesized using TOPO (4 g) and squalane (5 g) as the solvent. The solvent was degassed under vacuum at 85ºC for 30min on a Schlenk line outside the glovebox, then moved into the glovebox for the reaction. The reaction temperature for Ge nanorods was 350ºC. The precursor solution was prepared by combining PVP-HDE octadecane solution (1.2 mL), [$Sn(hmds)_2$] (20 mL) and trisilane (2 mL). Once this solution turned dark brown, diphenylgermane (48 mL) was added and then injected as described for the Si nanorods. After 5 min, the reaction flask was removed the heat and allowed to cool to room temperature.

The as-obtained Si or Ge nanorod dispersion was diluted with toluene (10 mL) and transferred to a centrifuge tube. Ethanol (ca. 15 mL) was added and the solution was centrifuged at 1000 rpm for 10 min. The supernatant, which should be clear, was discarded. The precipitate was redispersed in toluene and washed by repeating the precipitation procedure at least three times. The final product was dispersed and stored in chloroform.

3.2.3 Materials Characterization

Low-resolution transmission electron microscopy (TEM) images were obtained on a FEI Tecnai Spirit Bio Twin operated at 80 kV. High-resolution transmission microscopy (HRTEM), high-angle annular dark-field scanning transmission electron microscopy (HAADF-STEM), and energy-dispersive X-ray spectroscopy (EDS) elemental mapping images were obtained on a field emission JEOL 2010F TEM operated at 200 kV equipped with an Oxford INCA ED spectrometer. Scanning electron microscopy (SEM) images were obtained on a Zeiss Supra VP SEM operated at 2 kV accelerating voltage and working distance of 5 mm. X-ray diffraction (XRD) measurements were performed on a Rigaku R-Axis Spider diffractometer using $Cu_{K\alpha}$ radiation (λ = 1.54 Å). Small-angle X-ray scattering (SAXS) measurements were performed on a Bruker Nonius diffractometer with a Molecular Metrology system and Enraf–Nonius FR591 Cu anode (λ = 1.54 Å) operating at 3.0 kW.

3.3 Results and Discussion

The single-step reaction of Si nanorods (illustrated in Figure 3.1) proceeds by injecting bis[bis(trimethylsilyl)amino]tin(II) ([$Sn(hmds)_2$]), trisilane (Si_3H_8), and poly(vinylpyrrolidinone)hexadecane copolymer (PVP-HDE) into squalane at 410ºC.

Squalane boils at around 420ºC.[21,22] Dodecylamine is typically added as a capping ligand to prevent agglomeration;[21,22] however, it is possible to still make Si nanorods without dodecylamine, but more difficult to disperse them after purification. Key to the reaction is the in situ reduction of [$Sn(hmds)_2$] by trisilane to form Sn nanoparticles. The Sn nanoparticles are stabilized by PVP-HDE and are about 8nm in diameter (see Figure 3.2). The precursor solution is injected into squalane at 410ºC to initiate SLS growth of Si nanorods. Trisilane provides Si for nanorod growth and decomposes rapidly in the presence of the Sn seeds with the reaction reaching completion in one minute.

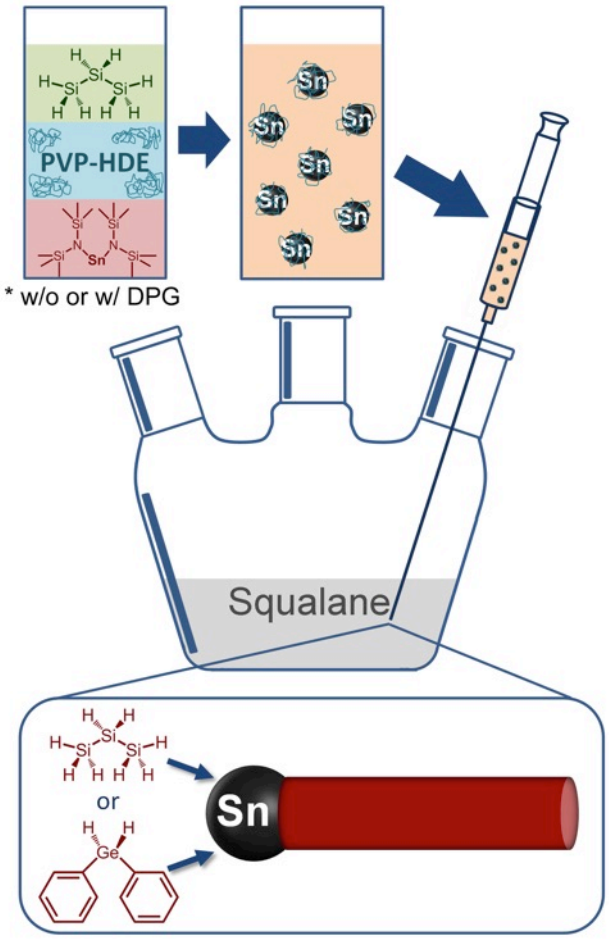

Figure 3.1 A single-step reaction for Si and Ge nanorods. The reactant solution of trisilane, PVP-HDE and [Sn(hmds)$_2$] is injected into squalane (with dodecylamine) at 410ºC. Sn nanoparticles capped by PVP-HDE formed by trisilane reduction seed the SLS growth of the Si (or Ge) nanorods. Ge nanorods are produced by injecting the reactant mixture including diphenylgermane (DPG) into squalane at 350ºC.

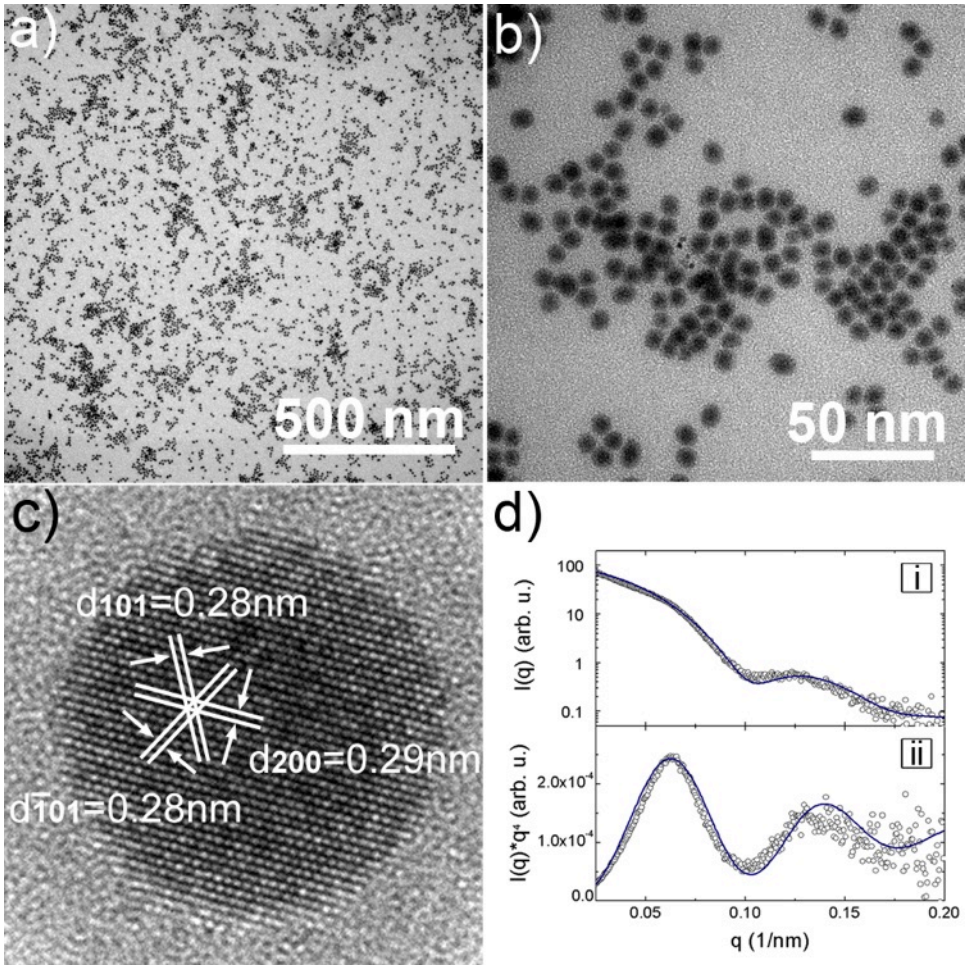

Figure 3.2 Sn nanoparticles formed in situ for Si and Ge nanorod seeding: (a) and (b) TEM images and (c) HRTEM image of the Sn nanoparticles. (d) SAXS of nanocrystals dispersed in toluene. Best fits (solid line) of the SAXS data in i) plot I(q) versus q and ii) a Porod plot with $I(q)\times q^4$ versus q give an average nanocrystal diameter of 8.4±1.0 nm. The Sn nanoparticles are stabilized by PVP-HDE added to the reaction and are well-dispersed. They can be stored in the glovebox as a solvent dispersion for over a month without precipitation.

Figure 3.3 shows TEM images of Si nanorods produced using this approach. The average diameter of the nanorods was typically between 6 and 7 nm (based on TEM images of about 50 nanorods per sample) and similar to the size of the Sn seed particles. The nanorod length could be tuned over a rather wide range by modifying the [Si]/[Sn]

molar ratio. Figure 3.3 shows nanorods made with four different average lengths, ranging from 25 to more than 100 nm. Very long nanorods were also possible, and aspect ratios exceeding 100 (i.e., nanowires) could be produced, as shown in Figure 3.4. These nanowires were made with a [Si]/[Sn] ratio of 400 and have lengths exceeding 1 mm. These very long nanorods required a longer reaction time of 10 min and the average diameter of 10 nm was slightly larger than the typical diameter of the shorter nanorods.

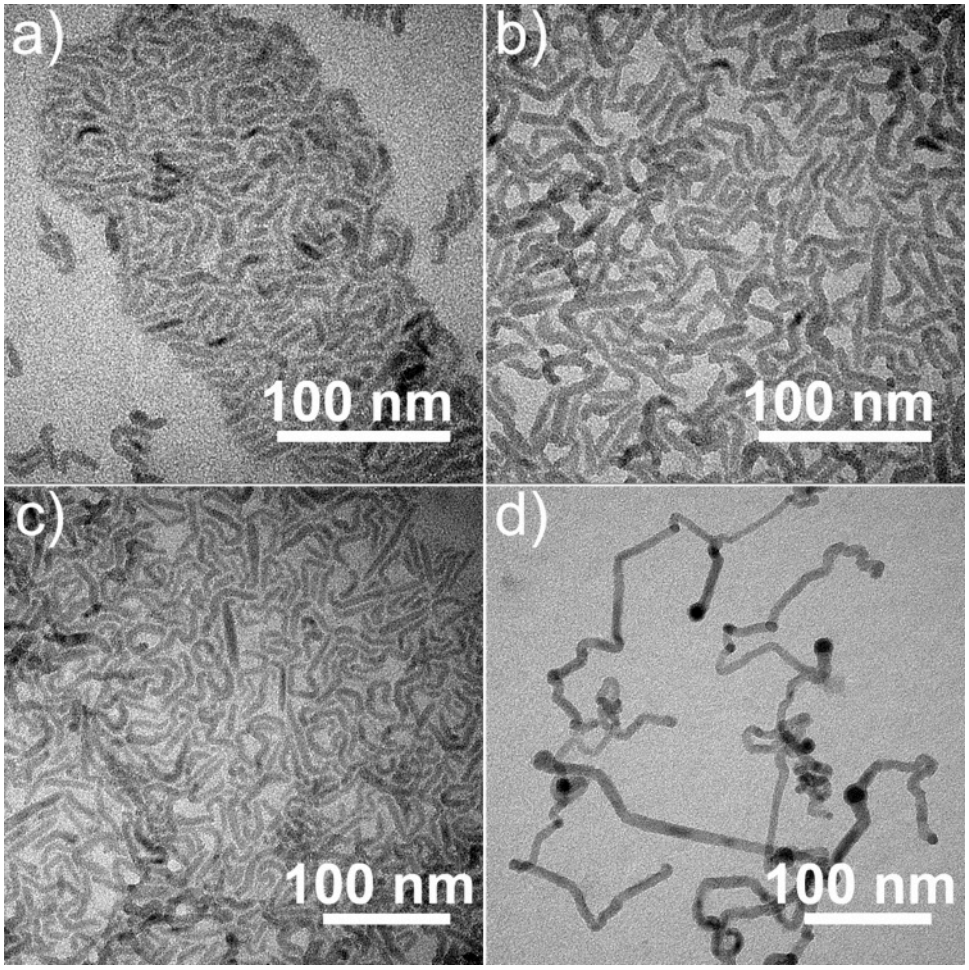

Figure 3.3 TEM images of in situ Sn seeded Si nanorods with varied [Si]/[Sn] atomic ratio calculated from the precursors in the synthesis: (a) [Si]/[Sn] = 24, the average length of the nanorods is 25 nm; (b) [Si]/[Sn]=36, the average length is 33 nm; (c) [Si]/[Sn]=48 the average length is 50 nm; (d) [Si]/[Sn] = 60, it's hard to give an average length of the tangled nanorods in this sample, but most of them are over 100 nm.

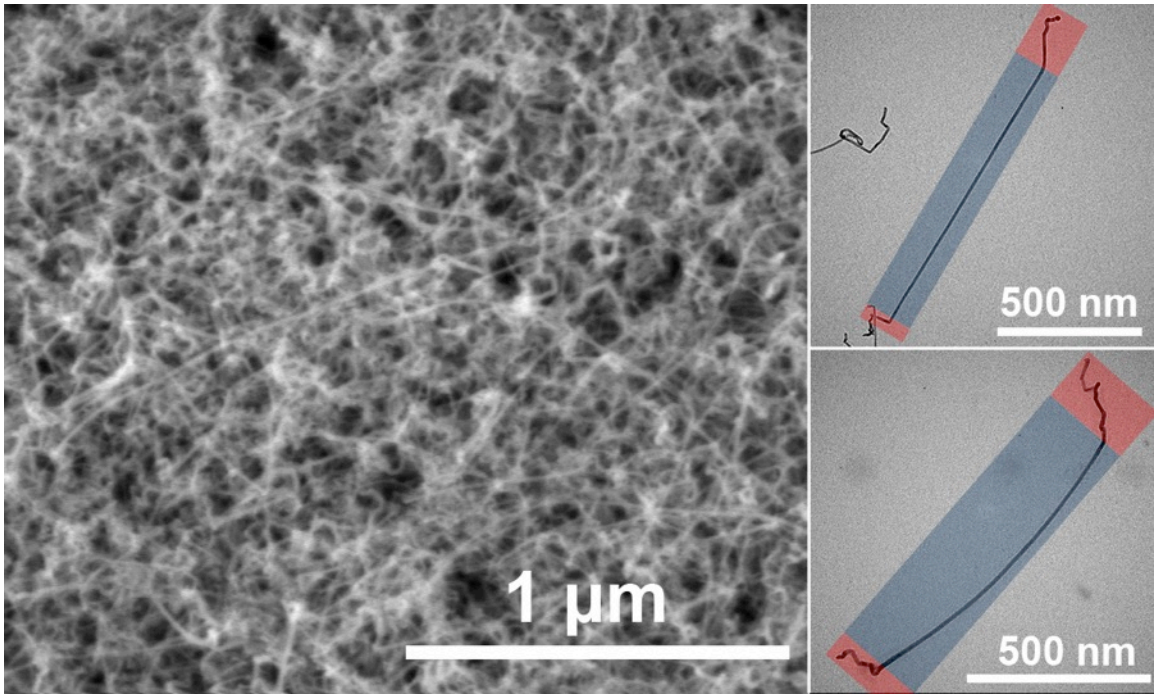

Figure 3.4 (a) SEM and b) and c) TEM images of high aspect ratio Si nanorods (i.e., nanowires) made with [Si]/[Sn]=400. The nanorods exhibit kinking at their ends, as highlighted by rectangle segments in b) and c), which indi- cates relatively unstable growth conditions at the beginning and end of the reactions.

The nanorods were crystalline diamond cubic Si (see XRD in Figure 3.7, below) and tended to grow in the [111] direction (Figure 3.5 a–b). Nanorods grown in the [1-10] direction were also observed (Figure 3.5c) and were generally kinked, with stacking faults and twins (Figure 3.5 e–f) usually at {111} planes, as commonly found in other Si nanowires[52–55] and nanorods.[21,22] Longer nanorods (> 100 nm) made with [Si]/[Sn] ratios higher than 60 exhibited a significant amount of branching (Figure 3.3d), indicating that under these conditions the Sn seeds either fused or induced geminate nucleation of multiple nanorods.[16,17,23] Much longer nanorods (> 1 µm ; i.e., nanowires), however, do not branch and have relatively straight midsections, but with significant kinking at their ends as seen in Figure 3.4b and c. Kinked growth usually indicates non-ideal growth

conditions, most likely related to the initial temperature drop that occurs upon reactant injection and reactant depletion at the end of the reaction.[41,56]

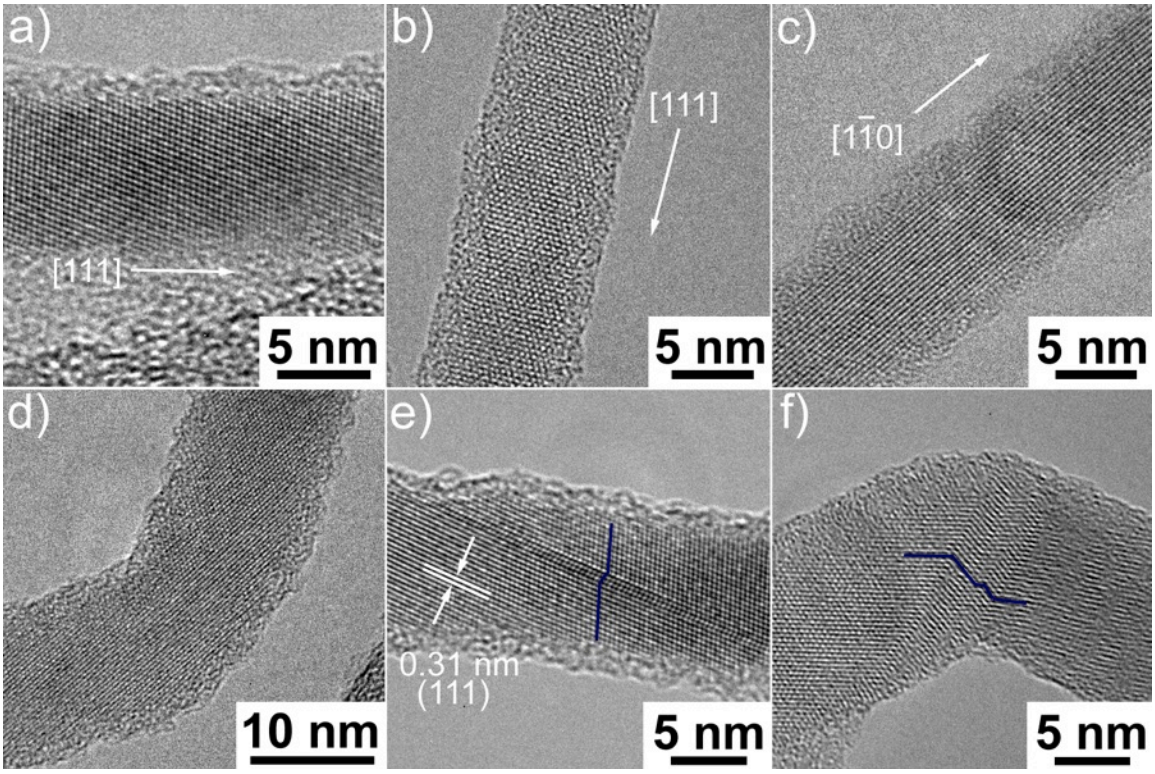

Figure 3.5 HRTEM images of Si nanorods made with [Si]/[Sn]=400. (a) and (b) Straight nanorods with [111] growth direction. (c) A straight nanorod with [1-10] growth direction. (d) A nanorod with one bend but no obvious crystal defect. (e) A nanorod with a dislocation. (f) A kinked nanorod exhibitinga series of twins. The wavy lines show the traces of {111} lattice plane cross the boundaries in (e) and (f).

The single-step reaction for Si nanorods could also be used to make Ge nanorods. Still using trisilane to reduce [$Sn(hmds)_2$] to Sn nanocrystals *in situ* (with a concentration of [Si]/[Sn]=1), diphenylgermane (DPG) was introduced as a Ge reactant. Dodecylamine was replaced with trioctylphosphine oxide as a capping ligand, since dodecylamine forms stable, unreactive amine–Ge complexes.[57] Figure 3.6 shows TEM images of Ge nanorods

with average diameter of 9 nm and length of 74 nm. Unlike the Si nanorods, the Ge nanorod length could not be easily manipulated and the product quality deteriorated significantly when reactions were carried out with higher or lower Ge concentrations. The Ge nanorods were also crystalline with diamond cubic crystal structure (see XRD in Figure 3.7). The primary growth direction of the Ge nanorods was <111>, with some bends associated with {111} twin defects. Overall, the Ge nanorods tended to be much straighter than the Si nanorods and there were many more Sn seeds still attached to the Ge nanorods than the Si nanorods. These differences might be related to the much slower decomposition of DPG compared to trisilane.

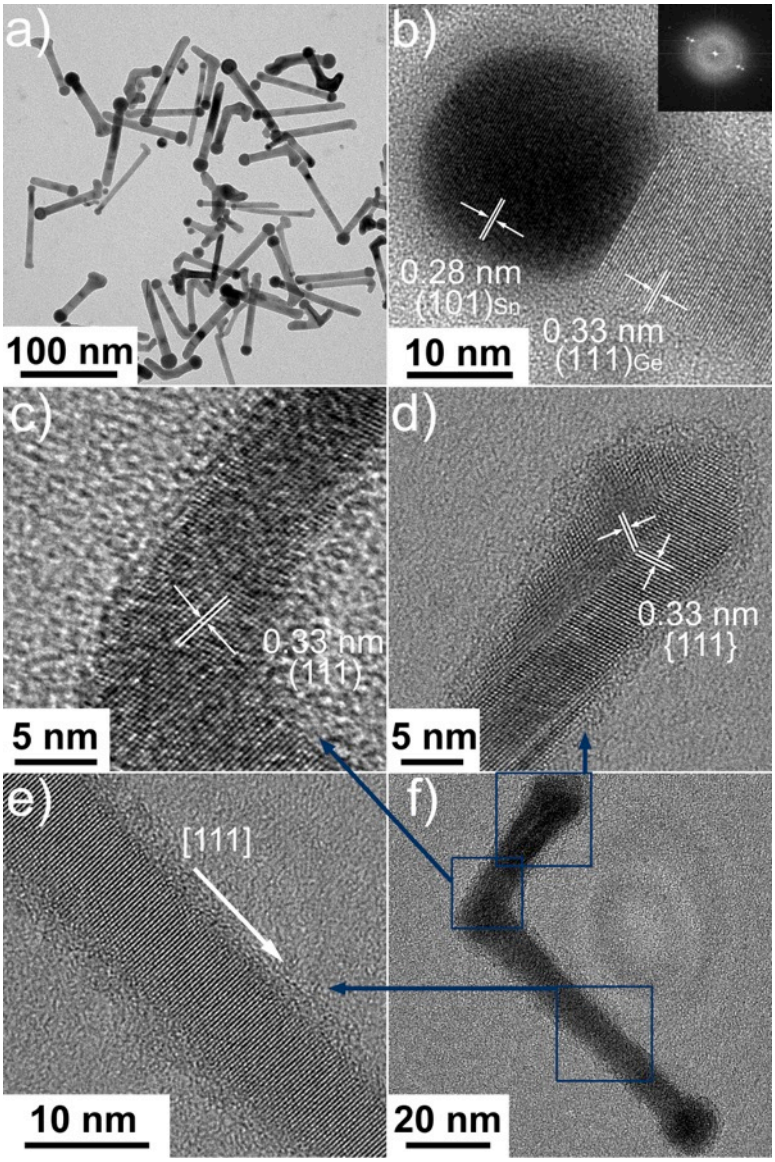

Figure 3.6 TEM images of Ge nanorods seeded with *in situ* grown Sn seeds. (a) Sn seeds are observed at the ends of most Ge nanorods. (b) HRTEM image of the Sn/Ge interface at the end of a Ge nanorod: the Sn (101) planes are aligned with Ge (111) planes. (c)–(e) HRTEM images of three different segments of the nanorod in (f).

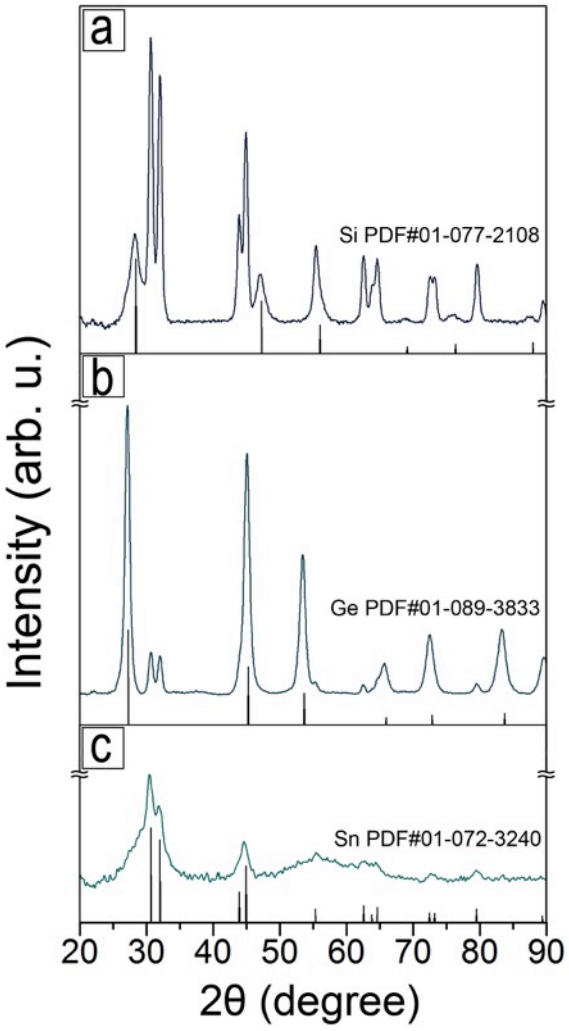

Figure 3.7 XRD of (a) Si and (b) Ge nanorods produced in a single reaction step with Sn seed particles formed in situ during the reaction. (c) XRD of the Sn nanoparticles isolated from the precursor solution. The reference patterns (black lines) and PDF numbers are shown for diamond cubic Si, Ge, and tetragonal Sn.

The interfaces between the Sn seeds and the Si and Ge nanorods were observably different. Most of the Ge nanorods still had Sn seeds at their tips, whereas many Si nanorods did not. It is fairly common for nanowires made by SLS reactions using low-melting metals not to have significant numbers of seed particles remaining on their tips.[49]

In the case of Si, the much longer (> 100 nm) Si nanorods had many more Sn seeds remaining at their tips. Figure 3.8 shows high-angle annular dark-field (HAADF) scanning transmission electron microscopy (STEM) images and energy-dispersive X-ray spectroscopy (EDS) maps of Si and Ge nanorods with Sn seeds at their tips. HAADF-STEM image contrast is very sensitive to atomic number (so-called Z-contrast imaging) and the Sn seeds are much brighter than the Si and Ge segments. EDS maps confirm that Sn is located in the seeds and that the nanorods are composed of Si or Ge. The HAADF-STEM images also show that the interface between Sn and the Si and Ge nanorods has slightly different structure. Figure 3.9 shows a TEM of the interface between a Sn seed and an Si nanorod. The interface is somewhat diffuse and the Sn seed is separated from the Si nanorod by an amorphous segment. The seed itself consists of multicrystalline domains of Si and Sn. In contrast, the interface between Sn seeds and Ge nanorods is sharp and flat. There appears to be epitaxial inter- facing between Sn and Ge, as shown in Figure 3.6b, in which the Ge (111) planes align in parallel with the (101) planes of Sn with a sharp boundary between them. This difference could also explain the observed adhesion of the Sn seeds at the tips of Ge nanorods and not Si nanorods.

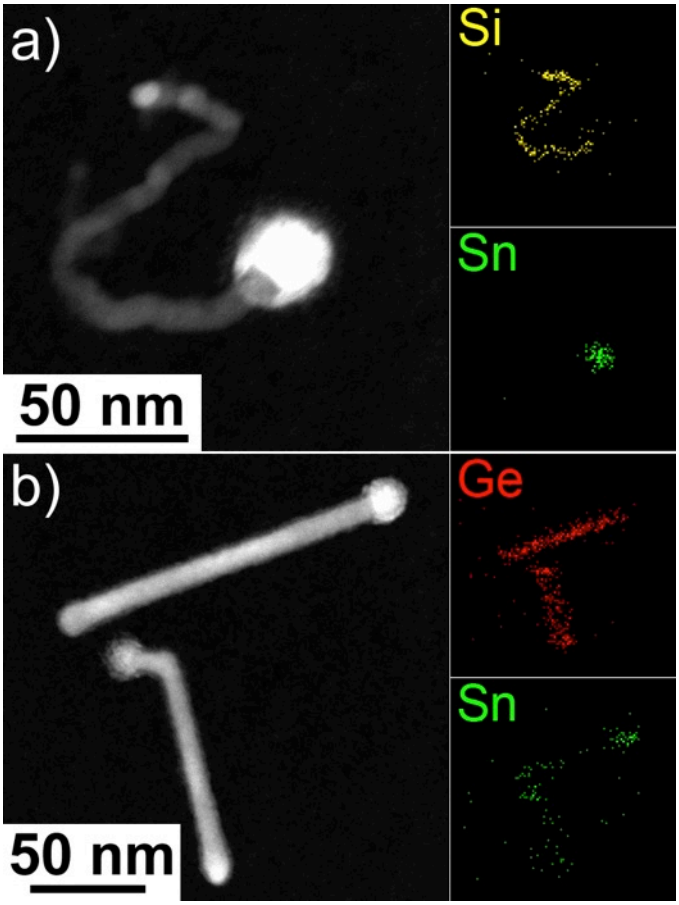

Figure 3.8 HAADF STEM images of (a) Si and (b) Ge nanorods with Sn seeds attached. The elemental maps of these nanorods confirm that the nanorod bodies are composed of Si and Ge, respectively, and that the seeds are composed of Sn. According to the quantified EDS data, less than 1 and 4 at.% of Sn is observed in the Si and Ge nanorods, respectively. This is consistent with the very low Sn solubility in Si and Ge: the solid solubility of Sn in Si at the reaction temperature of 410°C is approximate 0.013 at.%, while the solid solubility of Sn in Ge at 350°C is as high as 1.1 at. %.

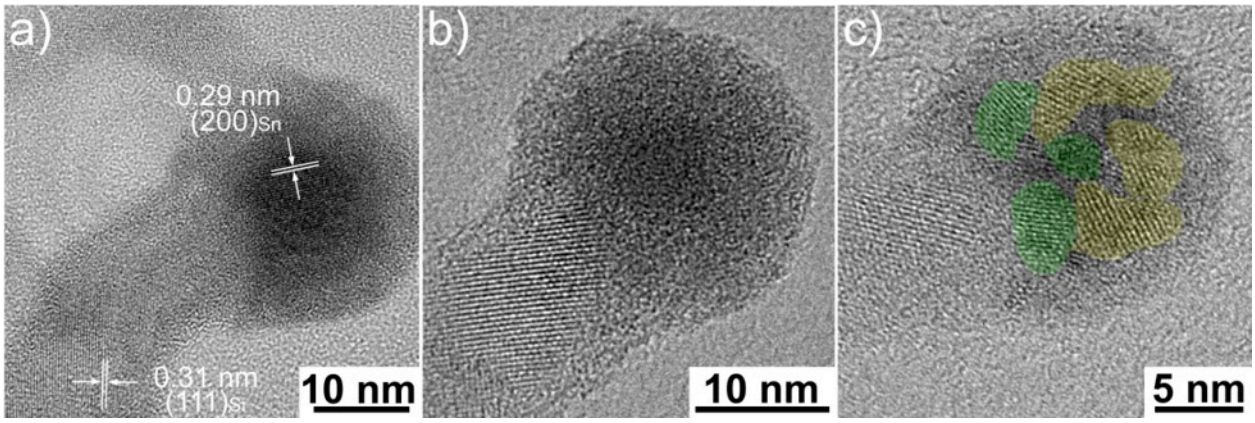

Figure 3.9 High-resolution TEM images of Sn-Si nanorod interfaces: (a) c-Si nanorods and c-Sn seed separated by an amorphous section; (b) c-Si nanorods with a-Sn seed; (c) polycrystalline seed containing Si grains (yellow) and Sn grains (green) which are determined by the measurement of interplanar spacings: 0.31 nm corresponds to (111) of diamond cubic Si; 0.29 nm corresponds to the (200) of tetragonal Sn.

3.4 CONCLUSIONS

In conclusion, Si and Ge nanorods with high crystallinity and controlled size can be obtained in a single reaction step by in situ Sn nanoparticle formation and seeding. Monodisperse Sn nanoparticles are generated during the reaction, which helps limit oxidation of the Sn seeds and improves repeatability and synthesis control. Furthermore, as this reaction is conducted in solvent under ambient pressure, it provides a convenient and fast way to prepare Si and Ge nanorods and significantly expands the synthetic conditions available to now make crystalline Si and Ge nanomaterials. Additionally, the use of Sn seeds for the Si and Ge nanorods is very well suited for use in lithium ion batteries as new electrode materials, as the incorporation of Sn into Si has been shown to have a beneficial impact on the lithiation properties of the materials.[50,51,58]

3.5 ACKNOWLEDGEMENTS

We acknowledge financial support of this work by the Rob- ert A. Welch Foundation (grant no. F-1464) and the Energy Frontier Research Center (EFRC) funded by the U.S. Depart- ment of Energy Office of Science and Office of Basic Energy Sciences, under Award no. DESC0001091. We also thank Yixuan Yu and Christian Bosoy for SAXS measurements and J. P. Zhou for HRTEM assistance.

3.6 REFERENCES

1. Brus, L. Luminescence of Silicon Materials: Chains, Sheets, Nanocrystals, Nanowires, Microcrystals, and Porous Silicon. *J. Phys. Chem.* **1994**, *98* (14), 3575–3581.

2. Hessel, C. M.; Henderson, E. J.; Veinot, J. G. C.; Uni, V.; February, R. V; Re, V.; Recei, M.; August, V. Hydrogen Silsesquioxane : A Molecular Precursor for Nanocrystalline Si - SiO 2 Composites and Freestanding Hydride-Surface-Terminated Silicon Nanoparticles. **2006**, No. 1, 6139–6146.

3. English, D. S.; Pell, L. E.; Yu, Z.; Barbara, P. F.; Korgel, B. a. Size Tunable Visible Luminescence from Individual Organic Monolayer Stabilized Silicon Nanocrystal Quantum Dots. *Nano Lett.* **2002**, *2* (7), 681–685.

4. Tilley, R. D.; Warner, J. H.; Yamamoto, K.; Matsui, I.; Fujimori, H. Micro-Emulsion Synthesis of Monodisperse Surface Stabilized Silicon Nanocrystals. *Chem. Commun. (Camb).* **2005**, No. 14, 1833–1835.

5. Yang, C. S.; Bley, R. A.; Kauzlarich, S. M.; Lee, H. W. H.; Delgado, G. R. Synthesis of Alkyl-Terminated Silicon Nanoclusters by a Solution Route. *J. Am. Chem. Soc.* **1999**, *121* (22), 5191–5195.

6. Jurbergs, D.; Rogojina, E.; Mangolini, L.; Kortshagen, U. Silicon Nanocrystals with Ensemble Quantum Yields Exceeding 60%. *Appl. Phys. Lett.* **2006**, *88* (23), 60–63.

7. Li, X.; He, Y.; Talukdar, S. S.; Swihart, M. T. Process for Preparing Macroscopic Quantities of Brightly Photoluminescent Silicon Nanoparticles with Emission Spanning the Visible Spectrum. *Langmuir* **2003**, *19* (20), 8490–8496.

8. Hessel, C. M.; Reid, D.; Panthani, M. G.; Rasch, M. R.; Goodfellow, B. W.; Wei, J.; Fujii, H.; Akhavan, V.; Korgel, B. a. Synthesis of Ligand-Stabilized Silicon Nanocrystals with Size-Dependent Photoluminescence Spanning Visible to Near-Infrared Wavelengths. *Chem. Mater.* **2012**, *24* (2), 393–401.

9. Lee, D. C.; Pietryga, J. M.; Robel, I.; Werder, D. J.; Schaller, R. D.; Klimov, V. I. Colloidal Synthesis of Infrared-Emitting Germanium Nanocrystals. *J. Am. Chem. Soc.* **2009**, *131* (10), 3436–3437.

10. Ruddy, D. A.; Johnson, J. C.; Smith, E. R.; Neale, N. R. Size and Bandgap Control in the Solution-Phase Synthesis of near-Infrared-Emitting Germanium Nanocrystals. *ACS Nano* **2010**, *4* (12), 7459–7466.

11. Gerion, D.; Zaitseva, N.; Saw, C.; Casula, M. F.; Fakra, S.; Buuren, T. Van; Galli, G.; Li, V.; Chimiche, S. Solution Synthesis of Germanium Nanocrystals : Success and Open Challenges. **2004**.

12. Lu, X.; Korgel, B. a.; Johnston, K. P. High Yield of Germanium Nanocrystals Synthesized from Germanium Diiodide in Solution. *Chem. Mater.* **2005**, *17* (25), 6479–6485.

13. Henderson, E. J.; Hessel, C. M.; Veinot, J. G. C. Synthesis and Photoluminescent Properties of Size-Controlled Germanium Nanocrystals from Phenyl Trichlorogermane-Derived Polymers. *J. Am. Chem. Soc.* **2008**, *130* (11), 3624–3632.

14. Taylor, B. R.; Kauzlarich, S. M.; Lee, H. W. H.; Delgado, G. R. Solution Synthesis of Germanium Nanocrystals Demonstrating Quantum Confinement. *Chem. Mater.* **1998**, *10* (1), 22–24.

15. Lu, X.; Hessel, C. M.; Yu, Y.; Bogart, T. D.; Korgel, B. A. Colloidal Luminescent Silicon Nanorods. *Nano Lett.* **2013**, *13* (7), 3101–3105.

16. Kuno, M. An Overview of Solution-Based Semiconductor Nanowires: Synthesis and Optical Studies. *Phys. Chem. Chem. Phys.* **2008**, *10* (5), 620.

17. Shabaev, a.; Efros, A. L. 1D Exciton Spectroscopy of Semiconductor Nanorods. *Nano Lett.* **2004**, *4* (10), 1821–1825.

18. Sigman, M. B.; Korgel, B. a. Strongly Birefringent Pb3O2Cl2 Nanobelts. *J. Am. Chem. Soc.* **2005**, *127* (28), 10089–10095.

19. Mohamed, M. B.; Burda, C.; El-Sayed, M. a. Shape Dependent Ultrafast Relaxation Dynamics of CdSe Nanocrystals: Nanorods vs Nanodots. *Nano Lett.* **2001**, *1* (11), 589–593.

20. Htoon, H.; Hollingworth, J. a.; Malko, a. V.; Dickerson, R.; Klimov, V. I. Light Amplification in Semiconductor Nanocrystals: Quantum Rods versus Quantum Dots. *Appl. Phys. Lett.* **2003**, *82* (26), 4776–4778.

21. Heitsch, A. T.; Hessel, C. M.; Akhavan, V. A.; Korgel, B. A. Colloidal Silicon Nanorod Synthesis. *Nano Lett.* **2009**, *9* (8), 3042–3047.

22. Hessel, C. M.; Heitsch, A. T.; Korgel, B. A. Gold Seed Removal from the Tips of Silicon Nanorods. *Nano Lett.* **2010**, *10* (1), 176–180.

23. Chockla, A. M.; Harris, J. T.; Korgel, B. a. Colloidal Synthesis of Germanium Nanorods. *Chem. Mater.* **2011**, *23* (7), 1964–1970.

24. Chockla, A. M.; Holmberg, V. C.; Korgel, B. a. Germanium Nanorod Extinction Spectra: Discrete Dipole Approximation Calculations and Experiment. *J. Phys. Chem. C* **2012**, *116* (42), 22625–22630.

25. Penn, R. L. Imperfect Oriented Attachment: Dislocation Generation in Defect-Free Nanocrystals. *Science* **1998**, *281* (5379), 969–971.

26. Tang, Z.; Kotov, N. a; Giersig, M. Spontaneous Organization of Single CdTe Nanoparticles into Luminescent Nanowires. *Science* **2002**, *297* (5579), 237–240.

27. Cho, K. S.; Talapin, D. V.; Gaschler, W.; Murray, C. B. Designing PbSe Nanowires and Nanorings through Oriented Attachment of Nanoparticles. *J. Am. Chem. Soc.* **2005**, *127* (19), 7140–7147.

28. Peng, X.; Manna, L.; Yang, W.; Wickham, J.; Scher, E.; Kadavanich, A.; Alivisatos, A. Shape Control of CdSe Nanocrystals. *Nature* **2000**, *404* (6773), 59–61.

29. Manna, L.; Scher, E. C.; Alivisatos, a. P. Synthesis of Soluble and Processable Rod-, Arrow-, Teardrop-, and Tetrapod-Shaped CdSe Nanocrystals. *J. Am. Chem. Soc.* **2000**, *122* (51), 12700–12706.

30. Jun, Y. W.; Lee, S. M.; Kang, N. J.; Cheon, J. Controlled Synthesis of Multi-Armed CdS Nanorod Architectures Using Monosurfactant System. *Journal of the American Chemical Society*, 2001, *123*, 5150–5151.

31. Park, J.; Koo, B.; Yoon, K. Y.; Hwang, Y.; Kang, M.; Park, J. G.; Hyeon, T. Generalized Synthesis of Metal Phosphide Nanorods via Thermal Decomposition of Continuously Delivered Metal-Phosphine Complexes Using a Syringe Pump. *J. Am. Chem. Soc.* **2005**, *127* (23), 8433–8440.

32. Shieh, F.; Saunders, A. E.; Korgel, B. a. General Shape Control of Colloidal CdS, CdSe, CdTe Quantum Rods and Quantum Rod Heterostructures. *J. Phys. Chem. B* **2005**, *109* (18), 8538–8542.

33. Wagner, R. S.; Ellis, W. C. Vapor-Liquid-Solid Mechanism of Single Crystal Growth. *Appl. Phys. Lett.* **1964**, *4* (5), 89–90.

34. Hu, J.; Odom, T. W.; Lieber, C. M. Chemistry and Physics in One Dimension: Synthesis and Properties of Nanowires and Nanotubes. *Accounts of Chemical Research*, 1999, *32*, 435–445.

35. Hanrath, T.; Korgel, B. A. Supercritical Fluid–Liquid–Solid (SFLS) Synthesis of Si and Ge Nanowires Seeded by Colloidal Metal Nanocrystals. *Adv. Mater.* **2003**, *15* (5), 437–440.

36. Wang, F.; Dong, A.; Sun, J.; Tang, R.; Yu, H.; Buhro, W. E. Solution-Liquid-Solid Growth of Semiconductor Nanowires. *Inorg. Chem.* **2006**, *45* (19), 7511–7521.

37. Kan, S.; Mokari, T.; Rothenberg, E.; Banin, U. Synthesis and Size-Dependent Properties of Zinc-Blende Semiconductor Quantum Rods. *Nat. Mater.* **2003**, *2* (3), 155–158.

38. Wang, F.; Tang, R.; Yu, H.; Gibbons, P. C.; Buhro, W. E. Size- and Shape-Controlled Synthesis of Bismuth Nanoparticles. *Chem. Mater.* **2008**, *20* (11), 3656–3662.

39. Wang, F.; Buhro, W. E. An Easy Shortcut Synthesis of Size-Controlled Bismuth Nanoparticles and Their Use in the SLS Growth of High-Quality Colloidal Cadmium Selenide Quantum Wires. *Small* **2010**, *6* (4), 573–581.

40. Lu, X.; Fanfair, D. D.; Johnston, K. P.; Korgel, B. A. High Yield Solution-Liquid-Solid Synthesis of Germanium Nanowires. *J. Am. Chem. Soc.* **2005**, *127* (45), 15718–15719.

41. Fanfair, D. D.; Korgel, B. A. Bismuth Nanocrystal-Seeded III-V Semiconductor Nanowire Synthesis. *Cryst. Growth Des.* **2005**, *5* (5), 1971–1976.

42. Fanfair, D. D.; Korgel, B. A. Twin-Related Branching of Solution-Grown ZnSe Nanowires. *Chem. Mater.* **2007**, *19* (20), 4943–4948.

43. Nedeljković, J. M.; Mićić, O. I.; Ahrenkiel, S. P.; Miedaner, A.; Nozik, A. J. Growth of InP Nanostructures via Reaction of Indium Droplets with Phosphide Ions: Synthesis of InP Quantum Rods and InP-TiO2 Composites. *J. Am. Chem. Soc.* **2004**, *126* (8), 2632–2639.

44. Yu, H.; Li, J.; Loomis, R. a; Wang, L.-W.; Buhro, W. E. Two- versus Three-Dimensional Quantum Confinement in Indium Phosphide Wires and Dots. *Nat. Mater.* **2003**, *2* (8), 517–520.

45. Grebinski, J. W.; Hull, K. L.; Zhang, J.; Kosel, T. H.; Kuno, M. Solution-Based Straight and Branched CdSe Nanowires. *Chem. Mater.* **2004**.

46. Read, C. G.; Biacchi, A. J.; Schaak, R. E. Au-Ge and Ag-Ge Heterodimers with Tunable Domain Sizes: A Supersaturation-Precipitation Route to Colloidal Hybrid Nanoparticles. *Chem. Mater.* **2013**.

47. Shweky, I.; Aharoni, A.; Mokari, T.; Rothenberg, E.; Nadler, M.; Popov, I.; Banin, U. Seeded Growth of InP and InAs Quantum Rods Using Indium Acetate and Myristic Acid. *Mater. Sci. Eng. C* **2006**, *26* (5-7), 788–794.

48. Li, Z.; Kornowski, A.; Myalitsin, A.; Mews, A. Formation and Function of Bismuth Nanocatalysts for the Solution-Liquid-Solid Synthesis of CdSe Nanowires. *Small* **2008**, *4* (10), 1698–1702.

49. Puthussery, J.; Kosel, T. H.; Kuno, M. Facile Synthesis and Size Control of II-VI Nanowires Using Bismuth Salts. *Small* **2009**, *5* (10), 1112–1116.

50. Chockla, A. M.; Klavetter, K. C.; Mullins, C. B.; Korgel, B. A. Tin-Seeded Silicon Nanowires for High Capacity Li-Ion Batteries. *Chem. Mater.* **2012**, *24* (19), 3738–3745.

51. Bogart, T. D.; Oka, D.; Lu, X.; Gu, M.; Wang, C.; Korgel, B. A. Lithium Ion Battery Peformance of Silicon Nanowires with Carbon Skin. *ACS Nano* **2014**, *8* (1), 915–922.

52. Davidson, F. M.; Lee, D. C.; Fanfair, D. D. D.; Korgel, B. A. Lamellar Twinning in Semiconductor Nanowires. *J. Phys. Chem. C* **2007**, *111* (7), 2929–2935.

53. Shin, N.; Chi, M.; Howe, J. Y.; Filler, M. a. Rational Defect Introduction in Silicon Nanowires. *Nano Lett.* **2013**, *13* (5), 1928–1933.

54. Arbiol, J.; Fontcuberta I Morral, A.; Estradé, S.; Peiró, F.; Kalache, B.; Roca I Cabarrocas, P.; Morante, J. R. Influence of the (111) Twinning on the Formation of Diamond Cubic/diamond Hexagonal Heterostructures in Cu-Catalyzed Si Nanowires. *J. Appl. Phys.* **2008**, *104* (6).

55. Conesa-Boj, S.; Zardo, I.; Estradé, S.; Wei, L.; Jean Alet, P.; Roca i Cabarrocas, P.; Morante, J. R.; Peiró, F.; Morral, A. F. I.; Arbiol, J. Defect Formation in Ga-Catalyzed Silicon Nanowires. *Cryst. Growth Des.* **2010**, *10* (4), 1534–1543.

56. Kodambaka, S.; Tersoff, J.; Reuter, M. C.; Ross, F. M. Diameter-Independent Kinetics in the Vapor-Liquid-Solid Growth of Si Nanowires. *Phys. Rev. Lett.* **2006**, *96* (9), 1–4.

57. Loscutoff, P. W.; Bent, S. F. Reactivity of the Germanium Surface: Chemical Passivation and Functionalization. *Annu. Rev. Phys. Chem.* **2006**, *57*, 467–495.

58. Hatchard, T. D.; Dahn, J. R. Study of the Electrochemical Performance of Sputtered $Si_{1-x}Sn_x$ Films. *J. Electrochem. Soc.* **2004**, *151* (10), A1628.

Chapter 4: Low Temperature Synthesis of Silicon Nanorods From Isotetrasilane, Neopentasilane, and Cyclohexasilane[††]

4.1 INTRODUCTION

Crystalline silicon (Si) nanorods and nanowires can be obtained by metal nanoparticle-seeded solution-liquid-solid (SLS) growth in solution.[1–5] This method requires a solvent, a silane reactant, and nanoparticles of a metal that forms a eutectic with Si, such as gold (Au) or tin (Sn). Similar to the vapor-liquid-solid (VLS) growth process for nanowires in the gas-phase,[6,7] SLS growth involves the decomposition of a silane reactant to Si, which dissolves into the metal seed to form a liquid droplet and then recrystallizes at the droplet surface to form the nanowire. The rate of nanowire growth and the morphology of the nanowire depend sensitively on the rate of Si addition to the seed.[8–10] A while back, we found that carbon-containing phenylsilanes, which are very effective for the synthesis of Si nanowires at higher temperatures in supercritical fluids[10–14] (i.e., by supercritical fluid-liquid-solid (SFLS) growth), are not sufficiently reactive at the lower SLS growth temperatures (<400^{o}C) to produce nanowires or nanorods, and the much more reactive trisilane (Si_3H_8) must be used.[1,2] Trisilane certainly works well for SLS growth of Si nanowires and nanorods, but still requires relatively high reaction temperatures (~400^{o}C)—significantly higher than the eutectic temperatures of both Si/Au and Si/Sn—and we have been searching for silane reactants to make Si nanorods and nanowires at significantly lower temperature. Here, we show that Si nanorods can be produced at reduced temperatures using isotetrasilane (Si_4H_{10}), neopentasilane (Si_5H_{12}) or

[††] Manuscript submitted to *Chemistry of Materials*: Lu, X.; Anderson, K. J.; Boudjouk, P. and Korgel B. A. Low Temperature Colloidal Synthesis of Silicon Nanorods From Isotetrasilane, Neopentasilane, and Cyclohexasilane

cyclohexasilane (Si_6H_{12}). Of these, cyclohexasilane enabled the lowest temperature growth, down as low as 200°C.

4.2 EXPERIMENTAL DETAILS

4.2.1 Materials

Bis[bis(trimethylsilyl)amino]tin(II) ($Sn(hmds)_2$, Aldrich), trisilane (Si_3H_8, Voltaix), isotetrasilane (Si_4H_{10}, Gelest, Inc.), neopentasilane (Si_5H_{12}, Gelest, Inc.), dodecylamine (98%, Aldrich), squalane (>95%, Aldrich), poly(vinylpyrrolidinone)-hexadecane (PVP-HDE) copolymer (Ganex V-216, ISP Technologies, Inc.) were obtained commercially and used without further purification. PVP-HDE is dissolved in dodecylamine to make a 33% w/w copolymer solution. The copolymer solution and the squalane are degassed under vacuum at 80°C for 45 min, and then stored in a nitrogen-filled glovebox prior to use.

4.2.2 Nanorod Synthesis

Si nanorod synthesis was carried out using a single-step Sn-seeded Si nanorod growth reaction similar to previously described methods.[16] The reactions were carried out on a Schlenk line setup operated inside a nitrogen-filled glovebox. In a typical reaction, 10 mL of squalane was heated to 380°C under N_2 flow in a flat bottom flask attached to the Schlenk line assembly. Separately, a precursor solution of 1 mL PVP-HDE dodecylamine solution (containing 27.5 mg of PVP-HDE), 20 μL of $Sn(hmds)_2$ and 76 μL of trisilane was prepared in a 3 mL vial, which immediately turned dark brown after mixing due to the formation of Sn nanoparticles. The precursor solution was drawn into a syringe equipped with a 6” needle. Prior to injection, the stopcock valve was closed. The mixture was injected through the septum into the hot solvent. After 3 min, the reaction

flask was removed from the heating mantle and allowed to cool to room temperature. The stopcock valve was closed throughout the reaction to reduce evaporation. In the other reactions, the precursor solutions were made of 70 μL of isotetrasilane, 68 μL of neopentasilane and 56 μL of cyclohexasilane, respectively, to maintain a consistent [Si] concentration in each reaction. Reaction temperatures ranging between 380°C and 180°C were explored.

Si nanorods were purified by adding 10 mL of toluene to the crude reaction solution, transferring to a centrifuge tube, and then adding about 15 mL of ethanol slowly. The mixture was centrifuged at 1000 rpm for 10 min to isolate the products. The supernatant was discarded. The precipitate was redispersed in toluene and washed by repeating the precipitation procedure for three times. The final nanorod product was dispersed and stored in chloroform.

4.2.3 Surface Passivation of Si Nanorods

Si nanorods was dried in a Teflon cup, then 4 mL of 37.5% HCl and 10 mL of 40% HF were added. The Si nanorods were stirred in the dark for 6 hours, and then isolated from the HF solution by centrifugation. The supernatant was discarded. The precipitate was washed with ethanol, and transferred to glass centrifuge tube for the third wash with chloroform. After centrifugation, the precipitate was dispersed in 8 mL of 1-octadecene and injected into a sealed flask with a 10 mL syringe. After degassing with three freeze-pump-thaw cycles on a Schlenk line, the dispersion was heated at 190ºC for 12 hr under N_2. The 1-octadecene passivated Si nanorods were washed three times with hexane and ethanol, and then redispersed in toluene for further characterization.

4.2.4 Materials Characterization

Low-resolution transmission electron microscopy (TEM) images were acquired using a FEI Tecnai Spirit Bio Twin operated at 80 kV. Samples were drop-cast from

chloroform dispersions onto carbon-coated 200 mesh copper TEM grids (Electron Microscope Science). High-resolution transmission microscopy (HRTEM) images were obtained on a field emission JEOL 2010F TEM operated at 200 kV. For high-resolution imaging, nanorods were drop cast onto 200 mesh copper TEM grids with lacey carbon (Electron Microscope Science) and found at the edge of the carbon support extended over the vacuum background.

X-ray diffraction (XRD) was obtained on a Rigaku R-Axis Spider diffractometer with an image plate detector and Cu Kα radiation (λ=1.54 Å). Samples were prepared on cryoloops and scanned for 10 min at 10 deg/s sample rotation under radiation at 40 kV and 40 mA.

Photoluminescence (PL) spectra and PL lifetime were acquired on a Fluorolog-3 spectrophotometer (Horiba Jobin Yvon) with InGaAs photomultiplier tube for visible detection and a Hamamatsu H10330-45 detector for NIR detection, using a quartz cuvette with a 10 mm optical path length. The PL emission quantum yield was quantified by comparing the integrated photon counts of the nanorods to a Rhodamine 101 standard in anhydrous ethanol. The PL emission lifetime was measured using the time-corrected single photon counting method. A NanoLED with wavelength of 402 nm was used as excitation light source and PL decay was measured at a detection wavelength of 655 nm.

4.3 Results and Discussion

4.3.1 Silicon Nanorods Synthesis

Figure 4.1 shows TEM images of Si nanorods obtained using trisilane, isotetrasilane, neopentasilane or cyclohexasilane in a single-step Sn-seeded SLS reaction conducted at a range of temperatures. The yields of these reactions, the nanorod

dimensions and the overall product morphology are summarized in Table 4.1. At 380^{o}C, all four silanes produce Si nanorods. At a slightly lower reaction temperature of 340^{o}C, trisilane no longer produces nanorods. The decreased reaction temperature leads to a reduced average nanorod length from 200 nm at 380^{o}C to 65 nm at 340^{o}C obtained using isotetrasilane and neopentasilane (Figures 4.1c and 4.1e). With a further reduction of growth temperature to 320^{o}C, isotetrasilane and neopentasilane no longer produced nanorods. Cyclohexasilane on the other hand yields nanorods at growth temperatures as low as 200^{o}C, which is even slightly below the Si-Sn eutectic temperature of 232^{o}C. The trend of decreasing minimum growth temperature for Si nanorods with an increasing number of Si atoms in the reactant follows expectations based on experience from chemical vapor deposition (CVD) in which tetrasilane for example has lower activation energies than trisilane and disilane and can be used to depos amorphous silicon films at lower temperature.[17]

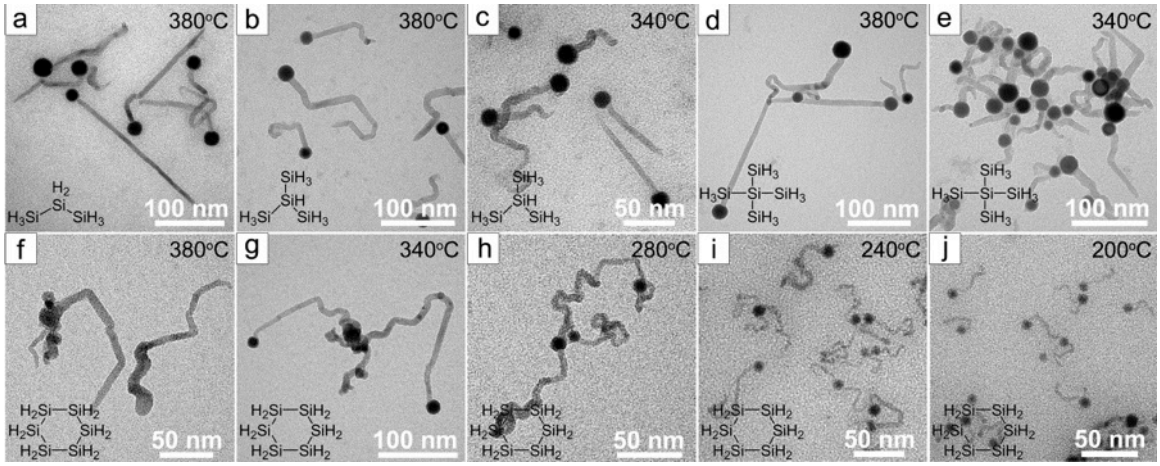

Figure 4.1 TEM images of Si nanorods obtained from Sn-seeded SLS reactions carried out at various temperatures with four different silane reactants: (a) trisilane at 380ºC; (b) isotetrasilane at 380ºC and (c) 340ºC; (d) neopentasilane at 380ºC and (e) 340ºC; (f) cyclohexasilane at 380ºC, (g) 340ºC, (h) 280ºC, (i) 240ºC and (j) 200ºC. The [Si]/[Sn] molar ratio was 35 in all reactions.

Table 4.1 Summary description of the reaction products obtained using four different silane reactants to grow Si nanorods in a single-step Sn-seeded SLS reaction. Si nanorod yields from Sn-seeded SLS reactions using four silanes carried out at different temperatures.[a]

Temp.	trisilane	isotetrasilane	neopentasilane	cyclohexasilane
380ºC	NRs (28.8%)	NRs (32.3%)	NRs (32.8%)	NRs (54.6%)[b]
360ºC	NRs (16.7%)	NRs (31.2%)	NRs (29.7%)	NRs (63.7%)
340ºC	short NRs (12.5%)	NRs (23.1%)	NRs (23.3%)	NRs (49.5%)
320ºC	-	short NRs (13.9%)	short NRs (17.0%)	NRs (44.4%)
300ºC	-	-	-	NRs (45.3%)
280ºC	-	-	-	NRs (38.6%)
260ºC	-	-	-	NRs (42.5%)
240ºC	-	-	-	NRs, thin (33.3%)
220ºC	-	-	-	NRs, thin (30.5%)
200ºC	-	-	-	NRs, thin (25.1%)
180ºC	-	-	-	-

[a] Since we do not know precisely the conversion of Sn reactant to Sn seed particles, the percentage production yield in parentheses is the quotient of the weight of dried product divided by the total mass of Sn and Si added to the reaction. If one assumes that $Sn(hmds)_2$ fully converts to Sn nanoparticles, the minimum production yield for the reaction would be 10.8%, i.e. no Si is produced.

[b] At 380ºC, many Sn seeds detach from the Si nanorods, which makes some of the Si nanorods shorter than the Si nanorods obtained at 360ºC and also seemed to result in lower yields at this reaction temperature.

In terms of reactivity, there is an important difference between cyclohexasilane and the other silanes. The decomposition of acyclic silanes, i.e. trisilane, isopentasilane and neopentasilane, yields lower silanes, like monosilane and disilane, that are not utilized in the solution nanorod growth because these molecules are too stable and volatile and do not decompose to Si in an appreciable way. The high reaction yield of cyclohexasilane on the other hand is enabled to a significant extent by the formation of silylene intermediates in a ring-opening process,[18] which are highly reactive and easily captured by the Sn seeds via chemisorption without Si atom loss. The high atom utilization of cyclohexasilane is reflected in both yield and nanorod morphology. The cyclohexasilane-generated Si nanorods are significantly longer than those obtained from the other reactants. Reactions carried out at 360°C gave nanorods with an average length of about 125 nm when trisilane, isotetrasilane or neopentasilane was used. Cyclohexasilane gave significantly longer nanorods with average length close to 300 nm.

Cyclohexasilane also enabled thinner nanorods to be produced by decreasing the reaction temperature. The nanorods had diameters of about 2-3 nm when grown at 240°C (Figurs 4.1i and 4.1j) compared to 8-9 nm when grown at 380°C. The nanorods grown at 200°C were produced below the Si-Sn eutectic temperature (232°C). These nanorods most likely evolve solid Sn seeds. Solid-phase seeding of semiconductor nanowires tends to give thinner nanowires compared to liquid-phase seeding[19] and *in situ* TEM has also shown that the same catalyst material yields smaller diameter nanowires when growth occurs below the eutectic temperature.[20] However, it is possible that the Sn nanoparticles at 200°C might be melted due to size-dependent melting point depression.[21]

4.3.2 Crystallinity and Crystal Structure

All of the nanorods produced using the four different silanes were crystalline with diamond cubic Si crystal structure. Figure 4.2 shows high resolution TEM images of Si nanorods made from the four different silanes at 380°C. The nanowires are crystalline and have predominantly grown in the [111] direction. Figure 4.3 shows XRD patterns for nanorods made with all four silanes used in this study. In all samples, the diffraction peaks from the Sn seeds are relatively strong. This is due in part to the fact that Sn scatters X-rays more strongly than Si. But there is also a significant amount of Sn in these reactions to seed the relatively short Si nanorods. Of the nanorods grown at 380°C, only those made with cyclohexasilane had Si diffraction peaks that were more prominent than the Sn-related peaks. This matches the relative yields of the reactions and the relative lengths of the nanorods. Cyclohexasilane gave higher conversions of reactant to Si and produced the longest nanorods.

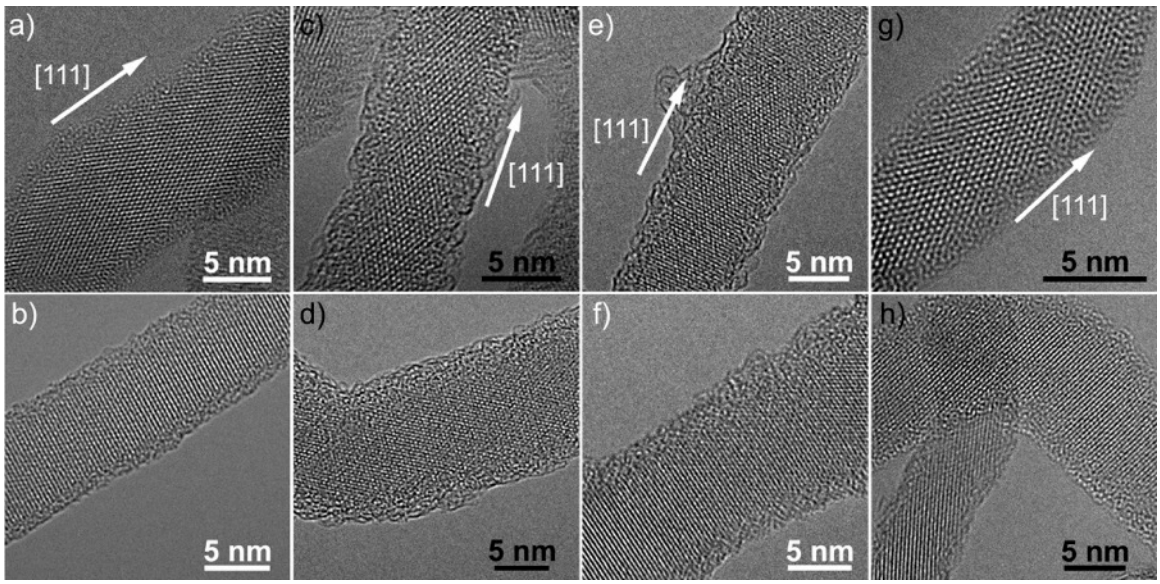

Figure 4.2 HRTEM images of Si nanorods obtained from reactions at 380°C using (a-b) trisilane; (c-d) isotetrasilane; (e-f) neopentasilane and (g-h) cyclohexasilane.

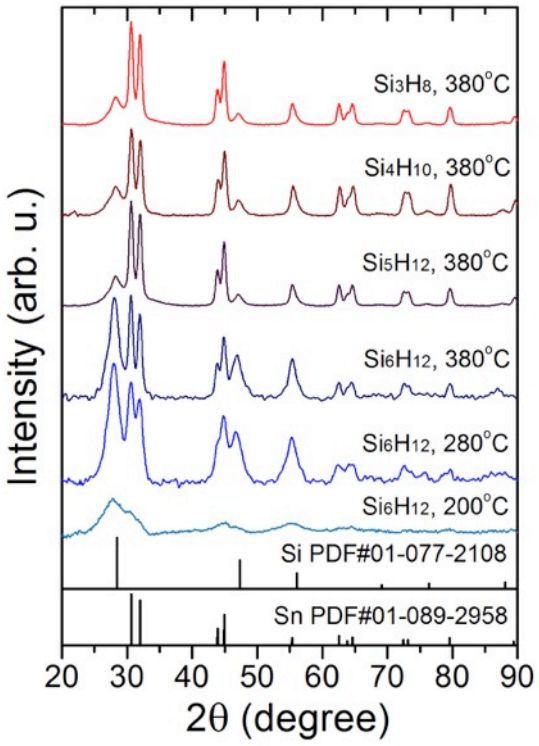

Figure 4.3 XRD of Si nanorods synthesized with Sn seeds using trisilane, isotetrasilane, or neopentasilane at 380°C, or cyclohexasilane at 380°C, 280°C or 200°C. All curves are normalized to the Sn (200) peak height, except the pattern for the Si nanorods generated with cyclohexasilane at 200°C. The reference patterns and corresponding PDF reference numbers are provided for diamond cubic Si and tetragonal Sn.

As shown in Figure 4.3, the diffraction peaks broadened for both Si and Sn as the nanorod growth temperature was lowered. This diffraction peak broadening with reduced growth temperature is consistent with the observed reductions in nanorod diameter with decreased temperature that were observed by TEM (See Figure 4.1j for example). The diffraction peaks from the nanorods made at 200°C are very broad, with significant overlap of the Si and Sn peaks. The nanorods are nonetheless crystalline, as further confirmed by TEM (Figure 4.4).

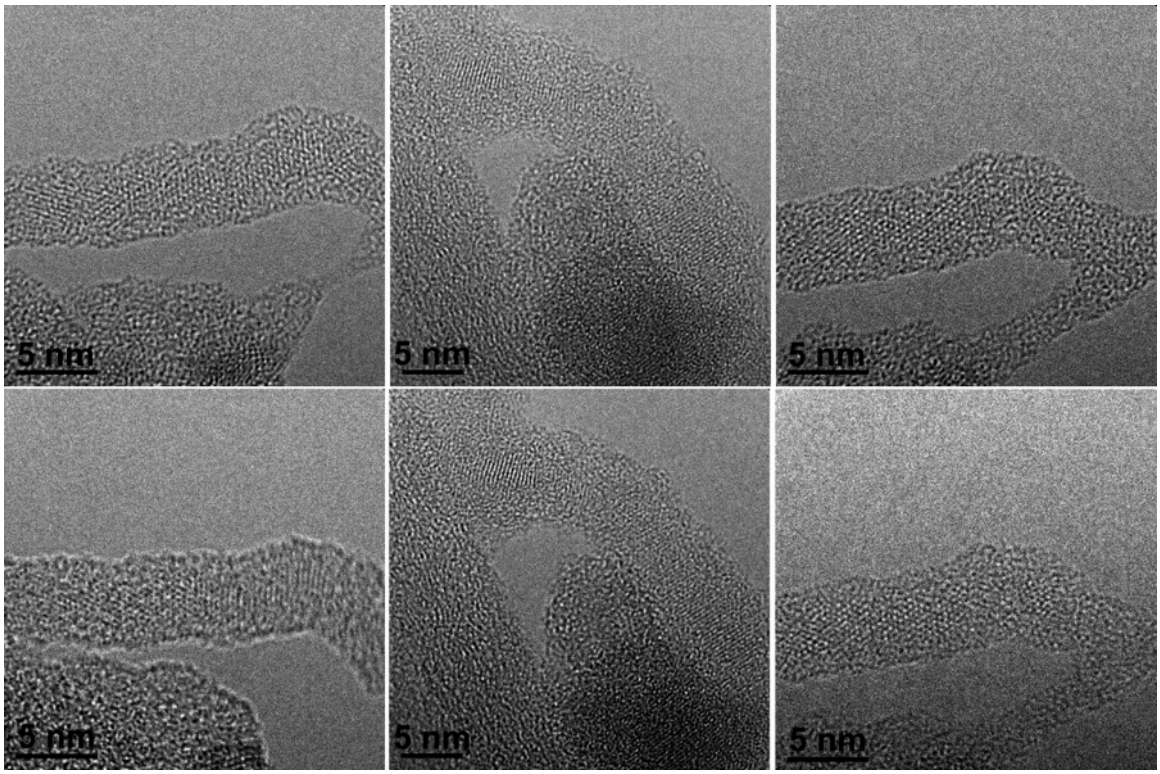

Figure 4.4 HRTEM images of the Si nanorods at 200°C with cyclohexasilane. The lattice fringes could be observed from those nanorods demonstrating that the Si nanorods obatained at such low temperature are still in crystalline phase.

4.3.3 Photoluminescence

None of the nanorods exhibited photoluminescence as synthesized. However, the nanorods could be made to become photoluminescent by etching away the Sn seeds and passivating the nanorod surfaces. Figure 4.5 shows a luminescent sample of Si nanorods made at 260°C from cyclohexasilane. Figure 4.5a shows a TEM image of the nanorods as synthesized. The darker Sn see particles are clearly visible at the ends of the nanorods. Figure 4.5b shows a TEM image of the sample after HF etching and

thermal hydrosilylation with 1-octadecene. The Sn seeds are no longer present and the nanorods fluoresce red. Figure 4.5c shows the PL emission spectra of the nanorods. The PL emission quantum yield of these nanorods dispersed in toluene at room temperature was 2%. Generally, the absorbance and emission spectra of these Si nanorods are similar to alkene-passivated Si nanocrystals[29-32] and Si nanorods made at higher temperature with trisilane and Sn seeds particles.[3] Figure 4.5d shows the time-dependent PL decay. The time-dependent PL intensity (N(t)) data in Figure 4.5d fit well to a triple exponential:[33]

$$N(t) = A_1 \exp\left[-\frac{t}{\tau_1}\right] + A_2 \exp\left[-\frac{t}{\tau_2}\right] + (1 - A_1 - A_2)\exp\left[-\frac{t}{\tau_3}\right] \qquad (1)$$

with characteristic lifetime values of $\tau_1 = 30$ ns, $\tau_2 = 700$ ns and $\tau_3 = 8.5$ μs. It appears that there are three competing electron-hole recombination processes in the luminescent Si nanorods. The microsecond lifetimes are characteristic of organic ligand-passivated Si nanocrystals.

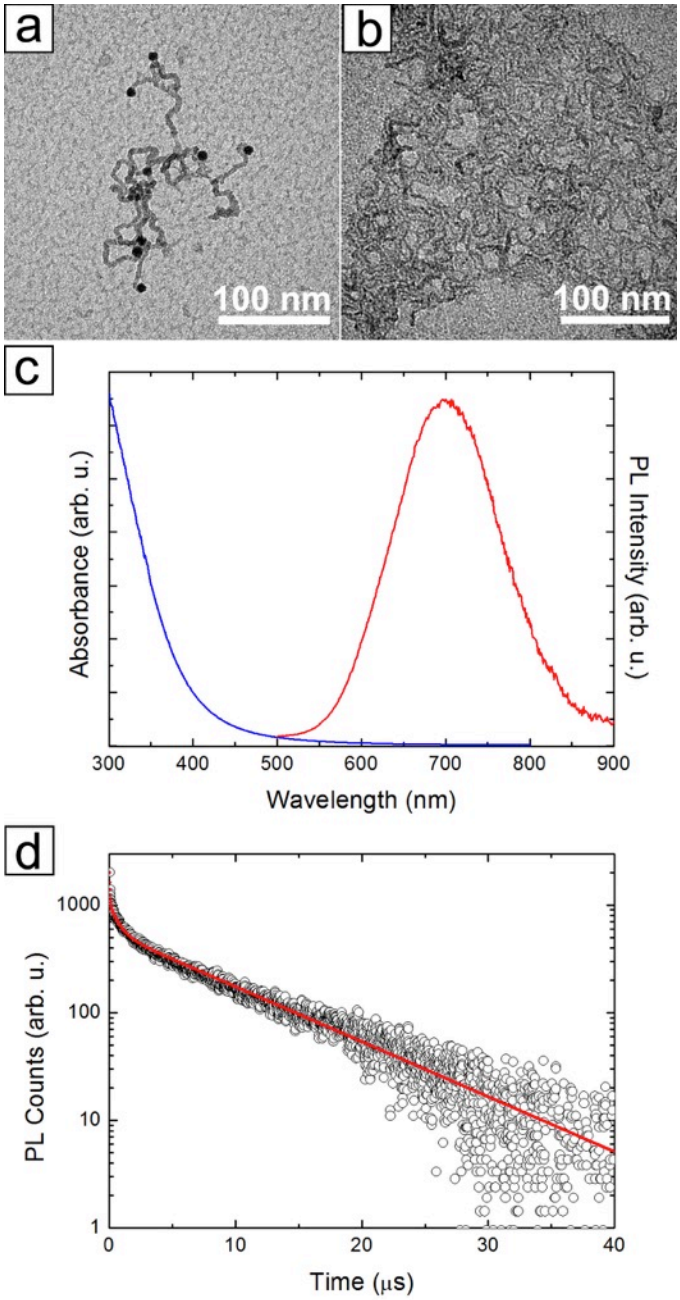

Figure 4.5 TEM images of Si nanorods obtained from cyclohexasilane at 260ºC (a) before and (b) after HF etching and thermal hydrosilylation with 1-octadecene. (c) Room-temperature optical absorbance (blue line) and PL spectra (λ_{exc} = 425 nm; red line) of octadecene-passivated Si nanorods dispersed in toluene. (d) The photoluminescence decay trace of passivated Si nanorods (λ_{exc} = 402 nm; λ_{em} = 655 nm). The PL decay lifetime was fitted

to Eqn (1) (red curve) to obtain characteristic values of $\tau_1 = 30$ ns, $\tau_2 = 700$ ns and $\tau_3 = 8.5$ μs.

4.3.4 Dehydrogenation of Silane Reactants

Figure 4.6 illustrates the mechanism of Sn-seeded Si nanorod growth. In the single-step reaction approach, Sn nanoparticles are formed *in situ* from $Sn(hmds)_2$ by reduction with silanes.[5] The Sn nanoparticles can catalyze the dissociation of Si-H bonds and release hydrogen gas[22] while the Si atoms dissolve into the Sn. Si nanorods then crystallize from the alloyed droplet when the Si concentration is higher than the solubility limit. The Sn-Si eutectic is located at 5×10^{-5} at.% Si and 1×10^{-4} °C below the melting point of Sn (231.9°C).[23] Saturation of the Sn seeds with Si is readily achieved; in fact, it only takes a single Si atom to overcome the solubility limit in Sn.[24] Some Sn seed particles grow up to 25 nm in diameter, and even these largest Sn seed particles only need 5 to 6 Si atoms to become saturated. This means that the decomposition of only one or two silane molecules can saturate a Sn seed particle and induce nanorod growth.

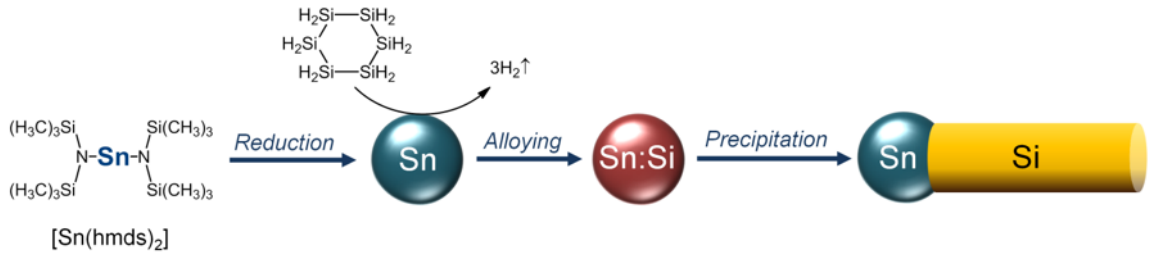

Figure 4.6 Illustration of Si nanorods synthesis using the example of cyclohexasilane. $Sn(hmds)_2$ is firstly reduced into Sn nanoparticles at room temperature. After injected to the hot solvent, those Sn nanoparticles catalyze the decomposition of cyclohexasilane releasing hydrogen. The Si atoms dissolves into the Sn droplet forming Sn:Si alloy. When reaching the critical concentration, Si precipitates from the surface of alloy droplet and recrystallize into the Si nanorod.

The nanorod growth rate depends on the rate that Si atoms are fed to the seeds, which is directly related to the silane decomposition rate.[9,12] Si atoms are produced from the silanes by the dissociation of Si-H and Si-Si bonds. The work by Shimoda et al.[25,26] utilizing cyclopentasilane to make the amorphous Si films reveals that Si-Si bonds in the polysilane break around 280°C and Si-H bonds break above 300°C. The Si-Si bonds break at lower temperature than required for Si-H dissociation. However, as Si-Si bond formation during crystallization of the Si nanorods is the reverse of the bond dissociation that occurs during reactant decomposition and does not require extra energy input, the difference in silane decomposition of the different reactants mostly reflects the different dehydrogenation pathways of the silanes, i.e. breaking of Si-H bonds. The minimum nanorod growth temperature is therefore related to the Si-H bond dissociation energy (BDE) of the silanes. The total Si-H BDE increases from 689.8 kcal/mol for

trisilane to 1010.4 kcal/mol for cyclohexasilane since there are a larger number of Si-H bonds in the cyclohexasilane molecule, but the Si-H BDE per Si atom drops significantly from trisilane (229.9 kcal/mol), isotetrasilane (216.1 kcal/mol), neopentasilane (208.6 kcal/mol) to cyclohexasilane (168.4 kcal/mol).[27,28] The reduced Si-H BDE of cyclohexasilane is consistent with the low nanorod growth temperature enabled by this reactant. Furthermore, like the other cyclic silanes,[25,26] cyclohexasilane is subject to the ring-opening process[18] and forms the highly reactive silylene intermediates which is easily to be caught by the Sn surface via the silylene insertion. This also contributes to the low activation energy for cyclohexasilanes in the Sn seeded Si nanorod growth.

Table 4.2 Calculation summary of bond dissociation energy of various silanes. (kcal/mol)

Silane	Si-H BDE	Si-H & Si-Si BDE	Si-H BDE per Si	Si-H & Si-Si BDE per Si
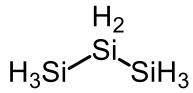 (Si_3H_8)	689.8	831.8	229.9	277.3
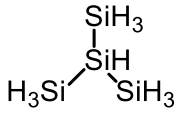 (Si_4H_{10})	864.2	1077.2	216.1	269.3
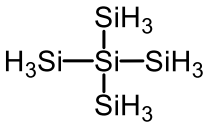 (Si_5H_{12})	1042.8	1326.8	208.6	265.4
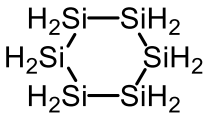 (Si_6H_{12})	1010.4	1418.4	168.4	236.4

4.4 CONCLUSIONS

Polysilicon hydrides are effective reactants for solution-based synthesis of crystalline Si nanorods. These molecules degrade to Si at sufficiently low temperature with the necessary reactivity to generate crystalline nanorods with Sn seeds in high boiling organic solvents at ambient pressure. Cyclohexasilane is able to generate Si nanorods at temperatures as low as 200^{o}C. The low volatility of the reactant also enables higher yields than the higher volatility trisilane for example, which leads to a significant loss of reactant by vaporization.

Now there is a reasonably wide choice of silicon reactants to generate significant yields of Si in solution under the typical reaction conditions used for other more common semiconductors.[34,35] The next steps for colloidal Si nanomaterials chemistry involves the application of this chemistry to more complicated systems, like for example, heterostructures involving silicon—either axial or core-shell. One of the ultimate goals in nanomaterials chemistry still remains an effective high yield route to crystalline Si nanocrystals with tunable size. Perhaps polysilicon hydrides could provide a suitable reactant for these materials. The challenge for nanocrystals is to somehow induce or enable their crystallinity at relatively low growth temperatures without the use of a crystallization promoter like Sn. The silanes also evolve significant amounts of hydrogen and hydrogen is also known to lower the crystallization temperature of Si. At any rate, polysilicon hydrides represent a potentially useful category of Si reactants for nanomaterials chemistry, which are largely unexplored.

4.5 Acknowledgements

We thank Barry Arkles of Gelest, Inc. for providing isotetrasilane and neopentasilane. We acknowledge financial support of this work by the Robert A. Welch Foundation (Grant No. F-1464) and the National Science Foundation (Grant No. CHE-1308813). K.J.A. and P.B. of NDSU acknowledge financial support by the Department of Energy under agreement number DE-FC36-08GO88160.

4.6 REFERENCES

1. Heitsch, A. T.; Fanfair, D. D.; Tuan, H.-Y.; Korgel, B. A. Solution-Liquid-Solid (SLS) Growth of Silicon Nanowires. *J. Am. Chem. Soc.* **2008**, *130*, 5436–5437.

2. Heitsch, A. T.; Hessel, C. M.; Akhavan, V. A.; Korgel, B. A. Colloidal Silicon Nanorod Synthesis. *Nano Lett.* **2009**, *9*, 3042–3047.

3. Lu, X.; Hessel, C. M.; Yu, Y.; Bogart, T. D.; Korgel, B. A. Colloidal Luminescent Silicon Nanorods. *Nano Lett.* **2013**, *13*, 3101–3105.

4. Hessel, C. M.; Heitsch, A. T.; Korgel, B. A. Gold Seed Removal from the Tips of Silicon Nanorods. *Nano Lett.* **2010**, *10*, 176–180.

5. Lu, X.; Korgel, B. A. A Single-Step Reaction for Silicon and Germanium Nanorods. *Chem. - A Eur. J.* **2014**, *20*, 5874–5879.

6. Givargizov, E. Fundamental Aspects of VLS Growth. *J. Cryst. Growth* **1975**, *31*, 20–30.

7. Schmidt, V.; Wittemann, J. V.; Senz, S.; Gösele, U. Silicon Nanowires: A Review on Aspects of Their Growth and Their Electrical Properties. *Adv. Mater.* **2009**, *21*, 2681–2702.

8. Schmidt, V.; Senz, S.; Gösele, U. Diameter Dependence of the Growth Velocity of Silicon Nanowires Synthesized via the Vapor-Liquid-Solid Mechanism. *Phys. Rev. B* **2007**, *75*, 045335.

9. Fanfair, D. D.; Korgel, B. A. ZnE (E = S, Se, Te) Nanowires Grown by the Solution–Liquid–Solid Mechanism: Importance of Reactant Decomposition Kinetics and the Solvent. *Cryst. Growth Des.* **2008**, *8*, 3246–3252.

10. Lu, X.; Hanrath, T.; Johnston, K. P.; Korgel, B. A. Growth of Single Crystal Silicon Nanowires in Supercritical Solution from Tethered Gold Particles on a Silicon Substrate. *Nano Lett.* **2003**, *3*, 93–99.

11. Barth, S.; Hernandez-Ramirez, F.; Holmes, J. D.; Romano-Rodriguez, A. Synthesis and Applications of One-Dimensional Semiconductors. *Prog. Mater. Sci.* **2010**, *55*, 563–627.

12. Lee, D. C.; Hanrath, T.; Korgel, B. a. The Role of Precursor-Decomposition Kinetics in Silicon-Nanowire Synthesis in Organic Solvents. *Angew. Chem. Int. Ed. Engl.* **2005**, *44*, 3573–3577.

13. Geaney, H.; Kennedy, T.; Dickinson, C.; Mullane, E.; Singh, A.; Laffir, F.; Ryan, K. M. High Density Growth of Indium Seeded Silicon Nanowires in the Vapor Phase of a High Boiling Point Solvent. *Chem. Mater.* **2012**, *24*, 2204–2210.

14. Geaney, H.; Mullane, E.; Ryan, K. M. Solution Phase Synthesis of Silicon and Germanium Nanowires. *J. Mater. Chem. C* **2013**, *1*, 4996.

15. Choi, S.; Kim, B.; Boudjouk, P.; Grier, D. G. Amine-Promoted Disproportionation and Redistribution of Trichlorosilane: Formation of Tetradecachlorocyclohexasilane Dianion 1. *J. Am. Chem. Soc.* **2001**, *123*, 8117–8118.

16. Lu, X.; Korgel, B. A. A Single-Step Reaction for Silicon and Germanium Nanorods. *Chem. - A Eur. J.* **2014**, *20*, 5874–5879.

17. Kanoh, H.; Sugiura, O.; Matsumura, M. Chemical Vapor Deposition of Amorphous Silicon Using Tetrasilane. *Japanese Journal of Applied Physics*, 1993, *32*, 2613–2619.

18. Iyer, G. R. S.; Hobbie, E. K.; Guruvenket, S.; Hoey, J. M.; Anderson, K. J.; Lovaasen, J.; Gette, C.; Schulz, D. L.; Swenson, O. F.; Elangovan, A.; Boudjouk, P. Solution-Based Synthesis of Crystalline Silicon from Liquid Silane through Laser and Chemical Annealing. *ACS Appl. Mater. Interfaces* **2012**, *4*, 2680–2685.

19. Tuan, H.; Lee, D. C.; Hanrath, T.; Korgel, B. A. Germanium Nanowire Synthesis: An Example of Solid-Phase Seeded Growth with Nickel Nanocrystals. *Chem. Mater.* **2005**, *17*, 5705–5711.

20. Kodambaka, S.; Tersoff, J.; Reuter, M. C.; Ross, F. M. Germanium Nanowire Growth below the Eutectic Temperature. *Science* **2007**, *316* (5825), 729–732.

21. Koppes, J. P.; Muza, A. R.; Stach, E. A.; Handwerker, C. H. Size-Dependent Melting Properties of Small Tin Particles: Nanocalorimetric Measurements. *Phys. Rev. Lett.* **2010**, *104*, 189601.

22. Sunkara, M. K.; Sharma, S.; Miranda, R.; Lian, G.; Dickey, E. C. Bulk Synthesis of Silicon Nanowires Using a Low-Temperature Vapor–liquid–solid Method. *Appl. Phys. Lett.* **2001**, *79*, 1546.

23. Olesinski, R.; Abbaschian, G. The Si– Sn (Silicon– Tin) System. *Bull. Alloy Phase Diagrams* **1984**, *5*, 273–276.

24. The average diameter of Sn nanoparticles is around 9 nm, which contain about 14,300 Sn atoms. The solubility of Si in Sn increases with raising reaction temperature. The Si solubility in Sn at the highest reaction temperature of 380ºC is 1.71×10^{-3} at.% Si. Saturation of a 9 nm seed particle requires less than one Si atom (~0.24 Si atom).

25. Shimoda, T.; Matsuki, Y.; Furusawa, M.; Aoki, T.; Yudasaka, I.; Tanaka, H.; Iwasawa, H.; Wang, D.; Miyasaka, M.; Takeuchi, Y. Solution-Processed Silicon Films and Transistors. *Nature* **2006**, *440*, 783–786.

26. Masuda, T.; Matsuki, Y.; Shimoda, T. Pyrolytic Transformation from Polydihydrosilane to Hydrogenated Amorphous Silicon Film. *Thin Solid Films* **2012**, *520*, 6603–6607.

27. Walsh, R. Bond Dissociation Energy Values in Silicon-Containing Compounds and Some of Their Implications. *Acc. Chem. Res.* **1981**, *14*, 246–252.

28. Wu, Y.-D.; Wong, C.-L. Substituent Effect on the Dissociation Energy of the Si-H Bond: A Density Functional Study. *J. Org. Chem.* **1995**, *60*, 821–828.

29. Hessel, C. M.; Reid, D.; Panthani, M. G.; Rasch, M. R.; Goodfellow, B. W.; Wei, J.; Fujii, H.; Akhavan, V.; Korgel, B. a. Synthesis of Ligand-Stabilized Silicon Nanocrystals with Size-Dependent Photoluminescence Spanning Visible to Near-Infrared Wavelengths. *Chem. Mater.* **2012**, *24*, 393–401.

30. Yu, Y.; Hessel, C. M.; Bogart, T. D.; Panthani, M. G.; Rasch, M. R.; Korgel, B. a. Room Temperature Hydrosilylation of Silicon Nanocrystals with Bifunctional Terminal Alkenes. *Langmuir* **2013**, *29*, 1533–1540.

31. Van Sickle, A. R.; Miller, J. B.; Moore, C.; Anthony, R. J.; Kortshagen, U. R.; Hobbie, E. K. Temperature Dependent Photoluminescence of Size-Purified Silicon Nanocrystals. *ACS Appl. Mater. Interfaces* **2013**, *5*, 4233–4238.

32. Mastronardi, M. L.; Maier-Flaig, F.; Faulkner, D.; Henderson, E. J.; Kübel, C.; Lemmer, U.; Ozin, G. a. Size-Dependent Absolute Quantum Yields for Size-Separated Colloidally-Stable Silicon Nanocrystals. *Nano Lett.* **2012**, *12*, 337–342.

33. Guichard, A.; Kekatpure, R.; Brongersma, M.; Kamins, T. Temperature-Dependent Auger Recombination Dynamics in Luminescent Silicon Nanowires. *Phys. Rev. B* **2008**, *78*, 235422.

34. Wong, F.; Dong, A.; Sun, J.; Tang, R.; Yu, H.; Buhro, W. E. Solution-Liquid-Solid Growth of Semiconductor Nanowires. *Inorg. Chem.* **2006**, *45*, 7511-7521.

35. Kuno, M. An Overview of Solution-Based Semiconductor Nanowires: Synthesis and Optical Studies. *Phys. Chem. Chem. Phys.* **2008**, *10*, 620-639.

Chapter 5: Enhanced Synthesis of Germanium Nanowires[‡‡]

5.1 INTRODUCTION

Semiconductor nanowires have been proposed for many uses, including thermoelectrics, thin film transistors, chemical sensors, photovoltaics, as semiconducting fabric, membranes and lithium ion battery electrodes, which often require large quantities of nanowires at reasonable cost.[1] Solution-based approaches of solution-liquid-solid (SLS)[2–4] and supercritical fluid-liquid-solid (SFLS)[5,6] growth provide versatile synthetic routes to semiconductor nanowires with tunable size and a wide range of compositions, including Si,[7,8] Ge,[9,10] III-V,[11–14] IV-VI,[15] and II-VI[16–22] compounds, and even ternary $CuInSe_2$.[23,24] These methods rely on the use of metal particles to seed nanowire growth, usually at reaction temperatures exceeding a metal-semiconductor eutectic similar to vapor-liquid-solid (VLS)[25,26] growth in the gas phase. For Ge nanowires, Au has been the most widely used seed metal for VLS and SFLS growth;[9,27–40] it forms a relatively low temperature eutectic with Ge (361^{o}C),[41] induces the growth of high quality nanowires and is chemically inert. Au, however, is a relatively expensive metal and creates electronic traps in Ge.[42] Therefore, a variety of other seed metals have been explored to grow Ge nanowires, including Ni,[43–47] Co,[44] Cu,[44,48–50] Mn,[44] Fe,[44] Bi,[10] Ag,[51] and stainless steel.[52] However, there have been few direct comparisons of how these different seed metals influence nanowire growth.

In our own search for a good alternative seed metal for Ge nanowires, we have observed significant differences between Au and Ni seeding of Ge nanowire growth in supercritical fluids. Au appears to *catalyze* the decomposition of the reactant diphenylgermane (DPG),[53] whereas Ni does not. The supercritical reaction temperatures

[‡‡] This chapter appears in *Chemistry of Materials* **2013**, 25, 2172-2177.

(<625^{o}C) are well below the Ni:Ge eutectic temperature of 762^{o}C and nanowire growth occurs through a *solid* phase seed, which can significantly influence the quality of the nanowires.[43,46] Comparatively, Ni is a relatively poor seed metal compared to Au under typical growth conditions. However, we discovered that greatly enhanced DPG decomposition by addition of monophenylsilane (MPS) to the reaction can lead to extremely high quality Ge nanowires from Ni seeds with very high product yields, approaching 100% conversion of DPG to Ge. MPS is a typical reactant for solution-based growth of Si nanowires,[5,8,54–59] but is employed here only as a phenyl group scavenger that does not participate in the growth reaction. Here, we report these findings.

5.2 Experimental Details

5.2.1 Materials

Anhydrous toluene (99.8%) was purchased from Sigma-Aldrich, diphenylgermane (DPG) and phenylsilane (MPS) were purchased from Gelest. Hydrogen tetrachloroaurate(III) trihydrate (≥99.9%), tetraoctylammonium bromide (98%), and sodium borohydride (≥98.0%) were purchased from Aldrich. Nickel(acetylacetonate)$_2$ (95%), trioctylphosphine (90%) and oleylamine (70%) were purchased from Aldrich. All chemicals were used as received.

Au nanocrystals averaging 2 nm in diameter were prepared by Brust's method.[60] Ni nanocrystals averaging 4 nm in diameter were prepared by the method of Hyeon's method.[61] The purified Au and Ni nanocrystals were redispersed in anhydrous toluene and stored in a glovebox.

5.2.2 Ge Nanowire Synthesis

Ge nanowires were synthesized in a 10 mL titanium tubular reactor connected to a high pressure liquid chromatography (HPLC) pump as previously described.[62] Au-seeded Ge nanowires were synthesized with a 28 mL reactant solution of 3.6 mg/L Au nanocrystals and 7.3 mM DPG in anhydrous toluene prepared in a nitrogen-filled glovebox. Ni-seeded Ge nanowires were made using a 28 mL reactant solution of 5 mg/L Ni nanocrystals and 7.3 mM DPG in anhydrous toluene prepared in the glovebox. Nanowires were also made by adding 7.3 mM MPS to the reactant solutions. Prior to precursor injection, the 10 mL titanium tubular reactor was filled with N_2 in the glovebox and then connected to the six-way valve and the backpressure regulator at two ends. After the reactor was preheated to 500^{o}C and pressurized to 10.3 MPa with anhydrous toluene, nanowire growth was carried out with the reactant solution fed into the reactor at a rate of 0.5 mL/min for 40 min. The outlet pressure was maintained at 10.3 MPa. After completing the injection of the reactants, the reactor was sealed and removed from the heating block. The effluent was also collected during each reaction. After the reactor cooling to room temperature, the nanowire product was collected and washed with a mixture of 4 mL of chloroform, 2 mL of toluene and 2 mL of ethanol, followed by centrifugation at 8000 rpm for 5 min. The purification procedure was repeated three times to remove unreacted reagent and molecular byproducts.

5.2.3 Materials Characterization

Scanning electron microscopy (SEM) images were acquired on a Zeiss Model SUPRA 40 VP SEM with an in-lens arrangement, a working voltage of 5.0 kV and a working distance of 5 mm. The SEM samples were prepared by drop-casting Ge nanowires onto silicon wafers and drying.

Low-resolution transmission electron microscopy (TEM) images were acquired on a FEI Tecnai Spirit Bio Twin operated at 80 kV. High-resolution transmission microscopy (HRTEM) images were acquired on a field emission JEOL 2010F TEM operated at 200 kV. TEM samples were prepared by drop-casting 5 μL of dilute Ge nanowire dispersion in chloroform onto a 200 mesh copper lacey carbon TEM grid (Electron Microscopy Science).

X-ray diffraction (XRD) was performed on a Rigaku R-Axis Spider diffractometer with an image plate detector using Cu K_α radiation (λ=1.54 Å) and a graphite monochromator. XRD samples were prepared by mixing a small amount of dried Ge nanowires with a droplet of mineral oil and mounting the mixture on cryoloop.

Gas chromatography-mass spectrometry (GC-MS) data were obtained using a Thermo TraceGC interfaced to a Thermo TSQ triple quadrupole mass spectrometer operating in positive CI mode, with methane as the reagent gas. Samples were injected in splitless mode onto a Restek Rxi-5Sil MS column (30 m, 0.25 mm ID, 0.25 μm) with an injector temperature of 280^{o}C, and separated at a constant flow of helium (1.2 mL/min) by ramping temperature from 40 to 320^{o}C at 30^{o}C/min.

5.3 Results and Discussions

5.3.1 Ge Nanowires Grown with Au vs Ni Seeds

We directly compared Ge nanowire growth in supercritical toluene using DPG as a reactant using Au and Ni nanocrystals as seeds. The optimum reaction temperature for SFLS growth of Ge nanowires from DPG using Au seeds is 380^{o}C.[33,62,64] Reactions at 380^{o}C using Ni seeds did not yield any nanowires and produced only microspheres and rods. It was necessary to raise the reaction temperature to 500^{o}C to produce any Ge

nanowires with Ni seeds. But even at the relatively high temperature of 500^{o}C, the yield and quality of Ge nanowires were relatively poor, especially compared to Au-seeded reactions. Figures 5.1A and 5.1B show SEM images of typical Ge nanowire product grown with Au and Ni seeds in supercritical toluene with DPG at 500^{o}C. Although Ge nanowires grown with Au seeds at 500^{o}C are not as pristine as those grown at 380^{o}C, due to more severe Au seeds agglomeration and secondary growth of Ge on the existing Ge nanowires, the nanowires are still mostly straight and long with high aspect ratio and diameters ranging between 10 and 40 nm. In contrast, the Ni-seeded Ge nanowires are highly kinked and relatively short with low reaction product yield (20% conversion of DPG to Ge).

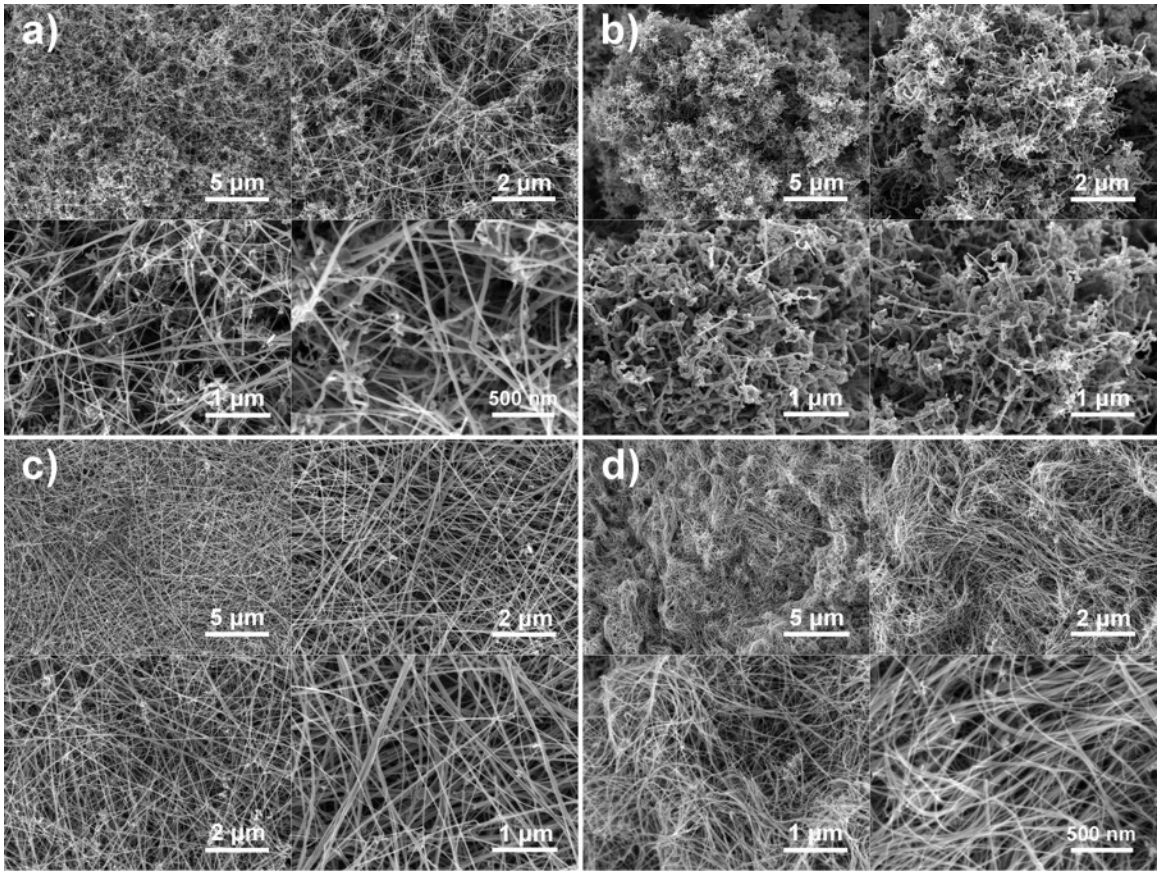

Figure 5.1 SEM images of Ge nanowires formed at 500ºC with (a) Au nanocrystal seeds; (b) Ni nanocrystal seeds; (c) Au nanocrystal seeds with addition of MPS; (d) Ni nanocrystal seeds with addition of MPS.

5.3.2 MPS Addition

The addition of monophenylsilane (MPS) to the DPG reaction with Ni nanocrystals greatly increases the quality of Ge nanowires. See for example the SEM images in Figure 5.1d of the Ni-seeded Ge nanowires grown with addition of MPS. The nanowires are long and straight with average diameter of 14 nm and a relatively narrow diameter distribution. The reaction yield of the Ni-seeded nanowires is also very high

with a conversion of DPG to Ge of 92%. The difference in quality and yield of product is dramatic.

MPS addition also improves the yield and quality of the Au-seeded reactions carried out at high temperature, as shown in the SEM images in Figure 5.1a and 5.1c. The Au-seeded nanowires grown with added MPS are noticeably straighter than those made without MPS present and the reaction yields are significantly higher. The Au-seeded Ge nanowires made at the higher temperature of 500°C have similar quality as those made without MPS under optimized conditions at 380°C. The yield of the reaction with MPS at 500°C increases to nearly 100% from 30%, which represents a significant advance in this synthetic approach. Table 5.1 summarizes the yield of the various Ge nanowire growth reactions.

Table 5.1 Molar conversion of DPG to Ge nanowire product for reactions in supercritical toluene at 500°C involving Au and Ni seeds with and without added MPS. The theoretical yield in the absence of MPS is 50%.[53]

Reaction	DPG Conversion (%)
Au seeds, no MPS	30.1
Ni seeds, no MPS	20.4
Au seeds, with MPS	93.5
Ni seeds, with MPS	92.2

5.3.3 Role of MPS

Figure 5.2 shows XRD data from Ge nanowires grown with Au and Ni seeds with and without MPS added. All of the XRD patterns index to diamond cubic Ge, indicating that MPS addition does not lead to significant Si incorporation into the nanowires. High-resolution TEM determinations of the nanowire crystal structure and lattice spacing are also consistent with diamond cubic Ge. Figure 5.3 shows examples of TEM images of Ge nanowires grown with Ni seeds and added MPS. Ni germanide alloy is found at the tips

of the nanowires, similar to other Ni-seeded Ge nanowire growth studies.[43-47] The [110] growth direction is similar to other SFLS-grown Ge nanowires.[6,43,46,63]

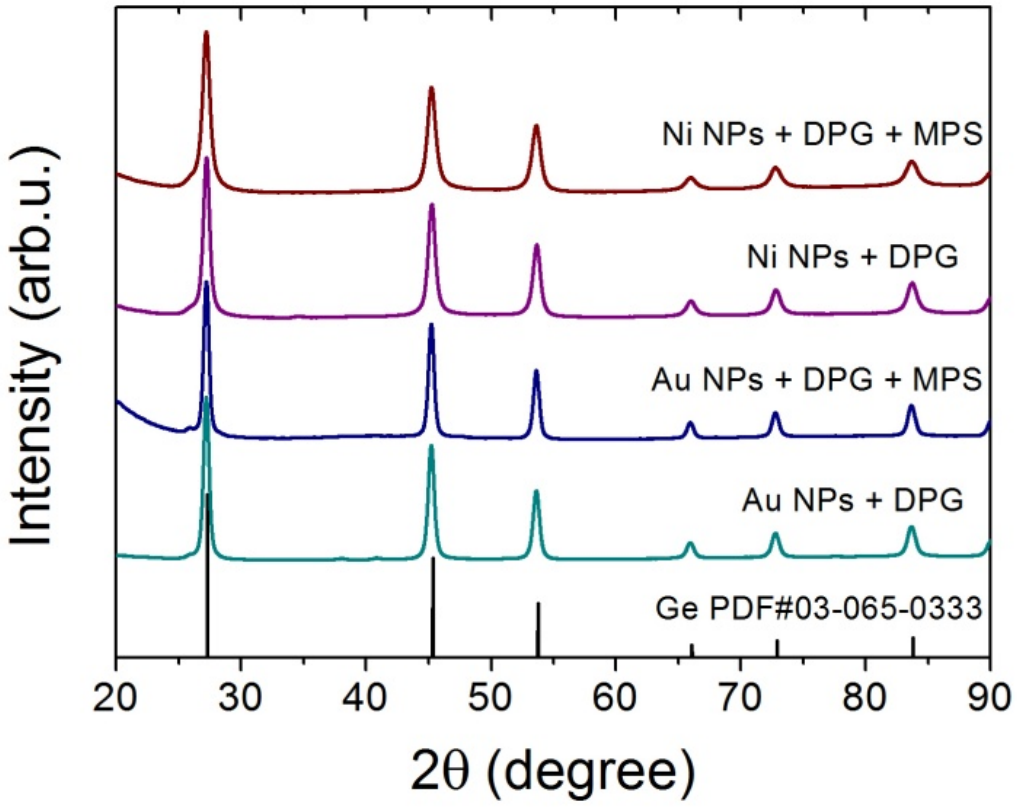

Figure 5.2 XRD of Ge nanowires made by decomposing DPG in supercritical toluene at 500ºC with either Au or Ni seeds with or without MPS MPS added to the reaction. The seed particle and reactants are indicated beside each diffraction pattern. A reference pattern for diamond cubic Ge is provided (PDF no.: 03-065-0333.).

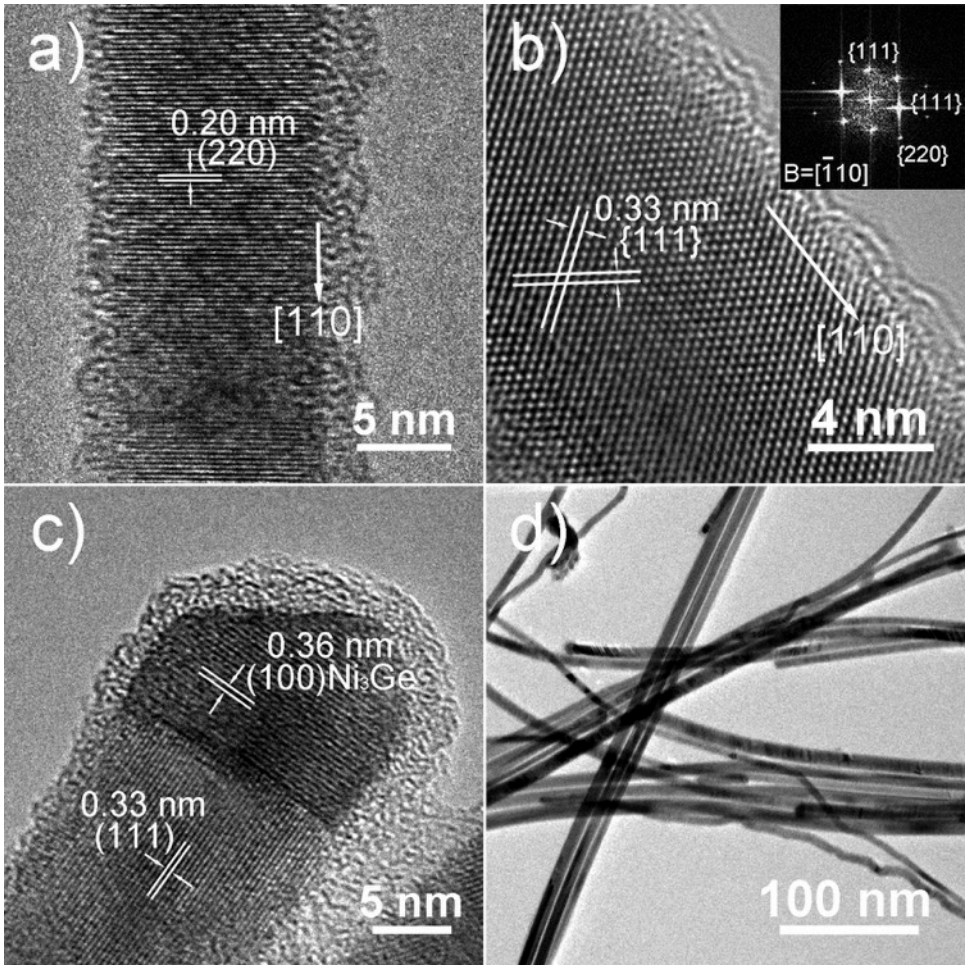

Figure 5.3 TEM images of Ge nanowires synthesized with Ni seeds and added MPS. (a) The core of a Ge nanowire with (220) fringes perpendicular to the [110] growth direction; (b) Ge nanowire showing crossed {111} fringes at 35° to the [110] growth direction. The inset shows the corresponding FFT pattern indexed to diamond cubic Ge; (c) Ge nanowires with Ni_3Ge at its tip. The d-spacing of 0.36 nm in the tip corresponds to the (100) planes of cubic Ni_3Ge.

There is no evidence of Si incorporation into the nanowires (i.e., Si-Ge alloying) and no separate Si diffraction peaks are detected either. MPS is behaving as a spectator to nanowire growth, while significantly enhancing DPG decomposition kinetics. DPG decomposition proceeds by phenyl redistribution into germane and higher order

phenylgermanes, triphenyl germane (TPG) and tetraphenyl germane (QPG).[53,65] The theoretical yield of Ge nanowires from DPG is only 50% because the TPG and QPG byproducts do not decompose,[63] explaining the low nanowire yields in Table 5.1 using DPG (without added MPS). Also without MPS added, the Au-seeded reactions also have noticeably higher conversions of DPG to Ge nanowires than the Ni-seeded reactions. This is consistent with previous studies showing that Au has a catalytic effect on DPG decomposition.[53] Ni apparently does not play the same role.

With MPS was added, the Ge yield from DPG increases to more than 90%—both with Au and Ni seeds—which is well above the theoretical yield. At 500^{o}C, MPS also undergoes phenyl redistribution, and decomposes typically to silane and tetraphenyl silane (QPS).[8,54] In the presence of DPG, it appears that phenylsilane becomes a phenyl sink, withdrawing phenyl groups from DPG to form higher order phenylsilanes while pushing the distribution of DPG decomposition products towards Ge. This reaction pathway is consistent with stronger Si-C bonding compared to Ge-C.[66]

5.3.4 Phenyl Redistribution between DPG and MPS

The phenyl redistribution pathway between DPG and MPS was confirmed by GC-MS analyses of reactor effluent. Figure 5.4 shows the GC-MS data obtained from Au and Ni seeded reactions with and without MPS. Without MPS added to the reaction, unreacted DPG is detected, along with significant TPG. QPG is not detected because it is insoluble and accumulates in the reactor. More DPG was observed in the effluent from the Ni seeded reactions than the Au seeded reactions, consistent with the lower product yield in those reactions.

From reactions with MPS added, the predominant byproduct observed by GC-MS was TPS and very little TPG. Some unreacted DPG was still observed in the reactions

with Ni seeds, consistent with the slightly lower yields using Ni than Au. These data confirm that MPS enhances DPG conversion to Ge by withdrawing phenyl groups as illustrated in Figure 5.5a. With the addition of MPS, the theoretical yield becomes 100%.

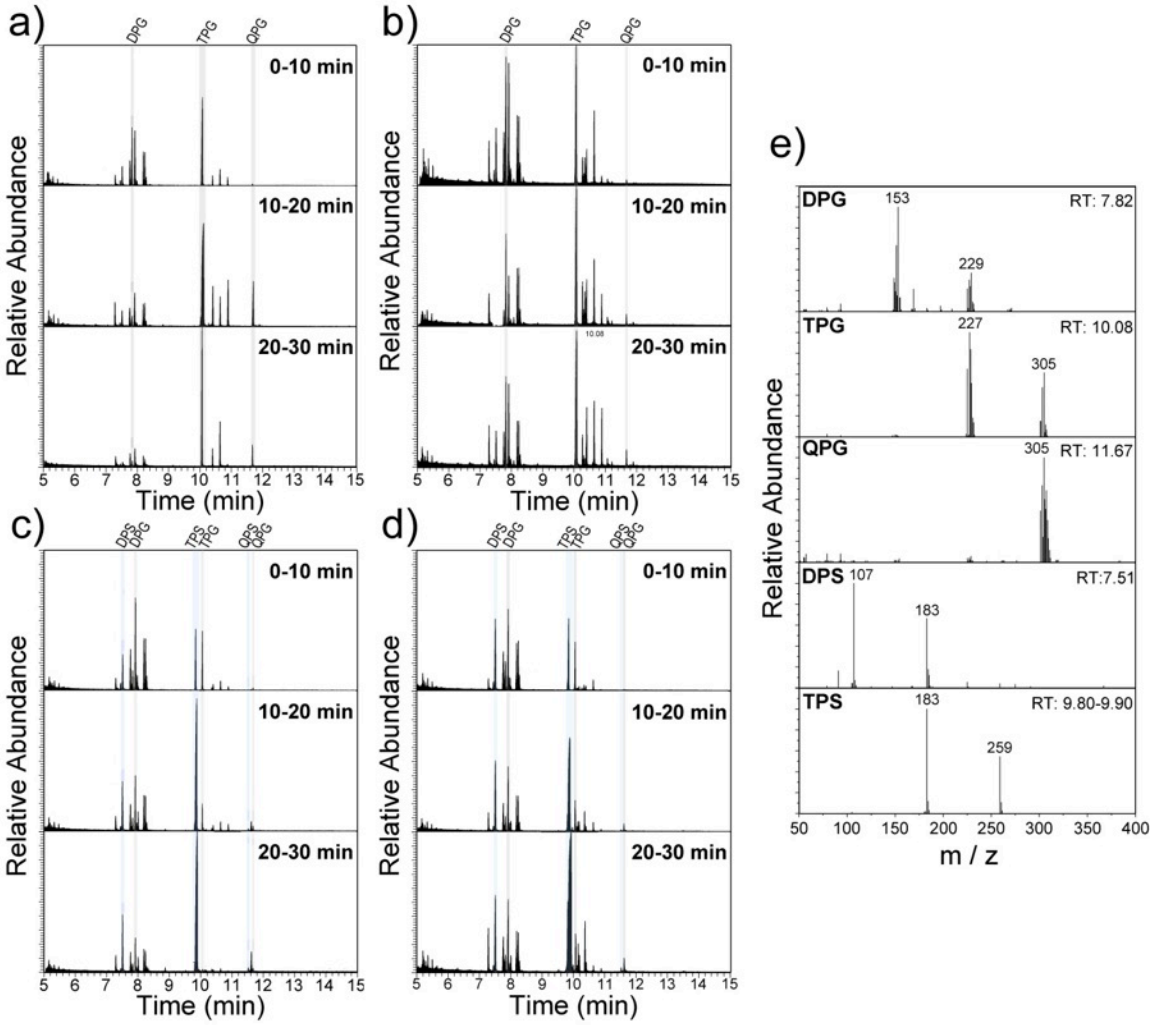

Figure 5.4 Gas chromatography spectra of effluents collected after different times from Ge nanowire growth reactions using (a) Au (no MPS), (b) Ni (no MPS), (c) Au with MPS, (d) Ni with MPS. Peak heights have been normalized to the highest peak in each column. (e) Mass spectra of major byproducts in the reaction.[68]

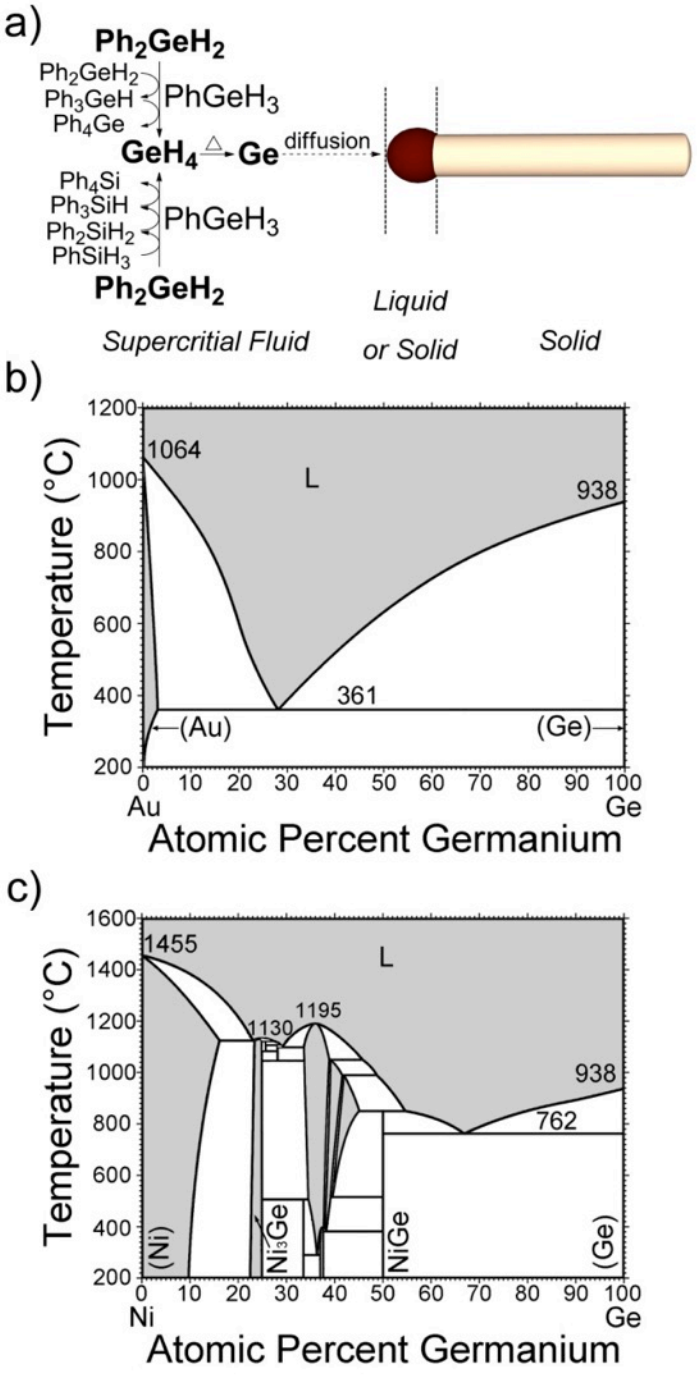

Figure 5.5 (a) DPG decomposition pathway with and without MPS. Ge nanowires form by SFLS or SFSS growth depending on whether the seed particles become liquid or remain solid; (b) Au-Ge[41] and (c) Ni-Ge[67] phase diagrams.

5.3.5 Ni vs. Au Seeding of Ge Nanowires

The Ge nanowire growth kinetics are substantially different when seeded with Au than with Ni. One obvious difference between the two metals is their significantly different Au:Ge and Ni:Ge eutectic temperatures (Figure 5.5). Au-seeded growth occurs above the Au:Ge eutectic and Ge nanowires crystallize from liquid Au:Ge droplets; whereas, Ni-seeded Ge nanowire growth occurs at temperatures well below the Ni:Ge eutectic and nanowires evolve from a solid nickel germanide phase. A crystalline Ni_3Ge seed at the end of a Ge nanowire is shown in the TEM image in Figure 5.3c. It is noteworthy that the Ni_3Ge alloy has a relatively small lattice mismatch of less than 10% with Ge. One other difference between the two metals is that Au appears to catalyze DPG decomposition,[53] whereas there is no evidence that Ni does. MPS addition to the Ni-seeded nanowire reactions is needed to speed DPG decomposition enough to evolve high quality nanowires. The addition of MPS does not affect the Ni:Ge phase behavior—and nanowire growth still occurs from solid-phase seeds—but but DPG decomposition becomes sufficiently fast in the presence of MPS to lead to nanowires with few crystal defects.

With sufficient reactant decomposition rates, one apparent advantage of solid-phase seeding compared to liquid-phase seeding appears to be less agglomeration of seed particles, as first reported by Tuan, et al.[43] The Ni-seeded nanowires (with MPS added) had a very narrow diameter distribution, much narrower than the nanowires produced with Au seeds. The average diameter of the Au-seeded Ge nanowires made in the presence of MPS was 40 nm. Thombare et al.[46] have also observed similar diameter-dependent differences in Ge nanowire growth from Ni seeds.

5.4 CONCLUSIONS

Ge nanowire synthesis using Ni nanocrystals as seeds can be carried out in supercritical toluene using DPG as a reactant. However, unlike Au, Ni seeds are rather poor catalysts for Ge nanowire growth—*unless* an additive is present to speed DPG decomposition. DPG decomposes by phenyl redistribution to germane and higher order phenylgermanes like triphenylgermane and tetraphenylgermane. Ge incorporates into the nanowires by decomposition of germane, while TPG and QPG are unreactive. MPS was found to significantly enhance DPG decomposition and greatly improve Ge nanowire growth by withdrawing phenyl groups from DPG and serving as a phenyl sink to push the reaction product to germane. This enables the production of a high yield of straight nanowires with narrow diameters and narrow diameter distributions using Ni seeds.

This study highlights the essential role of reactant decomposition kinetics and control for making high quality nanowires. The seed metal and its interaction with the semiconductor is obviously influential, but the rate at which the semiconductor is fed to the seed particle is also extremely important.

5.5 ACKNOWLEDGEMENTS

We acknowledge financial support from the Robert A. Welch Foundation (F-1494) and the Air Force Research Laboratory (FA-8650-07-2-5061). We also thank Vince Holmberg for helpful discussions and Karin Keller and Ian Riddington for assistance with GC-MS measurements.

5.6 REFERENCES

1. Korgel, B. A. Semiconductor Nanowires: A Chemical Engineering Perspective. *AIChE J*. **2009**, *55* (4), 842–848.

2. Trentler, T. J.; Hickman, K. M.; Goel, S. C.; Viano, a. M.; Gibbons, P. C.; Buhro, W. E. Solution-Liquid-Solid Growth of Crystalline III-V Semiconductors: An Analogy to Vapor-Liquid-Solid Growth. *Science*, 1995, *270*, 1791–1794.

3. Wang, F.; Dong, A.; Sun, J.; Tang, R.; Yu, H.; Buhro, W. E. Solution-Liquid-Solid Growth of Semiconductor Nanowires. *Inorg. Chem.* **2006**, *45* (19), 7511–7521.

4. Kuno, M. An Overview of Solution-Based Semiconductor Nanowires: Synthesis and Optical Studies. *Phys. Chem. Chem. Phys.* **2008**, *10* (5), 620.

5. Holmes, J. D. Control of Thickness and Orientation of Solution-Grown Silicon Nanowires. *Science*, 2000, *287*, 1471–1473.

6. Hanrath, T.; Korgel, B. A. Supercritical Fluid–Liquid–Solid (SFLS) Synthesis of Si and Ge Nanowires Seeded by Colloidal Metal Nanocrystals. *Adv. Mater.* **2003**, *15* (5), 437–440.

7. Heitsch, A. T.; Fanfair, D. D.; Tuan, H.-Y.; Korgel, B. A. Solution-Liquid-Solid (SLS) Growth of Silicon Nanowires. *J. Am. Chem. Soc.* **2008**, *130* (16), 5436–5437.

8. Tuan, H. Y.; Korgel, B. a. Importance of Solvent-Mediated Phenylsilane Decompositon Kinetics for High-Yield Solution-Phase Silicon Nanowire Synthesis. *Chem. Mater.* **2008**, *20* (4), 1239–1241.

9. Hanrath, T.; Korgel, B. A. Nucleation and Growth of Germanium Nanowires Seeded by Organic Monolayer-Coated Gold Nanocrystals. *J. Am. Chem. Soc.* **2002**, *124* (7), 1424–1429.

10. Lu, X.; Fanfair, D. D.; Johnston, K. P.; Korgel, B. A. High Yield Solution-Liquid-Solid Synthesis of Germanium Nanowires. *J. Am. Chem. Soc.* **2005**, *127* (45), 15718–15719.

11. Davidson, F. M.; Wiacek, R.; Korgel, B. a. Supercritical Fluid-Liquid-Solid Synthesis of Gallium Phosphide Nanowires. *Chem. Mater.* **2005**, *17* (2), 230–233.

12. Forrest, M. D.; Schricker, A. D.; Wiacek, R. J.; Korgel, B. A. Supercritical Fluid-Liquid-Solid Synthesis of Gallium Arsenide Nanowires Seeded by Alkanethiol-Stabilized Gold Nanocrystals. **2004**, No. 7, 646–649.

13. Yu, H.; Buhro, W. E. Solution-Liquid-Solid Growth of Soluble GaAs Nanowires. *Adv. Mater.* **2003**, *15* (5), 416–419.

14. Yu, H.; Li, J.; Loomis, R. a; Wang, L.-W.; Buhro, W. E. Two- versus Three-Dimensional Quantum Confinement in Indium Phosphide Wires and Dots. *Nat. Mater.* **2003**, *2* (8), 517–520.

15. Sun, J.; Buhro, W. E. The Use of Single-Source Precursors for the Solution-Liquid-Solid Growth of Metal Sulfide Semiconductor Nanowires. *Angew. Chem. Int. Ed. Engl.* **2008**, *47* (17), 3215–3218.

16. Yu, H.; Li, J.; Loomis, R. a.; Gibbons, P. C.; Wang, L. W.; Buhro, W. E. Cadmium Selenide Quantum Wires and the Transition from 3D to 2D Confinement. *J. Am. Chem. Soc.* **2003**, *125* (52), 16168–16169.

17. Grebinski, J. W.; Hull, K. L.; Zhang, J.; Kosel, T. H.; Kuno, M. Solution-Based Straight and Branched CdSe Nanowires. *Chem. Mater.* **2004**.

18. Kuno, M.; Ahmad, O.; Protasenko, V.; Bacinello, D.; Kosel, T. H. Solution-Based Straight and Branched CdTe Nanowires. *Chem. Mater.* **2006**, *18* (24), 5722–5732.

19. Fanfair, D. D.; Korgel, B. A. Twin-Related Branching of Solution-Grown ZnSe Nanowires. *Chem. Mater.* **2007**, *19* (20), 4943–4948.

20. Fanfair, D. D.; Korgel, B. A. ZnE (E = S, Se, Te) Nanowires Grown by the Solution–Liquid–Solid Mechanism: Importance of Reactant Decomposition Kinetics and the Solvent. *Cryst. Growth Des.* **2008**, *8* (9), 3246–3252.

21. Dong, A.; Wang, F.; Daulton, T. L.; Buhro, W. E. Solution-Liquid-Solid (SLS) Growth of ZnSe-ZnTe Quantum Wires Having Axial Heterojunctions. *Nano Lett.* **2007**, *7* (5), 1308–1313.

22. Ouyang, L.; Maher, K. N.; Yu, C. L.; McCarty, J.; Park, H. Catalyst-Assisted Solution-Liquid-Solid Synthesis of CdS/CdSe Nanorod Heterostructures. *J. Am. Chem. Soc.* **2007**, *129* (1), 133–138.

23. Wooten, A. J.; Werder, D. J.; Williams, D. J.; Casson, J. L.; Hollingsworth, J. A. Solution-Liquid-Solid Growth of Ternary Cu-In-Se Semiconductor Nanowires from Multiple- and Single-Source Precursors. *J. Am. Chem. Soc.* **2009**, *131* (44), 16177–16188.

24. Steinhagen, C.; Akhavan, V. A.; Goodfellow, B. W.; Panthani, M. G.; Harris, J. T.; Holmberg, V. C.; Korgel, B. A. Solution-Liquid-Solid Synthesis of CuInSe 2 Nanowires and Their Implementation in Photovoltaic Devices. *ACS Appl. Mater. Interfaces* **2011**, *3* (5), 1781–1785.

25. Wagner, R. S.; Ellis, W. C. Vapor-Liquid-Solid Mechanism of Single Crystal Growth. *Appl. Phys. Lett.* **1964**, *4* (5), 89–90.

26. Hu, J.; Odom, T. W.; Lieber, C. M. Chemistry and Physics in One Dimension: Synthesis and Properties of Nanowires and Nanotubes. *Accounts of Chemical Research*, 1999, *32*, 435–445.

27. Wang, D.; Dai, H. Low-Temperature Synthesis of Single-Crystal Germanium Nanowires by Chemical Vapor Deposition. *Angew. Chemie - Int. Ed.* **2002**, *41* (24), 4783–4786.

28. Wu, Y.; Yang, P. Direct Observation of Vapor-Liquid-Solid Nanowire Growth. *Journal of the American Chemical Society*, 2001, *123*, 3165–3166.

29. Tutuc, E.; Appenzeller, J.; Reuter, M. C.; Guha, S. Realization of a Linear Germanium Nanowire P-N Junction. *Nano Lett*. **2006**, *6* (9), 2070–2074.

30. Lensch-Falk, J. L.; Hemesath, E. R.; Perea, D. E.; Lauhon, L. J. Alternative Catalysts for VSS Growth of Silicon and Germanium Nanowires. *J. Mater. Chem*. **2009**, *19* (7), 849.

31. Greytak, A. B.; Lauhon, L. J.; Gudiksen, M. S.; Lieber, C. M. Growth and Transport Properties of Complementary Germanium Nanowire Field-Effect Transistors. *Appl. Phys. Lett*. **2004**, *84* (21), 4176–4178.

32. Holmberg, V. C.; Panthani, M. G.; Korgel, B. a. Phase Transitions, Melting Dynamics, and Solid-State Diffusion in a Nano Test Tube. *Science* **2009**, *326* (5951), 405–407.

33. Smith, D. A.; Holmberg, V. C.; Korgel, B. A. Flexible Germanium Nanowires: Ideal Strength, Room Temperature Plasticity, and Bendable Semiconductor Fabric. *ACS Nano* **2010**, *4* (4), 2356–2362.

34. Holmberg, V. C.; Rasch, M. R.; Korgel, B. a. PEGylation of Carboxylic Acid-Functionalized Germanium Nanowires. *Langmuir* **2010**, *26* (17), 14241–14246.

35. Holmberg, V. C.; Bogart, T. D.; Chockla, A. M.; Hessel, C. M.; Korgel, B. a. Optical Properties of Silicon and Germanium Nanowire Fabric. *J. Phys. Chem. C* **2012**, *116*, 22486–22491.

36. Ngo, L. T.; Almécija, D.; Sader, J. E.; Daly, B.; Petkov, N.; Holmes, J. D.; Erts, D.; Boland, J. J. Ultimate-Strength Germanium Nanowires. *Nano Lett*. **2006**, *6* (12), 2964–2968.

37. Dayeh, S. a.; Picraux, S. T. Direct Observation of Nanoscale Size Effects in Ge Semiconductor Nanowire Growth. *Nano Lett*. **2010**, *10* (10), 4032–4039.

38. Gamalski, a D.; Tersoff, J.; Sharma, R.; Ducati, C.; Hofmann, S. Formation of Metastable Liquid Catalyst during Subeutectic Growth of Germanium Nanowires. *Nano Lett*. **2010**, *10* (8), 2972–2976.

39. Wang, D.; Tu, R.; Zhang, L.; Dai, H. Deterministic One-to-One Synthesis of Germanium Nanowires and Individual Gold Nanoseed Patterning for Aligned Nanowire Arrays. *Angew. Chemie - Int. Ed*. **2005**, *44* (19), 2925–2929.

40. Yang, H.-J.; Tuan, H.-Y. High-Yield, High-Throughput Synthesis of Germanium Nanowires by Metal–organic Chemical Vapor Deposition and Their Functionalization and Applications. *Journal of Materials Chemistry*, 2012, *22*, 2215.

41. Okamoto, H.; Massalski, T. B. The Au–Ge (Gold-Germanium) System. *Bull. Alloy Phase Diagrams* **1984**, *5* (6), 601–610.

42. Dunlap, W. C. Electrical Properties of Gold-Germanium Alloys. *Physical Review*, 1953, *91*, 1282.

43. Tuan, H. Y.; Lee, D. C.; Hanrath, T.; Korgel, B. A. Germanium Nanowire Synthesis: An Example of Solid-Phase Seeded Growth with Nickel Nanocrystals. *Chem. Mater.* **2005**, *17* (23), 5705–5711.

44. Tuan, H.-Y.; Lee, D. C.; Korgel, B. A. Nanocrystal-Mediated Crystallization of Silicon and Germanium Nanowires in Organic Solvents: The Role of Catalysis and Solid-Phase Seeding. *Angew. Chem. Int. Ed. Engl.* **2006**, *45* (31), 5184–5187.

45. Barth, S.; Koleśnik, M. M.; Donegan, K.; Krstić, V.; Holmes, J. D. Diameter-Controlled Solid-Phase Seeding of Germanium Nanowires: Structural Characterization and Electrical Transport Properties. *Chem. Mater.* **2011**, *23* (14), 3335–3340.

46. Thombare, S. V.; Marshall, A. F.; McIntyre, P. C. Size Effects in Vapor-Solid-Solid Ge Nanowire Growth with a Ni-Based Catalyst. *J. Appl. Phys.* **2012**, *112* (5), 054325.

47. Chueh, Y. L.; Fan, Z.; Takei, K.; Hyunhyub, K.; Kapadia, R.; Rathore, A. a.; Miller, N.; Kyoungsik, Y.; Ming, W.; Haller, E. E.; Javey, A. Black Ge Based on Crystalline/amorphous Core/shell Nanoneedle Arrays. *Nano Lett.* **2010**, *10* (2), 520–523.

48. Geaney, H.; Dickinson, C.; Barrett, C. A.; Ryan, K. M. High Density Germanium Nanowire Growth Directly from Copper Foil by Self-Induced Solid Seeding. *Chem. Mater.* **2011**, *23* (21), 4838–4843.

49. Kang, K.; Kim, D. A.; Lee, H. S.; Kim, C. J.; Yang, J. E.; Jo, M. H. Low-Temperature Deterministic Growth of Ge Nanowires Using Cu Solid Catalysts. *Adv. Mater.* **2008**, *20* (24), 4684–4690.

50. Kang, K.; Gu, G. H.; Kim, D. A.; Park, C. G.; Jo, M. H. Self-Organized Growth of Ge Nanowires from Ni-Cu Bulk Alloys. *Chem. Mater.* **2008**, *20* (21), 6577–6579.

51. Biswas, S.; Singha, A.; Morris, M. a; Holmes, J. D. Inherent Control of Growth, Morphology, and Defect Formation in Germanium Nanowires. *Nano Lett.* **2012**, *12* (11), 5654–5663.

52. Dřínek, V.; Fajgar, R.; Klementová, M.; Šubrt, J. Deposition of Germanium Nanowires from Hexamethyldigermane: Influence of the Substrate Pretreatment. *Journal of The Electrochemical Society*, 2010, *157*, K218.

53. Chockla, A. M.; Korgel, B. A. Seeded Germanium Nanowire Synthesis in Solution. *J. Mater. Chem.* **2009**, *19* (7), 996.

54. Lee, D. C.; Hanrath, T.; Korgel, B. a. The Role of Precursor-Decomposition Kinetics in Silicon-Nanowire Synthesis in Organic Solvents. *Angew. Chem. Int. Ed. Engl.* **2005**, *44* (23), 3573–3577.

55. Yuan, F. W.; Tuan, H. Y. Supercritical Fluid-Solid Growth of Single-Crystalline Silicon Nanowires: An Example of Metal-Free Growth in an Organic Solvent. In *Crystal Growth and Design*; 2010; Vol. 10, pp 4741–4745.

56. Mullane, E.; Kennedy, T.; Geaney, H.; Dickinson, C.; Ryan, K. M. Synthesis of Tin Catalyzed Silicon and Germanium Nanowires in a Solvent–Vapor System and Optimization of the Seed/Nanowire Interface for Dual Lithium Cycling. *Chem. Mater.* **2013**, *25* (9), 1816–1822.

57. Coleman, N. R. B.; O'Sullivan, N.; Ryan, K. M.; Crowley, T. a.; Morris, M. a.; Spalding, T. R.; Steytler, D. C.; Holmes, J. D. Synthesis and Characterization of Dimensionally Ordered Semiconductor Nanowires within Mesoporous Silica. *J. Am. Chem. Soc.* **2001**, *123* (29), 7010–7016.

58. Yang, H.-J.; Yuan, F.-W.; Tuan, H.-Y. Vapor-Liquid-Solid Growth of Silicon Nanowires Using Organosilane as Precursor. *Chem. Commun. (Camb).* **2010**, *46* (33), 6105–6107.

59. Geaney, H.; Mullane, E.; Ramasse, Q. M.; Ryan, K. M. Atomically Abrupt Silicon-Germanium Axial Heterostructure Nanowires Synthesized in a Solvent Vapor Growth System. *Nano Lett.* **2013**, *13* (4), 1675–1680.

60. Brust, M.; Walker, M.; Bethell, D.; Schiffrin, D. J.; Whyman, R. Synthesis of Thiol-Derivatised Gold Nanoparticles in a Two-Phase Liquid-Liquid System. *J. Chem. Soc. Chem. Commun.* **1994**, No. 7, 801.

61. Park, J.; Kang, E.; Son, S. U.; Park, H. M.; Lee, M. K.; Kim, J.; Kim, K. W.; Noh, H. J.; Park, J. H.; Bae, C. J.; Park, J. G.; Hyeon, T. Monodisperse Nanoparticles of Ni and NiO: Synthesis, Characterization, Self-Assembled Superlattices, and Catalytic Applications in the Suzuki Coupling Reaction. *Adv. Mater.* **2005**, *17* (4), 429–434.

62. Holmberg, V. C.; Korgel, B. A. Corrosion Resistance of Thiol- and Alkene-Passivated Germanium Nanowires. *Chem. Mater.* **2010**, *22* (12), 3698–3703.

63. Hanrath, T.; Korgel, B. a. Crystallography and Surface Faceting of Germanium Nanowires. *Small* **2005**, *1* (7), 717–721.

64. Hanrath, T.; Korgel, B. A. Chemical Surface Passivation of Ge Nanowires. *J. Am. Chem. Soc.* **2004**, *126* (47), 15466–15472.

65. Chockla, A. M.; Harris, J. T.; Korgel, B. a. Colloidal Synthesis of Germanium Nanorods. *Chem. Mater.* **2011**, *23* (7), 1964–1970.

66. Werner, M.; Mehrer, H.; Hochheimer, H. D. Effect of Hydrostatic Pressure, Temperature, and Doping on Self-Diffusion in Germanium. *Phys. Rev. B* **1985**, *32* (6), 3930–3937.

67. Nash, A.; Nash, P. The Ge–Ni (Germanium-Nickel) System. *Bull. Alloy Phase Diagrams* **1987**, *8* (3), 255–264.

68. MPS and MPG are not observed in the spectra because the retention time of MPS or MPG is very close to toluene (~3 s). Data are collected only after 5 s.

Chapter 6: The Use of Metalorganic Compounds for Growing Germanium Nanowires[§§]

6.1 INTRODUCTION

Semiconductor nanowires exhibit properties that make them uniquely suitable for a variety of applications, especially those that require the electrical and optical properties of crystalline semiconductors with the mechanical flexibility of polymers.[1–5] Because of the mechanical toughness and electrochemical properties, silicon (Si) and germanium (Ge) nanowires have gained significant interest for use as anodes in lithium and sodium ion batteries recently.[6–10] Many of these applications require significant quantities of material that can be produced at reasonably low cost. Solution-based syntheses, such as solution-liquid-solid (SLS) and supercritical fluid-liquid-solid (SFLS) growth have proved capable of producing large quantities of nanowires with low cost. The production yield of Si nanowires in gram scale could be easily achieved using SFLS growth in the pilot-scale batch reactor.[11]

SFLS approach relies on supercritical toluene as solvent, liquid semiconductor precursors, and metal nanoparticles to introduce the growth of nanowires. The metal nanoparticles perform as semiconductor atom reservoir and catalyst to promote those semiconductor atoms precipitating at the interface into nanowires. Their quality determines both the quality and the quantity of obtained nanowires. With the development of colloidal nanoparticle synthesis, it is not difficult to make monodisperse metal nanoparticles on a laboratory scale. However, the chemical stability of those metal nanoparticles accompanying the scale-up difficulties still hinders the further development of nanowire production. An interesting research direction of solving this problem is

[§§] Manuscript in preparation. Lu, X.; Korgel, B. A. The Use of Metalorganic Compounds for Growing Germanium Nanowires in Supercritical Solvent

growing Si and Ge nanowires directly on the metal films.[12,13] Another direction is to use metal compounds instead of colloidal metal nanoparticles. Metalorganic reactants have been widely used in carbon nanotube growth reactions by chemical vapor deposition (CVD).[14,15] In solution-based reactions, especially the continuous flowing solution reactions, the usage of metal compounds faces more challenges, like solubility of the metal precursors and their reactivity at low temperatures. We have observed a few examples of nanowire and nanotube growth using organometallic reactants in our own group. For example, multiwall carbon nanotubes were synthesized in supercritical toluene using ferrocene and cobaltocene as molecular precursors to iron (Fe) and cobalt (Co) seeds;[16] Si nanowires were obtained in supercritical toluene using bis(bis(trimethylsilyl)amino)tin ([$Sn(hmds)_2$]) to generate tin (Sn) seed particles;[17] and we recently found the organotin compound can be used in place of Sn seed particles to grow Ge and Si nanorods in solution.[18]

Herein we expand the exploration of metalorganic compound-catalyzed nanowire synthesis with the demonstration of Ge nanowires. Ge nanowires can be obtained with various metal compounds, including metals with both low (Ga, In, Pb, Bi) and high (Mn, Fe, Ni, Cu) melting points. All of these metals offer an alternative to Au, which can hamper the electrical and optical properties of Ge and Si nanowires. This method can be applied to scaled-up production of semiconductor nanowires with any metal that is desired.

6.2 Experimental Details

6.2.1 Materials

Diphenylgermane (DPG, Gelest Inc.) and phenylsilane (MPS, Gelest Inc.), anhydrous toluene (99.8%, Sigma-Aldrich), manganese carbonyl ($Mn_2(CO)_{10}$, 98%, Aldrich), iron pentacarbonyl ($Fe(CO)_5$, >99.99%, Aldrich), bis(cyclopentadienyl) nickel(II) (nickelocene, Aldrich), copper bis(2,2,6,6-tetramethyl-3,5-heptanedionate) ($Cu(TMHD)_2$, 99%, Aldrich), gallium(III) acetylacetonate ($Ga(acac)_3$, 99.99%, Aldrich), indium(III) acetylacetonate ($In(acac)_3$, >99.99%, Aldrich), lead bis(2,2,6,6-tetramethyl-3,5-heptanedionate) ($Pb(TMHD)_2$, 97%, Aldrich), bismuth neodecanoate (Aldrich) were used as received. The metal compounds were stored in an Ar-filled glovebox and dissolve in toluene before use.

6.2.2 Ge Nanowire Synthesis

Ge nanowires were synthesized in supercritical toluene using a 10 mL titanium tubular reactor connected to a high pressure liquid chromatography (HPLC) pump as described in literature.[30] Taking Ni seeded Ge nanowire synthesis as example, a 28 mL of reaction solution containing 0.446 mM nickelocene, 35.7 mM DPG and 23.8 mM MPS in anhydrous toluene was prepared in the Ar-filled glovebox. Meanwhile, the titanium tubular reactor sealed in the glovebox was placed in the preheated brass heating block and connected to the six-way valve. Prior to precursor injection, the reactor was heated to 500°C and pressurized to 10.3 MPa with anhydrous toluene. Nanowire synthesis was carried out with the reactant solution injected into the reactor at a rate of 0.5 mL/min for 40 min. The pressure was maintained at 10.3 MPa by adjusting the back-pressure regulator. After reaction, the reactor was sealed and allowed to cool to room temperature. The contents of the reactor was collected and dispersed in a mixture of chloroform, toluene and ethanol, followed by centrifugation at 8000 rpm for 5 min. This purification procedure was repeated three times. The products were redispersed in chloroform for storage.

The synthesis with other metalorganic compounds is similar as mentioned above. The changes are summarized as following: Mn reaction solution contains 1.116 mM manganese carbonyl; Fe reaction solution contains 0.446 mM iron carbonyl; Cu reaction solution contains 0.446 mM $Cu(TMHD)_2$; Ga reaction solution contains 2.232 mM $Ga(acac)_3$ and the reaction was carried out at 400ºC, 6.9 MPa; In seeded nanowires used the reaction solution containing 2.232 mM $In(acac)_3$ and the reaction was carried out at 400ºC, 6.9 MPa; Pb reaction solution contains 2.232 mM $Pb(TMHD)_2$ and the reaction was carried out at 400ºC, 6.9 MPa; Bi reaction solution contains 2.232 mM bismuth neodecanoate and the reaction was carried out at 400ºC, 6.9 MPa.

6.2.3 Materials Characterization

Scanning electron microscopy (SEM) images were acquired on a Zeiss Model SUPRA 40 VP SEM with the in-lens arrangement, 5.0 kV of working voltage and 5 mm of working distance. The SEM samples were prepared by drying Ge nanowires onto silicon wafers.

X-ray diffraction (XRD) was performed on a Rigaku R-Axis Spider diffractometer using Cu K_α radiation (λ=1.54 Å) and a graphite monochromator.

Transmission electron microscopy (TEM) images were acquired on a FEI Tecnai Spirit Bio Twin operated at 80 kV.

High-resolution transmission microscopy (High-res TEM) images, high-angle annular dark-field scanning transmission electron microscopy (HAADF-STEM), energy-dispersive X-ray spectroscopy (EDS) elemental mapping and electron energy loss spectroscopy (EELS) line scan were acquired on a field emission JEOL 2010F TEM operated at 200 kV. TEM samples were prepared by drop-casting 5 µL of dilute Ge nanowire dispersion onto a 200 mesh copper lacey carbon TEM grid (Electron Microscopy Science).

6.3 RESULTS AND DISCUSSIONS

As illustrated in Figure 6.1, the nanowire formation process could be divided into three steps: i) metalorganic compounds thermally decompose into metal nanoparticles; ii) germanium precursor, i.e. diphenyl germane (DPG), crack at the surface of particles; iii) germanium atoms diffuse across the nanoparticles and grow out of catalyst particles into a nanowire.[19] Depending on the metal particles formed in the first step are whether liquid or solid, the growth mechanism is known as supercritical-fluid-liquid-solid (SFLS) or supercritical-fluid-solid-solid (SFSS) nanowire growth.

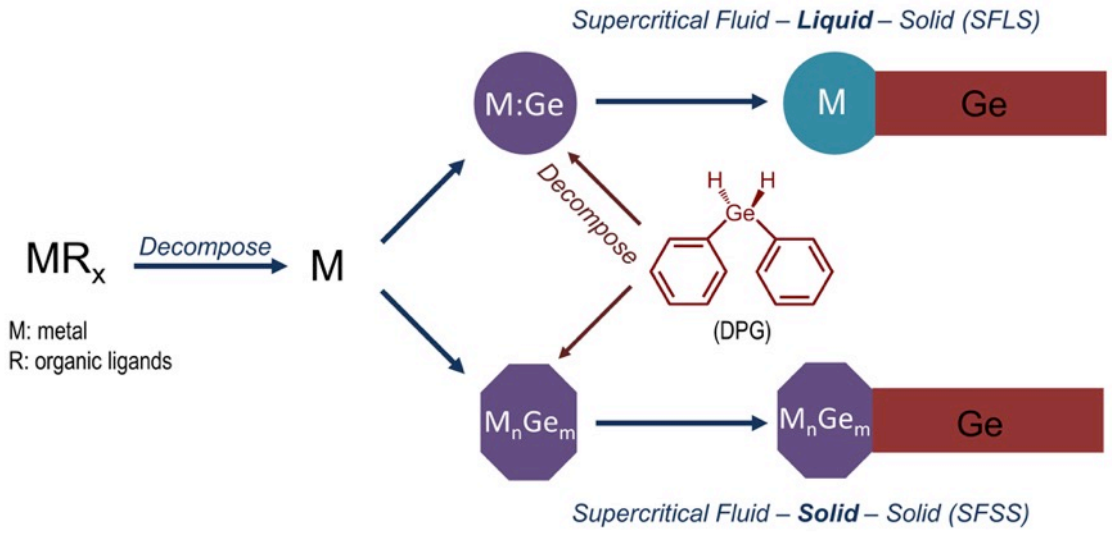

Figure 6.1 Illustration of the growth of the Ge nanowires. The metalogranic compounds thermally decompose into metal nanoparticles. Ge atoms feed to these metal nanoparticles by the decomposition of DPG and the Ge nanowires begin to grow. The nanowire growth can be divided into SFLS or SFSS mechanism depending on the state of the seed particles.

As the metal seeds formation is in the initial step, it decides whether the following steps can be carried out and also influences the quality of the nanowires. The first concern of the successful synthesis is choosing suitable metal precursors. For a

metalorganic compound to be adopted in the nanowire growth, it should have at least three characteristics. The prerequisite is that the metal compounds should have decent solvability in the reaction solvent, or they cannot be delivered to the reactor in a continuous flowing setup. For example, copper(II) acetylacetonate ($Cu(acac)_2$) has very low solvability in toluene; therefore, it is replaced by copper(II) bis(2,2,6,6-tetramethyl-3,5-heptanedionate) ($Cu(TMHD)_2$) which has the similar molecular structure but shows much higher solvability in toluene with four metyl groups replaced by butyl groups. Second, the decomposition of metal precursors should not interfere with the decomposition of the semiconductor precursor. Third, they should have suitable decomposition reaction kinetics; that is, metal precursors must decompose ahead of semiconductor precursors. This is crucial for the success. Taking iron (Fe) as an example, the first-order decomposition rate constant (k) of iron carbonyl ($Fe(CO)_5$) is several orders of magnitude higher than ferrocene.[15,20] Ferrocene only has decent decomposition rate above 1050ºC, while $Fe(CO)_5$ starts to decompose as low as room temperature (300K).[21] Though $Fe(CO)_5$ undergoes a series of decarbonylaztion steps and the complete decomposition requires temperature higher than 300K, $Fe(CO)_5$ has already achieved sufficient decomposition rate at our reaction temperature (500ºC). The different decomposition rates of metalorgranic compounds directly influence the morphologies of the products. With insufficient Fe feeding, ferrocene only yielded amorphous Ge spheres and few nanowires, while $Fe(CO)_5$ catalyzed reaction produced high yield of Ge nanowires (Figure 6.2).

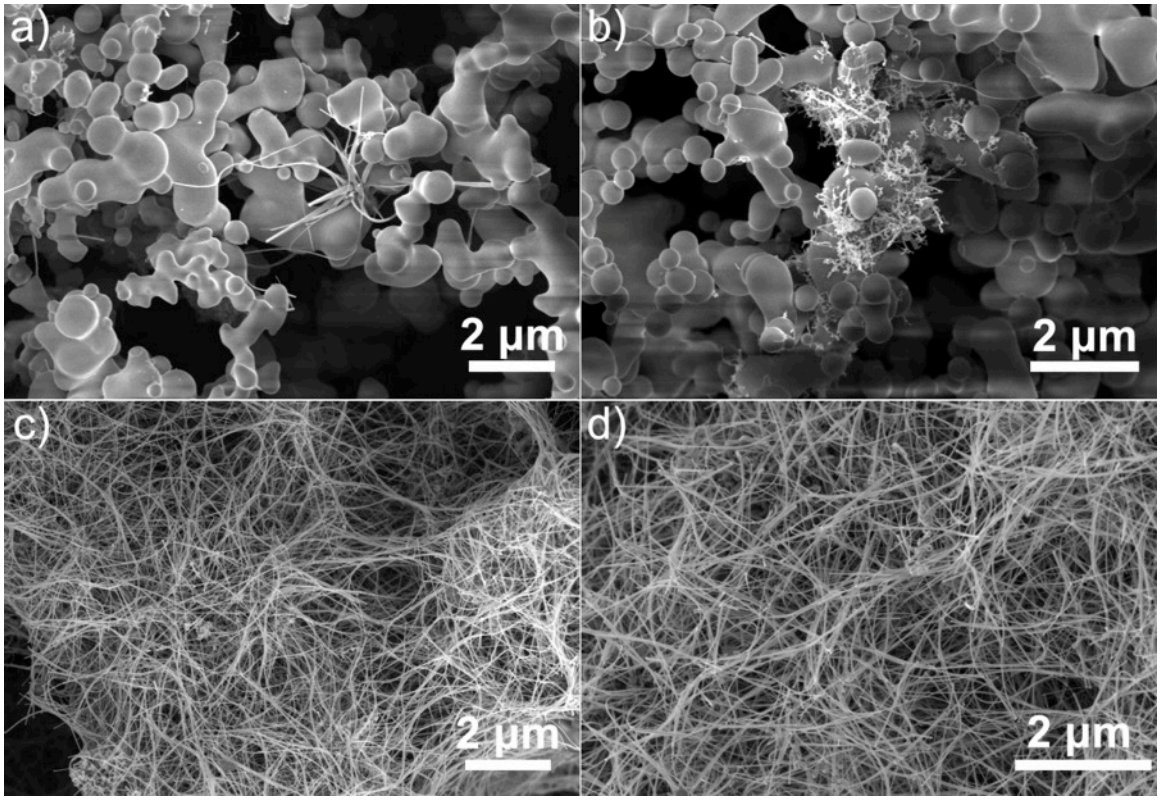

Figure 6.2 Reaction products obtained with (a-b) ferrocene and (c-d) iron carbonyl. With addition of ferrocene, few nanowires/nanorods formed. The majority of the products are amorphous Ge spheres, which form when DPG decomposed without enough seeding. With iron carbonyl, the obtained products are long nanowires.

Temperature, which affects the decomposition rate of metalorganic compounds, is another crucial parameter. The influence of reaction temperature can be reflected in the comparison experiments of the nickelocene catalyzed nanowire growth at 450ºC and 500ºC (Figure 6.3). According to literatures, nickelocene decompose into Ni above 450ºC at 101.325kPa without hydrogen in the system[22] but this pyrolysis favors low pressure.[23] The supercritical condition requires high pressure. So, a 450ºC reaction only yielded short nanowires accompanying amorphous Ge spheres, indicating the unbalanced decomposition of DPG and nickelocene. At 500ºC, the vast majority of the products are

long nanowires. Higher temperature also accelerate diffusion rate of Ge in catalyst particles, which is also preferred in solid state seeding.

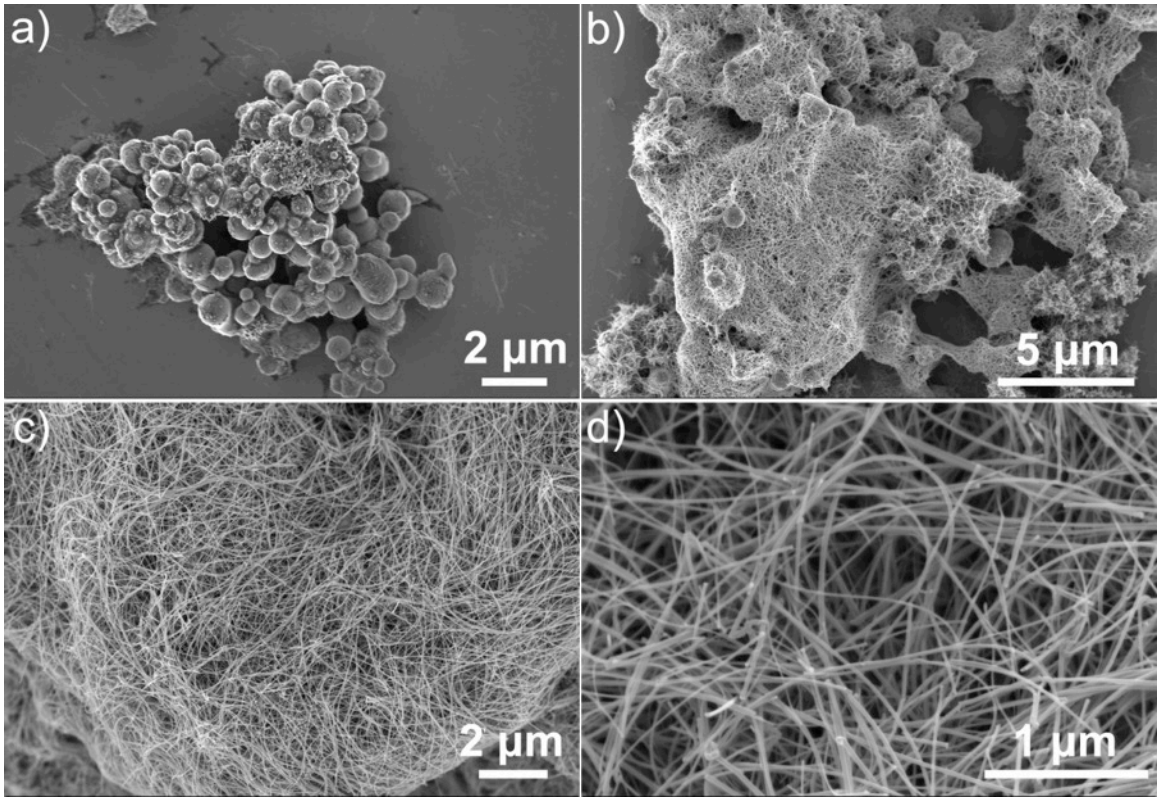

Figure 6.3 Ge nanowires catalyzed by nickelocene grown at (a-b) 450°C and (c-d) 500°C. At 450°C, short nanowires present with Ge spheres which is the by-product forming due to the lack of seeds. At 500°C, the majority of the obtained products are long nanowires.

Concentration of metalorganic compounds also affects. Taking gallium acetylacetonate ($Ga(acac)_3$) as an example, by employing the concentration of 0.446 mM, no nanowire was yielded from the $Ga(acac)_3$ reaction. Only by increasing the concentration of $Ga(acac)_3$ to 2.232 mM, Ge nanowires can be obtained. Higher concentration accelerates decomposition of metalorganic compounds. And, low melting point metals, like Ga, are easy to fuse together at reaction temperature and decrease their

efficiency of seeding the nanowire growth. They also evaporate more easily than high melting point metals.[17]

By choosing suitable metalorganic compounds and reaction conditions, Ge nanowires with various seeding could be obtained. Figure 6.4 shows the SEM and TEM images of the Ge nanowires catalyzed by eight different metalorganic compounds and Table 6.1 summarizes these reactions. Generally, SFSS nanowires are thinner and more uniform in diameter than SFLS nanowires.[24] The average diameters of SFSS nanowires are between 10 nm and 20 nm, whereas SFLS nanowires are over 50 nm. The solid seeds prevent the aggregation better than the liquid seeds and are more likely to produce nanowires with narrow diameter distribution. This result is in good accord with previous observation that solid state seeding has better control over the diameter of the nanowire.[25] For SFLS nanowires, the reaction temperatures (400ºC) are 370ºC, 244ºC, 73ºC and 129ºC higher than the eutectic temperature of Ga-Ge, In-Ge, Pb-Ge and Bi-Ge, respectively. Interestingly, the temperature differences are proportional to the average diameters of nanowires, indicating liquid phase seeding necessities lower temperature to narrow the nanowire diameters. Moreover, SFSS nanowires have higher yields than SFLS nanowire in general. Fe and Pb give the highest yield, which nearly achieve the theoretical maximum of DPG conversion.

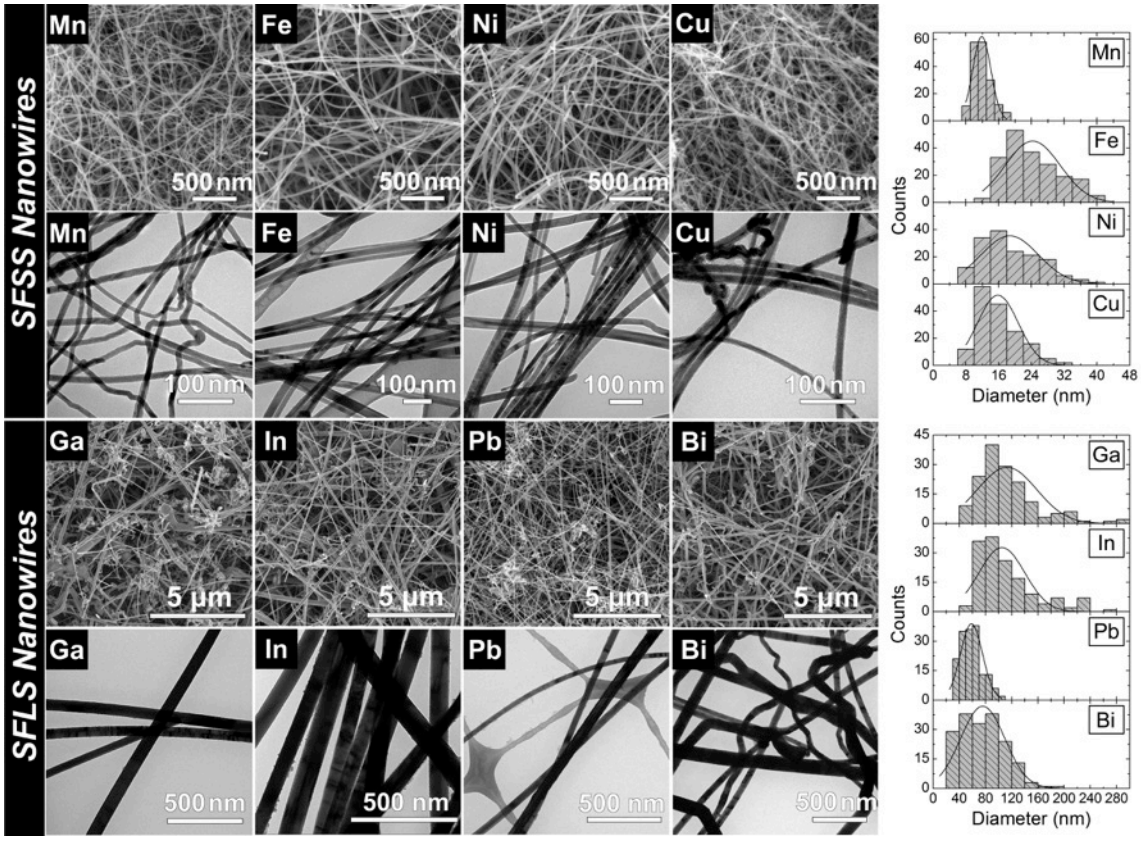

Figure 6.4 Overview of the Ge nanowire morphologies catalyzed by different metalorganic compounds. The top two rows are the SEM and TEM images of the SFSS nanowires, and the bottom two rows are of the SFLS nanowires. The statistical analysis of the nanowire diameters are plotted in the right column and also categorized into SFSS and SFLS nanowires. The images are arranged by the atomic number of the seed metal.

Table 6.1 Summary of metalorganics, reaction conditions and selected properties of the Ge nanowires.

Seeding Metal	Metalorganic Compound	Lowest Eutectic Temp. (°C)[a]	Growth Temp. (°C)	Average Diameter (nm)[b]	Yield (mg)	DPG Conversion[c]
Mn	$Mn_2(CO)_{10}$	720	500	11.9 ± 2.2	35.4	67.4%
Fe	$Fe(CO)_5$	838	500	24.3 ± 6.7	49.9	95%
Ni	Nicklocene	762	500	18.7 ± 7.0	46.6	88.7%
Cu	$Cu(TMHD)_2$	644	500	15.8 ± 5.0	38.7	73.6%
Ga	$Ga(acac)_3$	30	400[d]	119.2 ± 63.7	34.8	66.2%
In	$In(acac)_3$	156	400	104.9 ± 35.1	30.7	58.4%
Pb	$Pb(TMHD)_2$	327	400	58.5 ± 16.9	51.0	97.1%
Bi	Bi neodecanoate	271	400	75.7 ± 33.8	21.9	41.7%

[a] Refer to Supporting Information for phase diagrams.
[b] This statistical data is obtained from the measurement of over 150 nanowires under TEM.
[c] Molar conversion of DPG to Ge.
[d] Though $Ga(acac)_3$ decomposes around 196°C,[31] the reaction temperature is set at 400°C because the nanowire growth also requires efficient DPG decomposition .

Figure 6.5 shows XRD of the eight Ge nanowires from different seedings. All the major peaks can be indexed to diamond cubic germanium, indicating the good crystallinity of both SFSS and SFLS nanowires. Bi, Pb, In could be detected in SFLS nanowires; no Ga was detected because the melting point of Ga is close to room temperature. Since the sizes of solid seeds are much smaller than liquid seeds, only weak signal of Cu_3Ge was detected in SFSS nanowires (Figure 6.6). As Cu_3Ge is the most stable congruently melting phase next to the lowest eutectic in the Cu-Ge binary phase diagram, this result verifies the prediction of the first crystalline phase nucleated at subeutectic temperatures[26,27] and is in accord with previous research.[13,28]

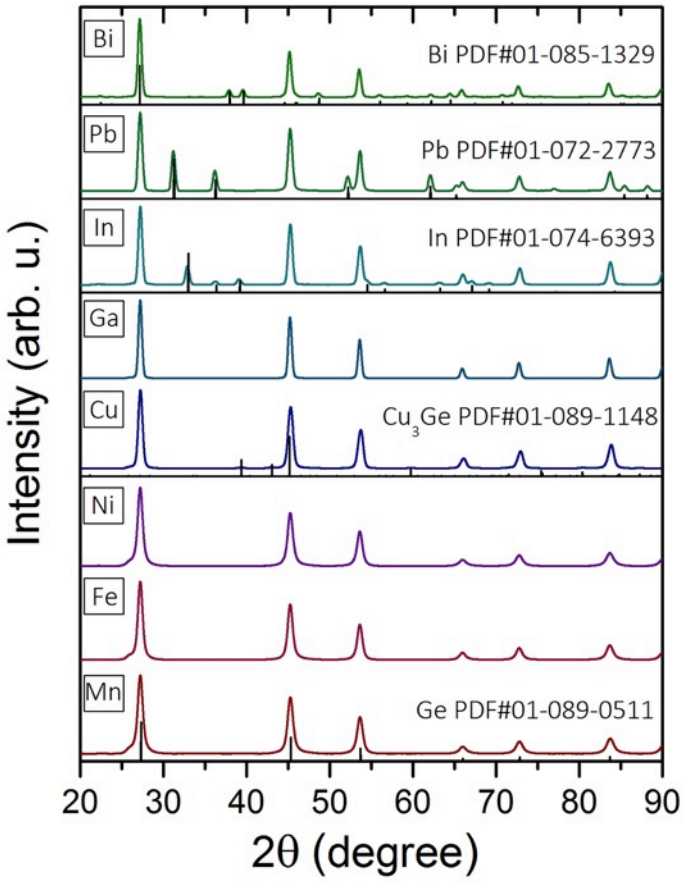

Figure 6.5 XRD of Ge nanowires catalyzed by different metalorganic compounds. All the curves are normalized to the (111) peak of Ge. The seeding metals are labeled on the left. The reference patterns of Ge, Cu_3Ge, In, Pb, Bi and PDF numbers are shown on the right.

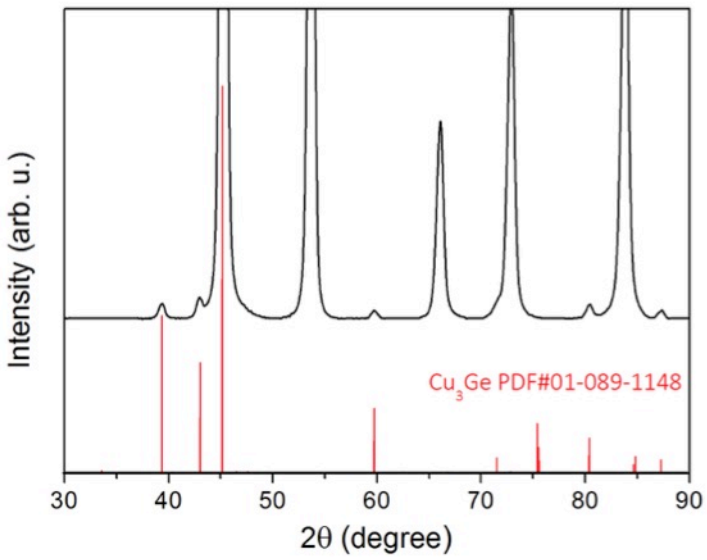

Figure 6.6 Zoomed-in XRD of Ge nanowires catalyzed $Cu(TMHD)_2$. The reference pattern of Cu_3Ge and PDF numbers is shown below.

Energy dispersive X-ray spectroscopy (EDS) mapping of those nanowires (Figure 6.7) supplements the absent information of the seeds composition in XRD. In SFLS nanowires, there is only metal signal detected in the seeds. In contrast, both of metal and Ge signals are detected in the seeds of SFSS nanowires, indicating those seeds are metal germanides instead of pure metals. SFLS nanowires are catalyzed by alloy droplet with low concentration of Ge. Upon cooling, the alloy droplet will phase segregate into pure metal. SFSS nanowires are seeded by the solid-state germanide that would not change composition upon cooling.

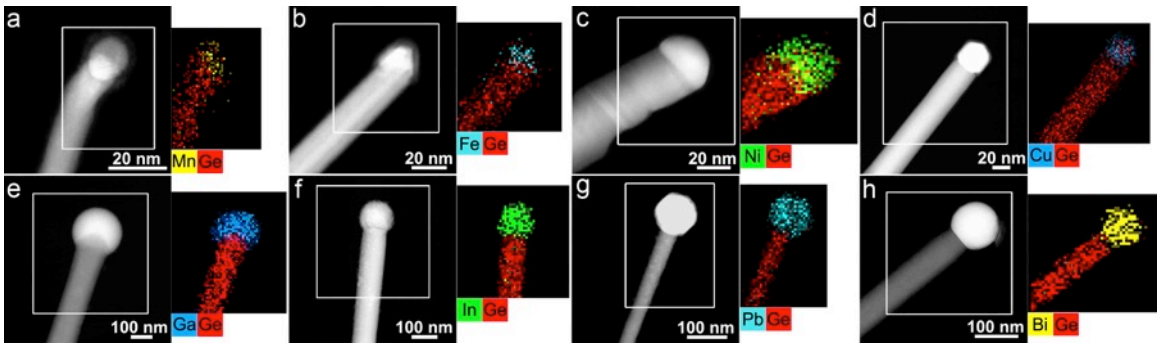

Figure 6.7 HAADF STEM images and EDS mappings of Ge nanowire taken in the seeding area: (a) Mn, (b) Fe, (c) Ni, (d) Cu, (e) Ga, (f) In, (g) Pb, (h) Bi seeded nanowires.

Three families of growth directions, <111>, <110> and <112>, have all been observed in our nanowires (Figure 6.8), with <111> the dominant growth direction. This is consistent with our previous observations in the pre-made nanoparticle seeded SFLS and SFSS Ge nanowires.[29]

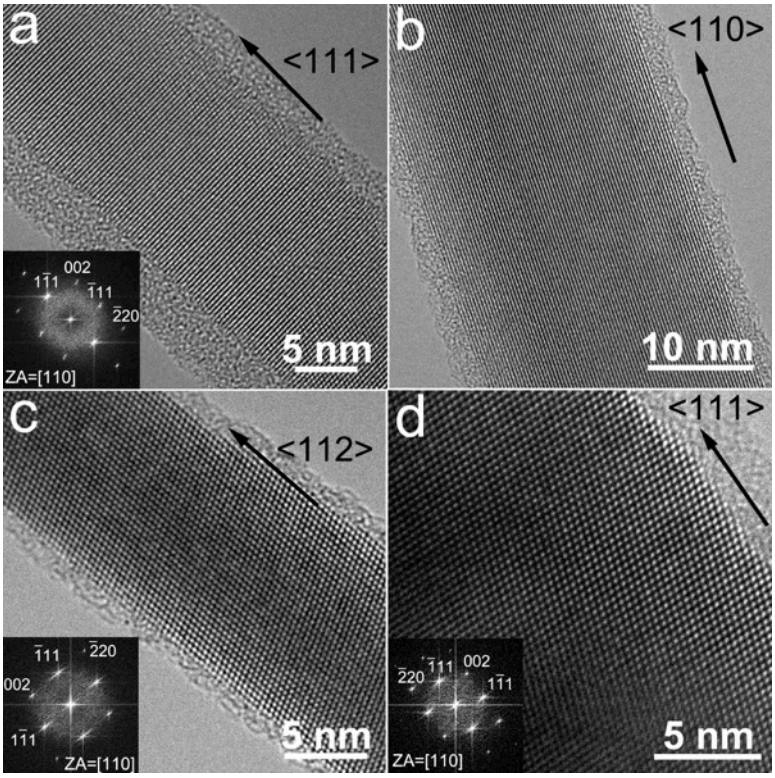

Figure 6.8 High-resolution TEM images of (a) Mn, (b) Fe, (c) Ni and (d) Bi seeded Ge nanowires.

6.4 CONCLUSIONS

In summary, we demonstrate a simplified growth of Ge nanowires in supercritical toluene by using the commercially available metalorgainc compounds to replace pre-synthesized metal nanoparticles. Both liquid state and solid state seeded Ge nanowires can be easily obtained by this method. The choice of metalorganic compounds is the key determinate in this reaction. The suitable metalorgainc compounds should have high decomposition kinetics under reaction condition and produce enough seeds before the homogenous nucleation of Ge. By abandoning the necessity of pre-made seed particles,

our approach represents a significant advance towards scalable production of Ge nanowires and provides insight to the synthesis of other semiconducting nanowires.

6.5 Acknowledgements

This work was supported by the Robert A. Welch Foundation (grant no. F-1464) and the National Science Foundation (grant no. CHE-1308813). X.T.L. thanks Philip Liu for assistance with EELS measurement and Timothy Bogart for helpful discussions.

6.6 References

1. Kuno, M. An Overview of Solution-Based Semiconductor Nanowires: Synthesis and Optical Studies. *Phys. Chem. Chem. Phys.* **2008**, *10* (5), 620.
2. Li, Y.; Qian, F.; Xiang, J.; Lieber, C. Nanowire Electronic and Optoelectronic Devices. *Mater. today* **2006**, *9* (10), 18–27.
3. Thelander, C.; Agarwal, P.; Brongersma, S. Nanowire-Based One-Dimensional Electronics. *Mater. today* **2006**, *9* (10), 28–35.
4. Law, M.; Goldberger, J.; Yang, P. Semiconductor Nanowires and Nanotubes. *Annu. Rev. Mater. Res.* **2004**, *34* (1), 83–122.
5. Hochbaum, A. I.; Yang, P. Semiconductor Nanowires for Energy Conversion. *Chem. Rev.* **2010**, *110* (1), 527–546.
6. Chan, C. K.; Peng, H.; Liu, G.; McIlwrath, K.; Zhang, X. F.; Huggins, R. A.; Cui, Y. High-Performance Lithium Battery Anodes Using Silicon Nanowires. *Nat. Nanotechnol.* **2008**, *3* (1), 31–35.
7. Bogart, T. D.; Chockla, A. M.; Korgel, B. A. High Capacity Lithium Ion Battery Anodes of Silicon and Germanium. *Curr. Opin. Chem. Eng.* **2013**, *2* (3), 286–293.
8. Chockla, A. M.; Harris, J. T.; Akhavan, V. A.; Bogart, T. D.; Holmberg, V. C.; Steinhagen, C.; Mullins, C. B.; Stevenson, K. J.; Korgel, B. A. Silicon Nanowire Fabric as a Lithium Ion Battery Electrode Material. *J. Am. Chem. Soc.* **2011**, *133* (51), 20914–20921.
9. Chockla, A. M.; Klavetter, K. C.; Mullins, C. B.; Korgel, B. a. Solution-Grown Germanium Nanowire Anodes for Lithium-Ion Batteries. *ACS Appl. Mater. Interfaces* **2012**, *4* (9), 4658–4664.

10. Kohandehghan, A.; Cui, K.; Kupsta, M.; Ding, J.; Memarzadeh Lotfabad, E.; Kalisvaart, W. P.; Mitlin, D. Activation with Li Enables Facile Sodium Storage in Germanium. *Nano Lett.* **2014**, *14* (10), 5873–5882.

11. Zhou, H.; Nanda, J.; Martha, S. K.; Unocic, R. R.; Meyer, H. M.; Sahoo, Y.; Miskiewicz, P.; Albrecht, T. F. Role of Surface Functionality in the Electrochemical Performance of Silicon Nanowire Anodes for Rechargeable Lithium Batteries. *ACS Appl. Mater. Interfaces* **2014**, *6* (10), 7607–7614.

12. Mullane, E.; Geaney, H.; Ryan, K. M. Size Controlled Growth of Germanium Nanorods and Nanowires by Solution Pyrolysis Directly on a Substrate. *Chem. Commun. (Camb).* **2012**, *48* (44), 5446–5448.

13. Richards, B. T.; Gaskey, B.; Levin, B. D. A.; Whitham, K.; Muller, D.; Hanrath, T. Direct Growth of Germanium and Silicon Nanowires on Metal Films. *J. Mater. Chem. C* **2014**, *2* (10), 1869.

14. Zhu, H. W.; Xu, C. L.; Wu, D. H.; Wei, B. Q.; Vajtai, R.; Ajayan, P. M. Direct Synthesis of Long Single-Walled Carbon Nanotube Strands. *Science* **2002**, *296* (5569), 884–886.

15. Moisala, A.; Nasibulin, A. G.; Brown, D. P.; Jiang, H.; Khriachtchev, L.; Kauppinen, E. I. Single-Walled Carbon Nanotube Synthesis Using Ferrocene and Iron Pentacarbonyl in a Laminar Flow Reactor. *Chem. Eng. Sci.* **2006**, *61* (13), 4393–4402.

16. Smith, D. K.; Lee, D. C.; Korgel, B. a. High Yield Multiwall Carbon Nanotube Synthesis in Supercritical Fluids. *Chem. Mater.* **2006**, *18* (14), 3356–3364.

17. Bogart, T. D.; Lu, X.; Korgel, B. A. Precision Synthesis of Silicon Nanowires with Crystalline Core and Amorphous Shell. *Dalton Trans.* **2013**, *42* (35), 12675–12680.

18. Lu, X.; Korgel, B. A. A Single-Step Reaction for Silicon and Germanium Nanorods. *Chem. - A Eur. J.* **2014**, *20* (20), 5874–5879.

19. Schmidt, V.; Wittemann, J. V; Gösele, U. Growth, Thermodynamics, and Electrical Properties of Silicon Nanowires. *Chem. Rev.* **2010**, *110* (1), 361–388.

20. Lewis, K. E.; Smith, G. P. Bond Dissociation Energies in Ferrocene. *J. Am. Chem. Soc.* **1984**, *106* (16), 4650–4651.

21. Xu, M. Mechanistic Studies of the Thermal Decomposition of Metal Carbonyls on Ni(100) Surfaces in Connection with Chemical Vapor Deposition Processes. *J. Vac. Sci. Technol. A Vacuum, Surfaces, Film.* **1996**, *14* (2), 415.

22. Brissonneau, L.; Sahnoun, R.; Mijoule, C.; Vahlas, C. Investigation of Nickelocene Decomposition during Chemical Vapor Deposition of Nickel. *J. Electrochem. Soc.* **2000**, *147* (4), 1443.

23. Hedaya, E. Techniques of Flash Vacuum Pyrolysis. Cyclopentadienyl Radical and Its Dimer. *Acc. Chem. Res.* **1969**, *2* (12), 367–373.

24. Tuan, H.; Lee, D. C.; Hanrath, T.; Korgel, B. A. Germanium Nanowire Synthesis: An Example of Solid-Phase Seeded Growth with Nickel Nanocrystals. *Chem. Mater.* **2005**, *17* (23), 5705–5711.

25. Kodambaka, S.; Tersoff, J.; Reuter, M. C.; Ross, F. M. Germanium Nanowire Growth below the Eutectic Temperature. *Science* **2007**, *316* (5825), 729–732.

26. Wittmer, M.; Nicolet, M.-A.; Mayer, J. W. The First Phase to Nucleate in Planar Transition Metal-Germanium Interfaces. *Thin Solid Films* **1977**, *42* (1), 51–59.

27. Walser, R. M.; Bené, R. W. First Phase Nucleation in Silicon–transition-Metal Planar Interfaces. *Appl. Phys. Lett.* **1976**, *28* (10), 624.

28. Geaney, H.; Dickinson, C.; Barrett, C. A.; Ryan, K. M. High Density Germanium Nanowire Growth Directly from Copper Foil by Self-Induced Solid Seeding. *Chem. Mater.* **2011**, *23* (21), 4838–4843.

29. Tuan, H.-Y.; Lee, D. C.; Korgel, B. A. Nanocrystal-Mediated Crystallization of Silicon and Germanium Nanowires in Organic Solvents: The Role of Catalysis and Solid-Phase Seeding. *Angew. Chem. Int. Ed. Engl.* **2006**, *45* (31), 5184–5187.

30. Holmberg, V. C.; Korgel, B. A. Corrosion Resistance of Thiol- and Alkene-Passivated Germanium Nanowires. *Chem. Mater.* **2010**, *22* (12), 3698–3703.

31. Chang, K.-W.; Wu, J.-J. Low-Temperature Catalytic Synthesis of Gallium Nitride Nanowires. *J. Phys. Chem. B* **2002**, *106*, 7796–7799.

Chapter 7: Conclusions and Future Direction

7.1 Conclusions

This section demonstrated several different solution-based synthetic methods for growing Si and Ge nanorods and nanowires. Chapter 2 showed the SLS growth of Si nanorods with narrow diameters (<10 nm) and quantum-confined optical properties by the decomposition of trisilane in hot squalane (~400ºC) in the presence of Sn nanocrystals stabilized by poly-(vinylpyrrolidinone-hexadecene). Photoluminescence with quantum yields of 4-5% was obtained from the Si nanorods by post-reaction surface etching with hydrofluoric acid to remove residual surface oxide, followed by thermal hydrosilylation passivation with 1-octadecene. Chapter 3 simplified this growth to a single reaction step by combining $Sn(hmds)_2$ with trisilane in the reaction solution. Trisilane reduces $Sn(hmds)_2$ to Sn *in situ*, simplifying the reaction procedure and improving repeatability by eliminating the need to use pre-synthesized seed particles. Si and Ge nanorods with various aspect ratio and Si-Ge heterostructured nanorods can be obtained with this approach. Chapter 4 examines silanes that are more reactive than trisilane to further lower the synthesis temperature for Si nanorods. Isotetrasilane, neopentasilane and cyclohexasilane have all exhibited Si nanorod synthesis at lower reaction temperatures than trisilane. Cyclohexasilane is particularly interesting, enabling Si nanorod growth with Sn seeds at temperatures as low as 200ºC. Chapter 5 showed that the addition of monophenylsilane dramatically improves the yield and quality of Ge nanowires, producing straight nanowires with relatively uniform diameter and nearly 100% conversion of diphenylgermane (DPG) to Ge. MPS participates in the phenyl redistribution reaction of DPG and serves as a phenyl sink that speeds DPG decomposition and increases the conversion to Ge to nearly 100%. Chapter 6 explores metalorganic compounds for single-step reactions for Ge nanowire growth. The relative

decomposition rates of metalorganic compounds and Ge precursor have been found to be important. The metal precursor must have faster decomposition kinetics than Ge precursor. So far, *in situ* Mn, Fe, Ni, Cu, Ga, In, Pb and Bi seeded Ge nanowires have been successfully grown in supercritical toluene.

7.2 FUTURE DIRECTION

Solution-based synthesis offers a high throughput, low cost route to producing Si and Ge nanomaterials in relative large quantities, comparing with vapor phase reactions. Replacing metal nanocrystals with metalorganic compounds is an advance to realize large-scale production of nanowires at reduced production cost and improved repeatability. A variety of different metalorganic compounds have been investigated for the Ge nanowires growth in this section. This exploration should be extended to the growth of Si nanowires in the future.

Sn seeds have been proved effectiveness in growing quantum-confined Si nanorods. To prevent aggregation at high reaction temperatures, Sn nanoparticles require the passivation of poly-(vinylpyrrolidinone-hexadecene). This copolymer, however, could yield Sn nanoparticles of a particular diameter that cannot be altered by temperatures, chemical concentrations or other common reaction parameters. For the development of Si nanorods growth, either Sn or the copolymer should be replaced.

Si-Ge heterostructured nanorods could be easily synthesized by multiple injections using the Sn-seeded SLS reaction described in this section. Si-Ge heterojunction is a type II heterojunction, which could be explored the use in photocatalysis.

SECTION II: *IN SITU TRANSMISSION ELECTRON MICROSCOPE STUDY OF SILICON AND GERMANIUM NANOSTRUCTURES AS ANODE MATERIALS*

This section focused on the *in situ* transmission electron microscope (TEM) study of Si and Ge nanowires as lithium ion battery anodes.

Chapter 8: Introduction to *In Situ* TEM Study of Anode Materials

Lithium ion batteries (LIBs) are the dominant power source for portable electronic devices. However, to power electric vehicles or store energy for electrical power grids, LIBs need significantly higher energy density, better power performance and longer cycle life.[1–3] Efforts have been made to develop more advanced electrolytes[4] and positive and negative electrodes with higher energy density.[5–7,8–10] Of the possible negative electrodes, or anodes, Si and Ge offer much higher lithium storage density compared to the commercially used graphite (Si: 3579 mAh/g, Ge: 1362 mAh/g, C: 372 mAh/g), making them some of the most promising replacements for the standard graphite anodes.[9,11]

8.1 LITHIUM ION BATTERIES

In a typical lithium ion battery (LIB), electrodes, i.e. cathode and anode, are separated by an electrically insulating Li ion permeable membrane and immersed in the ion-conductive electrolyte solution (Figure 8.1). LIBs operate by shuttling Li ions between the electrodes: during charging, a voltage is applied to force Li ions stored in cathode side flowing to the anode; during discharging, Li ions diffuse back into the cathode and electricity flows though the external circuit to power the devices.

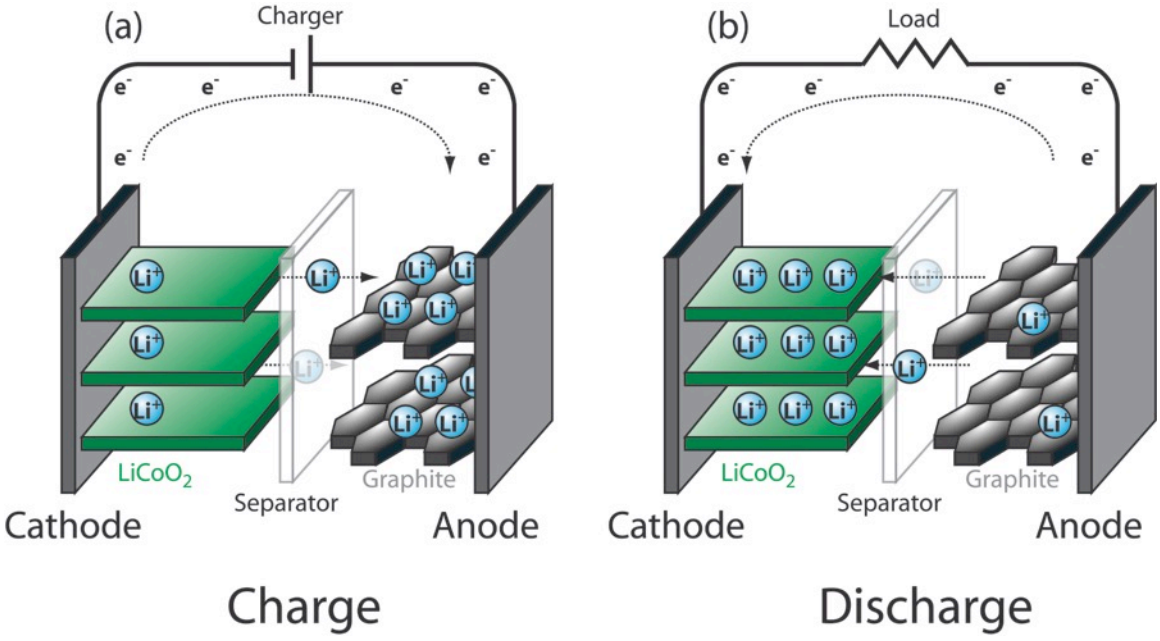

Figure 8.1 Schematic of a typical lithium ion battery.

Energy density of the battery is calculated as the product of the discharge voltage and the charge storage capacity of the electrodes. The open circuit voltage is determined by the redox potential difference between cathode and anode; the capacity of an electrode is determined by the amount of Li it can store. In the conventional LiB, the maximum theoretical capacity of $LiCoO_2$ (cathode) and LiC_6 (anode) are only 274 mAh/g and 372 mAh/g, respectively. The low energy density of conventional LIBs encourages people seeking for the replacement electrode materials with higher energy density.

8.2 Lithiation of Silicon and Germanium

On the anode side, Si and Ge are the leading candidates for replacing carbonaceous anodes. They provide much higher lithium storage density compared to the graphite (Si: 3579 mAh/g, Ge: 1362 mAh/g, C: 372 mAh/g).[12–14] Besides the high specific capacity, Si and Ge also have low working potential close to the Li metal and are

abundant in earth's crust, making them the most attractive anode materials in battery research.

At room temperature, the fully lithiated phase of Si is $Li_{15}Si_4$. Before reaching to the final lithiation state, Si first forms an amorphous Li_xSi alloy upon lithiation. Namely, Si lithiates via a two-step reaction:[15,16]

$$Si \xrightarrow{Li} a - Li_xSi \xrightarrow{Li} Li_{15}Si_4 \quad (1)$$

From the Equation 1, lithiation of Si gives rise to two plateaus in the voltage profile, or two peaks in the differential capacity plot, due to the two phase reactions (Figure 8.2). Region I relate to the phase separation between Si and a-Li_xSi and Region II indicates the two-phase regions of a-Li_xSi and $Li_{15}Si_4$. SEM imaging of the a-Si disks during electrochemical lithiation verifies this two-step process.[17] In the first step, a shell of a-Li_xSi ($x \sim 2.5$) forms and migrates into the Si core. After the entire disk has turned into a-$Li_{2.5}Si$, it then further lithiates to a-$Li_{3.7}Si$ (Figure 8.2c). The complete lithiation leads to a volume expansion around 280%. Similar as Si, Ge adopts a two-step, or multi-step, lithiation process to reach the fully lithiated $Li_{15}Ge_4$ phase.[18–20,13]

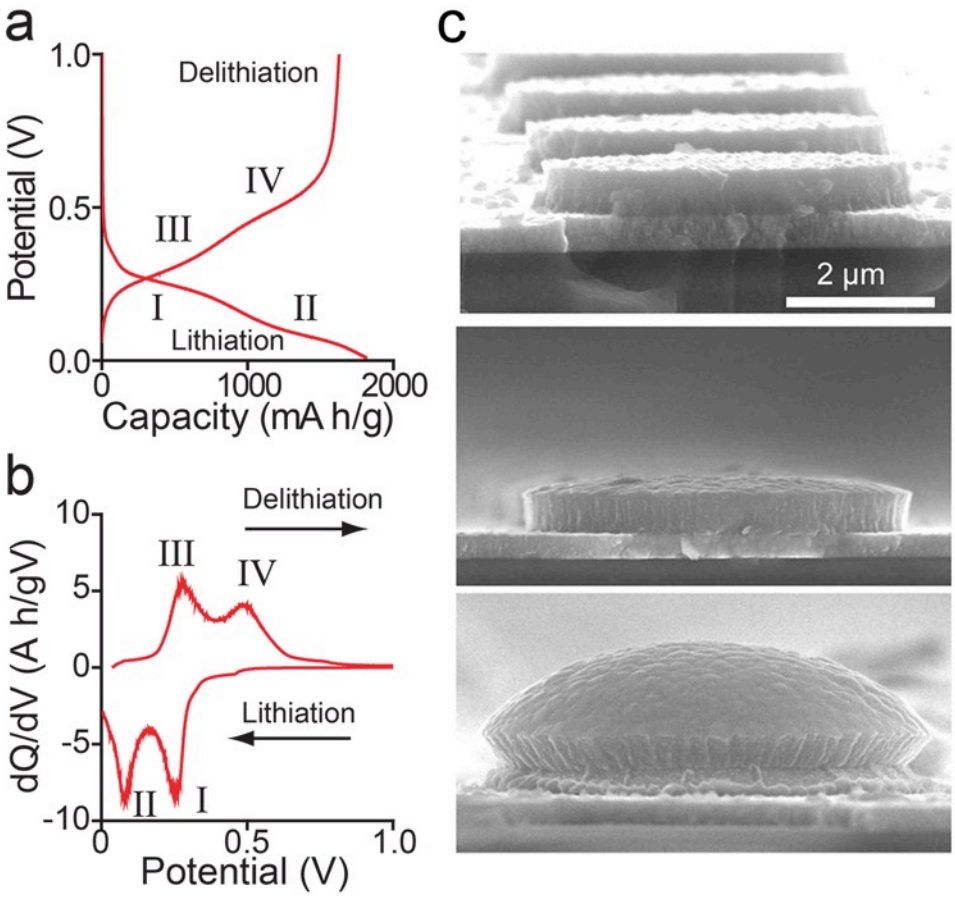

Figure 8.2 (a) Typical voltage profile and (b) differential capacity plot for a Si-based lithium ion battery anode. (c) SEM images shows the morphology evolution of a-Si disk during electrochemical lithiation: (top) as-fabricated a-Si electrode, (middle) intermediate lithiated state of the electrode, (bottom) fully lithiated state of the electode.

8.3 In Situ TEM Study of Anode Materials

Although Si and Ge are promising anode candidates of LIBs, the massive volume change of Si and Ge, up to nearly 300%, during lithiation/delithiation cycles can lead to materials degradation, resulting in capacity fade and battery failure.[21–23] Nanostructures can mostly tolerate the dramatic structural changes, but the details about how structure

changes and evolves during battery operation are only recently beginning to be uncovered.[10] A burst of research has occurred during the past few years in investigating the structural evolution of advanced LIB electrode materials that occur during cycling using various nanostructures, including nanowires, nanotubes, nanorods, and nanoparticles, as well as nanocomposites.[24] Among those nanostructures, nanowires are particularly useful because of their small and uniform diameter, needed to resist the formation and propagation of cracks, and their extended length, which provides a convenient one-dimensional path for charge and lithium transport.

High resolution TEM (HRTEM) provides observation of materials with atomic level resolution and various sample stages have been developed to enable application of various stimuli, thus enabling the TEM as a laboratory to study nanoscale phenomena in real-time with atomic resolution. A model system mimicking the lithium battery can be built inside the TEM to provide a unique testing ground for direct observation of what happens to electrode materials in LIBs during lithiation and delithiation.[25] An open-cell nanobattery setup that enable *in situ* TEM characterization of lithium battery materials is shown in Figure 8.3.

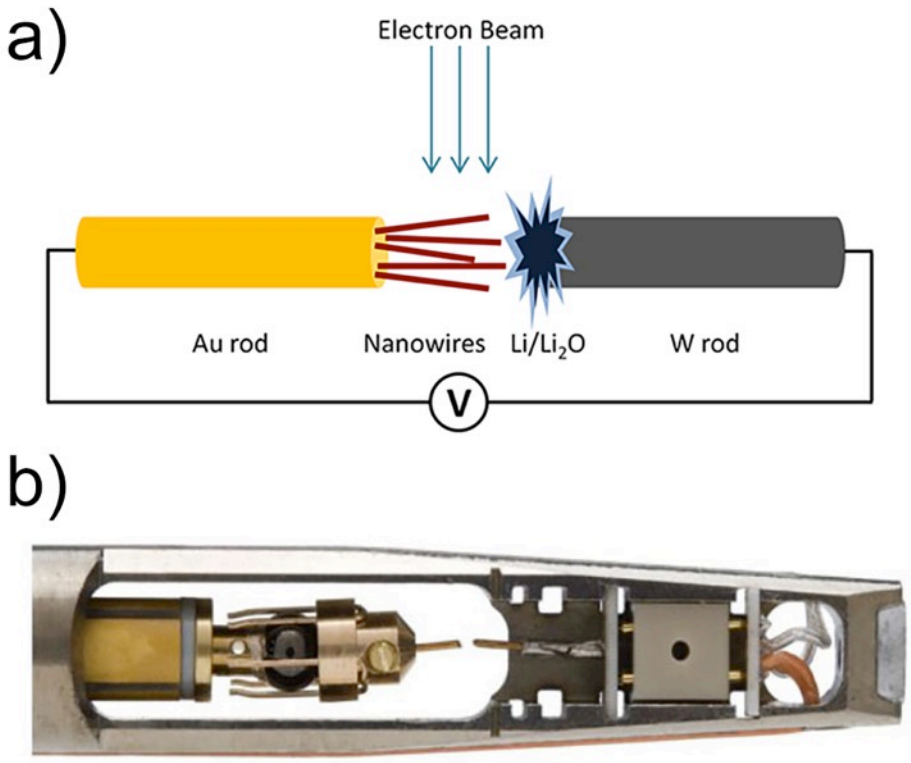

Figure 8.3 Setup of a nanobattery inside the TEM. (a) In the open cell setup, the key components include the anode materials (such as nanowires), Li source (the oxide layer of Li_2O works as electrolyte) and current collectors (Au rod and W rod in the figure). (b) Photograph of the front-piece of the Nanofactory TEM holder.

In the open cell configuration, anode nanomaterials are deposited on the current collector and directly make contact with lithium through a Li_2O layer that acts as a solid electrolyte. During lithiation, a voltage is applied to drive the Li ions into the anode from Li source. Upon delithiation, a reverse bias is applied to drive the Li back to the source. As nothing blocks the electron beam (i.e., like electrolyte), this setup is capable of observing the nanomaterials in atomic resolution. Therefore, it is an excellent method to study the structural evolution of anode materials upon charge cycling.

With *in situ* TEM, lithium insertion and extraction can be visualized in real time during electrochemical charge/discharge cycling, as occurs in a battery.[16] The structural evolution of individual nanostructures can be observed and related to anode performance in batteries and used to understand failure and improve performance. Recent *in situ* TEM studies, combined with *ex situ* experiments, have revealed that lithiation of Si is sensitive to the crystallographic orientation (Figure 8.4a-b).[26,27] But Ge undergoes a nearly isotropic lithiation with equivalent volume expansion along all directions (Figure 8.4c-d).[28,29] The anisotropic lithiation of Si is resulted from the different onset lithiation potentials of (100), (110) and (111) planes of Si. With highest onset lithiation potential, (110) planes undergo the fastest lithiation. Different planes in Ge, however, exhibit no obvious lithiation potential difference. This makes Ge having a more isotropic lithiation.[30,31] Along with those discoveries, c-Si particles has been found a critical fracture diameter of ~150 nm, above which the particles crack due to the significant mechanical stress.[32] Ge particles up to 620 nm do not fracture upon lithiation, due to the isotropy of the lithiation strain at the reaction front.[33] With assistance of *in situ* TEM, new guidelines can be developed for improving Si and Ge anode performance in LIBs.

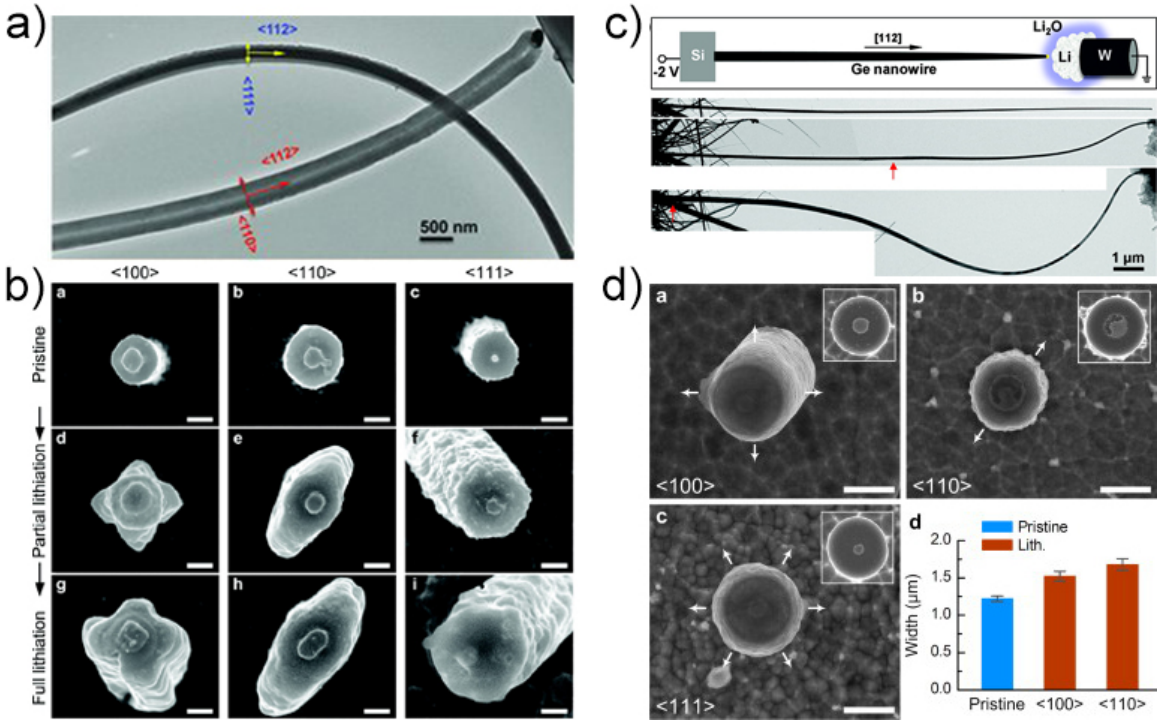

Figure 8.4 Comparison of *in situ* and *ex situ* results on the (a-b) anisotropic lithiation of Si and (c-d) isotropic lithiation of Ge.

8.4 Section Outline

The chapters in this section will focus on the *in situ* TEM investigation of the Si and Ge nanowires obtained from the solution-based synthesis (described in Section I) as the potential anode materials. Chapter 9 looks at the Si nanowires with significant amounts of Sn. The incorporation of Sn led to significantly enhanced lithiation rates compared to typical Si nanowires. Fast diffusion of Li results in the formation of pores during delithiation. Sn-containing Si Nanowires coated with an a-Si shell had similar fast lithiation and delithiation rates, but pore formation was not observed in these nanowires by *in situ* TEM. Chapter 10 investigates the Ge nanowires as a sodium ion battery material. Crystalline Ge nanowires can be sodiated only after an initial activation

with a lithiation step to amorphize the nanowires. Our *in situ* TEM results show that a-Ge nanowires can be charged with sodium at a very fast rate and that the final sodiation product exhibits over 300% volume expansion, close to Na_3Ge instead of NaGe. Desodiation led to pore formation in the nanowires. Chapter 11 finishes this section by summarizing the results from these *in situ* TEM studies and provides directions for future study.

8.5 REFERENCES

1. Tarascon, J. M.; Armand, M. Issues and Challenges Facing Rechargeable Lithium Batteries. *Nature* **2001**, *414* (6861), 359–367.

2. Goodenough, J. B.; Kim, Y. Challenges for Rechargeable Li Batteries. *Chem. Mater.* **2010**, *22* (3), 587–603.

3. Etacheri, V.; Marom, R.; Elazari, R.; Salitra, G.; Aurbach, D. Challenges in the Development of Advanced Li-Ion Batteries: A Review. *Energy Environ. Sci.* **2011**, *4* (9), 3243.

4. Aurbach, D.; Talyosef, Y.; Markovsky, B.; Markevich, E.; Zinigrad, E.; Asraf, L.; Gnanaraj, J. S.; Kim, H. J. Design of Electrolyte Solutions for Li and Li-Ion Batteries: A Review. *Electrochim. Acta* **2004**, *50* (2-3 SPEC. ISS.), 247–254.

5. Marom, R.; Amalraj, S. F.; Leifer, N.; Jacob, D.; Aurbach, D. A Review of Advanced and Practical Lithium Battery Materials. *J. Mater. Chem.* **2011**, *21* (27), 9938.

6. Fergus, J. W. Recent Developments in Cathode Materials for Lithium Ion Batteries. *J. Power Sources* **2010**, *195* (4), 939–954.

7. Xu, B.; Qian, D.; Wang, Z.; Meng, Y. S. Recent Progress in Cathode Materials Research for Advanced Lithium Ion Batteries. *Mater. Sci. Eng. R Reports* **2012**, *73* (5-6), 51–65.

8. Zhang, W.-J. A Review of the Electrochemical Performance of Alloy Anodes for Lithium-Ion Batteries. *J. Power Sources* **2011**, *196* (1), 13–24.

9. Bogart, T. D.; Chockla, A. M.; Korgel, B. A. High Capacity Lithium Ion Battery Anodes of Silicon and Germanium. *Curr. Opin. Chem. Eng.* **2013**, *2* (3), 286–293.

10. Liu, X. H.; Huang, J. Y. In Situ TEM Electrochemistry of Anode Materials in Lithium Ion Batteries. *Energy Environ. Sci.* **2011**, *4* (10), 3844.

11. Nitta, N.; Wu, F.; Lee, J. T.; Yushin, G. Li-Ion Battery Materials: Present and Future. *Mater. Today* **2015**, *18* (5), 252–264.

12. Obrovac, M. N.; Christensen, L. Structural Changes in Silicon Anodes during Lithium Insertion/Extraction. *Electrochem. Solid-State Lett.* **2004**, *7* (5), A93.

13. Yoon, S.; Park, C.-M.; Sohn, H.-J. Electrochemical Characterizations of Germanium and Carbon-Coated Germanium Composite Anode for Lithium-Ion Batteries. *Electrochem. Solid-State Lett.* **2008**, *11* (4), A42.

14. Fuller, C.; Severiens, J. Mobility of Impurity Ions in Germanium and Silicon. *Phys. Rev.* **1954**, *96* (1), 21–24.

15. Obrovac, M. N.; Krause, L. J. Reversible Cycling of Crystalline Silicon Powder. *J. Electrochem. Soc.* **2007**, *154* (2), A103.

16. Liu, X. H.; Liu, Y.; Kushima, A.; Zhang, S.; Zhu, T.; Li, J.; Huang, J. Y. In Situ TEM Experiments of Electrochemical Lithiation and Delithiation of Individual Nanostructures. *Adv. Energy Mater.* **2012**, *2* (7), 722–741.

17. Wang, J. W.; He, Y.; Fan, F.; Liu, X. H.; Xia, S.; Liu, Y.; Harris, C. T.; Li, H.; Huang, J. Y.; Mao, S. X.; Zhu, T. Two-Phase Electrochemical Lithiation in Amorphous Silicon. *Nano Lett.* **2013**, *13* (2), 709–715.

18. Graetz, J.; Ahn, C. C.; Yazami, R.; Fultz, B. Nanocrystalline and Thin Film Germanium Electrodes with High Lithium Capacity and High Rate Capabilities. *J. Electrochem. Soc.* **2004**, *151* (5), A698.

19. Laforge, B.; Levan-Jodin, L.; Salot, R.; Billard, a. Study of Germanium as Electrode in Thin-Film Battery. *J. Electrochem. Soc.* **2008**, *155* (2), A181.

20. Baggetto, L.; Notten, P. H. L. Lithium-Ion (De)Insertion Reaction of Germanium Thin-Film Electrodes: An Electrochemical and In Situ XRD Study. *J. Electrochem. Soc.* **2009**, *156* (3), A169.

21. Chan, C. K.; Peng, H.; Liu, G.; McIlwrath, K.; Zhang, X. F.; Huggins, R. A.; Cui, Y. High-Performance Lithium Battery Anodes Using Silicon Nanowires. *Nat. Nanotechnol.* **2008**, *3* (1), 31–35.

22. Chockla, A. M.; Harris, J. T.; Akhavan, V. A.; Bogart, T. D.; Holmberg, V. C.; Steinhagen, C.; Mullins, C. B.; Stevenson, K. J.; Korgel, B. A. Silicon Nanowire Fabric as a Lithium Ion Battery Electrode Material. *J. Am. Chem. Soc.* **2011**, *133* (51), 20914–20921.

23. Chockla, A. M.; Klavetter, K. C.; Mullins, C. B.; Korgel, B. a. Solution-Grown Germanium Nanowire Anodes for Lithium-Ion Batteries. *ACS Appl. Mater. Interfaces* **2012**, *4* (9), 4658–4664.

24. Wu, H.; Cui, Y. Designing Nanostructured Si Anodes for High Energy Lithium Ion Batteries. *Nano Today* **2012**, 414–429.

25. Huang, J. Y.; Zhong, L.; Wang, C. M.; Sullivan, J. P.; Xu, W.; Zhang, L. Q.; Mao, S. X.; Hudak, N. S.; Liu, X. H.; Subramanian, A.; Fan, H.; Qi, L.; Kushima, A.; Li, J. In Situ Observation of the Electrochemical Lithiation of a Single SnO_2 Nanowire Electrode. *Science* **2010**, *330* (6010), 1515–1520.

26. Liu, X. H.; Zheng, H.; Zhong, L.; Huang, S.; Karki, K.; Zhang, L. Q.; Liu, Y.; Kushima, A.; Liang, W. T.; Wang, J. W.; Cho, J.-H.; Epstein, E.; Dayeh, S. a; Picraux, S. T.; Zhu, T.; Li, J.; Sullivan, J. P.; Cumings, J.; Wang, C.; Mao, S. X.; Ye, Z. Z.; Zhang, S.; Huang, J. Y. Anisotropic Swelling and Fracture of Silicon Nanowires during Lithiation. *Nano Lett.* **2011**, *11* (8), 3312–3318.

27. Lee, S.; McDowell, M.; Choi, J.; Cui, Y. Anomalous Shape Changes of Silicon Nanopillars by Electrochemical Lithiation. *Nano Lett.* **2011**, 3034–3039.

28. Liu, X. H.; Huang, S.; Picraux, S. T.; Li, J.; Zhu, T.; Huang, J. Y. Reversible Nanopore Formation in Ge Nanowires during Lithiation-Delithiation Cycling: An in Situ Transmission Electron Microscopy Study. *Nano Lett.* **2011**, *11* (9), 3991–3997.

29. Lee, S. W.; Ryu, I.; Nix, W. D.; Cui, Y. Fracture of Crystalline Germanium during Electrochemical Lithium Insertion. *Extrem. Mech. Lett.* **2015**, *2*, 15–19.

30. Chan, M. K. Y.; Long, B. R.; Gewirth, A. a.; Greeley, J. P. The First-Cycle Electrochemical Lithiation of Crystalline Ge: Dopant and Orientation Dependence and Comparison with Si. *J. Phys. Chem. Lett.* **2011**, *2* (24), 3092–3095.

31. Chou, C.-Y.; Hwang, G. S. On the Origin of Anisotropic Lithiation in Crystalline Silicon over Germanium: A First Principles Study. *Appl. Surf. Sci.* **2014**, *323*, 78–81.

32. Liu, X. H.; Zhong, L.; Huang, S.; Mao, S. X.; Zhu, T.; Huang, J. Y. Size-Dependent Fracture of Silicon Nanoparticles during Lithiation. *ACS Nano* **2012**, *6* (2), 1522–1531.

33. Liang, W.; Yang, H.; Fan, F.; Liu, Y.; Liu, X. H.; Huang, J. Y.; Zhu, T.; Zhang, S. Tough Germanium Nanoparticles under Electrochemical Cycling. *ACS Nano* **2013**, *7* (4), 3427–3433.

Chapter 9: Fast Lithiation and Pore Evolution in Silicon Nanowires with High Concentrations of Tin[***]

9.1 INTRODUCTION

Lithium ion batteries (LIBs) are the dominant power source for portable electronic devices. However, to power electric vehicles or store energy for electrical power grids, LIBs need significantly higher energy density, better power performance and longer cycle life.[1-3] Efforts have been made to develop more advanced electrolytes[4,5] and electrodes with higher energy density.[6-11] Of the possible negative electrodes, or anodes, silicon (Si) offers the highest gravimetric and volumetric capacity (3579 mA h g^{-1}, 8334 A h L^{-1}, when fully lithiated to $Li_{15}Si_4$ at room temperature), only second to lithium metal, and is considered to be a promising replacement or complement for graphite.[12] One of the biggest problems with Si, however, is that it undergoes a massive volume change—of about ~280%—to become fully lithiated.[13] Nanoscale Si can largely tolerate this huge volume change,[10,14-22] but stabilizing battery performance over long periods of time is still a challenge.

There are several reasons for fade in Si electrode performance, not only the loss of structural integrity of the Si over time, which include the irreversible loss of lithium in unstable solid-electrolyte-interface (SEI) layers and a loss of electrical connectivity and mechanical integrity of the electrode layer due to its continual volume expansion and contraction.[23] With respect to the integrity of the electrode layer, Si nanowires have an advantage over nanoparticles, as they provide not only a resistance to fracture but also a continuous path for lithium uptake and electrical conductivity that can help improve battery performance.[12,15,24-26] However, intrinsic Si nanowires also have a very low

[***] Manuscript submitted to *ACS Applied Materials & Interfaces*: Lu, X. T.; Bogart, T. D.; Gu, M; Wang, C. M. and Korgel, B. A. Fast Lithiation and Pore Evolution in Silicon Nanowires with High Concentrations of Tin

electrical conductivity that can hamper the full lithiation of the electrode layer, especially in relatively thick, slurry-cast electrode layers.[16,17,27] The electrical conductivity of Si nanowires can be increased for better LIB performance by adding electrically-active dopants[28] or carbon coatings.[25,29-31] The addition of Sn to Si nanowires has also been shown improve the cycling performance of Si nanowires.[18,32-34] We recently showed that Sn can be incorporated into Si nanowires at relatively high concentrations[35] and that these nanowires exhibited significantly better performance than intrinsic Si nanowires in a LIB: slurry-cast electrode layers of Sn-containing Si nanowires exhibited relatively high capacity (~1 A h/cm^2 at the rate of 1*C* for 100 cycles) without any added conductive carbon.[33] Here, we report *in situ* TEM studies of Si nanowires with large concentrations of Sn undergoing very fast lithiation and delithiation. We find that the extremely fast delithiation rates lead to pore formation in the nanowires, and that this pore formation process is reversible: lithiation leads to a refilling of the pores and subsequent delithiation leads to their reappearance.

The evolution of pores has been observed by in germanium (Ge) nanowires *in situ* TEM during delithiation,[35] and in Si nanoparticles.[36] Pores have also been observed in Si nanowires after disassembling coin cell batteries after many charge/discharge cycles,[37] but their formation has never been observed directly by *in situ* TEM. The pores evolve as a result of rapid dealloying kinetics—essentially, pores form when the rate of Li diffusion out of the nanowire greatly exceeds the rate of Ge (or Si) self-diffusion to fill the vacancies created by the loss of Li.[35] Si lithiates (and delithiates) at a much slower rate than Ge,[38] making the direct observation of pore formation much less likely. The formation of pores in the Sn-containing Si nanowires, however, is consistent with much faster delithiation rates compared to intrinsic Si nanowires. We found that pore formation could be slowed significantly by coating the nanowires with a shell of amorphous Si (a-

Si). These still exhibited fast lithiation/delithiation rates in the nanowire core, but the shell largely prevented pore formation.

9.2 Experimental Details

9.2.1 Materials

All reagents and solvents were used as received without further purification. Toluene (anhydrous, 99.8%), ethanol (EtOH, 99.9%), chloroform, bis(bis(trimethylsilyl)amino)tin ($Sn(hmds)_2$, lot10396PKV, 99.8%), ethylene carbonate (EC, 99%), diethyl carbonate (DEC, ≥99%, anhydrous), lithium hexafluorophosphate ($LiPF_6$, ≥99.99%), alginic acid sodium salt (NaAlg), polyacrylic acid (PAA, Mv~450,000) were purchased from Sigma-Aldrich. Trisilane (Si_3H_8, 100%) was purchased from Voltaix.Fluoroethylene carbonate (FEC, >98%) was purchased from TCI America and Li metal foil (1.5 mm 99.9%) was purchased from Alfa Aesar. Conductive carbon super C65 was supplied by TIMCAL and Celgard 2400 membranes (25μm) were provided by Celgard. Copper foil (9 μm thick) and coin cells (2032 stainless steel) were purchased from MTI Corporation. Si nanowires were prepared by supercritical fluid-liquid-solid (SFLS) growth in toluene with trisilane and $Sn(hmds)_2$ using the procedure we have previously described.[35]

9.2.2 *In Situ* TEM Lithiation of Si Nanowires

Electrochemical experiments with *in situ* TEM imaging were performed on the Nanofactory TEM holder in a Titan 80-300™ scanning/transmission electron microscope (S/TEM).[34] Si nanowires are dropped on a gold wire working electrode; lithium metal on a tungsten wire counter electrode, a native Li_2O layer worked as a solid-state electrolyte. Inside the TEM, the Li/Li_2O electrode is moved by a piezo-positioner to touch the Si

nanowire. Once a connection is made, a bias of -2 V is applied to initiate lithiation. Delithiaton is carried out by applying a bias of 2V. The beam intensity was minimized during imaging to avoid significant beam effects.

9.2.3 Coin Cell Battery Tests

Si nanowire slurries were prepared by mixing 80 mg of Si nanowires with PAA, NaAlg, and conductive carbon in a 7:1:1:1 weight ratio in 2 mL of ethanol and 2 mL of DI-H_2O followed by probe sonication. The slurry was doctor-bladed (200 μm gap) onto a Cu foil and dried in air. The films were then heated to 150ºC under vacuum overnight. Individual 11 mm diameter circular electrodes were hole-punched from the coated Cu foil. Typical mass loadings were 0.5-1.0 mg cm^{-2}. Coin cells (2032 stainless steel) were assembled in an argon-filled glovebox (<0.1 ppm O_2) using Li foil as the counter electrode and 1.0 M $LiPF_6$ in 1:1 w/w EC:DEC with 5 wt% FEC as the electrolyte. The coin cell was crimped and removed from the glovebox for testing with an Arbin BT-2143 test unit cycling between 2.0 V and 0.01 V vs Li/Li^+.

9.2.4 *Ex Situ* TEM Characterization of Si Nanowires

For TEM analysis of the nanowires after cycling, the coin cells were disassembled in an argon-filled glovebox. The Cu foil covered with nanowires was soaked in DEC overnight and then rinsed with toluene. The nanowires were removed from the Cu foil by bath sonication and redispersed in chloroform and drop-cast onto a 200 mesh copper lacey carbon TEM grid (Electron Microscopy Science). TEM images were obtained using a FEI Tecnai Spirit Bio Twin operated at 80 kV.

9.3 Results and Discussions

9.3.1 Fast Lithiation in Sn-incorporated Si Nanowires

Crystalline Si nanowires were synthesized with a high concentration of Sn either with (c-@a-Si) or without (c-Si) a shell of amorphous Si using previously reported methods.[29,35] Figure 9.2 shows a scanning transmission electron microscopy (STEM) high-angle annular dark-field (HAADF) image of a c-Si nanowire and corresponding STEM-EELS elemental maps of Si and Sn. Sn is distributed across the nanowire, incorporating both into the core and depositing as nanoparticles on the surface. The Sn nanoparticles appear as bright dots in the STEM-HAADF image in Figure 9.2 and dark dots in the bright field TEM images in Figure 9.3. The c-Si and c-@a-Si nanowires studied by *in situ* TEM had approximately 10 at% and 3 at% Sn, respectively.

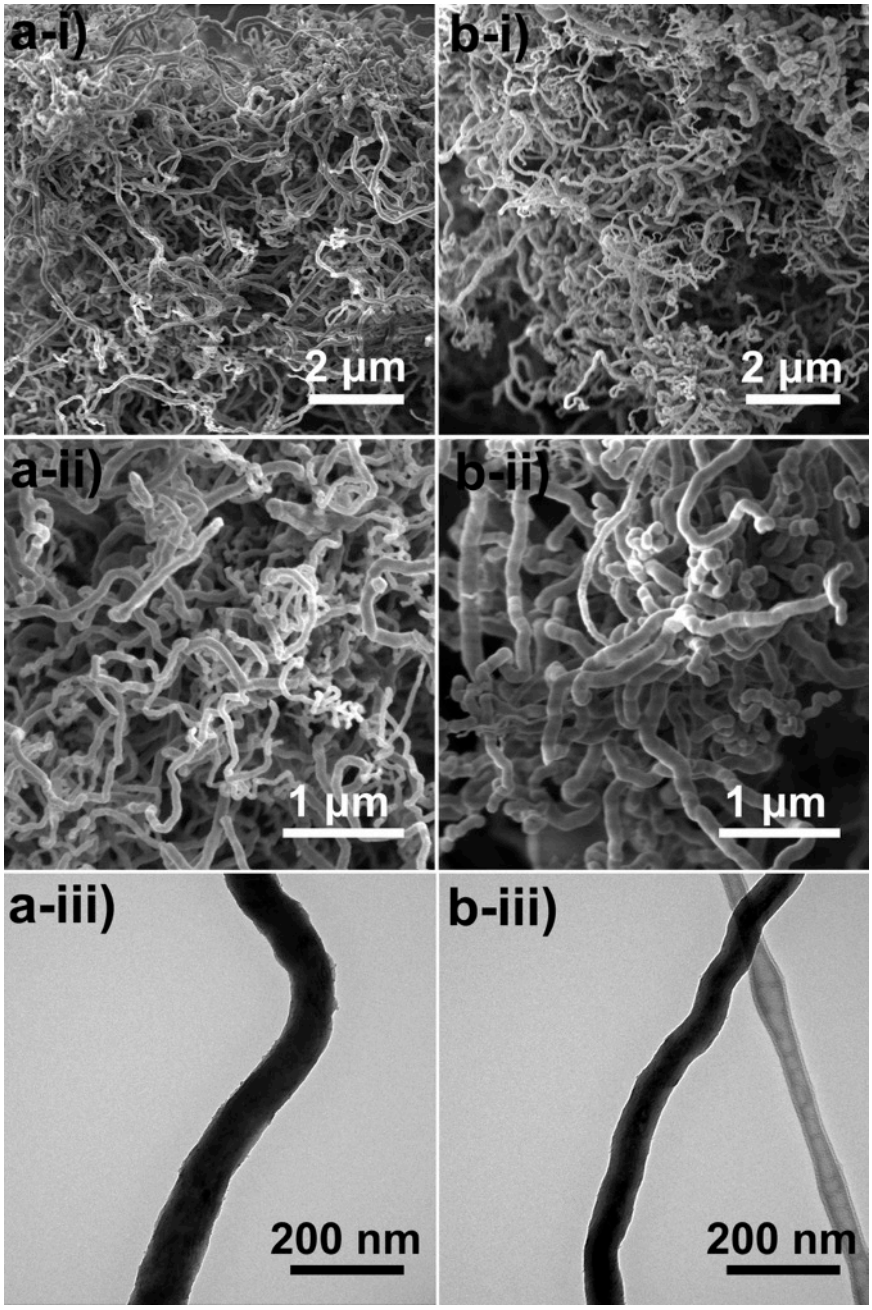

Figure 9.1 SEM and TEM images of Si nanowires made with different Si:Sn mole ratios. The SEM images in (a-i) and (a-ii) and TEM image in (a-iii) show the nanowires made with a Si:Sn mole ratio of 20:1. These nanowires have crystalline cores with no amorphous Si shell. The SEM images in (b-i) and (b-ii) and TEM image in (b-iii) show nanowires made with a Si:Sn mole ratio of 40:1. These nanowires have a crystalline core and an amorphous Si shell.

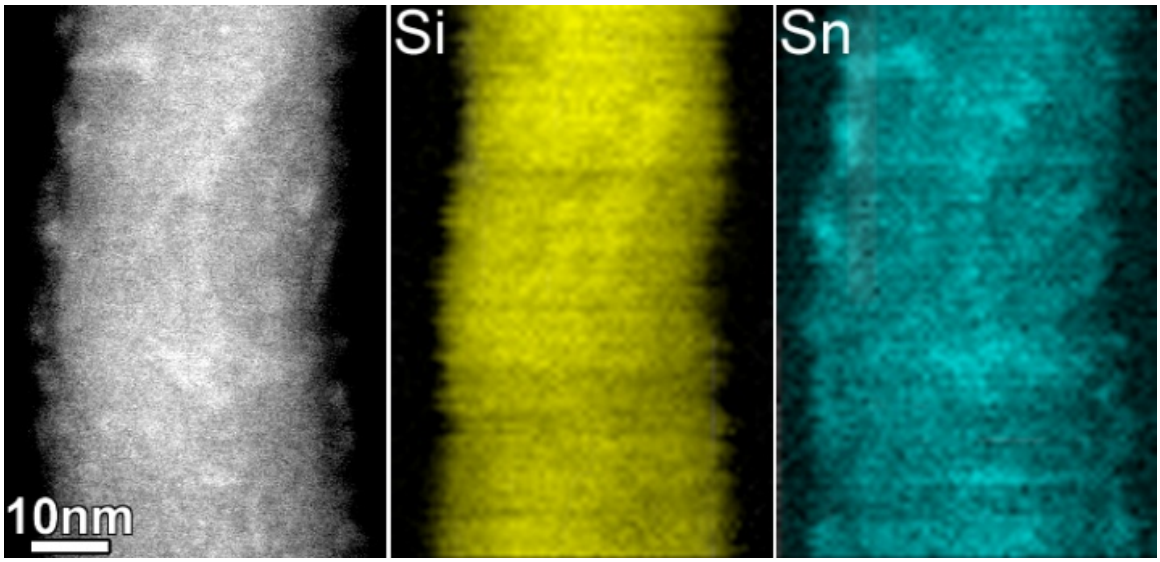

Figure 9.2 (Left) STEM HAADF image of a segment of a c-Si nanowire with associated EELS maps of (Middle) Si and (Right) Sn. Based on EDS, the Si nanowire has 10 at.% Sn.

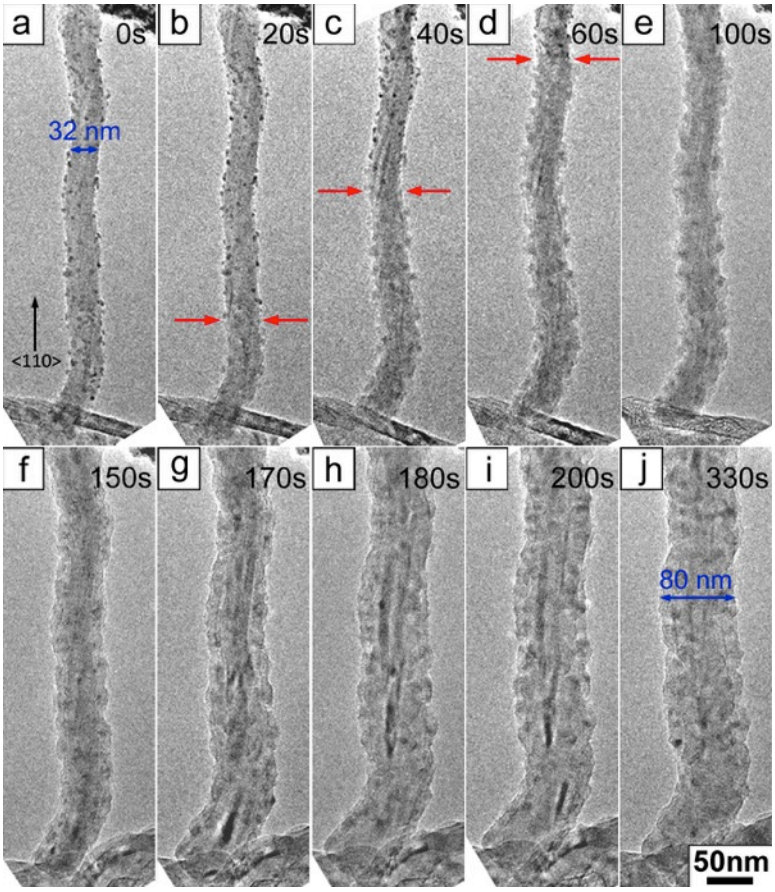

Figure 9.3 *In situ* TEM observation of a c-Si nanowire with 10 at.% Sn undergoing an initial lithiation cycle. The time when each image was taken is shown. Initially, in (a-e), lithiation begins on the nanowire surface. The Sn nanoparticles on the nanowire surface are used to mark the Li diffusion front as it propagates down the nanowire (yellow arrows). After the surface becomes saturated with Li, the lithiation front gradually moves towards the center of the nanowire and the nanowire diameter expands from 32 nm to 80 nm as shown in (f-g).

Figures 9.3a-j show the microstructural evolution of a c-Si nanowire with about 10 at.% Sn observed by *in situ* TEM during an initial lithiation cycle. Lithiation was initiated by applying a bias of -2 V vs Li. As observed in Figures 9.3a-e, lithiation occurs initially along the nanowire surface. Once the surface is saturated, the lithium diffusion front evolves into the core of the nanowire, as shown in Figures 9.3f-j. A similar

progression of rapid surface and interface diffusion preceding bulk lithiation has been observed before in other materials, such as a-Si coated carbon fibers.[39]

The surface diffusivity of Li was calculated using the Sn nanoparticles as markers to follow the Li diffusion front. The Sn nanoparticles swell as they lithiate, which decreases their imaging contrast. The pair of red arrows in Figures 9.3b-d shows the position of the Li diffusion front as it moves down the length of the nanowire. The surface diffusivity of Li on the Si nanowire is 1.5×10^{-11} cm^2/s. To compare this to a typical diffusion rate of Li in Si, a volume diffusivity can be estimated by considering the energy gain of Li when it diffuses from the surface to the core of the nanowire of ~0.2 eV,[40] giving a volume diffusivity of Li in Si of $\sim10^{-12}$ cm^2/s. This is two orders of magnitude higher than the diffusion coefficient of dilute Li in bulk Si, $\sim3\times10^{-14}$ cm^2/s.[41]

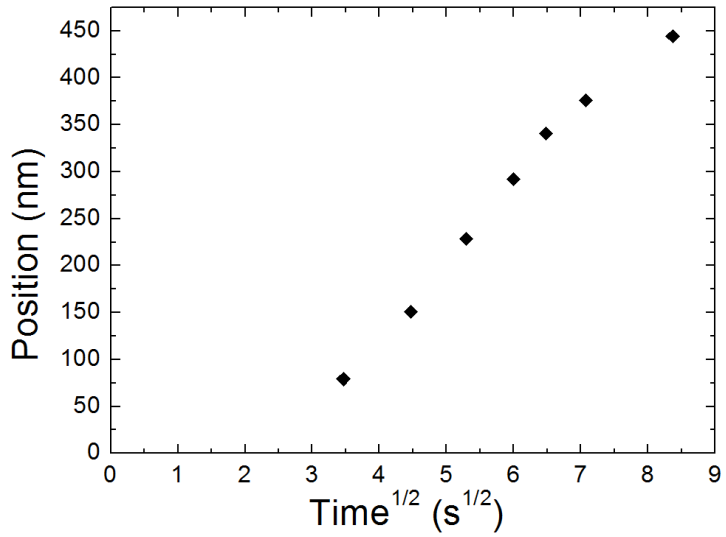

Figure 9.4 The position of the Li surface diffusion front plotted versus $t^{1/2}$. The diffusion coeffecient D, calculated from Fick's second law, $x(t) = 2\sqrt{D\,t}$, is $D=1.5\times10^{11}$ cm^2/s.

After 100 sec of lithiation, the nanowire in Figure 9.3 begins to expand as the core of the nanowire begins to be lithiated and converted to amorphous Li_xSi. Such a sequential core-into-shell progression of lithiation is known to occur for crystalline Si nanowires; however, the Li diffusion front is typically tapered, indicating that the surface Li diffusion in the axial direction occurs at about the same rate as the radial diffusion of Li into the core of the nanowire.[11,27] The Sn-containing Si nanowires do not exhibit such a tapered diffusion front and it appears that the rate of Li diffusion on the nanowire surface is much faster than the rate of lithiation into the core of the nanowire. Nonetheless, the core lithiation rate of the Sn-containing nanowires is still significantly faster than the lithiation rate of intrinsic Si nanowires. For example, the lithiation rate of the nanowire in Figure 9.3 is 280 nm h^{-1}, which is comparable to the lithitation rate of Ge nanowires[35] and much faster than the typical lithiation rate of 35 nm h^{-1} for intrinsic crystalline Si nanowires.[31] So, the lack of significant tapering of the diffusion front is mostly the result of the extremely fast surface diffusion rate.

The nanowire in Figure 9.3 has become fully lithiated after 330 sec. The fully lithiated nanowire shown in Figure 9.3j has a diameter of 80 nm. Considering that the initial diameter of the nanowire was 32 nm, the volume of the nanowire has expanded by 276%, which is very close to the expected value for the fully-lithiated phase of $Li_{15}Si_4$.

9.3.2 Pore Formation

After a third delithiation cycle, the nanowire begins to evolve pores. Figure 9.5a-i shows a segment of the nanowire in a lithiated state and Figure 9.5b-i shows the nanowire after it has been delithiated. Pores form as lithium is removed from the nanowire. Figures 9.5c-f show snapshots of the morphology of the nanowire after the fifth and sixth lithiation/delithiation cycles. Pores are formed in the nanowire after each delithiation

event, and these pores disappear as the nanowire swells with lithium. After lithiation, the pores have disappeared in the nanowire, except near the surface. In these later lithiation cycles, the diameter increase (of 120%) corresponds to a volume expansion of only 170% (compared to 280%), because of the void volume remaining within the nanowires after delithiation. The Si still fully lithiates and exhibits the expected volume expansion, but the nanowire diameter does not need to expand as much to accommodate the lithium because of the pore volume in the core of the nanowire. Figures 6.5d and 6.5f show the nanowire in its delithiated state after subsequent cycles. The pores reappear in the nanowire at nearly the same location, indicating that the pores do not completely disappear when the nanowire lithiates.

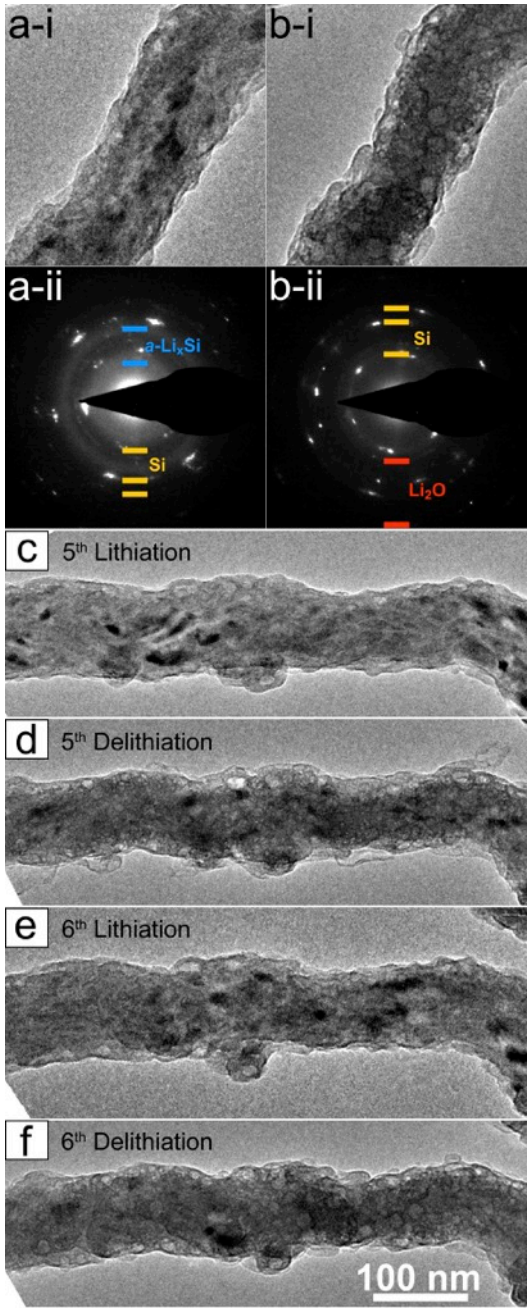

Figure 9.5 Pore evolution in a Sn-incorporated Si nanowire. (a-i) TEM image of the nanowire after lithiation and (a-ii) a corresponding EDP showing a-Li_xSi rings (labeled in blue) and unlithiated c-Si bright spots (labeled in yellow). (b-i) TEM image of the nanowire after delithiation and (b-ii) corresponding EDP showing a-Si rings and unlithiated c-Si bright spots (labeled in yellow). (c-f) shows TEM images of the Si nanowire as pores reversibly open and close during sequential lithiation and delithiation cycles.

The locations of the pores appear to be associated with domains in the nanowire that do not become fully lithiated. Even though the measured diameter expansion is consistent with nearly full lithiation of the nanowire, electron diffraction patterns (EDPs) of lithiated nanowires show rings from amorphous Li_xSi and bright spots from crystalline Si that indicate some regions of the nanowire do not get fully lithiated. Figure 9.5a-ii shows an example of a diffraction pattern taken from a region of a lithiated nanowire. Figure 9.5b-ii shows a diffraction pattern from the same region after delithiation: diffraction spots from crystalline Si are also observed. Figure 9.6 shows high-resolution TEM images of a nanowire in its lithiated and delithiated states with observable crystalline domains in each structure. These non-lithiated regions are the result of lithiation-induced stresses in the nanowire, which are known to limit the extent of lithiation in nanowires.[42] Previous reports of this behavior in Si nanowires have shown unreacted crystal domains with a staircase-like appearance.[43] In the Sn-containing Si nanowires studied here, the unreacted grains appear as randomly-dispersed islands surrounded by amorphous Li_xSi.

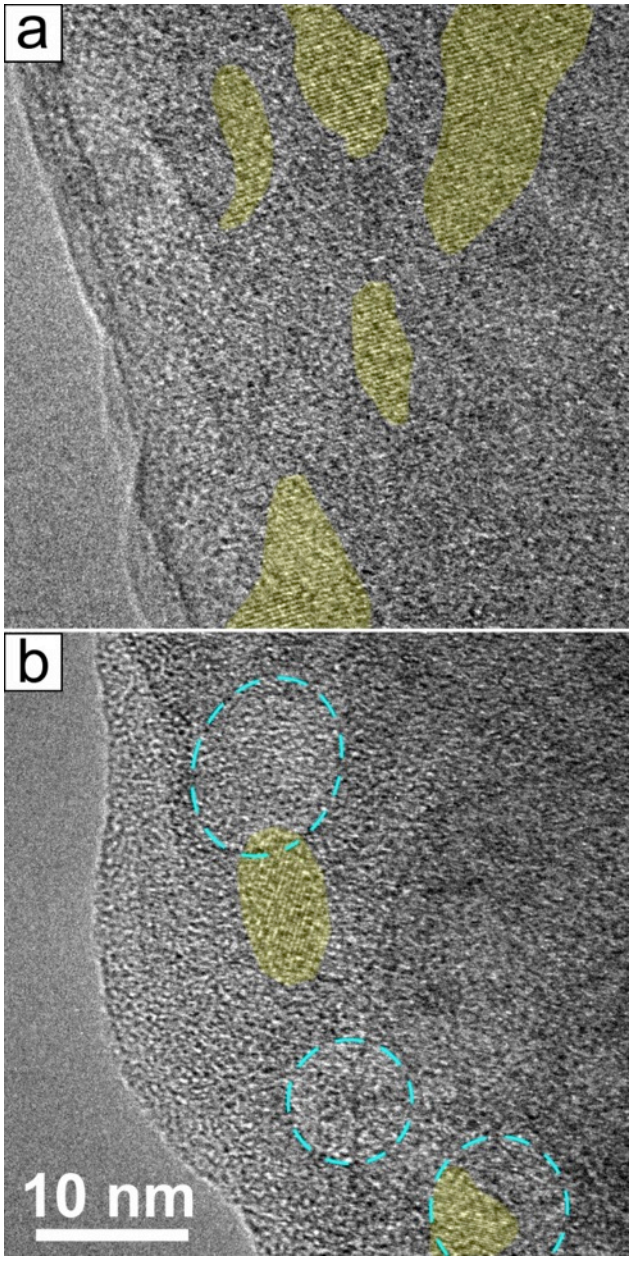

Figure 9.6 TEM images of a Sn-incorporated Si nanowire that has been (a) lihitated and (b) delithiated with unlithiated regions highlighted in yellow and pores in the delithiated nanowire identified with blue dashes.

Pore formation has been observed in various dealloying systems, including Li-Sn[44] and Ag-Au.[45] Pores result from the aggregation of vacancies that form during the phase separation or dealloying process when the diffusion rate of the out-diffusing species is much faster than the atomic diffusion rate of the host material. Pore formation has also been observed by *in situ* TEM of lithiated Ge nanowires that are undergoing delithiation.[35] In Ge, the rate of Li diffusion is much faster than Ge atom diffusion. Thus far, pore formation has not been observed by *in situ* TEM studies of delithiating Si nanowires because of the relatively slow Li diffusion rates in Si, which provide vacancies sufficient time to migrate to the nanowire surface or to be filled with Si atoms before nucleating a hole. Pore formation is observed in these Sn-containing Si nanowires because of the significantly increased Li diffusion rate.

There are still noticeable differences in the way pores form in the Sn-containing Si nanowires compared to Ge nanowires. First, the pores in the Si nanowires do not show up in the first lithiation/delithiation cycle. The pores do not become obvious until several charging/discharging cycles have been completed. Another difference is that there is no distinct delithiation front to clearly differentiate the delithiated porous region from the lithiated nonporous region in Si nanowires as there is in Ge nanowires.[35] The pore formation process in the Si nanowires appears to have slower kinetics than in the Ge nanowires. The other major difference is that nanocrystalline domains are still detected in the Si nanowires after lithiation/delilthiation cycles have been completed, as shown in Figure 9.6. These crystal grains prevent uniform structural changes in the nanowires and lead to an accumulation of stresses in the nanowire that can ultimately lead to pore formation.

Figure 9.7 illustrates this mechanism of pore formation in Sn-containing Si nanowires. First of all, the Si nanowires studied here have a variety of defects. Most of

the nanowires are not straight and contain defects that give rise to a torturous morphology. These defects include line and plane defects that can provide channels for fast Li diffusion.[39,46] A gathering of Sn along these defects can further increase Li diffusivity.[47] Such Li diffusion channels would naturally lead to domains of Si that do not get lithiated, thus creating a compressive stress in the nanowire and an intensified hoop tension[48] that eventually leads to crack formation. During delithitation, some vacancies migrate to the cracks and form pores. These pores increase in size after each lithiation/deslithiation cycle and finally become observable after several cycles.

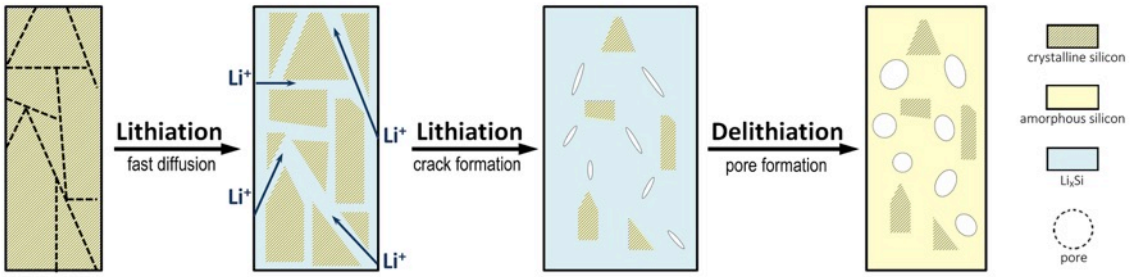

Figure 9.7 Pore formation in a crystalline Sn-containing Si nanowire. Fast Li diffusion along defects, including dislocations and twin boundaries, leaves crystalline domains that do not lithiate due to the buildup of stress. Intensified hoop tension around the unlithiated nanocrystalline domains then lead to cracks during lithiation. Pores appear in the cracked sites when Li ions are extracted and the nanowire shrinks. These pores become obvious after several lithiation/delithiation cycles.

Coating the Sn-containing nanowires with an amorphous Si shell (i.e., c-@a-Si nanowires) was found to significantly slow the formation of pores. High lithiation and delithiation rates were still observed in the c-@a-Si nanowires by *in situ* TEM, similar to the c-Si nanowires. For example, a complete charge/discharge cycle only took 150 s to complete in the segment in the field of view. But no pore formation was observed in

these nanowires, even after ten lithiation/delithiation cycles. The structural stability of the nanowires probably results from the isotropic expansion of the amorphous shell, which can counter the anisotropic expansion of the crystalline core that has been observed in Si nanowires during initial lithiation cycles.[49] The lithiated shell also exerts a uniform compressive stress onto the core that can help promote isotropic lithiation of the crystalline core.[50] This compressive stress also counters the expansion of the core and buffers the tension buildup around unreacted crystalline domains in the core, preventing the early appearance of pores.

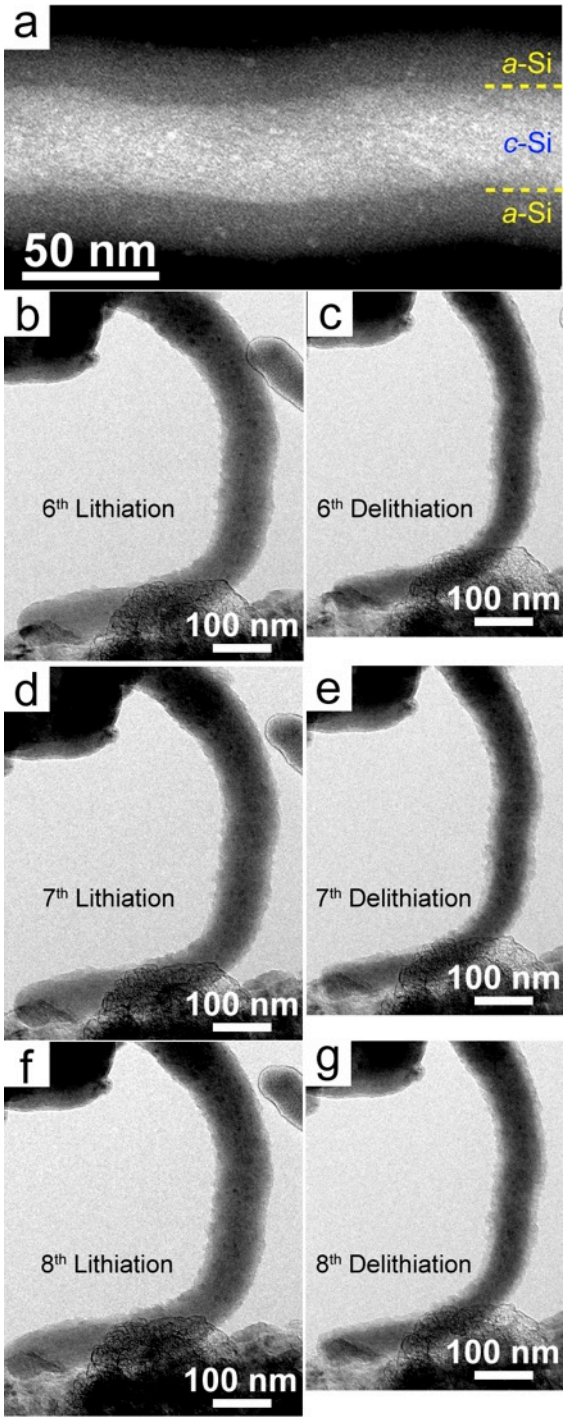

Figure 9.8 (a) STEM HAADF image of a crystalline Si nanowire containing Sn with an amorphous shell (c-Si@a-Si). The amorphous shell and crystalline core are distinguished by their differing contrast. (b-g) *In situ* TEM images of the nanowire undergoing three lithiation/delithiation cycles.

9.3.3 *Ex Situ* TEM Characterization

Post-mortem TEM characterization of Sn-incorporated Si nanowires was carried out after coin cell battery tests for comparison with *in situ* observations. Coin cells were made with nanowire slurries containing poly(acrylic acid) (PAA), sodium alginate (NaAlg) and conductive carbon cast onto Cu foil. The nanowires were cycled against Li metal in a half-cell at a relatively slow rate of C/10 for the first cycle and then at 1C for the remaining cycles. The batteries were stopped in the delithiated state and disassembled for imaging. Figures 9.9a and 9.9b show TEM images of crystalline Si nanowires with and without an amorphous Si shell after the first cycle of C/10. Both types of nanowires become amorphous after the initial cycle. After ten cycles at 1C, there is a noticeable difference in morphology between the two types of nanowires. The c-Si nanowires exhibit many small cavities (Figure 9.9c); whereas, the c-@a-Si nanowires did not show any visible pores, and the core-shell structure was largely unaffected (Figure 9.9d). After 100 cycles, the c-Si nanowires have become extremely porous (Figure 9.9e), similar to what was observed by *in situ* TEM after five cycles. This indicates that the result of the *in sit*u battery test is consistent with the *ex situ* test, while the cycle rate is much higher in the *in situ* TEM experiment setup and the structural evolution is accelerated with exposure to high energy electron beam.[51] The core-shell structure of the c-@a-Si nanowires was still visible after 100 cycles, as shown in Figure 9.9f. The shell has become porous, but the core is still relatively non-porous. This architecture appears to be useful for batteries and exhibits better stability, as also reflected by the slower loss of charge capacity compared to the c-Si nanowires after 100 electrochemical cycles in our previous publication.[33]

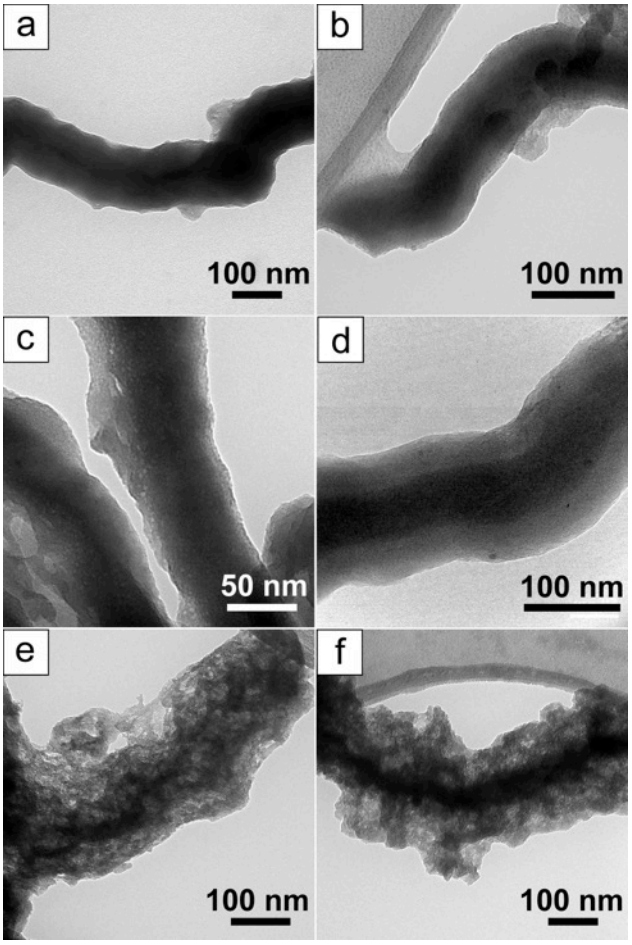

Figure 9.9 TEM images of Sn-incorporated Si nanowires with and without amorphous shells extracted in the delithiated state from half cells after cycling at a rate of 1C: (a) c-Si and (b) c-@a-Si nanowires after 1 cycle; (c) c-Si and (d) c-@a-Si nanowires after 10 cycles; (e) c-Si and (f) c-@a-Si nanowires after 100 cycles.

9.4 CONCLUSIONS

Very fast lithiation and pore formation was observed by *in situ* TEM of lithiating and delithiating Si nanowires containing high concentrations of Sn. The average lithiation rate was 280 nm h^{-1}, which is nearly an order of magnitude faster than the lithiation rate of intrinsic crystalline Si nanowires. The application of an amorphous Si shell on the

nanowires significantly limited the rate of pore formation while still retaining fast lithiation/delithiation kinetics. The shell-coated nanowires did not exhibit pore formation in the *in situ* TEM measurements, even after ten cycles of lithiation and delithiation, and *ex situ* TEM images of nanowires cycled in coin cell batteries showed that the rate of pore formation was significantly slowed by the application of the shell. These results further demonstrate that the incorporation of Sn in Si nanowires can provide significantly enhanced lithium ion battery performance for Si electrodes, with enhanced rate capability while retaining high capacity, even alleviating the need to add carbon to the electrode layer.

9.5 Acknowledgements

This work was funded by the Robert A. Welch Foundation (grant no. F-1464), the National Science Foundation (grant no. CHE-1308813) and as part of the program "Understanding Charge Separation and Transfer at Interfaces in Energy Materials," the Energy Frontier Research Center (EFRC: CST) funded by the U.S. Department of Energy Office of Science, Office of Basic Energy Sciences, under Award No. DE-SC0001091. CMW and MG acknowledge the support of the Assistant Secretary for Energy Efficiency and Renewable Energy, Office of Vehicle Technologies of the U.S. Department of Energy under Contract No. DE-AC02-05CH11231, Subcontract No. 6951379 under the advanced Batteries Materials Research (BMR) Program.The *in situ* TEM was conducted in the William R. Wiley Environmental Molecular Sciences Laboratory (EMSL), a national scientific user facility sponsored by DOE's Office of Biological and Environmental Research and located at PNNL. PNNL is operated by Battelle for the Department of Energy under Contract DE-AC05-76RLO1830.

9.6 REFERENCES

1. Tarascon, J. M.; Armand, M. Issues and Challenges Facing Rechargeable Lithium Batteries. *Nature* **2001**, *414*, 359–367.

2. Goodenough, J. B.; Kim, Y. Challenges for Rechargeable Li Batteries. *Chem. Mater.* **2010**, *22*, 587–603.

3. Etacheri, V.; Marom, R.; Elazari, R.; Salitra, G.; Aurbach, D. Challenges in the Development of Advanced Li-Ion Batteries: A Review. *Energy Environ. Sci.* **2011**, *4*, 3243.

4. Aurbach, D.; Talyosef, Y.; Markovsky, B.; Markevich, E.; Zinigrad, E.; Asraf, L.; Gnanaraj, J. S.; Kim, H. J. Design of Electrolyte Solutions for Li and Li-Ion Batteries: A Review. *Electrochim. Acta* **2004**, *50*, 247–254.

5. Chockla, A. M.; Bogart, T. D.; Hessel, C. M.; Klavetter, K. C.; Mullins, C. B.; Korgel, B. A. Influences of Gold, Binder and Electrolyte on Silicon Nanowire Performance in Li-Ion Batteries. *J. Phys. Chem. C* **2012**, *116*, 18079-18086.

6. Marom, R.; Amalraj, S. F.; Leifer, N.; Jacob, D.; Aurbach, D. A Review of Advanced and Practical Lithium Battery Materials. *J. Mater. Chem.***2011**, *21*, 9938.

7. Fergus, J. W. Recent Developments in Cathode Materials for Lithium Ion Batteries. *J. Power Sources* **2010**, *195*, 939–954.

8. Xu, B.; Qian, D.; Wang, Z.; Meng, Y. S. Recent Progress in Cathode Materials Research for Advanced Lithium Ion Batteries. *Mater. Sci. Eng. R Reports* **2012**, *73*, 51–65.

9. Zhang, W.-J. A Review of the Electrochemical Performance of Alloy Anodes for Lithium-Ion Batteries. *J. Power Sources* **2011**, *196*, 13–24.

10. Bogart, T. D.; Chockla, A. M.; Korgel, B. A. High Capacity Lithium Ion Battery Anodes of Silicon and Germanium. *Curr. Opin. Chem. Eng.* **2013**, *2*, 286–293.

11. Liu, X. H.; Huang, J. Y. In Situ TEM Electrochemistry of Anode Materials in Lithium Ion Batteries. *Energy Environ. Sci.* **2011**, *4*, 3844.

12. Wu, H.; Cui, Y. Designing Nanostructured Si Anodes for High Energy Lithium Ion Batteries. *Nano Today* **2012**, 414–429.

13. Obrovac, M. N.; Christensen, L. Structural Changes in Silicon Anodes during Lithium Insertion/Extraction. *Electrochem. Solid-State Lett.* **2004**, *7*, A93.

14. Obrovac, M. N.; Krause, L. J. Reversible Cycling of Crystalline Silicon Powder. *J. Electrochem. Soc.* **2007**, *154*, A103.

15. Chan, C. K.; Peng, H.; Liu, G.; McIlwrath, K.; Zhang, X. F.; Huggins, R. A.; Cui, Y. High-Performance Lithium Battery Anodes Using Silicon Nanowires. *Nat. Nanotechnol.* **2008**, *3*, 31–35.

16. Chockla, A. M.; Harris, J. T.; Akhavan, V. A.; Bogart, T. D.; Holmberg, V. C.; Steinhagen, C.; Mullins, C. B.; Stevenson, K. J.; Korgel, B. A. Silicon Nanowire Fabric as a Lithium Ion Battery Electrode Material. *J. Am. Chem. Soc.* **2011**, *133*, 20914–20921.

17. Chan, C. K.; Patel, R. N.; O'Connell, M. J.; Korgel, B. A.; Cui, Y. Solution-Grown Silicon Nanowires for Lithium-Ion Battery Anodes. *ACS Nano* **2010**, *4*, 1443–1450.

18. Chockla, A. M.; Klavetter, K. C.; Mullins, C. B.; Korgel, B. A. Tin-Seeded Silicon Nanowires for High Capacity Li-Ion Batteries. *Chem. Mater.* **2012**, *24*, 3738–3745.

19. Lee, S.; McDowell, M.; Choi, J.; Cui, Y. Anomalous Shape Changes of Silicon Nanopillars by Electrochemical Lithiation. *Nano Lett.* **2011**, 3034–3039.

20. Yang, H.; Huang, S.; Huang, X.; Fan, F.; Liang, W.; Liu, X. H.; Chen, L.-Q.; Huang, J. Y.; Li, J.; Zhu, T.; Zhang, S. Orientation-Dependent Interfacial Mobility Governs the Anisotropic Swelling in Lithiated Silicon Nanowires. *Nano Lett.* **2012**, *12*, 1953–1958.

21. Lee, S. W.; McDowell, M. T.; Berla, L. A.; Nix, W. D.; Cui, Y. Fracture of Crystalline Silicon Nanopillars during Electrochemical Lithium Insertion. *Proc. Natl. Acad. Sci. U. S. A.* **2012**, *109*, 4080–4085.

22. Kovalenko, I.; Zdyrko, B.; Magasinski, A.; Hertzberg, B.; Milicev, Z.; Burtovyy, R.; Luzinov, I.; Yushin, G. A Major Constituent of Brown Algae for Use in High-Capacity Li-Ion Batteries. *Science* **2011**, *334*, 75-79.

23. Korgel, B. A. Nanomaterials Developments for Higher-Performance Lithium Ion Batteries. *J. Phys. Chem. Lett.* **2014**, *5*, 749-750.

24. Laïk, B.; Eude, L.; Pereira-Ramos, J.-P.; Cojocaru, C. S.; Pribat, D.; Rouvière, E. Silicon Nanowires as Negative Electrode for Lithium-Ion Microbatteries. *Electrochim. Acta* **2008**, *53*, 5528–5532.

25. Huang, R.; Fan, X.; Shen, W.; Zhu, J. Carbon-Coated Silicon Nanowire Array Films for High-Performance Lithium-Ion Battery Anodes. *Appl. Phys. Lett.* **2009**, *95*, 133119.

26. Ruffo, R.; Hong, S. S.; Chan, C. K.; Huggins, R. A.; Cui, Y. Impedance Analysis of Silicon Nanowire Lithium Ion Battery Anodes. *J. Phys. Chem. C* **2009**, *113*, 11390–11398.

27. Liu, X. H.; Fan, F.; Yang, H.; Zhang, S.; Huang, J. Y.; Zhu, T. Self-Limiting Lithiation in Silicon Nanowires. *ACS Nano* **2013**, *7*, 1495–1503.

28. Kong, M.; Noh, J.; Byun, D.; Lee, J. Electrochemical Characteristics of Phosphorus Doped Silicon and Graphite Composite for the Anode Materials of Lithium Secondary Batteries. *J. Electroceramics* **2008**, *23*, 376–381.

29. Ng, S.-H.; Wang, J.; Wexler, D.; Konstantinov, K.; Guo, Z.-P.; Liu, H.-K. Highly Reversible Lithium Storage in Spheroidal Carbon-Coated Silicon Nanocomposites as Anodes for Lithium-Ion Batteries. *Angew. Chem. Int. Ed.* **2006**, *45*, 6896–6899.

30. Dimov, N.; Kugino, S.; Yoshio, M. Carbon-Coated Silicon as Anode Material for Lithium Ion Batteries: Advantages and Limitations. *Electrochim. Acta* **2003**, *48*, 1579–1587.

31. Liu, X. H.; Zhang, L. Q.; Zhong, L.; Liu, Y.; Zheng, H.; Wang, J. W.; Cho, J.-H.; Dayeh, S. A; Picraux, S. T.; Sullivan, J. P.; Mao, S. X.; Ye, Z. Z.; Huang, J. Y. Ultrafast Electrochemical Lithiation of Individual Si Nanowire Anodes. *Nano Lett.* **2011**, *11*, 2251–2258.

32. Kohandehghan, A.; Cui, K.; Kupsta, M.; Memarzadeh, E.; Kalisvaart, P.; Mitlin, D. Nanometer-Scale Sn Coatings Improve the Performance of Silicon Nanowire LIB Anodes. *J. Mater. Chem. A* **2014**, *2*, 11261-11279.

33. Bogart, T. D.; Lu, X.; Gu, M.; Wang, C.; Korgel, B. A. Enhancing the Lithiation Rate of Silicon Nanowires by the Inclusion of Tin. *RSC Adv.* **2014**, *4*, 42022–42028.

34. Bogart, T. D.; Oka, D.; Lu, X.; Gu, M.; Wang, C.; Korgel, B. A. Lithium Ion Battery Peformance of Silicon Nanowires with Carbon Skin. *ACS Nano* **2014**, *8*, 915–922.

35. Bogart, T. D.; Lu, X.; Korgel, B. A. Precision Synthesis of Silicon Nanowires with Crystalline Core and Amorphous Shell. *Dalton Trans.***2013**, *42*, 12675–12680.

36. Liu, X. H.; Huang, S.; Picraux, S. T.; Li, J.; Zhu, T.; Huang, J. Y. Reversible Nanopore Formation in Ge Nanowires during Lithiation-Delithiation Cycling: An in Situ Transmission Electron Microscopy Study. *Nano Lett.* **2011**, *11*, 3991–3997.

37. He, Y.; Piper, D. M.; Gu, M.; Travis, J. J.; George, S. M.; Lee, S.; Genc, A.; Pullan, L.; Liu, J.; Mao, S. X.; Zhang, J.; Ban, C.; Wang, C. In Situ Transmission Electron Microscopy Probing of Native Oxide and Artificial Layers on Silicon Nanoparticles for Lithium Ion Batteries. *ACS Nano* **2014**, *8*, 11816–11823.

38. Choi, J. W.; McDonough, J.; Jeong, S.; Yoo, J. S.; Chan, C. K.; Cui, Y. Stepwise Nanopore Evolution in One-Dimensional Nanostructures. *Nano Lett.* **2010**, *10*, 1409–1413.

39. Chou, C.-Y.; Kim, H.; Hwang, G. S. A Comparative First-Principles Study of the Structure, Energetics, and Properties of Li–M (M= Si, Ge, Sn) Alloys. *J. Phys. Chem. C* **2011**, *115*, 20018–20026.

40. Wang, J. W.; Liu, X. H.; Zhao, K.; Palmer, A.; Patten, E.; Burton, D.; Mao, S. X.; Suo, Z.; Huang, J. Y. Sandwich-Lithiation and Longitudinal Crack in Amorphous Silicon Coated on Carbon Nanofibers. *ACS Nano* **2012**, *6*, 9158–9167.

41. Chan, T.-L.; Chelikowsky, J. R. Controlling Diffusion of Lithium in Silicon Nanostructures. *Nano Lett*. **2010**, *10*, 821–825.

42. Pell, E. Diffusion Rate of Li in Si at Low Temperatures. *Phys. Rev*.**1960**, *119*, 1222–1225.

43. Liu, X. H.; Zhong, L.; Huang, S.; Mao, S. X.; Zhu, T.; Huang, J. Y. Size-Dependent Fracture of Silicon Nanoparticles during Lithiation. *ACS Nano* **2012**, *6*, 1522–1531.

44. Wang, L.; Liu, D.; Yang, S.; Tian, X.; Zhang, G.; Wang, W.; Wang, E.; Xu, Z.; Bai, X. Exotic Reaction Front Migration and Stage Structure in Lithiated Silicon Nanowires. *ACS Nano* **2014**, *8*, 8249–8254.

45. Chen, Q.; Sieradzki, K. Spontaneous Evolution of Bicontinuous Nanostructures in Dealloyed Li-Based Systems. *Nat. Mater*.**2013**, *12*, 1102–1106.

46. Erlebacher, J.; Aziz, M. J.; Karma, a; Dimitrov, N.; Sieradzki, K. Evolution of Nanoporosity in Dealloying. *Nature* **2001**, *410*, 450–453.

47. Fisher, J. C. Calculation of Diffusion Penetration Curves for Surface and Grain Boundary Diffusion. *J. Appl. Phys*.**1951**, *22*, 74.

48. Tersoff, J. Enhanced Solubility of Impurities and Enhanced Diffusion near Crystal Surfaces. *Phys. Rev. Lett*. **1995**, *74*, 5080–5083.

49. Liang, W.; Yang, H.; Fan, F.; Liu, Y.; Liu, X. H.; Huang, J. Y.; Zhu, T.; Zhang, S. Tough Germanium Nanoparticles under Electrochemical Cycling. *ACS Nano* **2013**, *7*, 3427–3433.

50. McDowell, M. T.; Lee, S. W.; Harris, J. T.; Korgel, B. A.; Wang, C.; Nix, W. D.; Cui, Y. In Situ TEM of Two-Phase Lithiation of Amorphous Silicon Nanospheres. *Nano Lett*.**2013**, *13*, 758–764.

51. Luo, L.; Wu, J.; Luo, J.; Huang, J.; Dravid, V. P. Dynamics of Electrochemical Lithiation/delithiation of Graphene-Encapsulated Silicon Nanoparticles Studied by in-Situ TEM. *Sci. Rep*. **2014**, *4*, 3863.

52. Smith, B. W.; Luzzi, D. E. Electron Irradiation Effects in Single Wall Carbon Nanotubes. *J. Appl. Phys*. **2001**, *90*, 3509.

Chapter 10: Germanium Nanowires as Sodium Ion Battery Anodes[†††]

10.1 INTRODUCTION

Li-ion batteries are widely used to power portable electronic devices and are now advancing into other commercial markets of electric vehicles and large-scale power grid storages.[1] Li-ion batteries, however, do have challenges related to cost, safety, lifetime and cycling performance.[2] Because sodium (Na) is naturally abundant, it has attracted attention as a potential replacement for Li in rechargeable batteries, i.e. Na-ion batteries.[3–6] Although Na has similar chemical properties as Li in many respects, electrodes that have been developed for Li-ion batteries do not always work for the Na-ion system. For instance, graphite is commercially used as the anode in Li-ion batteries, but shows very low and highly irreversible capacity in Na-ion batteries.[7] A suitable anode for Na ion batteries is needed. So far, non-graphitic carbon,[8–11] tin (Sn; the theoretical capacity is 847 $mAh{\cdot}g^{-1}$ for $Na_{15}Sn_4$ and the observed capacity has ranged from 300 $mAh{\cdot}g^{-1}$ to 864 $mAh{\cdot}g^{-1}$),[12,13] antimony (Sb; the theoretical capacity is 660 $mAh{\cdot}g^{-1}$ for Na_3Sb and the observed capacity has ranged between 544 $mAh{\cdot}g^{-1}$ and 600 $mAh{\cdot}g^{-1}$),[14–16] and their alloys[17,18] have shown some success in Na-ion batteries. Ceder et al.,[3] have calculated that both silicon (Si) and germanium (Ge) should alloy with Na at room temperature to form NaSi and NaGe. However, crystalline Si and Ge, which have been shown to be promising high storage anodes for Li-ion batteries,[19–21] have not worked in Na-ion batteries, apparently because of a high diffusion barrier for Na ions in the Si and Ge lattices.[22] Recently, the groups of Mullins[23] and Mitlin[18,24] have demonstrated that amorphous Ge (*a*-Ge) exhibits reversible Na insertion in batteries. The high defect density of *a*-Ge significantly lowers the activation barrier for Na diffusion.[23] Now, we find that in

[†††] Manuscript submitted to *Nano Letters*: Lu, X. T.; Adkins, E. R.; He, Y.; Zhong, L.; Mao, S. X.; Wang, C. M.; Korgel, B. A. Germanium as a Sodium Ion Battery Material: In Situ TEM Reveals Fast Sodiation Kinetics with High Capacity

addition to amorphization, the addition of tin (Sn) to the Ge nanowire surface, further enhances the sodiation rates.

We carried out real-time *in situ* TEM studies of the sodiation and desodiation of Ge nanowires coated with tin (Sn). The addition of Sn to Si nanowires significantly enhances the lithiation and delithiation rates of Si nanowires,[25,26,27] so we tried this approach to Ge nanowires to see if it would also enhance the sodiation/desodiation rate of Ge nanowires. As expected, *in situ* TEM experiments showed that crystalline Ge nanowires do not sodiate, but by amorphizing the nanowires with an initial lithiation/delithiation cycle, the nanowires become effective sodiation electrodes. The sodiation kinetics are very fast and the observed volume expansion is unexpectedly large. The volume of the amorphous Ge nanowires expand by more than 300%, which is significantly higher than expected based on a final sodiated phase of NaGe, and close to Na_3Ge. Significant pore formation was also observed in the nanowires after desodiation. Pores have also been observed in Ge nanowires after delithiation,[28,29] but the pores that form after sodiation are larger and more concentrated. During sodiation, the pores disappear and the Ge nanowires heal without any significant structural change. The *in situ* studies are carried out at an exceptionally fast *C*-rate of 360*C*,[30] showing that sodiation and desodiation of *a*-Ge nanowires can occur at high rates and yield relatively high sodium storage capacities in Na-ion batteries.

10.2 Experimental Details

10.2.1 Materials

Anhydrous toluene (99.8%, Sigma-Aldrich), tetraoctylammonium bromide (98%, Aldrich), sodium borohydride (≥98.0%, Aldrich), bis[bis(trimethylsilyl)amino]tin(II)

($Sn(hmds)_2$, Aldrich), hydrogen tetrachloroaurate(III) trihydrate (≥99.9%, Aldrich), diphenylgermane (DPG, Gelest Inc.), trisilane (Si_3H_8, Voltaix) were obtained commercially and used without further purification. Gold (Au) nanocrystals averaging 2 nm in diameter were prepared by Brust's method.[53]

10.2.2 Synthesis of Sn-coated Ge Nanowires

Ge nanowires were synthesized in a 10 mL titanium tubular reactor connected to a high pressure liquid chromatography (HPLC) pump. A 28 mL reactant solution of 18 mg/L Au nanocrystals and 35.7 mM diphenylgermane (DPG) in anhydrous toluene prepared in a nitrogen-filled glovebox. Prior to precursor injection, the 10 mL titanium tubular reactor was filled with N_2 in the glovebox and then connected to the six-way valve and the backpressure regulator at two ends. After the reactor was preheated to 380ºC and pressurized to 6.9 MPa with anhydrous toluene, nanowire growth was carried out with the reactant solution fed into the reactor at a rate of 0.5 mL/min for 40 min. The outlet pressure was maintained at 6.9 MPa. After completing the injection of the reactants, the reactor was sealed and removed from the heating block. After the reactor cooling to room temperature, the nanowire product was collected and washed with a mixture of 4 mL of chloroform, 2 mL of toluene and 2 mL of ethanol, followed by centrifugation at 8000 rpm for 5 min. The purification procedure was repeated three times to remove unreacted reagent and molecular byproducts.

Purified Ge nanowires were dispersed in 10 mL of anhydrous toluene with 50 mM $Sn(hmds)_2$ inside a N_2-filled glovebox. Dilute trisilane (~ 0.03 mmol) was added as a reducing agent to generate Sn nanoparticles on the nanowire surface. The dispersion was stirred overnight to obtain a uniform Sn nanoparticle coating on the nanowires.

10.2.3 *In Situ* TEM Lithiation/Sodiation of Si Nanowires

In situ TEM measurements were carried out with a Nanofactory TEM-STM holder inside a Titan 80-300™ scanning/transmission electron microscope (S/TEM). Nanowires were drop-cast onto a gold probe as a working electrode and lithium metal was mounted on a tungsten probe as a counter electrode. A native Li_2O layer formed by a short exposure of Li to air functions as a solid-state electrolyte.[31,32] Inside the TEM, a piezo-positioner moves the Li/Li_2O electrode into contact with the nanowire. After contact, a bias of -2 V is applied to initiate lithiation. Once lithiation is completed, a bias of 2V is applied for delithiation. After the lithiation/delithiation cycle was complete, the holder was brought out of the TEM and Li was replaced with Na in an Ar-filled glovebox. Similarly, *in situ* TEM imaging of sodiation/desodiation was carried out, with a thin layer of Na_2O and NaOH serving as the electrolyte.[13,33]

10.3 Results and Discussions

For these studies, Ge nanowires were synthesized by a supercritical fluid-liquid-solid (SFLS) method, and then a uniform Sn nanoparticle coating was deposited on the nanowires using previously described methods.[34,35,36] Sodiation of crystalline Ge (*c*-Ge) nanowires was first attempted, but no sodiation was observed (Figure 10.2). Sodiation of the nanowires was only observed after an initial lithiation/delithiation cycle was utilized to amorphize the nanowires, as shown in Figure 10.3a. Sodiation and desodiation of the nanowires was carried out by applying biases of -0.5 V vs Na and between 2 to 5 V vs Na, respectively. The applied potential for desodiation in the TEM is significantly larger than what is needed in actual Na-ion battery tests[13] in order to offset the spontaneous diffusion of Na,[37] activation of the electron beam,[38] and potential barrier at the contacts. This is common for in situ TEM studies; for example, *in situ* lithiation of Si requires the

application of -2V vs Li, whereas, the lithiation window in Li-Si half cells is 0 to +2V vs Li. This difference does not appear to change the behavior of the material.[32,39]

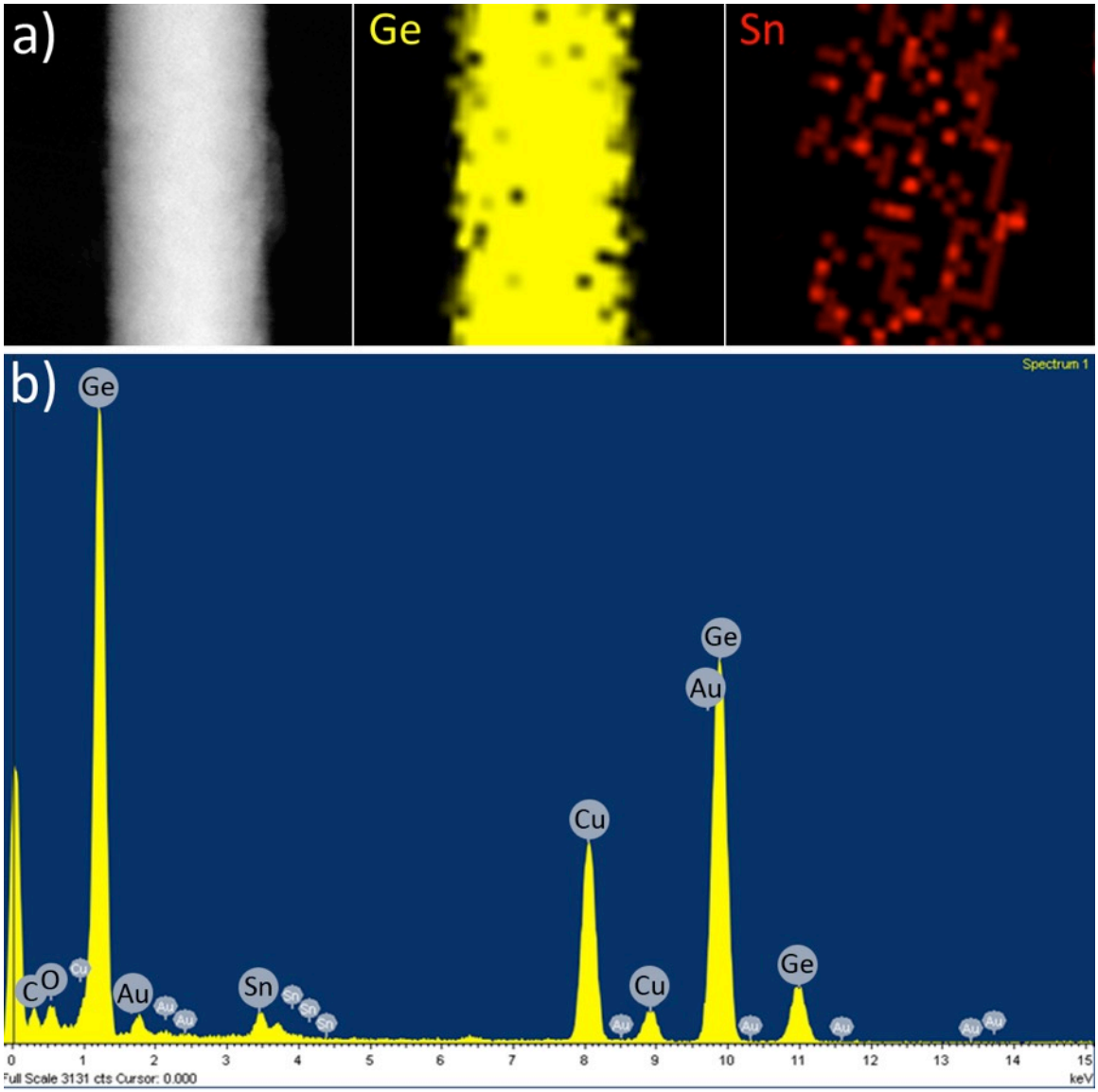

Figure 10.1 Elemental analysis of a Sn-coated Ge nanowire. (a) EDS mapping and (b) EDS spectrum of a Sn coated Ge nanowire.

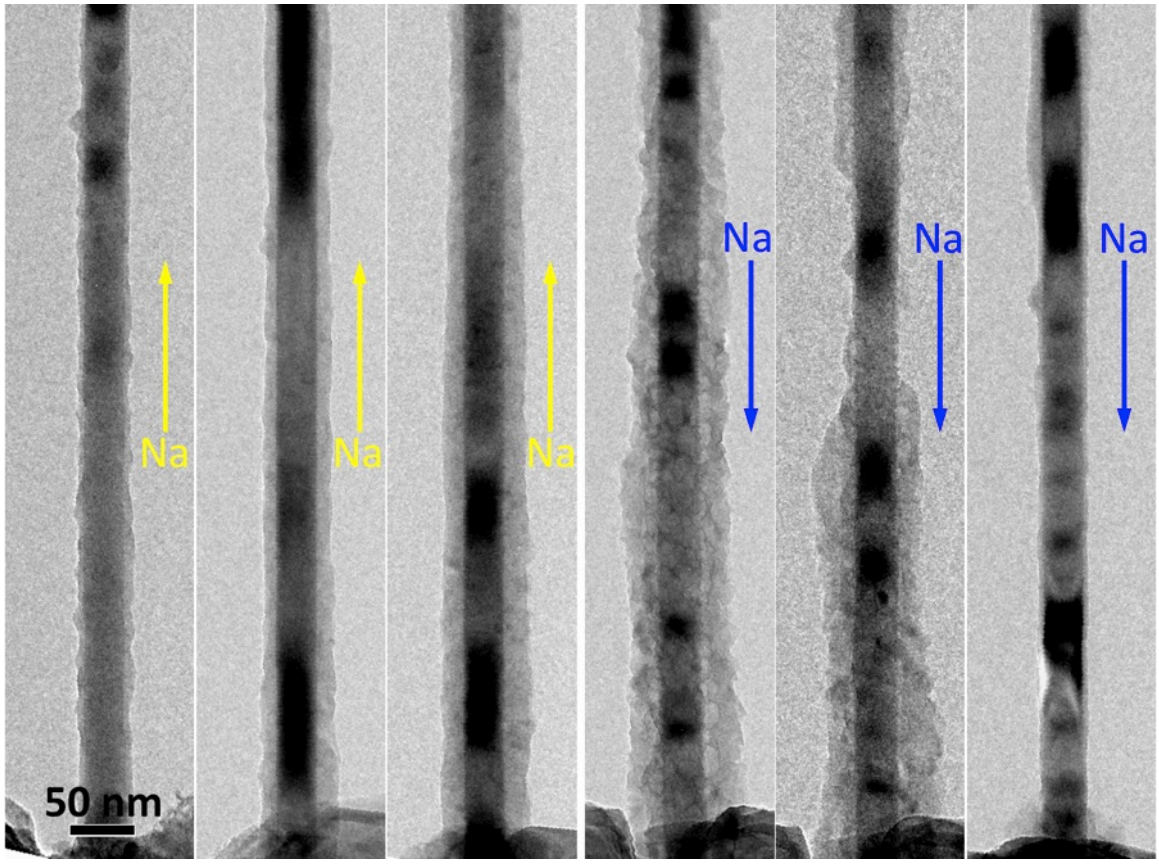

Figure 10.2 Fast surface diffusion of sodium along the length of a crystalline Ge nanowire. (Left) Only sodium diffusion on the surface of the *c*-Ge nanowire was observed by applying -2V bias for 2 hours, the diameter and crystalline structure of the Ge nanowire was unchanged. (Right) The surface sodium could be rapidly withdrawn in a few minutes by applying positive bias. The *c*-Ge nanowire was intact after this contrast experiment, indicating that the crystalline Ge nanowire cannot be sodiated without amorphization.

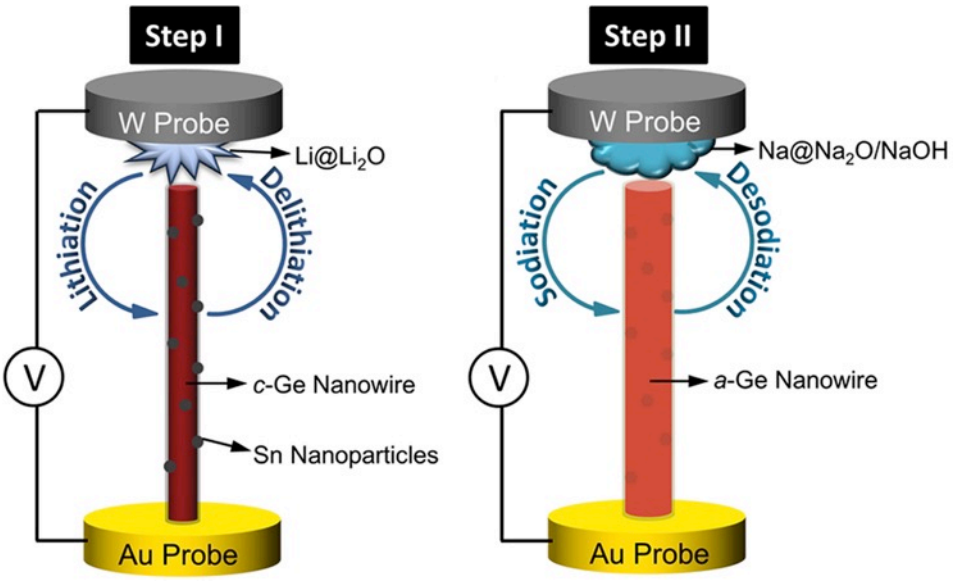

Figure 10.3 Schematic showing the *in situ* TEM experiment procedure. In a first step, a crystalline Ge nanowire is cycled against Li to obtain an amorphous structure. Then, Li is replaced by Na and the *a*-Ge nanowire is cycled against Na.

Figures 10.4b-f show TEM images of the first lithiation process of a <111>-oriented Ge nanowire with Sn particles coated on the surface. The two major orientations of our Ge nanowires are <111> and <110>. As these two nanowires do not exhibit significant difference upon lithiaion[40] and our discussion are focused on the sodiation after amorphization, the following discussion will not differentiate the original orientation of the nanowires. Since the Sn nanoparticles swell upon lithiation (Figure 10.4b-c), they were employed as markers for tracking the lithiation front as it moved down the length of the nanowire, as we have done previously with Si nanowires.[26] The Li diffusion front moves down the length of the nanowire at a rate of ~860 nm/min, which is slightly higher than what we previously measured in Sn included Si nanowires, which was 450 nm/min.[25] Similar to the case of Si, the Sn coating significantly enhances the surface lithiation rate in the Ge nanowires. As a result of a much slower bulk diffusion of

Li, the first lithiation of Ge nanowires occurs in a surface-into-core sequence, as shown in Figure 10.5a, which has been observed for other materials as well.[41,42] The average radial lithiation rate was 4.4 nm/min for the Ge nanowire with original diameter of 31.7 nm (Figure 10.4); and for the nanowire with initial diameter of 68 nm (Figure 10.5) this rate was slower, at 1.02 nm/min. The much slower lithiation rate into the thicker nanowire is the result of lithiation-induced stress, which accumulates more severely in thicker nanowire and prevents full lithiation in nanowires with diameter over 100 nm.[43] The lithiation rates we observe in the Sn particle-coated Ge nanowires are are close to the average radial migration rates observed in heavily doped <111> Si nanowires of 3.9 nm/min.[41]

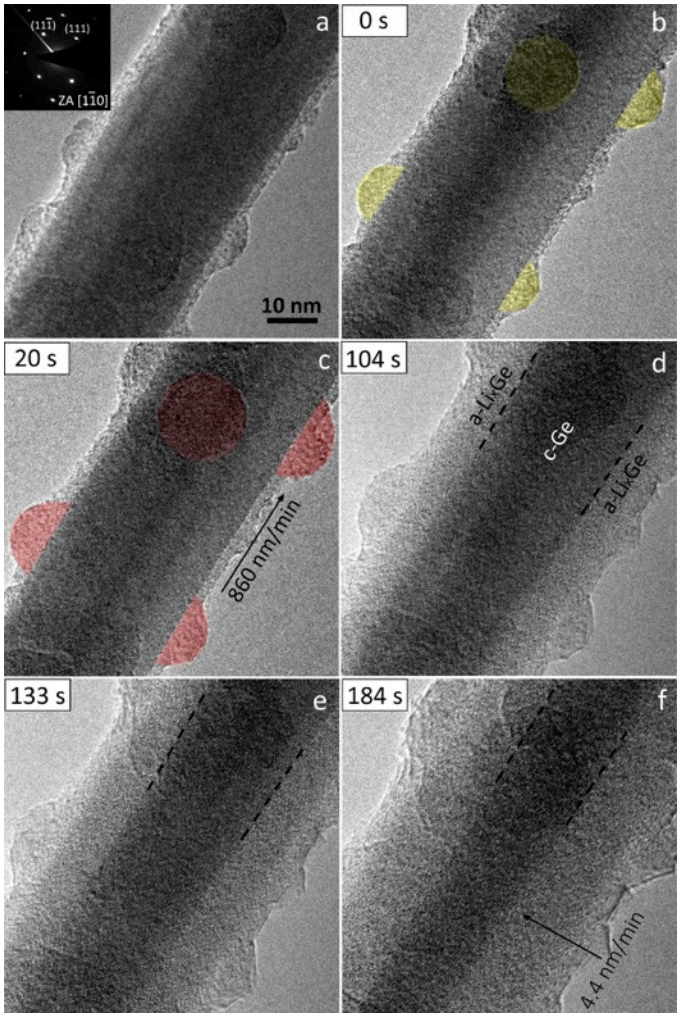

Figure 10.4 *In situ* TEM images of real-time lithiation of a lattice-resolved Ge nanowire with Sn coating the surface. (a) The pristine Ge nanowire with a [111] growth direction; (b-c) Lithiation swells the Sn nanoparticles decorating the nanowire surface (Sn nanoparticles are highlighted in yellow and red before and after lithiation, respectively), providing a marker Li diffusion along the length of the nanowire; (d-f) lithiation of the Ge nanowire occurred in the radial direction in a *core-into-shell mode* at much slower rate as reported previously.[28]

The Ge nanowires were delithiated and then cycled against Na. It is worth noting that we did not observe any pores[28] in the delithiated Ge nanowires after this single lithiation/delithiation cycle. The amorphized, delithiated Ge nanowires undergo visibly

rapid sodiation. Figure 10.5b shows a sequence of TEM images of an *a*-Ge nanowire undergoing its first sodiation cycle. Similar structural evolution was observed in several other nanowires during sodiation.

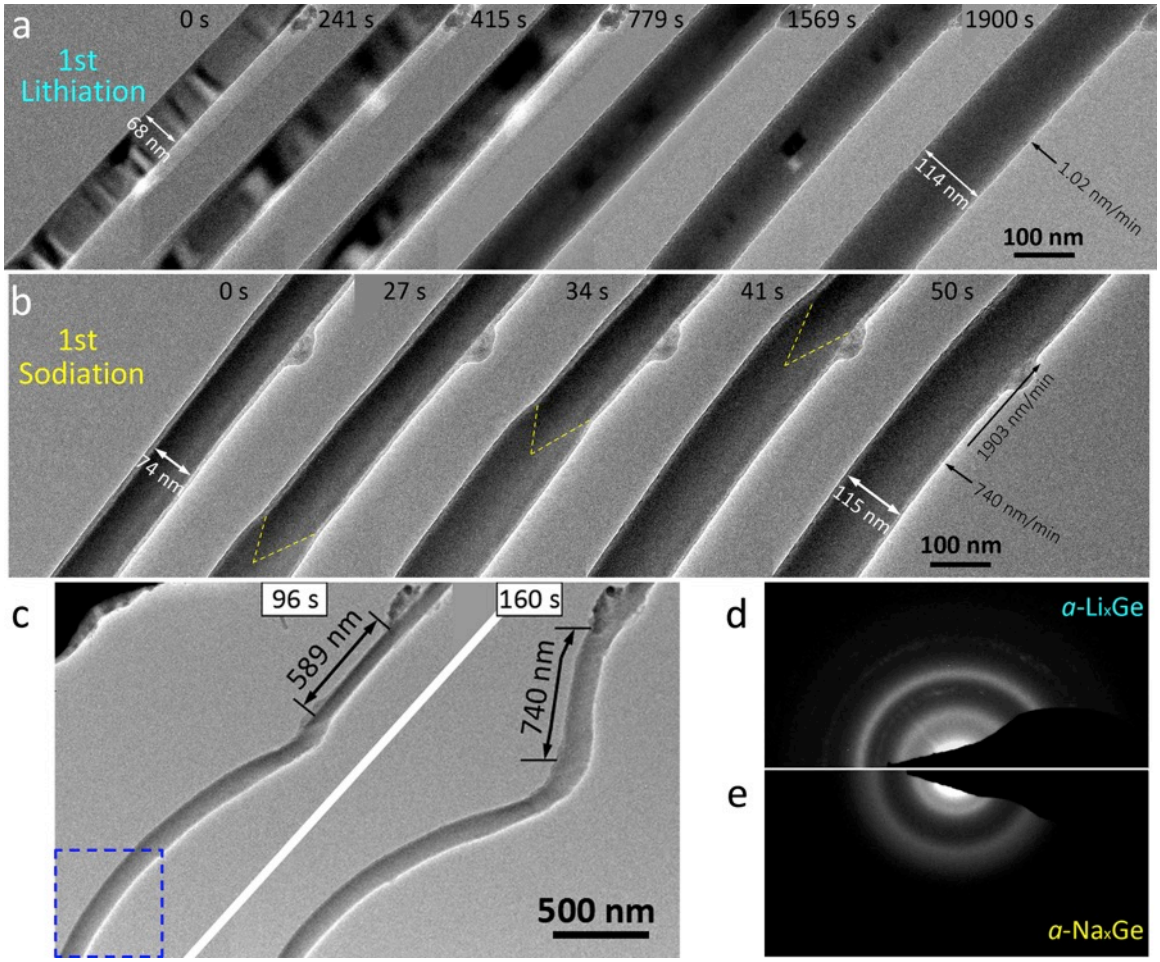

Figure 10.5 Time series images of (a) lithiation and (b-c) sodiation of a Sn-coated Ge nanowire, where sodiation proceeds faster than lithiation by two orders of magnitude. The segment investigated in (b) is the area marked with dotted blue frame in (c). Comparison of electron diffraction patterns of (d) a-Li_xGe and (e) a-Na_xGe feature an obvious shrinking of the diffraction rings of a-Na_xGe, indicating the further lattice expansion upon Na insertion.

The diameter of the Ge nanowire in Figure 10.5b expanded from 68 nm to 74 nm after the lithiation/delithiation cycle, corresponding to a volume expansion of 129% for amorphization. Ge typically undergoes isotropic lithiation,[44] occurring by a *surface-into-core* diffusion mechanism as others have described.[28] Sodiation of the nanowire on the other hand creates a *V-shaped* sodiation front, similar to the lithiation behavior of the carbon-coated and phosphorous-doped Si nanowires where ultrafast lithiation was observed.[45] The V-shape indicates that bulk Na diffusion into the Ge nanowire occurs at a rate nearly comparable to the surface diffusion rate of Na down the length of the nanowire. The sodiation rates in the axial and radial directions of the nanowire in Figure 10.5b were respectively, 1903 nm/min and 740 nm/min. For the nanowire segment in the viewing field with starting diameter of 74 nm and length of 630 nm, it only took 30 s to complete sodiation. This corresponds to an extremely fast charging rate of ~44.27 $A \cdot g^{-1}$, or 120C (with 1C = 369 $mA \cdot g^{-1}$ for the alloying of Ge to NaGe).[3] After sodiation, the nanowire diameter has expanded from 74 nm to 115 nm and, in the low-magnification image (Figure 10.5c), the length of one segment has increased from 589 nm to 740 nm (this measurement is subject to the curling of the nanowire and projection nature of the TEM image). This corresponds to a volume expansion of 303%,[46] which is much higher than expected based on a saturated NaGe phase, which would only lead to a volume expansion of 134%.[47] Electron diffraction confirmed that Na was inserting into the nanowires, as Figure 10.5d shows, comparing the electron diffraction patterns of Li_xGe and Na_xGe nanowires. The diffraction rings of Na_xGe are closer to the center spot, which is consistent with a more significant lattice expansion in the nanowire when Na inserts compared to Li.

Na_3Ge is the only other phase known to exist on the Na-Ge phase diagram[48] with higher Na content than NaGe, and better matches the volume expansion observed. If

Na_3Ge were indeed the final sodiation product, three times the amount of sodium would be incorporated into the nanowire than if it were NaGe, which would effectively increase the initial charging rate estimate ever further to 360C (with 1C = 1108 $mA \cdot g^{-1}$ for the alloying of Ge to Na_3Ge). Due to the other kinetic barriers in actual batteries,[49] like slow transport across the solid electrolyte interface (SEI) layers, such rate performance might not be achievable in a real battery setup with much higher mass loading. Nevertheless, these *in situ* observations show *a*-Ge nanowires might be a very effective negative electrode material for Na-ion batteries.

The electron beam had a strong effect on the sodiated nanowires and needed to be minimized during the measurements to avoid artifacts in the measurement. For instance, an instantaneous swelling of nanowires was observed immediately when the beam was illuminated after a long period of beam-blanked desodiation. The electron beam *induces* Na insertion into Ge, especially when the beam is at a high energy. Similarly, beam-induced lithiation of Si particles has been observed by others.[31] Beam-induced sodiation occurs because Na has a much lower activation energy for self-diffusion,[37] and sodiation is more kinetically favored than desodiation.[50] Migration of Na induced by the beam can become so severe that a thick shell of Na can form on the nanowire within a few minutes of illumination (Figure 10.2). Sodiation can also be readily triggered by the electron beam, even during the desodiation process. Therefore, a high positive voltage is applied to minimize the effect of the electron beam, as well as the retardation of interstitial diffusion of Na by defect-trapping in *a*-Ge.[51,52] We further improved the imaging of the desodiation processs by avoiding direct diffusion of Na from the Na reservoir into the nanowire by bridging the target nanowire with another set of nanowires (Figure 10.6).

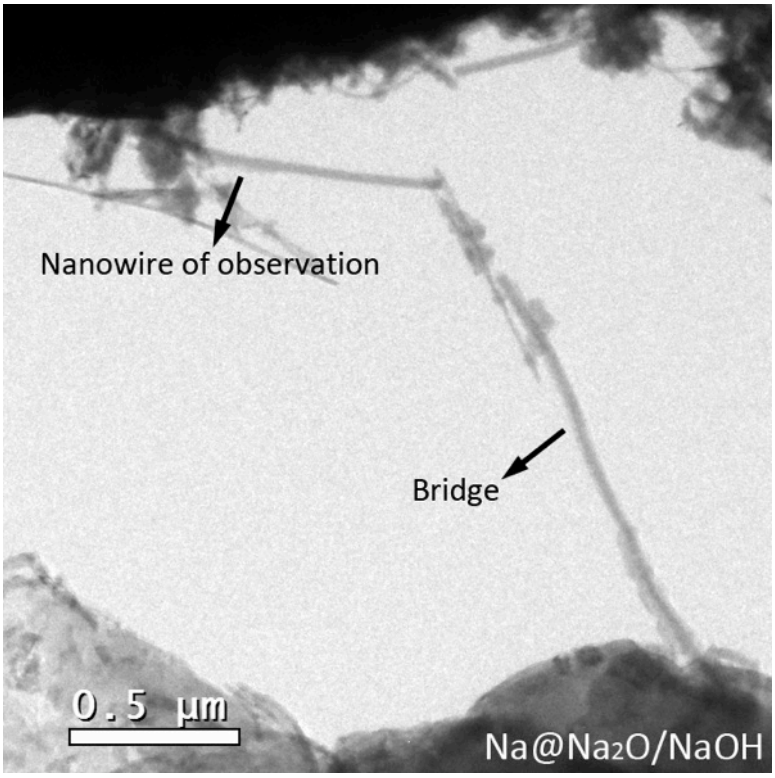

Figure 10.6 Bridging of nanowires to avoid fast surface diffusion of Na. Bridging the nanowires to avoid fast surface diffusion of Na from Na@Na_2O/NaOH reservoir.

Pores were observed in the nanowires after the first desodiation event; whereas, pores were not observed after the first lithiation/delithiation activation step. One would perhaps expect pore formation to be more likely after desodiation than delithiation because of the much larger atomic volume of Na (24.43 $Å^3$/atom, elemental volume) compared to Li (12.77 $Å^3$/atom). Figure 10.7 shows the comparison between pristine, delithiated and desodiated Ge nanowire. The delithiated Ge nanowire has nearly returned to its original diameter with without any visible pores. The desodiated Ge nanowire on the other hand contains a large concentration of pores and retains a much larger diameter than its starting diameter after desodiation. The porous structure creates an electron

diffraction pattern with significantly more diffuse diffraction rings in the desodiated nanowire (Figure 10.7e) compared to a delithiated nanowire (Figure 10.7d).

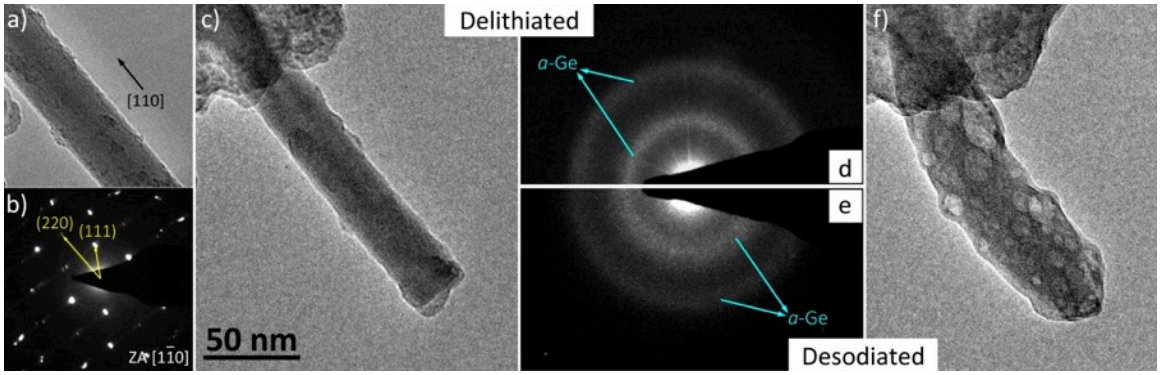

Figure 10.7 Pore formation during desodiation. (a-b) the pristine Ge nanowire with [110] growth direction before lithiation; (c) delithiated Ge nanowire features no pore after Li extraction and (d) electron diffraction pattern shows its amorphous structure; (f) pores appear in the nanowire after the first desodiation and (e) the diffraction rings of desodiated Ge nanowire broadened compared with delithiated Ge in (d), indicating more structural defects after Na extraction.

The *a*-Ge nanowires also exhibited the ability to recover structurally after desodiation when they were re-sodiated. Figure 10.8c shows a TEM image of nanowire that was desodiated at a very fast rate by applying a very high bias of +10 V vs Na. This led to the formation of giant pores in the nanowires without any change in outer diameter. Despite the massive size of the pores, these pores were almost completely filled during the subsequent sodiation step (Figure 10.8d). More strikingly, by manipulating the voltage at the normal range (< +5V), only small pores appeared during the second desodiation, totally different from the giant pore in the first desodiation (Figure 10.8e). This is different than the reversible pore formation that has been observed during the lithiation/delithiation of Ge nanowires that has showed a *memory effect* in which pores

would shrink during delithiation but never fully recover in subsequent cycles.[28] The observation here demonstrates that *a*-Ge nanowires have excellent structural robustness.

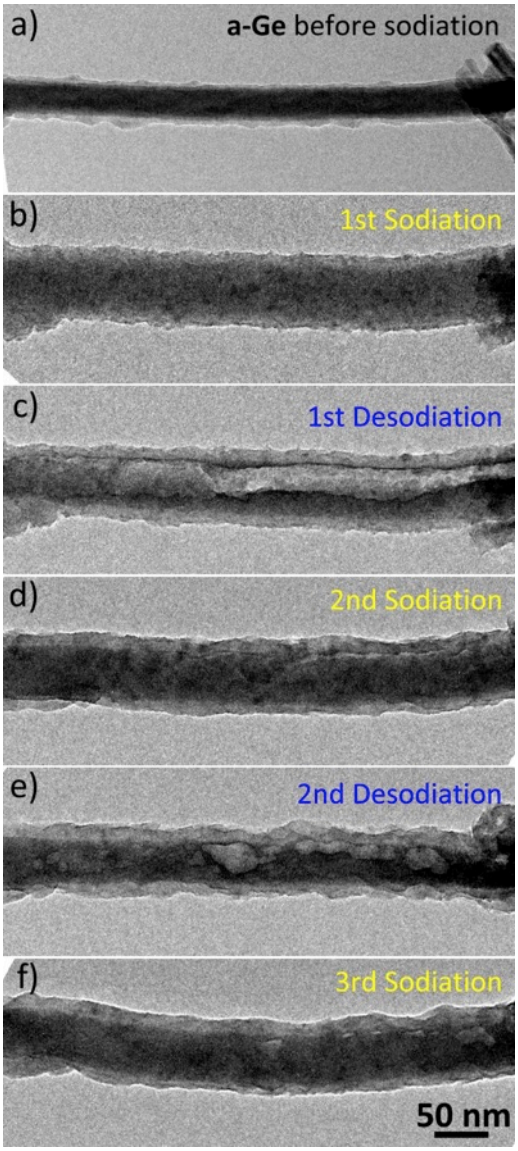

Figure 10.8 Structure evolution during sodiation/desodiation cycles. (a) The delithiated/amorphorized Ge nanowire. (b) Sodiated Ge nanowire. (c) A huge pore was created by applying high desodiation bias. (d) Porous structure was recovered from second sodiation. (e) Small pores, instead of huge one, reformed during second desodiation upon milder desodiation. (f) Those small pores could also be recovered from sodiation.

10.4 Conclusions

The sodiation/desodiation of Ge nanowires was studied with *in situ* TEM for the first time. The experiment confirmed that Ge nanowires could be sodiated only after their crystalline phase was completely amorphorized. Our result suggests that NaGe is not the final sodiation product and Ge could uptake much more Na than 1:1 ratio according to over 300% volume expansion after sodiation. Fast sodiation was demonstrated in those *a*-Ge nanowires. Moreover, porous structure was more easily formed from the desodiation rather than the delithiation process. This porous structure has excellent structural stability that could even recover from damage caused by ultrafast Na extraction. These results indicate that Ge provides a great anode candidate for Na-ion batteries, with significantly higher energy densities than previously thought to be attainable, excellent rate performance and structural robustness.

10.5 Acknowledgements

Funding for this work was provided by the Robert A. Welch Foundation (grant no. F-1464) and the National Science Foundation (grant no. CHE-1308813). CMW acknowledges the support of the Assistant Secretary for Energy Efficiency and Renewable Energy, Office of Vehicle Technologies of the U.S. Department of Energy under Contract No. DE-AC02-05CH11231, Subcontract No. 6951379 under the advanced Batteries Materials Research (BMR) Program. The *in situ* TEM experiments were conducted in the William R. Wiley Environmental Molecular Sciences Laboratory (EMSL), a national scientific user facility sponsored by DOE's Office of Biological and Environmental Research and located at PNNL. PNNL is operated by Battelle for the Department of Energy under Contract DE-AC05-76RLO1830.

10.6 REFERENCES

1. Tarascon, J. M.; Armand, M. Issues and Challenges Facing Rechargeable Lithium Batteries. *Nature* **2001**, *414*, 359–367.

2. Goodenough, J. B.; Kim, Y. Challenges for Rechargeable Li Batteries. *Chem. Mater.* **2010**, *22*, 587–603.

3. Chevrier, V. L.; Ceder, G. Challenges for Na-Ion Negative Electrodes. *Journal of The Electrochemical Society*, 2011, *158*, A1011.

4. Palomares, V.; Casas-Cabanas, M.; Castillo-Martínez, E.; Han, M. H.; Rojo, T. Update on Na-Based Battery Materials. A Growing Research Path. *Energy Environ. Sci.* **2013**, *6*, 2312.

5. Slater, M. D.; Kim, D.; Lee, E.; Johnson, C. S. Sodium-Ion Batteries. *Adv. Funct. Mater.* **2013**, *23*, 947–958.

6. Kim, S.-W.; Seo, D.-H.; Ma, X.; Ceder, G.; Kang, K. Electrode Materials for Rechargeable Sodium-Ion Batteries: Potential Alternatives to Current Lithium-Ion Batteries. *Adv. Energy Mater.* **2012**, *2*, 710–721.

7. Ge, P. Electrochemical Intercalation of Sodium in Graphite. *Solid State Ionics* **1988**, *28-30*, 1172–1175.

8. Alcántara, R.; Jiménez-Mateos, J. M.; Lavela, P.; Tirado, J. L. Carbon Black: A Promising Electrode Material for Sodium-Ion Batteries. *Electrochem. commun.* **2001**, *3*, 639–642.

9. Cao, Y.; Xiao, L.; Sushko, M. L.; Wang, W.; Schwenzer, B.; Xiao, J.; Nie, Z.; Saraf, L. V; Yang, Z.; Liu, J. Sodium Ion Insertion in Hollow Carbon Nanowires for Battery Applications. *Nano Lett.* **2012**, *12*, 3783–3787.

10. Liu, Y.; Fan, F.; Wang, J.; Liu, Y.; Chen, H.; Jungjohann, K. L.; Xu, Y.; Zhu, Y.; Bigio, D.; Zhu, T.; Wang, C. In Situ Transmission Electron Microscopy Study of Electrochemical Sodiation and Potassiation of Carbon Nanofibers. *Nano Lett.* **2014**, *14*, 3445–3452.

11. Wenzel, S.; Hara, T.; Janek, J.; Adelhelm, P. Room-Temperature Sodium-Ion Batteries: Improving the Rate Capability of Carbon Anode Materials by Templating Strategies. *Energy Environ. Sci.* **2011**, *4*, 3342.

12. Ellis, L. D.; Hatchard, T. D.; Obrovac, M. N. Reversible Insertion of Sodium in Tin. *J. Electrochem. Soc.* **2012**, *159*, A1801–A1805.

13. Wang, J. W.; Liu, X. H.; Mao, S. X.; Huang, J. Y. Microstructural Evolution of Tin Nanoparticles during in Situ Sodium Insertion and Extraction. *Nano Lett.* **2012**, *12*, 5897–5902.

14. Darwiche, A.; Marino, C.; Sougrati, M. T.; Fraisse, B.; Stievano, L.; Monconduit, L. Better Cycling Performances of Bulk Sb in Na-Ion Batteries Compared to Li-Ion

Systems: An Unexpected Electrochemical Mechanism. *J. Am. Chem. Soc.* **2012**, *134*, 20805–20811.

15. Qian, J.; Chen, Y.; Wu, L.; Cao, Y.; Ai, X.; Yang, H. High Capacity Na-Storage and Superior Cyclability of Nanocomposite Sb/C Anode for Na-Ion Batteries. *Chem. Commun. (Camb).* **2012**, *48*, 7070–7072.

16. He, M.; Kravchyk, K.; Walter, M.; Kovalenko, M. V. Monodisperse Antimony Nanocrystals for High-Rate Li-Ion and Na-Ion Battery Anodes: Nano versus Bulk. *Nano Lett.* **2014**, *14*, 1255–1262.

17. Xiao, L.; Cao, Y.; Xiao, J.; Wang, W.; Kovarik, L.; Nie, Z.; Liu, J. High Capacity, Reversible Alloying Reactions in SnSb/C Nanocomposites for Na-Ion Battery Applications. *Chem. Commun. (Camb).* **2012**, *48*, 3321–3323.

18. Farbod, B.; Cui, K.; Kalisvaart, W. P.; Kupsta, M.; Zahiri, B.; Kohandehghan, A.; Lotfabad, E. M.; Li, Z.; Luber, E. J.; Mitlin, D. Anodes for Sodium Ion Batteries Based on Tin-Germanium-Antimony Alloys. *ACS Nano* **2014**.

19. Bogart, T. D.; Chockla, A. M.; Korgel, B. A. High Capacity Lithium Ion Battery Anodes of Silicon and Germanium. *Curr. Opin. Chem. Eng.* **2013**, *2*, 286–293.

20. Wu, H.; Cui, Y. Designing Nanostructured Si Anodes for High Energy Lithium Ion Batteries. *Nano Today* **2012**, 414–429.

21. Liu, X. H.; Huang, J. Y. In Situ TEM Electrochemistry of Anode Materials in Lithium Ion Batteries. *Energy Environ. Sci.* **2011**, *4*, 3844.

22. Legrain, F.; Malyi, O. I.; Manzhos, S. Comparative Computational Study of the Diffusion of Li, Na, and Mg in Silicon Including the Effect of Vibrations. *Solid State Ionics* **2013**, *253*, 157–163.

23. Abel, P. R.; Lin, Y.-M.; de Souza, T.; Chou, C.-Y.; Gupta, A.; Goodenough, J. B.; Hwang, G. S.; Heller, A.; Mullins, C. B. Nanocolumnar Germanium Thin Films as a High-Rate Sodium-Ion Battery Anode Material. *J. Phys. Chem. C* **2013**, *117*, 18885–18890.

24. Kohandehghan, A.; Cui, K.; Kupsta, M.; Ding, J.; Memarzadeh Lotfabad, E.; Kalisvaart, W. P.; Mitlin, D. Activation with Li Enables Facile Sodium Storage in Germanium. *Nano Lett.* **2014**, *14*, 5873–5882.

25. Bogart, T. D.; Lu, X.; Gu, M.; Wang, C.; Korgel, B. A. Enhancing the Lithiation Rate of Silicon Nanowires by the Inclusion of Tin. *RSC Adv.* **2014**, *4*, 42022–42028.

26. Kohandehghan, A.; Cui, K.; Kupsta, M.; Memarzadeh, E.; Kalisvaart, P.; Mitlin, D. Nanometer-Scale Sn Coatings Improve the Performance of Silicon Nanowire LIB Anodes. *J. Mater. Chem. A* **2014**, *2*, 11261.

27. Lu, X.; Bogart, T. D.; Gu, M.; Wang, C.; Korgel, B. A. In Situ TEM Study of Fast Lithiation and Pore Evolution in Tin-Incorporated Silicon Nanowires. *submitted for publication*.

28. Liu, X. H.; Huang, S.; Picraux, S. T.; Li, J.; Zhu, T.; Huang, J. Y. Reversible Nanopore Formation in Ge Nanowires during Lithiation-Delithiation Cycling: An in Situ Transmission Electron Microscopy Study. *Nano Lett.* **2011**, *11*, 3991–3997.

29. Kennedy, T.; Mullane, E.; Geaney, H.; Osiak, M.; O'Dwyer, C.; Ryan, K. M. High-Performance Germanium Nanowire-Based Lithium-Ion Battery Anodes Extending over 1000 Cycles through in Situ Formation of a Continuous Porous Network. *Nano Lett.* **2014**, *14*, 716–723.

30. The *C* rate is a measure of the rate at which the electrode material is discharged/charged relative to its maximum capacity. A rate of 360*C* means that the discharge or charging will be completed in 1/360 hours or 10 seconds. The *C* rate in a working battery is usually much lower than this due to the various other kinetic and transport limitations in the battery.

31. Holmberg, V. C.; Korgel, B. A. Corrosion Resistance of Thiol- and Alkene-Passivated Germanium Nanowires. *Chem. Mater.* **2010**, *22*, 3698–3703.

32. Hanrath, T.; Korgel, B. A. Supercritical Fluid–Liquid–Solid (SFLS) Synthesis of Si and Ge Nanowires Seeded by Colloidal Metal Nanocrystals. *Adv. Mater.* **2003**, *15*, 437–440.

33. Lu, X.; Korgel, B. A. A Single-Step Reaction for Silicon and Germanium Nanorods. *Chem. - A Eur. J.* **2014**, *20*, 5874–5879.

34. Liu, X. H.; Zhong, L.; Huang, S.; Mao, S. X.; Zhu, T.; Huang, J. Y. Size-Dependent Fracture of Silicon Nanoparticles during Lithiation. *ACS Nano* **2012**, *6*, 1522–1531.

35. Liu, X. H.; Zheng, H.; Zhong, L.; Huang, S.; Karki, K.; Zhang, L. Q.; Liu, Y.; Kushima, A.; Liang, W. T.; Wang, J. W.; Cho, J.-H.; Epstein, E.; Dayeh, S. a; Picraux, S. T.; Zhu, T.; Li, J.; Sullivan, J. P.; Cumings, J.; Wang, C.; Mao, S. X.; Ye, Z. Z.; Zhang, S.; Huang, J. Y. Anisotropic Swelling and Fracture of Silicon Nanowires during Lithiation. *Nano Lett.* **2011**, *11*, 3312–3318.

36. Gu, M.; Kushima, A.; Shao, Y.; Zhang, J.-G.; Liu, J.; Browning, N. D.; Li, J.; Wang, C. Probing the Failure Mechanism of SnO2 Nanowires for Sodium-Ion Batteries. *Nano Lett.* **2013**, *13*, 5203–5211.

37. Schott, V.; Fähnle, M.; Madden, P. A. Theory of Self-Diffusion in Alkali Metals: I. Results for Monovacancies in Li, Na, and K. *J. Phys. Condens. Matter* **2000**, *12*, 1171–1194.

38. Egerton, R. F.; Li, P.; Malac, M. Radiation Damage in the TEM and SEM. *Micron* **2004**, *35*, 399–409.

39. Lee, S.; McDowell, M.; Choi, J.; Cui, Y. Anomalous Shape Changes of Silicon Nanopillars by Electrochemical Lithiation. *Nano Lett.* **2011**, 3034–3039.

40. Lee, S. W.; Ryu, I.; Nix, W. D.; Cui, Y. Fracture of Crystalline Germanium during Electrochemical Lithium Insertion. *Extrem. Mech. Lett.* **2015**, *2*, 15–19.

41. Liu, X. H.; Wang, J. W.; Huang, S.; Fan, F.; Huang, X.; Liu, Y.; Krylyuk, S.; Yoo, J.; Dayeh, S. a; Davydov, A. V; Mao, S. X.; Picraux, S. T.; Zhang, S.; Li, J.; Zhu, T.; Huang, J. Y. In Situ Atomic-Scale Imaging of Electrochemical Lithiation in Silicon. *Nat. Nanotechnol.* **2012**, *7*, 749–756.

42. Gu, M.; Wang, Z.; Connell, J. G.; Perea, D. E.; Lauhon, L. J.; Gao, F.; Wang, C. Electronic Origin for the Phase Transition from Amorphous Li(x)Si to Crystalline Li15Si4. *ACS Nano* **2013**, *7*, 6303–6309.

43. Liu, X. H.; Fan, F.; Yang, H.; Zhang, S.; Huang, J. Y.; Zhu, T. Self-Limiting Lithiation in Silicon Nanowires. *ACS Nano* **2013**, *7*, 1495–1503.

44. Liang, W.; Yang, H.; Fan, F.; Liu, Y.; Liu, X. H.; Huang, J. Y.; Zhu, T.; Zhang, S. Tough Germanium Nanoparticles under Electrochemical Cycling. *ACS Nano* **2013**, *7*, 3427–3433.

45. Liu, X. H.; Zhang, L. Q.; Zhong, L.; Liu, Y.; Zheng, H.; Wang, J. W.; Cho, J.-H.; Dayeh, S. a; Picraux, S. T.; Sullivan, J. P.; Mao, S. X.; Ye, Z. Z.; Huang, J. Y. Ultrafast Electrochemical Lithiation of Individual Si Nanowire Anodes. *Nano Lett.* **2011**, *11*, 2251–2258.

46. The volume expansion of 303% is calculated based on the diameter of the swelled a-Ge upon Na insertion (first image in Figure 10.5a). Using the volume of a crystalline Ge nanowire as the basis (first image in Figure 10.5b), this value is 390%.

47. Witte, J.; Schnering, H. G.; Klemm, W. Das Verhalten Der Alkalimetalle Zu Halbmetallen. XI. Die Kristallstruktur von NaSi Und NaGe. *Zeitschrift für Anorg. und Allg. Chemie* **1964**, *327*, 260–273.

48. Okamoto, H. Supplemental Literature Review of Binary Phase Diagrams: Al-Br, B-Cd, Cd-Mg, Cd-Ti, Er-Fe, Fe-Nd, Ge-Na, Ge-Ni, Ge-Sc, Hf-W, Pb-Yb, and Re-Ti. *J. Phase Equilibria Diffus.* **2013**, *35*, 195–207.

49. Tang, Y.; Zhang, Y.; Li, W.; Ma, B.; Chen, X. Rational Material Design for Ultrafast Rechargeable Lithium-Ion Batteries. *Chem. Soc. Rev.* **2015**.

50. Chan, T.-L.; Chelikowsky, J. R. Controlling Diffusion of Lithium in Silicon Nanostructures. *Nano Lett.* **2010**, *10*, 821–825.

51. Coffa, S.; Poate, J. M.; Jacobson, D. C.; Frank, W.; Gustin, W. Determination of Diffusion Mechanisms in Amorphous Silicon. *Phys. Rev. B* **1992**, *45*, 8355–8358.

52. Coffa, S.; Poate, J. M.; Jacobson, D. C.; Polman, A. Impurity Trapping and Gettering in Amorphous Silicon. *Appl. Phys. Lett.* **1991**, *58*, 2916.

53. Brust, M.; Walker, M.; Bethell, D.; Schiffrin, D. J.; Whyman, R. Synthesis of Thiol-Derivatised Gold Nanoparticles in a Two-Phase Liquid-Liquid System. *J. Chem. Soc. Chem. Commun.* **1994**, No. 7, 801.

Chapter 11: Conclusions and Future Direction

11.1 Conclusions

This section analyzed the performance of the nanowires as anode materials with *in situ* TEM technique. Chapter 9 showed that incorporation of Sn enhanced rate capability of Si nanowire anodes, which verifies the result obtained in previous half-cell battery test.[1] In situ TEM experiments also showed that fast Li diffusion rate in Sn-incorporated Si nanowires also led to the premature formation of pores, while the application of an amorphous Si shell on the nanowires significantly limited the rate of pore formation while still retaining fast lithiation/delithiation kinetics. Chapter 10 presented the sodiation/desodiation of Ge nanowires after their crystalline phase was completely amorphorized by lithiation cycle. The result suggested that Ge could uptake much more Na than 1:1 ratio and demonstrated the fast sodiation capability of this novel anode.

The two examples of the *in situ* TEM study illustrate the power of this advanced analytical tool in the battery research. *In situ* TEM provides the real time record of the electrochemical and mechanical responses of electrode materials. Combined with traditional battery characterizations, these experiments are greatly useful for giving the guidelines for the rational design and modification of Si- and Ge-based anodes that suffer from more severe structure-related problems.

11.2 Future Directions

Besides material design and modification, the anode performance depends also on the battery formulation, such as the electrolyte and binder. The open cell configuration provides high-resolution recording of structural and chemical evolution of the anode

materials during lithiation/delithiation, but it does not mimic the liquid electrolyte environment of the electrodes and operation in real batteries. To observe the behavior of the nanomaterials under more realistic environmental conditions, especially concerning the interactions between the electrolyte and the nanostructure surface, a closed-cell configuration is needed. Such a direct observation of an actual slurry-based anode undergoing charge cycling by *in situ* TEM is more challenging, but extremely valuable. The liquid cell setup addresses the shortcomings of the open cell.[2,3] In a liquid cell (Figure 11.1), the anode nanomaterials are welded on the Pt electrode, while the Li metal is on the counter electrode. Both electrodes are immersed in the electrolyte, which is sealed by Si_3N_4 membranes. This setup is very similar to the half-cell LIBs in *ex situ* testing of anode materials. Li ions are not transported through point contact (in open cell), but in the actual electrolyte, i.e. $LiPF_6$ dissolved in ethylene carbonate (EC) and diethylene carbonate (DEC) with added fluoroethylene carbonate (FEC). Liquid cell characterization is important because it reflects the actual diffusion mode of Li ions in real batteries, not only via one-dimensional transport down the length of the nanowire but also three-dimensionally on all the interfaces of the anode contacting the electrolyte. It offers more representative structural information. Liquid cell characterization also involves the solid-electrolyte-interphase (SEI) layer, which forms due to side reactions with the solvent in the battery—primarily composed of the carbonate byproducts. A positive effect of the SEI is that it covers and protects the anode from degradation. However, it increases electrical resistance and hinders Li ion diffusion. By trapping a significant amount of Li, it also decreases the battery capacity.[4] So, understanding SEI layer formation and behavior during battery cycling is crucial to understanding and improving anode performance. SEI chemistry is especially not well understood for Si and Ge anodes. *In situ* TEM imaging using a liquid cell offers a way to directly resolve the

interfacial reactions and SEI layer formation. By recording lithiation/delithiation cycles in real time relationships could be established between: 1) the structural evolution of anode upon charge cycles and crack formation and propagation mechanisms of the SEI layer, 2) solvent selection and SEI growth, and 3) anode failure and the stabilizing effect of the SEI layer.

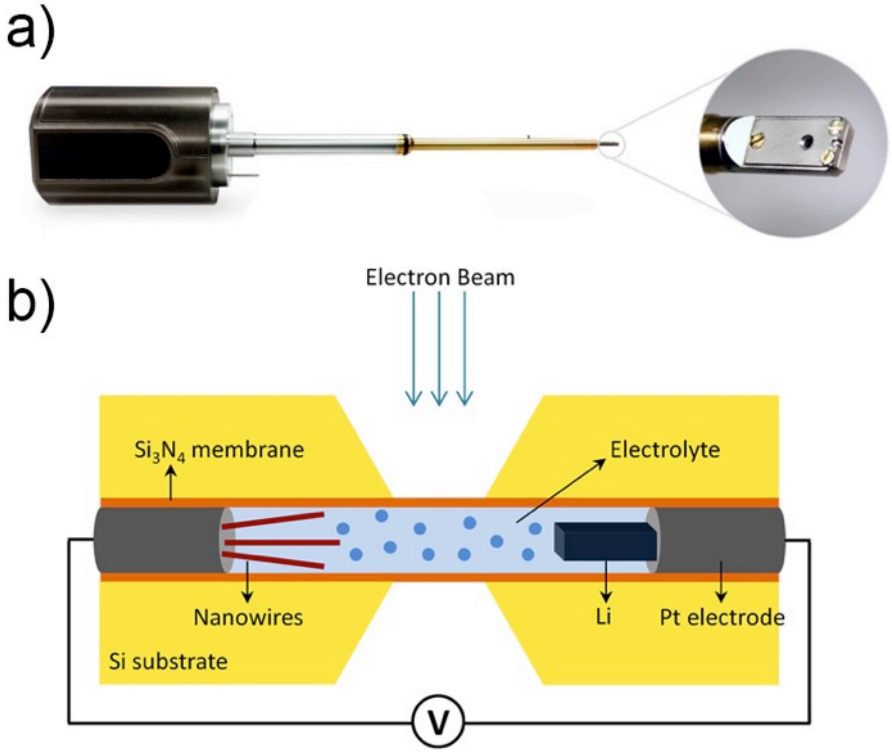

Figure 11.1 (a) Photograph of a liquid-cell TEM holder and (b) illustration of the liquid-cell nanobattery: Si_3N_4 membranes are used to seal the electrolyte in the cell, while allowing the transmission of the electron beam.

11.3 REFERENCES

1. Bogart, T. D.; Lu, X.; Gu, M.; Wang, C.; Korgel, B. A. Enhancing the Lithiation Rate of Silicon Nanowires by the Inclusion of Tin. *RSC Adv*. **2014**, *4* (79), 42022–42028.

2. Gu, M.; Parent, L. R.; Mehdi, B. L.; Unocic, R. R.; McDowell, M. T.; Sacci, R. L.; Xu, W.; Connell, J. G.; Xu, P.; Abellan, P.; Chen, X.; Zhang, Y.; Perea, D. E.; Evans,

J. E.; Lauhon, L. J.; Zhang, J.-G.; Liu, J.; Browning, N. D.; Cui, Y.; Arslan, I.; Wang, C.-M. Demonstration of an Electrochemical Liquid Cell for Operando Transmission Electron Microscopy Observation of the Lithiation/delithiation Behavior of Si Nanowire Battery Anodes. *Nano Lett*. **2013**, *13* (12), 6106–6112.

3. Zeng, Z.; Liang, W.; Liao, H.; Xin, H.; Chu, Y.-H.; Zheng, H. Visualization of Electrode-Electrolyte Interfaces in LiPF6/EC/DEC Electrolyte for Lithium Ion Batteries via In-Situ TEM. *Nano Lett*. **2014**.

4. Bogart, T. D.; Chockla, A. M.; Korgel, B. A. High Capacity Lithium Ion Battery Anodes of Silicon and Germanium. *Curr. Opin. Chem. Eng*. **2013**, *2* (3), 286–293.

Bibliography

Abel, P. R.; Lin, Y.-M.; de Souza, T.; Chou, C.-Y.; Gupta, A.; Goodenough, J. B.; Hwang, G. S.; Heller, A.; Mullins, C. B. Nanocolumnar Germanium Thin Films as a High-Rate Sodium-Ion Battery Anode Material. *J. Phys. Chem. C* **2013**, *117*, 18885–18890.

Alcántara, R.; Jiménez-Mateos, J. M.; Lavela, P.; Tirado, J. L. Carbon Black: A Promising Electrode Material for Sodium-Ion Batteries. *Electrochem. commun.* **2001**, *3*, 639–642.

Alivisatos, A. P. Semiconductor Clusters, Nanocrystals, and Quantum Dots. *Science*, 1996, *271*, 933–937.

Arbiol, J.; Fontcuberta I Morral, A.; Estradé, S.; Peiró, F.; Kalache, B.; Roca I Cabarrocas, P.; Morante, J. R. Influence of the (111) Twinning on the Formation of Diamond Cubic/diamond Hexagonal Heterostructures in Cu-Catalyzed Si Nanowires. *J. Appl. Phys.* **2008**, *104* (6).

Aurbach, D.; Talyosef, Y.; Markovsky, B.; Markevich, E.; Zinigrad, E.; Asraf, L.; Gnanaraj, J. S.; Kim, H. J. Design of Electrolyte Solutions for Li and Li-Ion Batteries: A Review. *Electrochim. Acta* **2004**, *50*, 247–254.

Baggetto, L.; Notten, P. H. L. Lithium-Ion (De)Insertion Reaction of Germanium Thin-Film Electrodes: An Electrochemical and In Situ XRD Study. *J. Electrochem. Soc.* **2009**, *156* (3), A169.

Barnard, A. S.; Xu, H. First Principles and Thermodynamic Modeling of CdS Surfaces and Nanorods. *J. Phys. Chem. C* **2007**, *111* (49), 18112–18117.

Barth, S.; Hernandez-Ramirez, F.; Holmes, J. D.; Romano-Rodriguez, A. Synthesis and Applications of One-Dimensional Semiconductors. *Prog. Mater. Sci.* **2010**, *55*, 563–627.

Barth, S.; Koleśnik, M. M.; Donegan, K.; Krstić, V.; Holmes, J. D. Diameter-Controlled Solid-Phase Seeding of Germanium Nanowires: Structural Characterization and Electrical Transport Properties. *Chem. Mater.* **2011**, *23* (14), 3335–3340.

Beard, M. C.; Knutsen, K. P.; Yu, P.; Luther, J. M.; Song, Q.; Metzger, W. K.; Ellingson, R. J.; Nozik, A. J. Multiple Exciton Generation in Colloidal Silicon Nanocrystals. *Nano Lett.* **2007**, *7* (8), 2506–2512.

Biswas, S.; Singha, A.; Morris, M. a; Holmes, J. D. Inherent Control of Growth, Morphology, and Defect Formation in Germanium Nanowires. *Nano Lett.* **2012**, *12* (11), 5654–5663.

Bogart, T. D.; Chockla, A. M.; Korgel, B. A. High Capacity Lithium Ion Battery Anodes of Silicon and Germanium. *Curr. Opin. Chem. Eng.* **2013**, *2* (3), 286–293.

Bogart, T. D.; Lu, X.; Gu, M.; Wang, C.; Korgel, B. A. Enhancing the Lithiation Rate of Silicon Nanowires by the Inclusion of Tin. *RSC Adv*. **2014**, *4*, 42022–42028.

Bogart, T. D.; Lu, X.; Korgel, B. A. Precision Synthesis of Silicon Nanowires with Crystalline Core and Amorphous Shell. *Dalton Trans*.**2013**, *42*, 12675–12680.

Bogart, T. D.; Oka, D.; Lu, X.; Gu, M.; Wang, C.; Korgel, B. A. Lithium Ion Battery Peformance of Silicon Nanowires with Carbon Skin. *ACS Nano* **2014**, *8* (1), 915–922.

Brissonneau, L.; Sahnoun, R.; Mijoule, C.; Vahlas, C. Investigation of Nickelocene Decomposition during Chemical Vapor Deposition of Nickel. *J. Electrochem. Soc*. **2000**, *147* (4), 1443.

Brus, L. Luminescence of Silicon Materials: Chains, Sheets, Nanocrystals, Nanowires, Microcrystals, and Porous Silicon. *J. Phys. Chem*. **1994**, *98* (14), 3575–3581.

Brust, M.; Walker, M.; Bethell, D.; Schiffrin, D. J.; Whyman, R. Synthesis of Thiol-Derivatised Gold Nanoparticles in a Two-Phase Liquid-Liquid System. *J. Chem. Soc. Chem. Commun*. **1994**, No. 7, 801.

Burda, C.; Chen, X.; Narayanan, R.; El-Sayed, M. a. Chemistry and Properties of Nanocrystals of Different Shapes. *Chem. Rev*. **2005**, *105* (4), 1025–1102.

CANNON, W. R.; DANFORTH, S. C.; FLINT, J. H.; HAGGERTY, J. S.; MARRA, R. A. Sinterable Ceramic Powders from Laser-Driven Reactions: I, Process Description and Modeling. *J. Am. Ceram. Soc*. **1982**, *65* (7), 324–330.

Cao, Y.; Xiao, L.; Sushko, M. L.; Wang, W.; Schwenzer, B.; Xiao, J.; Nie, Z.; Saraf, L. V; Yang, Z.; Liu, J. Sodium Ion Insertion in Hollow Carbon Nanowires for Battery Applications. *Nano Lett*. **2012**, *12*, 3783–3787.

Chan, C. K.; Patel, R. N.; O'Connell, M. J.; Korgel, B. A.; Cui, Y. Solution-Grown Silicon Nanowires for Lithium-Ion Battery Anodes. *ACS Nano* **2010**, *4*, 1443–1450.

Chan, C. K.; Peng, H.; Liu, G.; McIlwrath, K.; Zhang, X. F.; Huggins, R. A.; Cui, Y. High-Performance Lithium Battery Anodes Using Silicon Nanowires. *Nat. Nanotechnol*. **2008**, *3* (1), 31–35.

Chan, M. K. Y.; Long, B. R.; Gewirth, A. a.; Greeley, J. P. The First-Cycle Electrochemical Lithiation of Crystalline Ge: Dopant and Orientation Dependence and Comparison with Si. *J. Phys. Chem. Lett*. **2011**, *2* (24), 3092–3095.

Chan, T.-L.; Chelikowsky, J. R. Controlling Diffusion of Lithium in Silicon Nanostructures. *Nano Lett*. **2010**, *10*, 821–825.

Chandler-Henderson, R. R.; Sweryda-Krawiec, B.; Coffer, J. L. Steric Considerations in the Amine-Induced Quenching of Luminescent Porous Silicon. *J. Phys. Chem*. **1995**, *99* (21), 8851–8855.

Chang, K.-W.; Wu, J.-J. Low-Temperature Catalytic Synthesis of Gallium Nitride Nanowires. *J. Phys. Chem. B* **2002**, *106*, 7796–7799.

Chen, Q.; Sieradzki, K. Spontaneous Evolution of Bicontinuous Nanostructures in Dealloyed Li-Based Systems. *Nat. Mater.***2013**, *12*, 1102–1106.

Cheng, S.; Ren, T.; Ying, P.; Yu, R.; Zhang, W.; Zhang, J.; Li, C. Enhanced Growth of Crystalline-Amorphous Core-Shell Silicon Nanowires by Catalytic Thermal CVD Using in Situ Generated Tin Catalyst. *Sci. China Chem.* **2012**, *55* (12), 2573–2579.

Chevrier, V. L.; Ceder, G. Challenges for Na-Ion Negative Electrodes. *Journal of The Electrochemical Society*, 2011, *158*, A1011.

Cho, K. S.; Talapin, D. V.; Gaschler, W.; Murray, C. B. Designing PbSe Nanowires and Nanorings through Oriented Attachment of Nanoparticles. *J. Am. Chem. Soc.* **2005**, *127* (19), 7140–7147.

Chockla, A. M.; Bogart, T. D.; Hessel, C. M.; Klavetter, K. C.; Mullins, C. B.; Korgel, B. A. Influences of Gold, Binder and Electrolyte on Silicon Nanowire Performance in Li-Ion Batteries. *J. Phys. Chem. C* **2012**, *116*, 18079-18086.

Chockla, A. M.; Harris, J. T.; Akhavan, V. A.; Bogart, T. D.; Holmberg, V. C.; Steinhagen, C.; Mullins, C. B.; Stevenson, K. J.; Korgel, B. A. Silicon Nanowire Fabric as a Lithium Ion Battery Electrode Material. *J. Am. Chem. Soc.* **2011**, *133* (51), 20914–20921.

Chockla, A. M.; Harris, J. T.; Korgel, B. a. Colloidal Synthesis of Germanium Nanorods. *Chem. Mater.* **2011**, *23* (7), 1964–1970.

Chockla, A. M.; Holmberg, V. C.; Korgel, B. a. Germanium Nanorod Extinction Spectra: Discrete Dipole Approximation Calculations and Experiment. *J. Phys. Chem. C* **2012**, *116* (42), 22625–22630.

Chockla, A. M.; Klavetter, K. C.; Mullins, C. B.; Korgel, B. a. Solution-Grown Germanium Nanowire Anodes for Lithium-Ion Batteries. *ACS Appl. Mater. Interfaces* **2012**, *4* (9), 4658–4664.

Chockla, A. M.; Klavetter, K. C.; Mullins, C. B.; Korgel, B. A. Tin-Seeded Silicon Nanowires for High Capacity Li-Ion Batteries. *Chem. Mater.* **2012**, *24* (19), 3738–3745.

Chockla, A. M.; Korgel, B. A. Seeded Germanium Nanowire Synthesis in Solution. *J. Mater. Chem.* **2009**, *19* (7), 996.

Choi, J. W.; McDonough, J.; Jeong, S.; Yoo, J. S.; Chan, C. K.; Cui, Y. Stepwise Nanopore Evolution in One-Dimensional Nanostructures. *Nano Lett.* **2010**, *10*, 1409–1413.

Choi, S.; Kim, B.; Boudjouk, P.; Grier, D. G. Amine-Promoted Disproportionation and Redistribution of Trichlorosilane: Formation of Tetradecachlorocyclohexasilane Dianion 1. *J. Am. Chem. Soc.* **2001**, *123*, 8117–8118.

Chou, C.-Y.; Hwang, G. S. On the Origin of Anisotropic Lithiation in Crystalline Silicon over Germanium: A First Principles Study. *Appl. Surf. Sci.* **2014**, *323*, 78–81.

Chou, C.-Y.; Kim, H.; Hwang, G. S. A Comparative First-Principles Study of the Structure, Energetics, and Properties of Li–M (M= Si, Ge, Sn) Alloys. *J. Phys. Chem. C* **2011**, *115*, 20018–20026.

Chueh, Y. L.; Fan, Z.; Takei, K.; Hyunhyub, K.; Kapadia, R.; Rathore, A. a.; Miller, N.; Kyoungsik, Y.; Ming, W.; Haller, E. E.; Javey, A. Black Ge Based on Crystalline/amorphous Core/shell Nanoneedle Arrays. *Nano Lett.* **2010**, *10* (2), 520–523.

Coffa, S.; Poate, J. M.; Jacobson, D. C.; Frank, W.; Gustin, W. Determination of Diffusion Mechanisms in Amorphous Silicon. *Phys. Rev. B* **1992**, *45*, 8355–8358.

Coffa, S.; Poate, J. M.; Jacobson, D. C.; Polman, A. Impurity Trapping and Gettering in Amorphous Silicon. *Appl. Phys. Lett.* **1991**, *58*, 2916.

Coleman, N. R. B.; O'Sullivan, N.; Ryan, K. M.; Crowley, T. a.; Morris, M. a.; Spalding, T. R.; Steytler, D. C.; Holmes, J. D. Synthesis and Characterization of Dimensionally Ordered Semiconductor Nanowires within Mesoporous Silica. *J. Am. Chem. Soc.* **2001**, *123* (29), 7010–7016.

Conesa-Boj, S.; Zardo, I.; Estradé, S.; Wei, L.; Jean Alet, P.; Roca i Cabarrocas, P.; Morante, J. R.; Peiró, F.; Morral, A. F. I.; Arbiol, J. Defect Formation in Ga-Catalyzed Silicon Nanowires. *Cryst. Growth Des.* **2010**, *10* (4), 1534–1543.

Cui, Y.; Zhong, Z.; Wang, D.; Wang, W. U.; Lieber, C. M. High Performance Silicon Nanowire Field Effect Transistors. *Nano Lett.* **2003**, *3* (2), 149–152.

Cunningham, P. D.; Boercker, J. E.; Foos, E. E.; Lumb, M. P.; Smith, A. R.; Tischler, J. G.; Melinger, J. S. Enhanced Multiple Exciton Generation in Quasi-One-Dimensional Semiconductors. *Nano Lett.* **2011**, *11* (8), 3476–3481.

Darwiche, A.; Marino, C.; Sougrati, M. T.; Fraisse, B.; Stievano, L.; Monconduit, L. Better Cycling Performances of Bulk Sb in Na-Ion Batteries Compared to Li-Ion Systems: An Unexpected Electrochemical Mechanism. *J. Am. Chem. Soc.* **2012**, *134*, 20805–20811.

Davidson, F. M.; Lee, D. C.; Fanfair, D. D. D.; Korgel, B. A. Lamellar Twinning in Semiconductor Nanowires. *J. Phys. Chem. C* **2007**, *111* (7), 2929–2935.

Davidson, F. M.; Wiacek, R.; Korgel, B. a. Supercritical Fluid-Liquid-Solid Synthesis of Gallium Phosphide Nanowires. *Chem. Mater.* **2005**, *17* (2), 230–233.

Dayeh, S. a.; Picraux, S. T. Direct Observation of Nanoscale Size Effects in Ge Semiconductor Nanowire Growth. *Nano Lett.* **2010**, *10* (10), 4032–4039.

Dimov, N.; Kugino, S.; Yoshio, M. Carbon-Coated Silicon as Anode Material for Lithium Ion Batteries: Advantages and Limitations. *Electrochim. Acta* **2003**, *48*, 1579–1587.

Dong, A.; Wang, F.; Daulton, T. L.; Buhro, W. E. Solution-Liquid-Solid (SLS) Growth of ZnSe-ZnTe Quantum Wires Having Axial Heterojunctions. *Nano Lett.* **2007**, *7* (5), 1308–1313.

Dřínek, V.; Fajgar, R.; Klementová, M.; Šubrt, J. Deposition of Germanium Nanowires from Hexamethyldigermane: Influence of the Substrate Pretreatment. *Journal of The Electrochemical Society*, 2010, *157*, K218.

Dunlap, W. C. Electrical Properties of Gold-Germanium Alloys. *Physical Review*, 1953, *91*, 1282.

Egerton, R. F.; Li, P.; Malac, M. Radiation Damage in the TEM and SEM. *Micron* **2004**, *35*, 399–409.

Ellis, L. D.; Hatchard, T. D.; Obrovac, M. N. Reversible Insertion of Sodium in Tin. *J. Electrochem. Soc.* **2012**, *159*, A1801–A1805.

English, D. S.; Pell, L. E.; Yu, Z.; Barbara, P. F.; Korgel, B. a. Size Tunable Visible Luminescence from Individual Organic Monolayer Stabilized Silicon Nanocrystal Quantum Dots. *Nano Lett.* **2002**, *2* (7), 681–685.

Erlebacher, J.; Aziz, M. J.; Karma, a; Dimitrov, N.; Sieradzki, K. Evolution of Nanoporosity in Dealloying. *Nature* **2001**, *410*, 450–453.

Etacheri, V.; Marom, R.; Elazari, R.; Salitra, G.; Aurbach, D. Challenges in the Development of Advanced Li-Ion Batteries: A Review. *Energy Environ. Sci.* **2011**, *4* (9), 3243.

Fanfair, D. D.; Korgel, B. A. Bismuth Nanocrystal-Seeded III-V Semiconductor Nanowire Synthesis. *Cryst. Growth Des.* **2005**, *5* (5), 1971–1976.

Fanfair, D. D.; Korgel, B. A. Twin-Related Branching of Solution-Grown ZnSe Nanowires. *Chem. Mater.* **2007**, *19* (20), 4943–4948.

Fanfair, D. D.; Korgel, B. A. ZnE (E = S, Se, Te) Nanowires Grown by the Solution–Liquid–Solid Mechanism: Importance of Reactant Decomposition Kinetics and the Solvent. *Cryst. Growth Des.* **2008**, *8*, 3246–3252.

Farbod, B.; Cui, K.; Kalisvaart, W. P.; Kupsta, M.; Zahiri, B.; Kohandehghan, A.; Lotfabad, E. M.; Li, Z.; Luber, E. J.; Mitlin, D. Anodes for Sodium Ion Batteries Based on Tin-Germanium-Antimony Alloys. *ACS Nano* **2014**.

Fergus, J. W. Recent Developments in Cathode Materials for Lithium Ion Batteries. *J. Power Sources* **2010**, *195* (4), 939–954.

Fisher, J. C. Calculation of Diffusion Penetration Curves for Surface and Grain Boundary Diffusion. *J. Appl. Phys.***1951**, *22*, 74.

Forrest, M. D.; Schricker, A. D.; Wiacek, R. J.; Korgel, B. A. Supercritical Fluid-Liquid-Solid Synthesis of Gallium Arsenide Nanowires Seeded by Alkanethiol-Stabilized Gold Nanocrystals. **2004**, No. 7, 646–649.

Fuller, C.; Severiens, J. Mobility of Impurity Ions in Germanium and Silicon. *Phys. Rev.* **1954**, *96* (1), 21–24.

Gamalski, a D.; Tersoff, J.; Sharma, R.; Ducati, C.; Hofmann, S. Formation of Metastable Liquid Catalyst during Subeutectic Growth of Germanium Nanowires. *Nano Lett.* **2010**, *10* (8), 2972–2976.

Garnett, E.; Yang, P. Light Trapping in Silicon Nanowire Solar Cells. *Nano Lett.* **2010**, *10* (3), 1082–1087.

Ge, P. Electrochemical Intercalation of Sodium in Graphite. *Solid State Ionics* **1988**, *28-30*, 1172–1175.

Geaney, H.; Dickinson, C.; Barrett, C. A.; Ryan, K. M. High Density Germanium Nanowire Growth Directly from Copper Foil by Self-Induced Solid Seeding. *Chem. Mater.* **2011**, *23* (21), 4838–4843.

Geaney, H.; Kennedy, T.; Dickinson, C.; Mullane, E.; Singh, A.; Laffir, F.; Ryan, K. M. High Density Growth of Indium Seeded Silicon Nanowires in the Vapor Phase of a High Boiling Point Solvent. *Chem. Mater.* **2012**, *24*, 2204–2210.

Geaney, H.; Mullane, E.; Ramasse, Q. M.; Ryan, K. M. Atomically Abrupt Silicon-Germanium Axial Heterostructure Nanowires Synthesized in a Solvent Vapor Growth System. *Nano Lett.* **2013**, *13* (4), 1675–1680.

Geaney, H.; Mullane, E.; Ryan, K. M. Solution Phase Synthesis of Silicon and Germanium Nanowires. *J. Mater. Chem. C* **2013**, *1*, 4996.

Gerion, D.; Zaitseva, N.; Saw, C.; Casula, M. F.; Fakra, S.; Buuren, T. Van; Galli, G.; Li, V.; Chimiche, S. Solution Synthesis of Germanium Nanocrystals : Success and Open Challenges. **2004**.

Givargizov, E. Fundamental Aspects of VLS Growth. *J. Cryst. Growth* **1975**, *31*, 20–30.

Goodenough, J. B.; Kim, Y. Challenges for Rechargeable Li Batteries. *Chem. Mater.* **2010**, *22* (3), 587–603.

Graetz, J.; Ahn, C. C.; Yazami, R.; Fultz, B. Nanocrystalline and Thin Film Germanium Electrodes with High Lithium Capacity and High Rate Capabilities. *J. Electrochem. Soc.* **2004**, *151* (5), A698.

Grebinski, J. W.; Hull, K. L.; Zhang, J.; Kosel, T. H.; Kuno, M. Solution-Based Straight and Branched CdSe Nanowires. *Chem. Mater.* **2004**, 16, 5260-5272.

Greytak, A. B.; Lauhon, L. J.; Gudiksen, M. S.; Lieber, C. M. Growth and Transport Properties of Complementary Germanium Nanowire Field-Effect Transistors. *Appl. Phys. Lett.* **2004**, *84* (21), 4176–4178.

Gu, M.; Kushima, A.; Shao, Y.; Zhang, J.-G.; Liu, J.; Browning, N. D.; Li, J.; Wang, C. Probing the Failure Mechanism of SnO2 Nanowires for Sodium-Ion Batteries. *Nano Lett.* **2013**, *13*, 5203–5211.

Gu, M.; Parent, L. R.; Mehdi, B. L.; Unocic, R. R.; McDowell, M. T.; Sacci, R. L.; Xu, W.; Connell, J. G.; Xu, P.; Abellan, P.; Chen, X.; Zhang, Y.; Perea, D. E.; Evans, J. E.; Lauhon, L. J.; Zhang, J.-G.; Liu, J.; Browning, N. D.; Cui, Y.; Arslan, I.; Wang, C.-M. Demonstration of an Electrochemical Liquid Cell for Operando Transmission Electron Microscopy Observation of the Lithiation/delithiation Behavior of Si Nanowire Battery Anodes. *Nano Lett.* **2013**, *13* (12), 6106–6112.

Gu, M.; Wang, Z.; Connell, J. G.; Perea, D. E.; Lauhon, L. J.; Gao, F.; Wang, C. Electronic Origin for the Phase Transition from Amorphous Li(x)Si to Crystalline Li15Si4. *ACS Nano* **2013**, *7*, 6303–6309.

Guichard, A. R.; Barsic, D. N.; Sharma, S.; Kamins, T. I.; Brongersma, M. L. Tunable Light Emission from Quantum-Confined Excitons in TiSi 2-Catalyzed Silicon Nanowires. *Nano Lett.* **2006**, *6* (9), 2140–2144.

Guichard, A. R.; Kekatpure, R. D.; Brongersma, M. L.; Kamins, T. I. Temperature-Dependent Auger Recombination Dynamics in Luminescent Silicon Nanowires. *Phys. Rev. B - Condens. Matter Mater. Phys.* **2008**, *78* (23), 235422.

Guichard, A.; Kekatpure, R.; Brongersma, M.; Kamins, T. Temperature-Dependent Auger Recombination Dynamics in Luminescent Silicon Nanowires. *Phys. Rev. B* **2008**, *78*, 235422.

Hanrath, T.; Korgel, B. A. Chemical Surface Passivation of Ge Nanowires. *J. Am. Chem. Soc.* **2004**, *126* (47), 15466–15472.

Hanrath, T.; Korgel, B. a. Crystallography and Surface Faceting of Germanium Nanowires. *Small* **2005**, *1* (7), 717–721.

Hanrath, T.; Korgel, B. A. Nucleation and Growth of Germanium Nanowires Seeded by Organic Monolayer-Coated Gold Nanocrystals. *J. Am. Chem. Soc.* **2002**, *124* (7), 1424–1429.

Hanrath, T.; Korgel, B. A. Supercritical Fluid–Liquid–Solid (SFLS) Synthesis of Si and Ge Nanowires Seeded by Colloidal Metal Nanocrystals. *Adv. Mater.* **2003**, *15* (5), 437–440.

Harris, J. T.; Hueso, J. L.; Korgel, B. a. Hydrogenated Amorphous Silicon (a-Si:H) Colloids. *Chem. Mater.* **2010**, *22* (23), 6378–6383.

Hatchard, T. D.; Dahn, J. R. Study of the Electrochemical Performance of Sputtered $Si_{1-x}Sn_x$ Films. *J. Electrochem. Soc.* **2004**, *151* (10), A1628.

Hayashi, S.; Nagareda, T.; Kanzawa, Y.; Yamamoto, K. Photoluminescence of Si-Rich SiO2 Films: Si Clusters as Luminescent Centers. *Jpn. J. Appl. Phys.* **1993**, *32* (Part 1, No. 9A), 3840–3845.

He, M.; Kravchyk, K.; Walter, M.; Kovalenko, M. V. Monodisperse Antimony Nanocrystals for High-Rate Li-Ion and Na-Ion Battery Anodes: Nano versus Bulk. *Nano Lett.* **2014**, *14*, 1255–1262.

He, Y.; Piper, D. M.; Gu, M.; Travis, J. J.; George, S. M.; Lee, S.; Genc, A.; Pullan, L.; Liu, J.; Mao, S. X.; Zhang, J.; Ban, C.; Wang, C. In Situ Transmission Electron Microscopy Probing of Native Oxide and Artificial Layers on Silicon Nanoparticles for Lithium Ion Batteries. *ACS Nano* **2014**, *8*, 11816–11823.

Hedaya, E. Techniques of Flash Vacuum Pyrolysis. Cyclopentadienyl Radical and Its Dimer. *Acc. Chem. Res.* **1969**, *2* (12), 367–373.

Heitsch, A. T.; Fanfair, D. D.; Tuan, H.-Y.; Korgel, B. A. Solution-Liquid-Solid (SLS) Growth of Silicon Nanowires. *J. Am. Chem. Soc.* **2008**, *130* (16), 5436–5437.

Heitsch, A. T.; Hessel, C. M.; Akhavan, V. A.; Korgel, B. A. Colloidal Silicon Nanorod Synthesis. *Nano Lett.* **2009**, *9* (8), 3042–3047.

Henderson, E. J.; Hessel, C. M.; Veinot, J. G. C. Synthesis and Photoluminescent Properties of Size-Controlled Germanium Nanocrystals from Phenyl Trichlorogermane-Derived Polymers. *J. Am. Chem. Soc.* **2008**, *130* (11), 3624–3632.

Hessel, C. M.; Heitsch, A. T.; Korgel, B. A. Gold Seed Removal from the Tips of Silicon Nanorods. *Nano Lett.* **2010**, *10* (1), 176–180.

Hessel, C. M.; Henderson, E. J.; Veinot, J. G. C.; Uni, V.; February, R. V; Re, V.; Recei, M.; August, V. Hydrogen Silsesquioxane : A Molecular Precursor for Nanocrystalline Si-SiO2 Composites and Freestanding Hydride-Surface-Terminated Silicon Nanoparticles. **2006**, No. 1, 6139–6146.

Hessel, C. M.; Reid, D.; Panthani, M. G.; Rasch, M. R.; Goodfellow, B. W.; Wei, J.; Fujii, H.; Akhavan, V.; Korgel, B. a. Synthesis of Ligand-Stabilized Silicon Nanocrystals with Size-Dependent Photoluminescence Spanning Visible to near-Infrared Wavelengths. *Chem. Mater.* **2012**, *24* (2), 393–401.

Hessel, C. M.; Wei, J.; Reid, D.; Fujii, H.; Downer, M. C.; Korgel, B. a. Raman Spectroscopy of Oxide-Embedded and Ligand-Stabilized Silicon Nanocrystals. *J. Phys. Chem. Lett.* **2012**, *3* (9), 1089–1093.

Hochbaum, A. I.; Yang, P. Semiconductor Nanowires for Energy Conversion. *Chem. Rev.* **2010**, *110* (1), 527–546.

Holmberg, V. C.; Bogart, T. D.; Chockla, A. M.; Hessel, C. M.; Korgel, B. a. Optical Properties of Silicon and Germanium Nanowire Fabric. *J. Phys. Chem. C* **2012**, *116*, 22486–22491.

Holmberg, V. C.; Korgel, B. A. Corrosion Resistance of Thiol- and Alkene-Passivated Germanium Nanowires. *Chem. Mater.* **2010**, *22* (12), 3698–3703.

Holmberg, V. C.; Panthani, M. G.; Korgel, B. a. Phase Transitions, Melting Dynamics, and Solid-State Diffusion in a Nano Test Tube. *Science* **2009**, *326* (5951), 405–407.

Holmberg, V. C.; Rasch, M. R.; Korgel, B. a. PEGylation of Carboxylic Acid-Functionalized Germanium Nanowires. *Langmuir* **2010**, *26* (17), 14241–14246.

Holmes, J. D. Control of Thickness and Orientation of Solution-Grown Silicon Nanowires. *Science*, 2000, *287*, 1471–1473.

Htoon, H.; Hollingworth, J. a.; Malko, a. V.; Dickerson, R.; Klimov, V. I. Light Amplification in Semiconductor Nanocrystals: Quantum Rods versus Quantum Dots. *Appl. Phys. Lett.* **2003**, *82* (26), 4776–4778.

Hu, J.; Odom, T. W.; Lieber, C. M. Chemistry and Physics in One Dimension: Synthesis and Properties of Nanowires and Nanotubes. *Accounts of Chemical Research*, 1999, *32*, 435–445.

Huang, J. Y.; Zhong, L.; Wang, C. M.; Sullivan, J. P.; Xu, W.; Zhang, L. Q.; Mao, S. X.; Hudak, N. S.; Liu, X. H.; Subramanian, A.; Fan, H.; Qi, L.; Kushima, A.; Li, J. In Situ Observation of the Electrochemical Lithiation of a Single SnO_2 Nanowire Electrode. *Science* **2010**, *330* (6010), 1515–1520.

Huang, R.; Fan, X.; Shen, W.; Zhu, J. Carbon-Coated Silicon Nanowire Array Films for High-Performance Lithium-Ion Battery Anodes. *Appl. Phys. Lett.* **2009**, *95*, 133119.

Iyer, G. R. S.; Hobbie, E. K.; Guruvenket, S.; Hoey, J. M.; Anderson, K. J.; Lovaasen, J.; Gette, C.; Schulz, D. L.; Swenson, O. F.; Elangovan, A.; Boudjouk, P. Solution-Based Synthesis of Crystalline Silicon from Liquid Silane through Laser and Chemical Annealing. *ACS Appl. Mater. Interfaces* **2012**, *4*, 2680–2685.

Jeon, M.; Kamisako, K. Synthesis and Characterization of Silicon Nanowires Using Tin Catalyst for Solar Cells Application. *Mater. Lett.* **2009**, *63* (9-10), 777–779.

Jun, Y. W.; Lee, S. M.; Kang, N. J.; Cheon, J. Controlled Synthesis of Multi-Armed CdS Nanorod Architectures Using Monosurfactant System. *Journal of the American Chemical Society*, 2001, *123*, 5150–5151.

Jurbergs, D.; Rogojina, E.; Mangolini, L.; Kortshagen, U. Silicon Nanocrystals with Ensemble Quantum Yields Exceeding 60%. *Appl. Phys. Lett.* **2006**, *88* (23), 60–63.

Kan, S.; Mokari, T.; Rothenberg, E.; Banin, U. Synthesis and Size-Dependent Properties of Zinc-Blende Semiconductor Quantum Rods. *Nat. Mater.* **2003**, *2* (3), 155–158.

Kang, K.; Gu, G. H.; Kim, D. A.; Park, C. G.; Jo, M. H. Self-Organized Growth of Ge Nanowires from Ni-Cu Bulk Alloys. *Chem. Mater.* **2008**, *20* (21), 6577–6579.

Kang, K.; Kim, D. A.; Lee, H. S.; Kim, C. J.; Yang, J. E.; Jo, M. H. Low-Temperature Deterministic Growth of Ge Nanowires Using Cu Solid Catalysts. *Adv. Mater.* **2008**, *20* (24), 4684–4690.

Kanoh, H.; Sugiura, O.; Matsumura, M. Chemical Vapor Deposition of Amorphous Silicon Using Tetrasilane. *Japanese Journal of Applied Physics*, 1993, *32*, 2613–2619.

Kennedy, T.; Mullane, E.; Geaney, H.; Osiak, M.; O'Dwyer, C.; Ryan, K. M. High-Performance Germanium Nanowire-Based Lithium-Ion Battery Anodes Extending over 1000 Cycles through in Situ Formation of a Continuous Porous Network. *Nano Lett.* **2014**, *14*, 716–723.

Kim, S.-W.; Seo, D.-H.; Ma, X.; Ceder, G.; Kang, K. Electrode Materials for Rechargeable Sodium-Ion Batteries: Potential Alternatives to Current Lithium-Ion Batteries. *Adv. Energy Mater.* **2012**, *2*, 710–721.

Kodambaka, S.; Tersoff, J.; Reuter, M. C.; Ross, F. M. Diameter-Independent Kinetics in the Vapor-Liquid-Solid Growth of Si Nanowires. *Phys. Rev. Lett.* **2006**, *96* (9), 1–4.

Kodambaka, S.; Tersoff, J.; Reuter, M. C.; Ross, F. M. Germanium Nanowire Growth below the Eutectic Temperature. *Science* **2007**, *316* (5825), 729–732.

Kohandehghan, A.; Cui, K.; Kupsta, M.; Ding, J.; Memarzadeh Lotfabad, E.; Kalisvaart, W. P.; Mitlin, D. Activation with Li Enables Facile Sodium Storage in Germanium. *Nano Lett.* **2014**, *14* (10), 5873–5882.

Kohandehghan, A.; Cui, K.; Kupsta, M.; Memarzadeh, E.; Kalisvaart, P.; Mitlin, D. Nanometer-Scale Sn Coatings Improve the Performance of Silicon Nanowire LIB Anodes. *J. Mater. Chem. A* **2014**, *2*, 11261-11279.

Kӧnenkamp, R.; Word, R. C.; Schlegel, C. Vertical Nanowire Light-Emitting Diode. *Appl. Phys. Lett.* **2004**, *85* (24), 6004.

Kong, M.; Noh, J.; Byun, D.; Lee, J. Electrochemical Characteristics of Phosphorus Doped Silicon and Graphite Composite for the Anode Materials of Lithium Secondary Batteries. *J. Electroceramics* **2008**, *23*, 376–381.

Koppes, J. P.; Muza, A. R.; Stach, E. A.; Handwerker, C. H. Size-Dependent Melting Properties of Small Tin Particles: Nanocalorimetric Measurements. *Phys. Rev. Lett.* **2010**, *104*, 189601.

Korgel, B. a; Tuan, H. Y.; Ghezelbash, A. Silicon Nanowires and Silica Nanotubes Seeded by Copper Nanoparticles in an Organic Solvent. *Chem. Mater.* **2008**, *20* (6), 2306–2313.

Korgel, B. A. Nanomaterials Developments for Higher-Performance Lithium Ion Batteries. *J. Phys. Chem. Lett.* **2014**, *5*, 749-750.

Korgel, B. A. Semiconductor Nanowires: A Chemical Engineering Perspective. *AIChE J.* **2009**, *55* (4), 842–848.

Kovalenko, I.; Zdyrko, B.; Magasinski, A.; Hertzberg, B.; Milicev, Z.; Burtovyy, R.; Luzinov, I.; Yushin, G. A Major Constituent of Brown Algae for Use in High-Capacity Li-Ion Batteries. *Science* **2011**, *334*, 75-79.

Kovalenko, M. V; Manna, L.; Cabot, A.; Hens, Z.; Talapin, D. V; Kagan, C. R.; Klimov, X. V. I.; Rogach, A. L.; Reiss, P.; Milliron, D. J.; Guyot-sionnnest, P.; Konstantatos, G.; Parak, W. J.; Hyeon, T.; Korgel, B. A.; Murray, C. B.; Heiss, W. Prospects of Nanoscience with Nanocrystals. *ACS Nano* **2015**, *9* (2), 1012–1057.

Kuno, M. An Overview of Solution-Based Semiconductor Nanowires: Synthesis and Optical Studies. *Phys. Chem. Chem. Phys.* **2008**, *10* (5), 620.

Kuno, M.; Ahmad, O.; Protasenko, V.; Bacinello, D.; Kosel, T. H. Solution-Based Straight and Branched CdTe Nanowires. *Chem. Mater.* **2006**, *18* (24), 5722–5732.

Laforge, B.; Levan-Jodin, L.; Salot, R.; Billard, a. Study of Germanium as Electrode in Thin-Film Battery. *J. Electrochem. Soc.* **2008**, *155* (2), A181.

Laïk, B.; Eude, L.; Pereira-Ramos, J.-P.; Cojocaru, C. S.; Pribat, D.; Rouvière, E. Silicon Nanowires as Negative Electrode for Lithium-Ion Microbatteries. *Electrochim. Acta* **2008**, *53*, 5528–5532.

Law, M.; Goldberger, J.; Yang, P. Semiconductor Nanowires and Nanotubes. *Annu. Rev. Mater. Res.* **2004**, *34* (1), 83–122.

Lee, D. C.; Hanrath, T.; Korgel, B. a. The Role of Precursor-Decomposition Kinetics in Silicon-Nanowire Synthesis in Organic Solvents. *Angew. Chem. Int. Ed. Engl.* **2005**, *44*, 3573–3577.

Lee, D. C.; Smith, D. K.; Heitsch, A. T.; Korgel, B. A. Colloidal Magnetic Nanocrystals: Synthesis, Properties and Applications. *Annual Reports Section "C" (Physical Chemistry)*, 2007, *103*, 351.

Lee, S. W.; McDowell, M. T.; Berla, L. A.; Nix, W. D.; Cui, Y. Fracture of Crystalline Silicon Nanopillars during Electrochemical Lithium Insertion. *Proc. Natl. Acad. Sci. U. S. A.* **2012**, *109*, 4080–4085.

Lee, S. W.; Ryu, I.; Nix, W. D.; Cui, Y. Fracture of Crystalline Germanium during Electrochemical Lithium Insertion. *Extrem. Mech. Lett.* **2015**, *2*, 15–19.

Lee, S.; McDowell, M.; Choi, J.; Cui, Y. Anomalous Shape Changes of Silicon Nanopillars by Electrochemical Lithiation. *Nano Lett*. **2011**, 3034–3039.

Legrain, F.; Malyi, O. I.; Manzhos, S. Comparative Computational Study of the Diffusion of Li, Na, and Mg in Silicon Including the Effect of Vibrations. *Solid State Ionics* **2013**, *253*, 157–163.

Lensch-Falk, J. L.; Hemesath, E. R.; Perea, D. E.; Lauhon, L. J. Alternative Catalysts for VSS Growth of Silicon and Germanium Nanowires. *J. Mater. Chem.* **2009**, *19* (7), 849.

Lewis, K. E.; Smith, G. P. Bond Dissociation Energies in Ferrocene. *J. Am. Chem. Soc.* **1984**, *106* (16), 4650–4651.

Li, X.; He, Y.; Talukdar, S. S.; Swihart, M. T. Process for Preparing Macroscopic Quantities of Brightly Photoluminescent Silicon Nanoparticles with Emission Spanning the Visible Spectrum. *Langmuir* **2003**, *19* (20), 8490–8496.

Li, Y.; Qian, F.; Xiang, J.; Lieber, C. Nanowire Electronic and Optoelectronic Devices. *Mater. today* **2006**, *9* (10), 18–27.

Li, Z.; Kornowski, A.; Myalitsin, A.; Mews, A. Formation and Function of Bismuth Nanocatalysts for the Solution-Liquid-Solid Synthesis of CdSe Nanowires. *Small* **2008**, *4* (10), 1698–1702.

Liang, W.; Yang, H.; Fan, F.; Liu, Y.; Liu, X. H.; Huang, J. Y.; Zhu, T.; Zhang, S. Tough Germanium Nanoparticles under Electrochemical Cycling. *ACS Nano* **2013**, *7* (4), 3427–3433.

Liu, X. H.; Fan, F.; Yang, H.; Zhang, S.; Huang, J. Y.; Zhu, T. Self-Limiting Lithiation in Silicon Nanowires. *ACS Nano* **2013**, *7*, 1495–1503.

Liu, X. H.; Huang, J. Y. In Situ TEM Electrochemistry of Anode Materials in Lithium Ion Batteries. *Energy Environ. Sci.* **2011**, *4*, 3844.

Liu, X. H.; Huang, S.; Picraux, S. T.; Li, J.; Zhu, T.; Huang, J. Y. Reversible Nanopore Formation in Ge Nanowires during Lithiation-Delithiation Cycling: An in Situ Transmission Electron Microscopy Study. *Nano Lett*. **2011**, *11* (9), 3991–3997.

Liu, X. H.; Liu, Y.; Kushima, A.; Zhang, S.; Zhu, T.; Li, J.; Huang, J. Y. In Situ TEM Experiments of Electrochemical Lithiation and Delithiation of Individual Nanostructures. *Adv. Energy Mater*. **2012**, *2* (7), 722–741.

Liu, X. H.; Wang, J. W.; Huang, S.; Fan, F.; Huang, X.; Liu, Y.; Krylyuk, S.; Yoo, J.; Dayeh, S. a; Davydov, A. V; Mao, S. X.; Picraux, S. T.; Zhang, S.; Li, J.; Zhu, T.; Huang, J. Y. In Situ Atomic-Scale Imaging of Electrochemical Lithiation in Silicon. *Nat. Nanotechnol*. **2012**, *7*, 749–756.

Liu, X. H.; Zhang, L. Q.; Zhong, L.; Liu, Y.; Zheng, H.; Wang, J. W.; Cho, J.-H.; Dayeh, S. A; Picraux, S. T.; Sullivan, J. P.; Mao, S. X.; Ye, Z. Z.; Huang, J. Y. Ultrafast

Electrochemical Lithiation of Individual Si Nanowire Anodes. *Nano Lett*. **2011**, *11*, 2251–2258.

Liu, X. H.; Zheng, H.; Zhong, L.; Huang, S.; Karki, K.; Zhang, L. Q.; Liu, Y.; Kushima, A.; Liang, W. T.; Wang, J. W.; Cho, J.-H.; Epstein, E.; Dayeh, S. a; Picraux, S. T.; Zhu, T.; Li, J.; Sullivan, J. P.; Cumings, J.; Wang, C.; Mao, S. X.; Ye, Z. Z.; Zhang, S.; Huang, J. Y. Anisotropic Swelling and Fracture of Silicon Nanowires during Lithiation. *Nano Lett*. **2011**, *11* (8), 3312–3318.

Liu, X. H.; Zhong, L.; Huang, S.; Mao, S. X.; Zhu, T.; Huang, J. Y. Size-Dependent Fracture of Silicon Nanoparticles during Lithiation. *ACS Nano* **2012**, *6* (2), 1522–1531.

Liu, Y.; Fan, F.; Wang, J.; Liu, Y.; Chen, H.; Jungjohann, K. L.; Xu, Y.; Zhu, Y.; Bigio, D.; Zhu, T.; Wang, C. In Situ Transmission Electron Microscopy Study of Electrochemical Sodiation and Potassiation of Carbon Nanofibers. *Nano Lett*. **2014**, *14*, 3445–3452.

Loscutoff, P. W.; Bent, S. F. Reactivity of the Germanium Surface: Chemical Passivation and Functionalization. *Annu. Rev. Phys. Chem*. **2006**, *57*, 467–495.

Lu, X.; Fanfair, D. D.; Johnston, K. P.; Korgel, B. A. High Yield Solution-Liquid-Solid Synthesis of Germanium Nanowires. *J. Am. Chem. Soc*. **2005**, *127* (45), 15718–15719.

Lu, X.; Hanrath, T.; Johnston, K. P.; Korgel, B. A. Growth of Single Crystal Silicon Nanowires in Supercritical Solution from Tethered Gold Particles on a Silicon Substrate. *Nano Lett*. **2003**, *3*, 93–99.

Lu, X.; Hessel, C. M.; Yu, Y.; Bogart, T. D.; Korgel, B. A. Colloidal Luminescent Silicon Nanorods. *Nano Lett*. **2013**, *13* (7), 3101–3105.

Lu, X.; Korgel, B. A. A Single-Step Reaction for Silicon and Germanium Nanorods. *Chem. - A Eur. J*. **2014**, *20*, 5874–5879.

Lu, X.; Korgel, B. a.; Johnston, K. P. High Yield of Germanium Nanocrystals Synthesized from Germanium Diiodide in Solution. *Chem. Mater*. **2005**, *17* (25), 6479–6485.

Lu, Z. H.; Lockwood, D. J.; Baribeau, J.-M. Quantum Confinement and Light Emission in SiO2/Si Superlattices. *Nature* **1995**, *378* (6554), 258–260.

Luo, L.; Wu, J.; Luo, J.; Huang, J.; Dravid, V. P. Dynamics of Electrochemical Lithiation/delithiation of Graphene-Encapsulated Silicon Nanoparticles Studied by in-Situ TEM. *Sci. Rep*. **2014**, *4*, 3863.

Mangolini, L.; Kortshagen, U. Plasma-Assisted Synthesis of Silicon Nanocrystal Inks. *Adv. Mater*. **2007**, *19* (18), 2513–2519.

Mangolini, L.; Thimsen, E.; Kortshagen, U. High-Yield Plasma Synthesis of Luminescent Silicon Nanocrystals. *Nano Lett*. **2005**, *5* (4), 655–659.

Manna, L.; Scher, E. C.; Alivisatos, a. P. Synthesis of Soluble and Processable Rod-, Arrow-, Teardrop-, and Tetrapod-Shaped CdSe Nanocrystals. *J. Am. Chem. Soc*. **2000**, *122* (51), 12700–12706.

Marom, R.; Amalraj, S. F.; Leifer, N.; Jacob, D.; Aurbach, D. A Review of Advanced and Practical Lithium Battery Materials. *J. Mater. Chem*. **2011**, *21* (27), 9938.

Mastronardi, M. L.; Hennrich, F.; Henderson, E. J.; Maier-Flaig, F.; Blum, C.; Reichenbach, J.; Lemmer, U.; Kübel, C.; Wang, D.; Kappes, M. M.; Ozin, G. a. Preparation of Monodisperse Silicon Nanocrystals Using Density Gradient Ultracentrifugation. *J. Am. Chem. Soc*. **2011**, *133* (31), 11928–11931.

Mastronardi, M. L.; Maier-Flaig, F.; Faulkner, D.; Henderson, E. J.; Kübel, C.; Lemmer, U.; Ozin, G. a. Size-Dependent Absolute Quantum Yields for Size-Separated Colloidally-Stable Silicon Nanocrystals. *Nano Lett*. **2012**, *12* (1), 337–342.

Masuda, T.; Matsuki, Y.; Shimoda, T. Pyrolytic Transformation from Polydihydrosilane to Hydrogenated Amorphous Silicon Film. *Thin Solid Films* **2012**, *520*, 6603–6607.

McDowell, M. T.; Lee, S. W.; Harris, J. T.; Korgel, B. A.; Wang, C.; Nix, W. D.; Cui, Y. In Situ TEM of Two-Phase Lithiation of Amorphous Silicon Nanospheres. *Nano Lett*.**2013**, *13*, 758–764.

Mohamed, M. B.; Burda, C.; El-Sayed, M. a. Shape Dependent Ultrafast Relaxation Dynamics of CdSe Nanocrystals: Nanorods vs Nanodots. *Nano Lett*. **2001**, *1* (11), 589–593.

Moisala, A.; Nasibulin, A. G.; Brown, D. P.; Jiang, H.; Khriachtchev, L.; Kauppinen, E. I. Single-Walled Carbon Nanotube Synthesis Using Ferrocene and Iron Pentacarbonyl in a Laminar Flow Reactor. *Chem. Eng. Sci*. **2006**, *61* (13), 4393–4402.

Mullane, E.; Geaney, H.; Ryan, K. M. Size Controlled Growth of Germanium Nanorods and Nanowires by Solution Pyrolysis Directly on a Substrate. *Chem. Commun. (Camb)*. **2012**, *48* (44), 5446–5448.

Mullane, E.; Kennedy, T.; Geaney, H.; Dickinson, C.; Ryan, K. M. Synthesis of Tin Catalyzed Silicon and Germanium Nanowires in a Solvent–Vapor System and Optimization of the Seed/Nanowire Interface for Dual Lithium Cycling. *Chem. Mater*. **2013**, *25* (9), 1816–1822.

Murray, C. B.; Kagan, C. R.; Bawendi, M. G. SYNTHESIS AND CHARACTERIZATION OF MONODISPERSE NANOCRYSTALS AND CLOSE-PACKED NANOCRYSTAL ASSEMBLIES. *Annu. Rev. Mater. Res*. **2000**, *30* (1), 545–610.

Nash, A.; Nash, P. The Ge–Ni (Germanium-Nickel) System. *Bull. Alloy Phase Diagrams* **1987**, *8* (3), 255–264.

Nedeljković, J. M.; Mićić, O. I.; Ahrenkiel, S. P.; Miedaner, A.; Nozik, A. J. Growth of InP Nanostructures via Reaction of Indium Droplets with Phosphide Ions: Synthesis of InP Quantum Rods and InP-TiO2 Composites. *J. Am. Chem. Soc.* **2004**, *126* (8), 2632–2639.

Ng, S.-H.; Wang, J.; Wexler, D.; Konstantinov, K.; Guo, Z.-P.; Liu, H.-K. Highly Reversible Lithium Storage in Spheroidal Carbon-Coated Silicon Nanocomposites as Anodes for Lithium-Ion Batteries. *Angew. Chem. Int. Ed.* **2006**, *45*, 6896–6899.

Ngo, L. T.; Almécija, D.; Sader, J. E.; Daly, B.; Petkov, N.; Holmes, J. D.; Erts, D.; Boland, J. J. Ultimate-Strength Germanium Nanowires. *Nano Lett.* **2006**, *6* (12), 2964–2968.

Nitta, N.; Wu, F.; Lee, J. T.; Yushin, G. Li-Ion Battery Materials: Present and Future. *Mater. Today* **2015**, *18* (5), 252–264.

Obrovac, M. N.; Christensen, L. Structural Changes in Silicon Anodes during Lithium Insertion/Extraction. *Electrochem. Solid-State Lett.* **2004**, *7* (5), A93.

Obrovac, M. N.; Krause, L. J. Reversible Cycling of Crystalline Silicon Powder. *J. Electrochem. Soc.* **2007**, *154*, A103.

Okamoto, H. Supplemental Literature Review of Binary Phase Diagrams: Al-Br, B-Cd, Cd-Mg, Cd-Ti, Er-Fe, Fe-Nd, Ge-Na, Ge-Ni, Ge-Sc, Hf-W, Pb-Yb, and Re-Ti. *J. Phase Equilibria Diffus.* **2013**, *35*, 195–207.

Okamoto, H.; Massalski, T. B. The Au–Ge (Gold-Germanium) System. *Bull. Alloy Phase Diagrams* **1984**, *5* (6), 601–610.

Olesinski, R.; Abbaschian, G. The Si– Sn (Silicon– Tin) System. *Bull. Alloy Phase Diagrams* **1984**, *5*, 273–276.

Ouyang, L.; Maher, K. N.; Yu, C. L.; McCarty, J.; Park, H. Catalyst-Assisted Solution-Liquid-Solid Synthesis of CdS/CdSe Nanorod Heterostructures. *J. Am. Chem. Soc.* **2007**, *129* (1), 133–138.

Palomares, V.; Casas-Cabanas, M.; Castillo-Martínez, E.; Han, M. H.; Rojo, T. Update on Na-Based Battery Materials. A Growing Research Path. *Energy Environ. Sci.* **2013**, *6*, 2312.

Park, J.; Kang, E.; Son, S. U.; Park, H. M.; Lee, M. K.; Kim, J.; Kim, K. W.; Noh, H. J.; Park, J. H.; Bae, C. J.; Park, J. G.; Hyeon, T. Monodisperse Nanoparticles of Ni and NiO: Synthesis, Characterization, Self-Assembled Superlattices, and Catalytic Applications in the Suzuki Coupling Reaction. *Adv. Mater.* **2005**, *17* (4), 429–434.

Park, J.; Koo, B.; Yoon, K. Y.; Hwang, Y.; Kang, M.; Park, J. G.; Hyeon, T. Generalized Synthesis of Metal Phosphide Nanorods via Thermal Decomposition of Continuously Delivered Metal-Phosphine Complexes Using a Syringe Pump. *J. Am. Chem. Soc.* **2005**, *127* (23), 8433–8440.

Pavesi, L.; Dal Negro, L.; Mazzoleni, C.; Franzò, G.; Priolo, F. Optical Gain in Silicon Nanocrystals. *Nature* **2000**, *408* (6811), 440–444.

Pell, E. Diffusion Rate of Li in Si at Low Temperatures. *Phys. Rev.***1960**, *119*, 1222–1225.

Pell, L. E.; Schricker, A. D.; Mikulec, F. V; Korgel, B. a. Synthesis of Amorphous Silicon Colloids by Trisilane Thermolysis in High Temperature Supercritical Solvents. *Langmuir* **2004**, *20* (16), 6546–6548.

Peng, X.; Manna, L.; Yang, W.; Wickham, J.; Scher, E.; Kadavanich, A.; Alivisatos, A. Shape Control of CdSe Nanocrystals. *Nature* **2000**, *404* (6773), 59–61.

Peng, Z. A.; Peng, X. Formation of High-Quality CdTe, CdSe, and CdS Nanocrystals Using CdO as Precursor. *J. Am. Chem. Soc.* 2001, *123*, 183–184.

Penn, R. L. Imperfect Oriented Attachment: Dislocation Generation in Defect-Free Nanocrystals. *Science* **1998**, *281* (5379), 969–971.

Puthussery, J.; Kosel, T. H.; Kuno, M. Facile Synthesis and Size Control of II-VI Nanowires Using Bismuth Salts. *Small* **2009**, *5* (10), 1112–1116.

Qian, F.; Gradecak, S.; Li, Y.; Wen, C.-Y.; Lieber, C. M. Core/multishell Nanowire Heterostructures as Multicolor, High-Efficiency Light-Emitting Diodes. *Nano Lett.* **2005**, *5* (11), 2287–2291.

Qian, J.; Chen, Y.; Wu, L.; Cao, Y.; Ai, X.; Yang, H. High Capacity Na-Storage and Superior Cyclability of Nanocomposite Sb/C Anode for Na-Ion Batteries. *Chem. Commun. (Camb).* **2012**, *48*, 7070–7072.

Rathi, S. J.; Jariwala, B. N.; Beach, J. D.; Stradins, P.; Taylor, P. C.; Weng, X.; Ke, Y.; Redwing, J. M.; Agarwal, S.; Collins, R. T. Tin-Catalyzed Plasma-Assisted Growth of Silicon Nanowires. *J. Phys. Chem. C* **2011**, *115* (10), 3833–3839.

Read, C. G.; Biacchi, A. J.; Schaak, R. E. Au-Ge and Ag-Ge Heterodimers with Tunable Domain Sizes: A Supersaturation-Precipitation Route to Colloidal Hybrid Nanoparticles. *Chem. Mater.* **2013**.

Richards, B. T.; Gaskey, B.; Levin, B. D. A.; Whitham, K.; Muller, D.; Hanrath, T. Direct Growth of Germanium and Silicon Nanowires on Metal Films. *J. Mater. Chem. C* **2014**, *2* (10), 1869.

Robel, I.; Bunker, B. a.; Kamat, P. V.; Kuno, M. Exciton Recombination Dynamics in CdSe Nanowires: Bimolecular to Three-Carrier Auger Kinetics. *Nano Lett.* **2006**, *6* (7), 1344–1349.

Ruddy, D. A.; Johnson, J. C.; Smith, E. R.; Neale, N. R. Size and Bandgap Control in the Solution-Phase Synthesis of near-Infrared-Emitting Germanium Nanocrystals. *ACS Nano* **2010**, *4* (12), 7459–7466.

Ruffo, R.; Hong, S. S.; Chan, C. K.; Huggins, R. A.; Cui, Y. Impedance Analysis of Silicon Nanowire Lithium Ion Battery Anodes. *J. Phys. Chem. C* **2009**, *113*, 11390–11398.

Sankaran, R. M.; Holunga, D.; Flagan, R. C.; Giapis, K. P. Synthesis of Blue Luminescent Si Nanoparticles Using Atmospheric-Pressure Microdischarges. *Nano Lett.* **2005**, *5* (3), 537–541.

Saunders, A. E.; Ghezelbash, A.; Sood, P.; Korgel, B. a. Synthesis of High Aspect Ratio Quantum-Size CdS Nanorods and Their Surface-Dependent Photoluminescence. *Langmuir* **2008**, *24* (16), 9043–9049.

Schmidt, V.; Senz, S.; Gösele, U. Diameter Dependence of the Growth Velocity of Silicon Nanowires Synthesized via the Vapor-Liquid-Solid Mechanism. *Phys. Rev. B* **2007**, *75*, 045335.

Schmidt, V.; Wittemann, J. V; Gösele, U. Growth, Thermodynamics, and Electrical Properties of Silicon Nanowires. *Chem. Rev.* **2010**, *110* (1), 361–388.

Schmidt, V.; Wittemann, J. V.; Senz, S.; Gösele, U. Silicon Nanowires: A Review on Aspects of Their Growth and Their Electrical Properties. *Adv. Mater.* **2009**, *21*, 2681–2702.

Schott, V.; Fähnle, M.; Madden, P. A. Theory of Self-Diffusion in Alkali Metals: I. Results for Monovacancies in Li, Na, and K. *J. Phys. Condens. Matter* **2000**, *12*, 1171–1194.

Shabaev, a.; Efros, A. L. 1D Exciton Spectroscopy of Semiconductor Nanorods. *Nano Lett.* **2004**, *4* (10), 1821–1825.

Shieh, F.; Saunders, A. E.; Korgel, B. a. General Shape Control of Colloidal CdS, CdSe, CdTe Quantum Rods and Quantum Rod Heterostructures. *J. Phys. Chem. B* **2005**, *109* (18), 8538–8542.

Shimoda, T.; Matsuki, Y.; Furusawa, M.; Aoki, T.; Yudasaka, I.; Tanaka, H.; Iwasawa, H.; Wang, D.; Miyasaka, M.; Takeuchi, Y. Solution-Processed Silicon Films and Transistors. *Nature* **2006**, *440*, 783–786.

Shin, N.; Chi, M.; Howe, J. Y.; Filler, M. a. Rational Defect Introduction in Silicon Nanowires. *Nano Lett.* **2013**, *13* (5), 1928–1933.

Shweky, I.; Aharoni, A.; Mokari, T.; Rothenberg, E.; Nadler, M.; Popov, I.; Banin, U. Seeded Growth of InP and InAs Quantum Rods Using Indium Acetate and Myristic Acid. *Mater. Sci. Eng. C* **2006**, *26* (5-7), 788–794.

Sigman, M. B.; Korgel, B. a. Strongly Birefringent Pb3O2Cl2 Nanobelts. *J. Am. Chem. Soc.* **2005**, *127* (28), 10089–10095.

Slater, M. D.; Kim, D.; Lee, E.; Johnson, C. S. Sodium-Ion Batteries. *Adv. Funct. Mater.* **2013**, *23*, 947–958.

Smith, B. W.; Luzzi, D. E. Electron Irradiation Effects in Single Wall Carbon Nanotubes. *J. Appl. Phys.* **2001**, *90*, 3509.

Smith, D. A.; Holmberg, V. C.; Korgel, B. A. Flexible Germanium Nanowires: Ideal Strength, Room Temperature Plasticity, and Bendable Semiconductor Fabric. *ACS Nano* **2010**, *4* (4), 2356–2362.

Smith, D. K.; Lee, D. C.; Korgel, B. a. High Yield Multiwall Carbon Nanotube Synthesis in Supercritical Fluids. *Chem. Mater.* **2006**, *18* (14), 3356–3364.

Steinhagen, C.; Akhavan, V. A.; Goodfellow, B. W.; Panthani, M. G.; Harris, J. T.; Holmberg, V. C.; Korgel, B. A. Solution-Liquid-Solid Synthesis of CuInSe 2 Nanowires and Their Implementation in Photovoltaic Devices. *ACS Appl. Mater. Interfaces* **2011**, *3* (5), 1781–1785.

Sun, J.; Buhro, W. E. The Use of Single-Source Precursors for the Solution-Liquid-Solid Growth of Metal Sulfide Semiconductor Nanowires. *Angew. Chem. Int. Ed. Engl.* **2008**, *47* (17), 3215–3218.

Sunkara, M. K.; Sharma, S.; Miranda, R.; Lian, G.; Dickey, E. C. Bulk Synthesis of Silicon Nanowires Using a Low-Temperature Vapor–liquid–solid Method. *Appl. Phys. Lett.* **2001**, *79*, 1546.

Sze, S. M.; Ng, K. K. *Physics of Semiconductor Devices*; John Wiley & Sons, 2006; Vol. 3.

Talapin, D. V; Lee, J. S.; Kovalenko, M. V; Shevchenko, E. V. Prospects of Colloidal Nanocrystals for Electronic and Optoelectronic Applications. *Chem. Rev.* **2010**, *110* (1), 389–458.

Tang, Y.; Zhang, Y.; Li, W.; Ma, B.; Chen, X. Rational Material Design for Ultrafast Rechargeable Lithium-Ion Batteries. *Chem. Soc. Rev.* **2015**.

Tang, Z.; Kotov, N. a; Giersig, M. Spontaneous Organization of Single CdTe Nanoparticles into Luminescent Nanowires. *Science* **2002**, *297* (5579), 237–240.

Tarascon, J. M.; Armand, M. Issues and Challenges Facing Rechargeable Lithium Batteries. *Nature* **2001**, *414* (6861), 359–367.

Taylor, B. R.; Kauzlarich, S. M.; Lee, H. W. H.; Delgado, G. R. Solution Synthesis of Germanium Nanocrystals Demonstrating Quantum Confinement. *Chem. Mater.* **1998**, *10* (1), 22–24.

Tersoff, J. Enhanced Solubility of Impurities and Enhanced Diffusion near Crystal Surfaces. *Phys. Rev. Lett.* **1995**, *74*, 5080–5083.

Thelander, C.; Agarwal, P.; Brongersma, S. Nanowire-Based One-Dimensional Electronics. *Mater. today* **2006**, *9* (10), 28–35.

Thombare, S. V.; Marshall, A. F.; McIntyre, P. C. Size Effects in Vapor-Solid-Solid Ge Nanowire Growth with a Ni-Based Catalyst. *J. Appl. Phys.* **2012**, *112* (5), 054325.

Tian, B.; Zheng, X.; Kempa, T. J.; Fang, Y.; Yu, N.; Yu, G.; Huang, J.; Lieber, C. M. Coaxial Silicon Nanowires as Solar Cells and Nanoelectronic Power Sources. *Nature* **2007**, *449* (7164), 885–889.

Tilley, R. D.; Warner, J. H.; Yamamoto, K.; Matsui, I.; Fujimori, H. Micro-Emulsion Synthesis of Monodisperse Surface Stabilized Silicon Nanocrystals. *Chem. Commun. (Camb).* **2005**, No. 14, 1833–1835.

Trentler, T. J.; Hickman, K. M.; Goel, S. C.; Viano, a. M.; Gibbons, P. C.; Buhro, W. E. Solution-Liquid-Solid Growth of Crystalline III-V Semiconductors: An Analogy to Vapor-Liquid-Solid Growth. *Science*, 1995, *270*, 1791–1794.

Tuan, H. Y.; Korgel, B. a. Importance of Solvent-Mediated Phenylsilane Decompositon Kinetics for High-Yield Solution-Phase Silicon Nanowire Synthesis. *Chem. Mater.* **2008**, *20* (4), 1239–1241.

Tuan, H. Y.; Lee, D. C.; Hanrath, T.; Korgel, B. A. Germanium Nanowire Synthesis: An Example of Solid-Phase Seeded Growth with Nickel Nanocrystals. *Chem. Mater.* **2005**, *17* (23), 5705–5711.

Tuan, H.-Y.; Lee, D. C.; Hanrath, T.; Korgel, B. A. Catalytic Solid-Phase Seeding of Silicon Nanowires by Nickel Nanocrystals in Organic Solvents. *Nano Lett.* **2005**, *5* (4), 681–684.

Tuan, H.-Y.; Lee, D. C.; Korgel, B. A. Nanocrystal-Mediated Crystallization of Silicon and Germanium Nanowires in Organic Solvents: The Role of Catalysis and Solid-Phase Seeding. *Angew. Chem. Int. Ed. Engl.* **2006**, *45* (31), 5184–5187.

Tuan, H.; Lee, D. C.; Hanrath, T.; Korgel, B. A. Germanium Nanowire Synthesis: An Example of Solid-Phase Seeded Growth with Nickel Nanocrystals. *Chem. Mater.* **2005**, *17*, 5705–5711.

Tutuc, E.; Appenzeller, J.; Reuter, M. C.; Guha, S. Realization of a Linear Germanium Nanowire P-N Junction. *Nano Lett.* **2006**, *6* (9), 2070–2074.

Van Sickle, A. R.; Miller, J. B.; Moore, C.; Anthony, R. J.; Kortshagen, U. R.; Hobbie, E. K. Temperature Dependent Photoluminescence of Size-Purified Silicon Nanocrystals. *ACS Appl. Mater. Interfaces* **2013**, *5*, 4233–4238.

Wagner, R. S.; Ellis, W. C. Vapor-Liquid-Solid Mechanism of Single Crystal Growth. *Appl. Phys. Lett.* **1964**, *4* (5), 89–90.

Wagner, R. S.; Ellis, W. C.; Jackson, K. A.; Arnold, S. M. Study of the Filamentary Growth of Silicon Crystals from the Vapor. *J. Appl. Phys.* **1964**, *35* (10), 2993.

Walser, R. M.; Bené, R. W. First Phase Nucleation in Silicon–transition-Metal Planar Interfaces. *Appl. Phys. Lett.* **1976**, *28* (10), 624.

Walsh, R. Bond Dissociation Energy Values in Silicon-Containing Compounds and Some of Their Implications. *Acc. Chem. Res.* **1981**, *14*, 246–252.

Wang, D.; Dai, H. Low-Temperature Synthesis of Single-Crystal Germanium Nanowires by Chemical Vapor Deposition. *Angew. Chemie - Int. Ed.* **2002**, *41* (24), 4783–4786.

Wang, F.; Buhro, W. E. An Easy Shortcut Synthesis of Size-Controlled Bismuth Nanoparticles and Their Use in the SLS Growth of High-Quality Colloidal Cadmium Selenide Quantum Wires. *Small* **2010**, *6* (4), 573–581.

Wang, F.; Dong, A.; Sun, J.; Tang, R.; Yu, H.; Buhro, W. E. Solution-Liquid-Solid Growth of Semiconductor Nanowires. *Inorg. Chem.* **2006**, *45* (19), 7511–7521.

Wang, F.; Tang, R.; Yu, H. Size-and Shape-Controlled Synthesis of Bismuth Nanoparticles. *Chem. …* **2008**, No. 28, 3656–3662.

Wang, F.; Tang, R.; Yu, H.; Gibbons, P. C.; Buhro, W. E. Size- and Shape-Controlled Synthesis of Bismuth Nanoparticles. *Chem. Mater.* **2008**, *20* (11), 3656–3662.

Wang, J. W.; He, Y.; Fan, F.; Liu, X. H.; Xia, S.; Liu, Y.; Harris, C. T.; Li, H.; Huang, J. Y.; Mao, S. X.; Zhu, T. Two-Phase Electrochemical Lithiation in Amorphous Silicon. *Nano Lett.* **2013**, *13* (2), 709–715.

Wang, J. W.; Liu, X. H.; Mao, S. X.; Huang, J. Y. Microstructural Evolution of Tin Nanoparticles during in Situ Sodium Insertion and Extraction. *Nano Lett.* **2012**, *12*, 5897–5902.

Wang, J. W.; Liu, X. H.; Zhao, K.; Palmer, A.; Patten, E.; Burton, D.; Mao, S. X.; Suo, Z.; Huang, J. Y. Sandwich-Lithiation and Longitudinal Crack in Amorphous Silicon Coated on Carbon Nanofibers. *ACS Nano* **2012**, *6*, 9158–9167.

Wang, L.; Liu, D.; Yang, S.; Tian, X.; Zhang, G.; Wang, W.; Wang, E.; Xu, Z.; Bai, X. Exotic Reaction Front Migration and Stage Structure in Lithiated Silicon Nanowires. *ACS Nano* **2014**, *8*, 8249–8254.

Wenzel, S.; Hara, T.; Janek, J.; Adelhelm, P. Room-Temperature Sodium-Ion Batteries: Improving the Rate Capability of Carbon Anode Materials by Templating Strategies. *Energy Environ. Sci.* **2011**, *4*, 3342.

Werner, M.; Mehrer, H.; Hochheimer, H. D. Effect of Hydrostatic Pressure, Temperature, and Doping on Self-Diffusion in Germanium. *Phys. Rev. B* **1985**, *32* (6), 3930–3937.

Wilcoxon, J. P.; Samara, G. a. Tailorable, Visible Light Emission from Silicon Nanocrystals. *Appl. Phys. Lett.* **1999**, *74* (21), 3164.

Wilson, W. L.; Szajowski, P. F.; Brus, L. E. Quantum Confinement in Size-Selected, Surface-Oxidized Silicon Nanocrystals. *Science* **1993**, *262* (5137), 1242–1244.

Witte, J.; Schnering, H. G.; Klemm, W. Das Verhalten Der Alkalimetalle Zu Halbmetallen. XI. Die Kristallstruktur von NaSi Und NaGe. *Zeitschrift für Anorg. und Allg. Chemie* **1964**, *327*, 260–273.

Wittmer, M.; Nicolet, M.-A.; Mayer, J. W. The First Phase to Nucleate in Planar Transition Metal-Germanium Interfaces. *Thin Solid Films* **1977**, *42* (1), 51–59.

Wong, F.; Dong, A.; Sun, J.; Tang, R.; Yu, H.; Buhro, W. E. Solution-Liquid-Solid Growth of Semiconductor Nanowires. *Inorg. Chem.* **2006**, *45*, 7511-7521.

Wooten, A. J.; Werder, D. J.; Williams, D. J.; Casson, J. L.; Hollingsworth, J. A. Solution-Liquid-Solid Growth of Ternary Cu-In-Se Semiconductor Nanowires from Multiple- and Single-Source Precursors. *J. Am. Chem. Soc.* **2009**, *131* (44), 16177–16188.

Wu, H.; Cui, Y. Designing Nanostructured Si Anodes for High Energy Lithium Ion Batteries. *Nano Today* **2012**, 414–429.

Wu, Y.-D.; Wong, C.-L. Substituent Effect on the Dissociation Energy of the Si-H Bond: A Density Functional Study. *J. Org. Chem.* **1995**, *60*, 821–828.

Wu, Y.; Yang, P. Direct Observation of Vapor-Liquid-Solid Nanowire Growth. *Journal of the American Chemical Society*, 2001, *123*, 3165–3166.

Xiao, L.; Cao, Y.; Xiao, J.; Wang, W.; Kovarik, L.; Nie, Z.; Liu, J. High Capacity, Reversible Alloying Reactions in SnSb/C Nanocomposites for Na-Ion Battery Applications. *Chem. Commun. (Camb).* **2012**, *48*, 3321–3323.

Xu, B.; Qian, D.; Wang, Z.; Meng, Y. S. Recent Progress in Cathode Materials Research for Advanced Lithium Ion Batteries. *Mater. Sci. Eng. R Reports* **2012**, *73*, 51–65.

Xu, M. Mechanistic Studies of the Thermal Decomposition of Metal Carbonyls on Ni(100) Surfaces in Connection with Chemical Vapor Deposition Processes. *J. Vac. Sci. Technol. A Vacuum, Surfaces, Film.* **1996**, *14* (2), 415.

Yang, C. S.; Bley, R. A.; Kauzlarich, S. M.; Lee, H. W. H.; Delgado, G. R. Synthesis of Alkyl-Terminated Silicon Nanoclusters by a Solution Route. *J. Am. Chem. Soc.* **1999**, *121* (22), 5191–5195.

Yang, H.-J.; Tuan, H.-Y. High-Yield, High-Throughput Synthesis of Germanium Nanowires by Metal–organic Chemical Vapor Deposition and Their Functionalization and Applications. *J Mater. Chem.* **2012**, *22*, 2215.

Yang, H.-J.; Yuan, F.-W.; Tuan, H.-Y. Vapor-Liquid-Solid Growth of Silicon Nanowires Using Organosilane as Precursor. *Chem. Commun. (Camb).* **2010**, *46* (33), 6105–6107.

Yang, H.; Huang, S.; Huang, X.; Fan, F.; Liang, W.; Liu, X. H.; Chen, L.-Q.; Huang, J. Y.; Li, J.; Zhu, T.; Zhang, S. Orientation-Dependent Interfacial Mobility Governs the Anisotropic Swelling in Lithiated Silicon Nanowires. *Nano Lett.* **2012**, *12*, 1953–1958.

Yoon, S.; Park, C.-M.; Sohn, H.-J. Electrochemical Characterizations of Germanium and Carbon-Coated Germanium Composite Anode for Lithium-Ion Batteries. *Electrochem. Solid-State Lett.* **2008**, *11* (4), A42.

Yu, H.; Buhro, W. E. Solution-Liquid-Solid Growth of Soluble GaAs Nanowires. *Adv. Mater.* **2003**, *15* (5), 416–419.

Yu, H.; Li, J.; Loomis, R. a; Wang, L.-W.; Buhro, W. E. Two- versus Three-Dimensional Quantum Confinement in Indium Phosphide Wires and Dots. *Nat. Mater.* **2003**, *2* (8), 517–520.

Yu, H.; Li, J.; Loomis, R. a.; Gibbons, P. C.; Wang, L. W.; Buhro, W. E. Cadmium Selenide Quantum Wires and the Transition from 3D to 2D Confinement. *J. Am. Chem. Soc.* **2003**, *125* (52), 16168–16169.

Yu, L.; O'Donnell, B.; Alet, P.-J.; Conesa-Boj, S.; Peiró, F.; Arbiol, J.; Cabarrocas, P. R. I. Plasma-Enhanced Low Temperature Growth of Silicon Nanowires and Hierarchical Structures by Using Tin and Indium Catalysts. *Nanotechnology* **2009**, *20* (22), 225604.

Yu, Y.; Hessel, C. M.; Bogart, T. D.; Panthani, M. G.; Rasch, M. R.; Korgel, B. a. Room Temperature Hydrosilylation of Silicon Nanocrystals with Bifunctional Terminal Alkenes. *Langmuir* **2013**, *29* (5), 1533–1540.

Yuan, F. W.; Tuan, H. Y. Supercritical Fluid-Solid Growth of Single-Crystalline Silicon Nanowires: An Example of Metal-Free Growth in an Organic Solvent. In *Crystal Growth and Design*; 2010; Vol. 10, pp 4741–4745.

Zeng, Z.; Liang, W.; Liao, H.; Xin, H.; Chu, Y.-H.; Zheng, H. Visualization of Electrode-Electrolyte Interfaces in LiPF6/EC/DEC Electrolyte for Lithium Ion Batteries via In-Situ TEM. *Nano Lett.* **2014**.

Zhang, W.-J. A Review of the Electrochemical Performance of Alloy Anodes for Lithium-Ion Batteries. *J. Power Sources* **2011**, *196* (1), 13–24.

Zhou, H.; Nanda, J.; Martha, S. K.; Unocic, R. R.; Meyer, H. M.; Sahoo, Y.; Miskiewicz, P.; Albrecht, T. F. Role of Surface Functionality in the Electrochemical Performance of Silicon Nanowire Anodes for Rechargeable Lithium Batteries. *ACS Appl. Mater. Interfaces* **2014**, *6* (10), 7607–7614.

Zhu, H. W.; Xu, C. L.; Wu, D. H.; Wei, B. Q.; Vajtai, R.; Ajayan, P. M. Direct Synthesis of Long Single-Walled Carbon Nanotube Strands. *Science* **2002**, *296* (5569), 884–886.

Vita

Xiaotang Lu was born in Huangshan, Anhui province of China, and lived there with her family until 2004. She graduated from Tunxi High School in 2004 and went on to attend the Nanjing University of Science and Technology, where she graduated with honors and a Bachelor of Chemistry in 2008. Upon graduation, she enrolled at Tsinghua University to pursue the Master of Science degree under supervision of Dr. Yadong Li and Dr. Qing Peng. In 2011, Xiaotang enrolled in the Material Science and Engineering graduate program at the University of Texas at Austin where she began her Ph. D. studies in semiconductor nanowires under the supervision of Dr. Brian A. Korgel.

The author can be reached at tarringlu@gmail.com

This dissertation was typed by the author.